Title
An analysis of electromicrobial production technologies for Earth and Space applications

Author
Abel, Anthony

Publication Date
2022

Peer reviewed|Thesis/dissertation

An analysis of electromicrobial production technologies for Earth and Space applications

By

Anthony J Abel

A dissertation submitted in partial satisfaction of the

requirements for the degree of

Doctor of Philosophy

in

Chemical Engineering

in the

Graduate Division

of the

University of California, Berkeley

Committee in charge:

Professor Douglas S. Clark, Chair
Professor Wenjun Zhang
Professor Adam P. Arkin

Spring 2022

Abstract

An analysis of electromicrobial production technologies for Earth and Space applications

by

Anthony Abel

Doctor of Philosophy in Chemical Engineering

University of California, Berkeley

Professor Douglas S. Clark, Chair

Biotechnological strategies for producing commodity chemicals from CO_2 instead of fossil fuels have traditionally relied on sugars derived from staple crops such as corn and sugarcane. Although this method has been demonstrated at large scales, substantially replacing fossil fuel feedstocks with crop-derived sugars would require dedicating a significant amount of arable land to the chemical industry instead of food production.

Anticipating abundant clean electricity generation from solar cells, wind turbines, or other renewable energy technologies in the near future, researchers have proposed that various electromicrobial production (EMP) processes could avoid the "food vs. fuel" conundrum of traditional bioprocessing strategies. Although nomenclature varies in the literature, I define EMP as any process that converts CO_2 into a value-added product (*i.e.*, contains some form of primary production), uses electricity as the primary source of energy driving that transformation, and uses microbes to produce the final product.

In this thesis, I develop multiphysics models to analyze and evaluate a variety of EMP processes using a comprehensive life cycle assessment (LCA) framework. In Chapter 2, I apply this method to "mediated" EMP systems that rely on molecular hydrogen (H_2), formic acid, and acetic acid as substrates for microbial growth and product formation. In these systems, electrolyzers produce the substrate molecules, which are then supplied to downstream bioreactors. This analysis indicated that all three EMP strategies could outcompete traditional bioprocessing if the electricity grid was sufficiently decarbonized and demonstrated that H_2-mediated EMP systems outperformed the other options. The latter result is due mainly to the high performance of water electrolysis compared to earlier-stage CO_2 electrolysis, so I also used the LCA framework to identify what performance metrics the CO_2 electrolyzer system would need to reach.

In Chapters 3, 4, and 5, I evaluate novel EMP strategies that integrate electrochemical and biochemical processes into a single reactor. In Chapter 3, I analyze formate-mediated EMP; In Chapters 4 and 5, I analyze EMP based on direct electron transfer from an electrode to the microbe. Based on current technology, neither of these strategies is able to outcompete their more well-established counterparts analyzed in Chapter 2. Therefore, I also discuss research avenues that may improve the performance of these strategies.

EMP processes have applications beyond simply those on Earth. As a member of the Center for the Utilization of Biological Engineering in Space (CUBES), I also analyzed EMP technologies for their ability to support exploratory human missions to Mars. These, and other processes necessary to support a human habitat, require a substantial amount of power. Therefore, in Chapter 6, I evaluate energy generation and storage options on Mars that would supply power to EMP processes for *in situ* resource utilization. I demonstrate that both miniaturized nuclear fission reactors and photovoltaic panels would adequately support a human habitat, and that solar panels would outcompete nuclear energy over ~50% of the planet's surface.

The results of this thesis develop a roadmap for deploying EMP processes on both Earth and Mars and indicate that "electrifying" biotechnology may have a key role to play in sustainable commodity chemical production in the future.

Table of Contents

Acknowledgements

A PhD thesis is an odd document to compile, and the Acknowledgements section is the oddest part to write. First, studying, reading, thinking, writing, learning, researching, resting, breathing, playing, *living* are all collaborative activities that co-constitute "me" and all the entities with which I am intra-acting (to borrow a phrase from Karen Barad), so to write a document on which my name appears alone seems to not do justice to all these entanglements. Second, even from a more traditional academic or Western scientific perspective, this thesis was collaboratively produced: three of the six chapters have first appeared elsewhere as co-first-authored papers between me and coworkers. Third, the structure of writing and reading in this language necessarily imposes a temporal hierarchy in who I acknowledge and how when no such hierarchy exists in my being. Fourth, to the extent that acknowledgements typically focus on people the author would like to thank, this section will highlight only the positive aspects of my experiences while in graduate school. As a result, it will miss half the story, and half of how "I" have come to be writing it. I can't resolve any of these contradictions, so I offer them here only as a simple declaration of their existence (an *acknowledgement*).

Research-related thanks go first. I am tremendously indebted to Jeremy Adams, with whom many of the ideas in this thesis were developed. Dr. Jacob Hilzinger is the reason I feel comfortable thinking through biology, and none of the work would have come out right without Dr. Kyle Sander's practical and pragmatic advice. Dr. Philomena Weng taught me how to use COMSOL, which is responsible for all but one of the chapters in this thesis. Aaron Berliner, Helen Bergstrom, Jorge Luis Meraz, Stefano Cestellos-Blanco, Joshua Hubbard, Kaitlyn Engler, George Makrygiorgos, Dr. Dawei Xu, Clintton Jessel, Jeremy Lee, and Christine Balolong were all instrumental in various parts (ranging from some to all) of my work. Doug Clark (my primary advisor) gave me a lot of freedom and support to pursue projects I was interested in and made sure all of "i"s were dotted and "t"s were crossed. Adam Arkin, who took on increasingly more of a mentorship role as my time in graduate school progressed, helped me to navigate both research and academia. Amor Menezes, Ali Mesbah, Lance Seefeldt, and Wenjun Zhang all supported my research and me as a researcher. The Center for the Utilization of Biological Engineering in Space (CUBES) was a fascinating research home, and my work was supported by them (through NASA) and by the National Science Foundation Graduate Research Fellowship Program.

In other semi-professional contexts, Helen Bergstrom, Adrian Davey, Meron Tesfaye, Jeremy Adams, Kerby Lynch, Katie Latimer, and Cole Rainey were incredible people to learn from and work with, and I will carry those experiences with me for the rest of my life. Dr. Dawei Xu, Jeff Reimer, and Markita Landry also provided valuable support, perspective, and advice.

The "I" writing this would not be here, nor would I have completed a PhD without Helen Bergstrom, John Abel, Joseph Abel, Alta Abel, John Meredith, Jeremy Adams, Adrian Davey, Meron Tesfaye, Nathan Tessema Ersaro, Nicole Ersaro, Joshua Hubbard, Victoria Sadowski, Marisa Watanabe, Fiona McBride, Cory Hargus, Ana Alvarez, Oded Ritov, Caroline Palmer, Matt Wong, Kaitlyn Engler, Bridgette LaFaye, Daniel Schoepflin, Patrick Bastian, Yannik Pitcan, Otto Kienitz, Mohamad Jarada, Isaac Berkowitz, Nat Goh, Pluto Sussman, El Talpense (formerly Celia's), Punjabi Dhaba, Thai Basil, Artichoke Basille's, Banh Mi & Rolls Factory, The Stuffed Inn, The New England Patriots, and The Pittsburgh Penguins. I cannot thank any of you enough.

Chapter 1: The promise of electromicrobial production

1.1 Context

Anthropogenic climate change is a significant challenge facing the world. Already some 4.5 million people die annually due to its impacts, disproportionately in Global South nations,[1] and rampant disease, flooding, and food and water insecurity are projected to generate more than 200 million climate refugees by 2050.[2] To prevent ever worsening effects, the Intergovernmental Panel on Climate Change (IPCC) urges limiting total global warming to 1.5 °C, which requires zero greenhouse gas emissions by ~2050.[3]

Such a rapid phase-out of fossil fuel consumption will require massive changes across the world economy, including in electricity generation, energy storage, transportation, construction, and commodity chemical production.[3,4] Moreover, it must account for and correct the continuing inequitable distribution of energy access and use among Global North and Global South states in order to meet sustainable development goals.[5,6]

A complete accounting of the necessary changes to the current political economic world-system is well beyond the scope of thesis. Here, I focus on a small subset of technologies that could replace portions of the existing chemical production industry. Although this thesis focuses on the scientific and technological development of processes that could sustainably produce commodity chemicals, I emphasize that complete and rapid adoption of a decarbonized world economy does not guarantee that sustainable development goals are achieved. In short, societal challenges are not addressed by technological development.

1.2 Towards a sustainable chemical industry

The commodity chemical industry is expected to be extremely challenging to decarbonize for several reasons. First, fossil fuels serve as the main feedstocks, so entirely new processes that rely on alternative feedstocks (*e.g.*, CO_2) will need to be developed and scaled.[7] Second, the current economic and technological paradigms favor large-scale facilities with large sunk capital costs, which will require incentives for "early retirement".[8] Third, although adopting processes that produce commodity chemicals from CO_2 could promote a "circular" carbon economy,[9] CO_2 sourced from power plant emissions or other fossil sources is significantly cheaper than CO_2 collected via direct air capture (DAC) devices.[10] Moreover, commodity chemical production from DAC-derived CO_2 can result in the perverse incentive to keep atmospheric concentrations of CO_2 high because capture costs are reduced as the atmospheric CO_2 concentration increases.[11] Nevertheless, developing processes that sustainably produce commodity chemicals from non-fossil feedstocks (atmospheric CO_2, N_2, and O_2; water, *etc.*) will be necessary to decarbonize the chemical industry.

Scientists and engineers have developed myriad strategies towards this goal. I categorize these efforts into three broad classes: (1) primarily or entirely biotechnological approaches; (2) primarily or entirely non-biological approaches; and (3) hybrid approaches that include some non-biological elements and some biotechnological ones (Fig. 1.1).

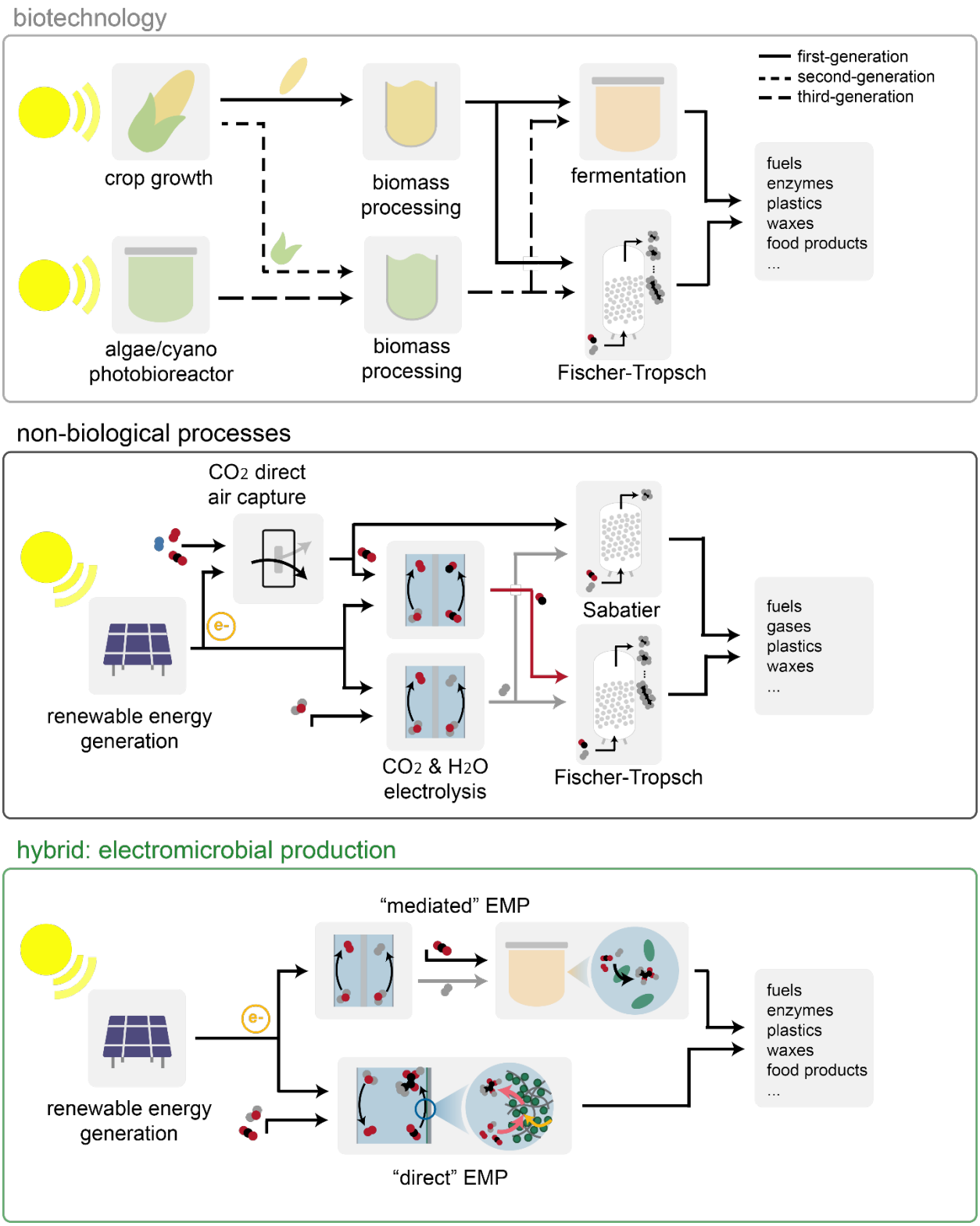

Figure 1.1. Overview of chemical production strategies from CO_2. Biotechnological (top), non-biological processes (middle), and hybrid (electromicrobial production) processes have all been proposed and experimentally demonstrated at a variety of scales.

Primarily biotechnological strategies comprise first-, second-, and some third-generation "biorefineries".[12,13] So-called "first-generation" biorefineries[12] rely on vegetable oils, corn or sugarcane-derived sugars, or similar primary agricultural products. Ethanol is probably the most well-known product of first-generation biorefineries, which is produced by *E. coli* or yeast species that ferment plant-derived sugars.[12,14] In addition to ethanol, dozens of products, including biodiesel, other fermentable molecules (*e.g.* lactic acid, the monomer of *poly*-lactic acid), therapeutic or industrial enzymes, among many others, can all be produced from plant-derived sugars.[14–16] Although this approach is relatively well-established and in some cases cost-effective, two main concerns have limited its adoption. First, this strategy requires dedicating food products (*e.g.*, corn, sugars, and vegetable oils) to fuels or commodity chemical production, a trade-off commonly referred to as the "food vs. fuel" debate.[12] Second, developing and dedicating significant amounts of additional arable land to such production can harm biodiversity and would likely rely on substantial water and fertilizer use, limiting the environmental benefits that could be derived from CO_2-based chemical production.

Second- and third-generation biorefinery concepts have sought to overcome the limitations imposed by the food vs. fuel debate. For example, strategies to convert non-food biomass such as lignocellulosic materials into fermentable sugars have been developed.[12,17] Alternative strategies for biomass production, for example *via* algal or cyanobacterial cultivation have also been developed.[18,19] Then, multiple techniques can be applied to convert this material into fuels or feedstocks for downstream chemical synthesis.[12] These strategies may overcome some of the environmental trade-offs of first-generation biorefineries by making use of marginal resources or marginal land. However, the low efficiency of photosynthetic organisms at capturing and converting light energy may limit the otherwise broad applicability of this approach.[20,21]

In parallel to primarily biotechnological strategies, researchers have also pursued purely abiotic approaches (Fig. 1.1).[22–26] In these systems, renewable energy sources (*e.g.*, solar, wind, hydro, or geothermal) are used to power electrochemical reduction of water to H_2, various electrochemical or physicochemical CO_2 reduction strategies, CO_2 capture, and downstream conversion or processing steps. Abiotic strategies can take advantage of the high efficiency of solar or wind-derived electricity generation. In addition, these processes can be readily integrating into existing chemical facilities. For example, H_2 (produced from water electrolysis) and CO (produced by CO_2 electroreduction) can be mixed in appropriate ratio to generate syngas and supplied to existing Fischer-Tropsch processes.[23] Alternatively, CO_2 can be reduced with H_2 to produce synthetic natural gas in the Sabatier reaction, which can directly replace existing natural gas production.[24] However, catalyst stability or availability, low selectivity for more complex or larger molecules, and (in some cases) requirements for high pressure or temperature, all present potential challenges to the promise of such non-biological strategies for CO_2-based chemical production.

In recent years, hybrid abiotic/biotechnological approaches to CO_2-derived commodity chemical production have been pursued (Fig. 1.1).[20,26–32] This strategy is commonly referred to as "electromicrobial production" (EMP), which I define as any process that converts CO_2 into a value-added product (*i.e.*, contains some form of primary production), uses electricity as the primary source of energy driving that transformation, and uses microbes to produce the final product. Hence, several related, but distinct, technologies fall under two broad categories I define as "mediated" EMP and "direct" EMP (Fig. 1.2). In mediated systems, electricity is first used to

generate some reduced mediator molecule, which microbes then oxidize to derive the energy and electrons necessary to reduce CO_2. Several mediator molecules have been proposed and experimentally demonstrated, including H_2,[28,33,34] CO or syngas,[35–37] formate/ic acid,[38–40] methane and/or methanol,[39,41,42] humic substances or quinones,[43] and ferrous iron.[44] Mediator molecule production can occur either upstream in dedicated reactors (*e.g.*, CO_2 electrolyzers producing CO or formic acid),[45,46] or by co-locating electrochemical reduction and microbial growth in the same reactor (Fig. 1.2).[27,28] In direct systems, electrons are passed directly into cellular energy pools by electron conduit proteins that traverse the cell wall and make direct electrical contact with the cathode (Fig. 1.2).[30,47–50] In either case, EMP strategies have been pursued because they aim to couple highly efficient abiotic energy harvesting (solar and wind) with the selectivity and durability of whole-cell biocatalysis.[29] However, EMP processes are largely at a nascent stage, so scale-up pathways and the relative viability of these approaches compared to each other and to competing strategies are unclear.[51]

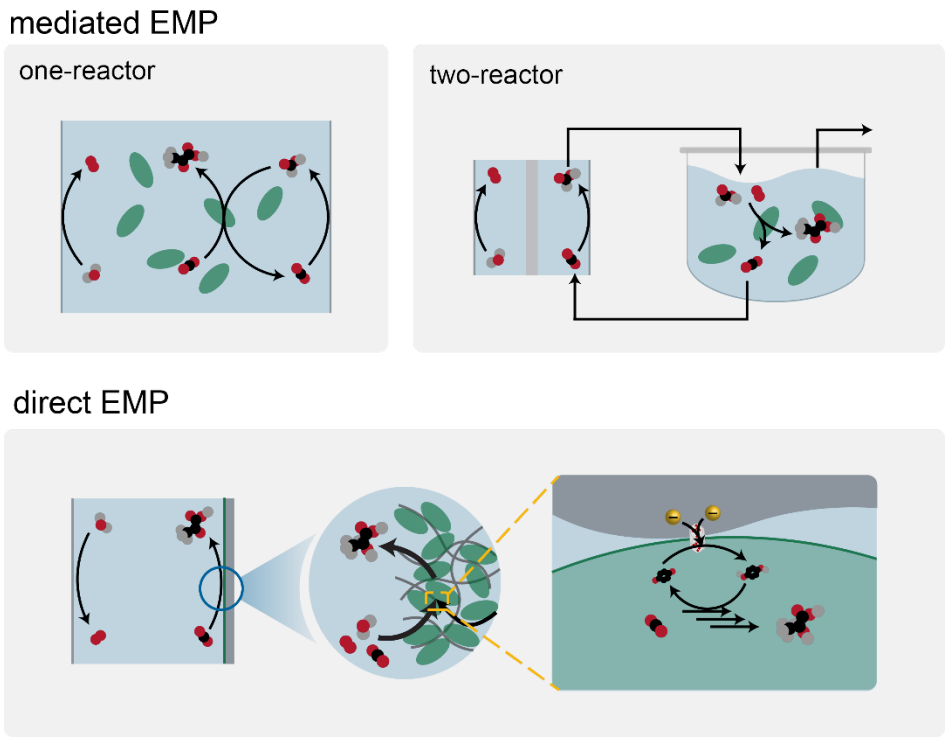

Figure 1.2. Electromicrobial production (EMP) strategies. Mediated (top) one-reactor and two-reactor systems rely on transfer of reducing power through a mediator molecule. Direct (bottom) systems transfer electrons through proteins that make direct electrical contact with the cathode.

1.3 Roadmap

In this thesis, I am to reduce this gap in the literature. I develop multiphysics models to analyze and evaluate a variety of EMP processes using a comprehensive life cycle assessment (LCA) framework. In Chapter 2, I apply this method to three of the most common mediated EMP systems. The analysis indicated that all three could outcompete a first-generation biorefinery strategy if the electricity grid was sufficiently decarbonized and demonstrated that H_2-mediated

systems outperformed the other options. In Chapter 3, I compare the co-location of electrochemical CO_2 reduction with microbial growth in one reactor to upstream CO_2 reduction to formate followed by subsequent formatotrophic growth in a downstream bioreactor and show that the decoupled (two-reactor) system outperforms the co-located (one reactor) system. In Chapters 4 and 5, I analyze the direct EMP strategy. First, in Chapter 4, I identify microbial physiology and reactor design strategies that can result in the most productive system. Second, in Chapter 5, I show that significant and unavoidable engineering challenges likely preclude the direct strategy from competing with H_2-mediated EMP.

Finally, in Chapter 6, I take a small ~156-million-mile (at the time of writing) detour. The research in this thesis was performed as part of the Center for the Utilization of Biological Engineering in Space, which aims to develop biotechnological strategies for *in situ* resource utilization on Mars.[52] Because the Martian atmosphere is composed of ~95% CO_2,[53] commodity chemical production on Mars can proceed in a largely similar fashion to that of a circular carbon economy on Earth. However, energy generation strategies may be quite different: the Martian atmosphere is too thin for wind to be a primary energy source,[54] and the Martian atmosphere, temperature, and distance from Earth combine to cause significant changes in the behavior of solar panels.[55] Hence, in Chapter 6, I analyze different energy generation and storage options for a crewed mission to Mars, and demonstrate that both nuclear fission and solar cells coupled to water electrolysis for energy storage in H_2 would be viable approaches for such an endeavor.

1.4 References

1 DARA and Climate Vulnerable Forum, *Climate Vulnerability Monitor: A Guide to the Cold Calculus of a Hot Planet*, 2nd edn., 2012.

2 V. Clement, K. K. Rigaud, A. de Sherbinin, B. Jones, S. Adamo, J. Schewe, N. Sadiq and E. SHabahat, *Groundswell Part 2: Acting on Internail Climate Migration*, Washington, DC, 2021.

3 *Global warming of 1.5°C: An IPCC Special Report*, Intergovernmental Panel on Climate Change, 2018, vol. 2.

4 M. Z. Jacobson, M. A. Delucchi and M. A. Cameron, *One Earth*, 2019, **1**, 449–463.

5 F. Sultana, *Polit. Geogr.*, 2022, 102638.

6 *Transforming our world: the 2030 Agenda for Sustainable Development*, United Nations, A/RES/70/1., 2015.

7 P. G. Levi and J. M. Cullen, *Environ. Sci. Technol.*, 2018, **52**, 1725–1734.

8 Z. J. Schiffer and K. Manthiram, *Joule*, 2017, **1**, 10–14.

9 R. G. Grim, Z. Huang, M. T. Guarnieri, J. R. Ferrell, L. Tao and J. A. Schaidle, *Energy Environ. Sci.*, 2020, **13**, 472–494.

10 M. Fasihi, O. Efimova and C. Breyer, *J. Clean. Prod.*, 2019, **224**, 957–980.

11 A. Malm and W. Carton, *Hist. Mater.*, 2021, **354**, 1–46.

12 S. N. Naik, V. V. Goud, P. K. Rout and A. K. Dalai, *Renew. Sustain. Energy Rev.*, 2010, **14**, 578–597.

13 Z. Liu, K. Wang, Y. Chen, T. Tan and J. Nielsen, *Nat. Catal.*, 2020, **3**, 274–288.

14 T. Werpy and G. Petersen, *Top Value Added Chemicals from Biomass Volume I-Results of Screening for Potential Candidates from Sugars and Synthesis Gas*, 2004.

15 J. Puetz and F. M. Wurm, *Processes*, 2019, **7**, 476.

16 J. D. Adams, J. J. Røise, D. S. Lee and N. Murthy, *Chem. Commun.*, 2020, **56**, 3175–3178.
17 M. Hess, A. Sczyrba, R. Egan, T.-W. Kim, H. Chokhawala, G. Schroth, S. Luo, D. S. Clark, F. Chen, T. Zhang, R. I. Mackie, L. A. Pennacchio, S. G. Tringe, A. Visel, T. Woyke, Z. Wang and E. M. Rubin, *Science (80-.).*, 2011, **331**, 463–467.
18 J. Quinn, L. de Winter and T. Bradley, *Bioresour. Technol.*, 2011, **102**, 5083–5092.
19 W. Du, F. Liang, Y. Duan, X. Tan and X. Lu, *Metab. Eng.*, 2013, **19**, 17–25.
20 N. J. Claassens, D. Z. Sousa, V. A. P. M. Dos Santos, W. M. De Vos and J. Van Der Oost, *Nat. Rev. Microbiol.*, 2016, **14**, 692–706.
21 R. E. Blankenship, D. M. Tiede, J. Tiede, G. W. Barber, G. Brudvig, M. Fleming, M. R. Ghirardi, W. Gunner, D. M. Junge, A. Kramer, T. A. Melis, C. C. Moore, D. G. Moser, A. J. Nocera, D. R. Nozik, W. W. Ort, R. C. Parson, R. T. Prince and Sayre, *Science (80-.).*, 2011, **332**, 805–809.
22 M. Jouny, W. Luc and F. Jiao, *Ind. Eng. Chem. Res.*, 2018, **57**, 2165–2177.
23 J. M. Spurgeon and B. Kumar, *Energy Environ. Sci.*, 2018, **11**, 1536–1551.
24 D. Parra, X. Zhang, C. Bauer and M. K. Patel, *Appl. Energy*, 2017, **193**, 440–454.
25 M. Götz, J. Lefebvre, F. Mörs, A. McDaniel Koch, F. Graf, S. Bajohr, R. Reimert and T. Kolb, *Renew. Energy*, 2016, **85**, 1371–1390.
26 P. De Luna, C. Hahn, D. Higgins, S. A. Jaffer, T. F. Jaramillo and E. H. Sargent, *Science (80-.).*, , DOI:10.1126/science.aav3506.
27 H. Li, P. H. Opgenorth, D. G. Wernick, S. Rogers, T. Wu, W. Higashide, P. Malati, Y. Huo, K. M. Cho and J. C. Liao, *Science (80-.).*, 2012, **335**, 1596.
28 C. Liu, B. C. Colón, M. Ziesack, P. A. Silver and D. G. Nocera, *Science (80-.).*, 2016, **352**, 1210–1213.
29 N. J. Claassens, C. A. R. Cotton, D. Kopljar and A. Bar-Even, *Nat. Catal.*, 2019, **2**, 437–447.
30 R. Karthikeyan, R. Singh and A. Bose, *J. Ind. Microbiol. Biotechnol.*, 2019, **46**, 1419–1426.
31 K. P. Nevin, T. L. Woodard, A. E. Franks, Z. M. Summers and D. R. Lovley, *MBio*, 2010, **1**, 330–338.
32 W. Bai, T. O. Ranaivoarisoa, R. Singh, K. Rengasamy and A. Bose, *Commun. Biol.*, 2021, **4**, 1–16.
33 C. Windhorst and J. Gescher, *Biotechnol. Biofuels*, 2019, **12**, 163.
34 C. Kantzow, A. Mayer and D. Weuster-Botz, *J. Biotechnol.*, 2015, **212**, 11–18.
35 F. R. Bengelsdorf, M. H. Beck, C. Erz, S. Hoffmeister, M. M. Karl, P. Riegler, S. Wirth, A. Poehlein, D. Weuster-Botz and P. Dürre, *Adv. Appl. Microbiol.*, 2018, **103**, 143–221.
36 K. Asimakopoulos, H. N. Gavala and I. V. Skiadas, *Chem. Eng. J.*, 2018, **348**, 732–744.
37 F. E. Liew, R. Nogle, T. Abdalla, B. J. Rasor, C. Canter, R. O. Jensen, L. Wang, J. Strutz, P. Chirania, S. De Tissera, A. P. Mueller, Z. Ruan, A. Gao, L. Tran, N. L. Engle, J. C. Bromley, J. Daniell, R. Conrado, T. J. Tschaplinski, R. J. Giannone, R. L. Hettich, A. S. Karim, S. D. Simpson, S. D. Brown, C. Leang, M. C. Jewett and M. Köpke, *Nat. Biotechnol.*, , DOI:10.1038/s41587-021-01195-w.
38 O. Yishai, S. N. Lindner, J. Gonzalez de la Cruz, H. Tenenboim and A. Bar-Even, *Curr. Opin. Chem. Biol.*, 2016, **35**, 1–9.
39 S. Kim, S. N. Lindner, S. Aslan, O. Yishai, S. Wenk, K. Schann and A. Bar-Even, *Nat. Chem. Biol.*, 2020, **16**, 538–545.

40 N. J. Claassens, G. Bordanaba-Florit, C. A. R. Cotton, A. De Maria, M. Finger-Bou, L. Friedeheim, N. Giner-Laguarda, M. Munar-Palmer, W. Newell, G. Scarinci, J. Verbunt, S. T. de Vries, S. Yilmaz and A. Bar-Even, *bioRxiv*, 2020, 2020.03.11.987487.
41 T. Gassler, M. Sauer, B. Gasser, M. Egermeier, C. Troyer, T. Causon, S. Hann, D. Mattanovich and M. G. Steiger, *Nat. Biotechnol.*, 2020, **38**, 210–216.
42 J. L. Meraz, K. L. Dubrawski, S. H. El Abbadi, K. H. Choo and C. S. Criddle, *J. Environ. Eng.*, , DOI:10.1061/(ASCE)EE.1943-7870.0001703.
43 D. R. Lovley, J. L. Fraga, J. D. Coates and E. L. Blunt-Harris, *Environ. Microbiol.*, 1999, **1**, 89–98.
44 J. Guan, S. A. Berlinger, X. Li, Z. Chao, V. Sousa e Silva, S. Banta and A. C. West, *J. Biotechnol.*, 2017, **245**, 21–27.
45 H. Yang, J. J. Kaczur, S. D. Sajjad and R. I. Masel, *J. CO2 Util.*, 2017, **20**, 208–217.
46 L. C. Weng, A. T. Bell and A. Z. Weber, *Energy Environ. Sci.*, 2019, **12**, 1950–1968.
47 A. R. Rowe, S. Xu, E. Gardel, A. Bose, P. Girguis, J. P. Amend and M. Y. El-Naggar, *MBio*, 2019, **10**, 1659–1677.
48 A. R. Rowe, P. Rajeev, A. Jain, S. Pirbadian, A. Okamoto, J. A. Gralnick, M. Y. El-Naggar and K. H. Nealson, *MBio*, 2018, **9**, 1–19.
49 Y. Jiao and D. K. Newman, *J. Bacteriol.*, 2007, **189**, 1765–1773.
50 T. Ishii, S. Kawaichi, H. Nakagawa, K. Hashimoto and R. Nakamura, *Front. Microbiol.*, 2015, **6**, 994.
51 A. Prévoteau, J. M. Carvajal-Arroyo, R. Ganigué and K. Rabaey, *Curr. Opin. Biotechnol.*, 2020, **62**, 48–57.
52 A. J. Berliner, J. M. Hilzinger, A. J. Abel, M. J. McNulty, G. Makrygiorgos, N. J. H. Averesch, S. Sen Gupta, A. Benvenuti, D. F. Caddell, S. Cestellos-Blanco, A. Doloman, S. Friedline, D. Ho, W. Gu, A. Hill, P. Kusuma, I. Lipsky, M. Mirkovic, J. Luis Meraz, V. Pane, K. B. Sander, F. Shi, J. M. Skerker, A. Styer, K. Valgardson, K. Wetmore, S.-G. Woo, Y. Xiong, K. Yates, C. Zhang, S. Zhen, B. Bugbee, D. S. Clark, D. Coleman-Derr, A. Mesbah, S. Nandi, R. M. Waymouth, P. Yang, C. S. Criddle, K. A. McDonald, L. C. Seefeldt, A. A. Menezes and A. P. Arkin, *Front. Astron. Sp. Sci.*, 2021, **8**, 1–14.
53 C. R. Webster, P. R. Mahaffy, G. J. Flesch, P. B. Niles, J. H. Jones, L. A. Leshin, S. K. Atreya, J. C. Stern, L. E. Christensen, T. Owen, H. Franz, R. O. Pepin and A. Steele, *Science (80-.).*, 2013, **341**, 260–263.
54 V. Schorbach and T. Weiland, *Acta Astronaut.*, 2022, **191**, 472–478.
55 G. Landis, T. Kerslake, D. Scheiman and P. Jenkins, 2012, 1–10.

Chapter 2: A comparative analysis of electromicrobial production systems[†]

2.1 Abstract

Electromicrobial production (EMP) processes, in which electricity or electrochemically-derived mediator molecules serve as energy sources to drive biochemical processes, represent and attractive strategy for the conversion of CO_2 into carbon-based products. However, these systems have yet to be employed on an industrial scale, limiting our understanding of their potential performance and environmental benefits/impacts. In this chapter, I describe the development and application of a comprehensive framework to analyze EMP systems relying on reactor, process, and life cycle impact models. This framework is used to analyze three proposed EMP systems relying on formate, H_2, and acetate as intermediate molecules, each producing three hypothetical products: biomass, lactic acid, and industrial enzymes. Physics-based bioreactor models predict that EMP systems can achieve productivities up to 0.65 g/L/h for biomass production and 0.42 g/L/h for the production of lactic acid. Despite improved solubility of formate as a substrate, formate-fed EMP systems do not lead to improved productivities compared to H_2-fed systems due to O_2 gas-liquid mass transfer limitations (for biomass and enzymes) or salinity-induced toxicity issues (for lactic acid). Life cycle impact model results demonstrated that EMP systems can achieve a smaller carbon footprint than traditional bioprocessing strategies provided the electric grid supplying electricity to the EMP system is composed of at least 90% renewable energy sources. For each of the three products I consider, the H_2-mediated Knallgas bacteria system achieves the lowest overall global warming potential, indicating that this EMP strategy may be best-suited for industrial efforts based on current technology. I also identify environmental hotspots and process limitations that are key targets for future engineering and research efforts for each EMP system. This analysis demonstrates the utility of an integrated assessment framework and should help guide the design of working, scalable, and sustainable EMP systems.

2.2 Introduction

Ongoing and worsening ecological and humanitarian crises caused by anthropogenic climate change have precipitated efforts to transition away from fossil fuel-based commodity chemical production. Whole-cell biocatalysis provides a theoretically carbon neutral method of producing value-added products if all of the required carbon is originally fixed from atmospheric carbon dioxide (CO_2). Many petroleum-based products including fuels, plastics, and commodity chemicals can be produced biologically.[1–3] Moreover, some products, such as proteins, can only be produced biologically and have wide-ranging applications including in food production, chemical sensing, and as therapeutics.[4–6] Traditional bioprocesses rely on heterotrophic microbes that require exogenous sources of carbon and energy (Fig. 2.1).

[†]This chapter was originally submitted as a preprint to *bioRxiv* and has been adapted with permission from the coauthors

Glucose from corn starch and sucrose from sugarcane are currently the most common feedstocks in bioprocessing. These biochemical processes rely on extensive agricultural production and therefore compete with the food supply and require land use changes that have significant negative impacts on the environment. Moreover, the high carbon footprint associated with fertilizer production and application, especially when growing corn as a feedstock, causes traditional bioprocesses to have a relatively high carbon footprint. To alleviate some of these challenges, researchers have proposed cyanobacteria and algae as alternative microorganisms to be used in bioprocessing, and have demonstrated photosynthetic production of fuels, plastics, and pharmaceuticals.[7] However, these systems are still limited by slow growth rates and the relatively inefficient energy conversion of photosynthesis.[8] To overcome these shortcomings, and with the expectation of cheaper and cleaner electricity in the intermediate future, various electromicrobial production (EMP) processes have been proposed and demonstrated (Fig. 2.1).

Although nomenclature for bioelectrochemical systems varies in the literature, I define EMP processes as any process that converts CO_2 into a value-added product (*i.e.*, contains some form of primary production), uses electricity as the primary source of energy driving that transformation, and uses microbes to produce the final product. Perhaps most notable are systems based on Knallgas (aerobic hydrogen-oxidizing) bacteria, such as *Cupriavidus necator*, which use molecular hydrogen (H_2), produced by the electrolysis of water, to fix CO_2. *C. necator* has historically been studied for production of its natively-produced polymer polyhydroxybutyrate (PHB)[9] and of biomass for use as a single cell protein.[10] More recently, *C. necator* has been engineered to produce other carbonaceous products including fuels and commodity chemicals.[11–13] As an alternative, formatotrophic microorganisms have been employed, in which formic acid produced from the electrochemical reduction of CO_2 is used as an energy source or assimilated by microbes to produce value-added products.[14–16] Naturally formatotrophic microbes such as *C. necator* have been studied for this purpose,[17] as have organisms engineered to express formate-assimilating pathways.[18] Two-step systems have also been developed based on bio-acetate as an intermediary molecule, in which CO_2 and H_2 are consumed by the acetogen *Sporomusa ovata* to produce acetate, which is then converted by a heterotroph such as *E. coli* to produce various value-added products.[19,20] Other EMP strategies are possible; however, the three EMP systems described here are well-represented in the literature and have been employed for a wide variety of products through genetic engineering.

To date, research efforts have focused primarily on studying the fundamental metabolisms that permit EMP processes or on engineering metabolic pathways to enable production of specific products in relevant microbial chassis. Despite these successful bench-scale demonstrations, progress towards scaled and integrated processes has remained limited. Moreover, rigorous calculations of productivity and efficiency limits that can enable comparisons among EMP processes have been elusive, in part due to significantly different operating conditions across laboratories. Physics-based models that capture relevant phenomena (microbial growth, production and consumption of species, acid/base reactions, gas/liquid mass transfer, *etc.*) can enable like-to-like comparisons across EMP processes. Additionally, such models are necessary to quantify design and operation strategies that optimize performance and to identify process parameters that limit productivity and efficiency.

To that end, several computational analyses of EMP processes have been developed. Claassens *et al.* developed a data-driven analysis to calculate metabolic efficiencies and to quantify the specific growth rates of organisms relying on H_2, formate, acetate, and other substrates for biomass formation.[21] Salimijazi *et al.* developed thermodynamic models of metabolism in a variety of EMP systems based on direct electron transfer or H_2-mediated growth.[22] They used their model to calculate the limiting efficiency of these EMP systems and the relative area necessary for photovoltaic cells and bioreactors. Recently, Leger *et al.* compared biomass production efficiency for photovoltaics-driven EMP using H_2, formate, and methanol as mediator molecules.[23] Their analysis included quantification of biomass yields and energy demands for supporting processes such as carbon capture and electrolysis. They demonstrated that EMP-based biomass production could use sunlight more efficiently than crop growth. Because these analyses focused on quantifying metabolic limits to energy efficiency, their analyses did not consider other factors that may induce upper-bounds on the productivity or practical efficiency, including gas-liquid mass transfer, pH control, and salinity effects.

EMP systems also rely on subprocesses, such as electrocatalysis and carbon capture, that are outside the purview of most literature that focuses on the microbial and biochemical reaction engineering components of these processes. While metabolic efficiencies, productivities, and yields of these systems may be compared, these analyses do not consider differences in electrocatalytic efficiencies and productivities that affect the viability of the process as a whole. Hence, development of end-to-end process models that rely on the material and energy balances quantified in individual reactor models is necessary for a comprehensive analysis of the relative merits of EMP process options.

Life cycle assessment (LCA) is a tool for quantifying the environmental impact of products and processes across their entire life cycle in relevant categories including greenhouse gas emissions, human and environmental health effects, and resource depletion. LCAs, which follow the standards set by ISO 14040 and 14044,[24,25] aggregate and analyze material and energy flows as well as emissions from every step in the supply chain within a given system boundary and quantify the impact of a process in the desired categories. LCAs aid in decision-making in process design as they can be used to evaluate the environmental impacts of multiple alternatives and inform strategies to lower their footprints. Life cycle assessment has been critical in evaluating the environmental tradeoffs of biochemical production strategies, particularly in the development of biofuels.[7,26,27] Because EMP systems have been proposed as more sustainable alternatives to traditional bioprocesses, conducting LCAs on these systems is a crucial tool in assessing these claims. Principles of life cycle assessment have been applied to analyze EMP systems to date. For example, Nangle *et al.* included land use calculations in addition to demonstrating lithoautotrophic production of novel chemicals.[28] Leger *et al.* recently produced a comprehensive analysis of energy and land occupation footprints in the electromicrobial production of single-celled protein (SCP),[23] expanding on similar assessments of SCP production[29,30]. However, comprehensive life cycle assessments that simultaneously consider various EMP pathways, products, and impact categories to develop broad insights to the field are still needed.

In this chapter, I present a detailed LCA of three major EMP process options relying respectively on acetate, H_2, and formate/ic acid as mediator molecules and compare their impacts to a traditional bioprocessing scheme relying on corn-derived glucose (Fig. 2.1). I chose biomass,

enzymes, and lactic acid as examples to represent the breadth of products that can be manufactured by EMP systems. Biomass is useful as a reference product to assess energy demands solely to grow the bacteria. Enzymes are useful representatives of low yield, high value biomacromolecules while lactic acid is a good example of a low-value, high yield commodity chemical. To enable this analysis, I developed two-phase bioreactor models that describe microbial growth and product formation, acid/base reactions, gas/liquid mass transfer, gas and liquid phase flow, and active pH control. The models are used to evaluate the effects of reactor parameters and operating conditions on critical performance metrics including productivity, titer, and material and energy efficiency, and are coupled to process models that present a complete picture of material and energy demands for the EMP processes. The analysis demonstrates the utility of integrating reactor, process, and life cycle impact models for comprehensively evaluating biotechnological processes. Together, the presented models, methodology, and analysis provide a framework for analyzing EMP systems that can help enable working, scalable, and sustainable electromicrobial production processes.

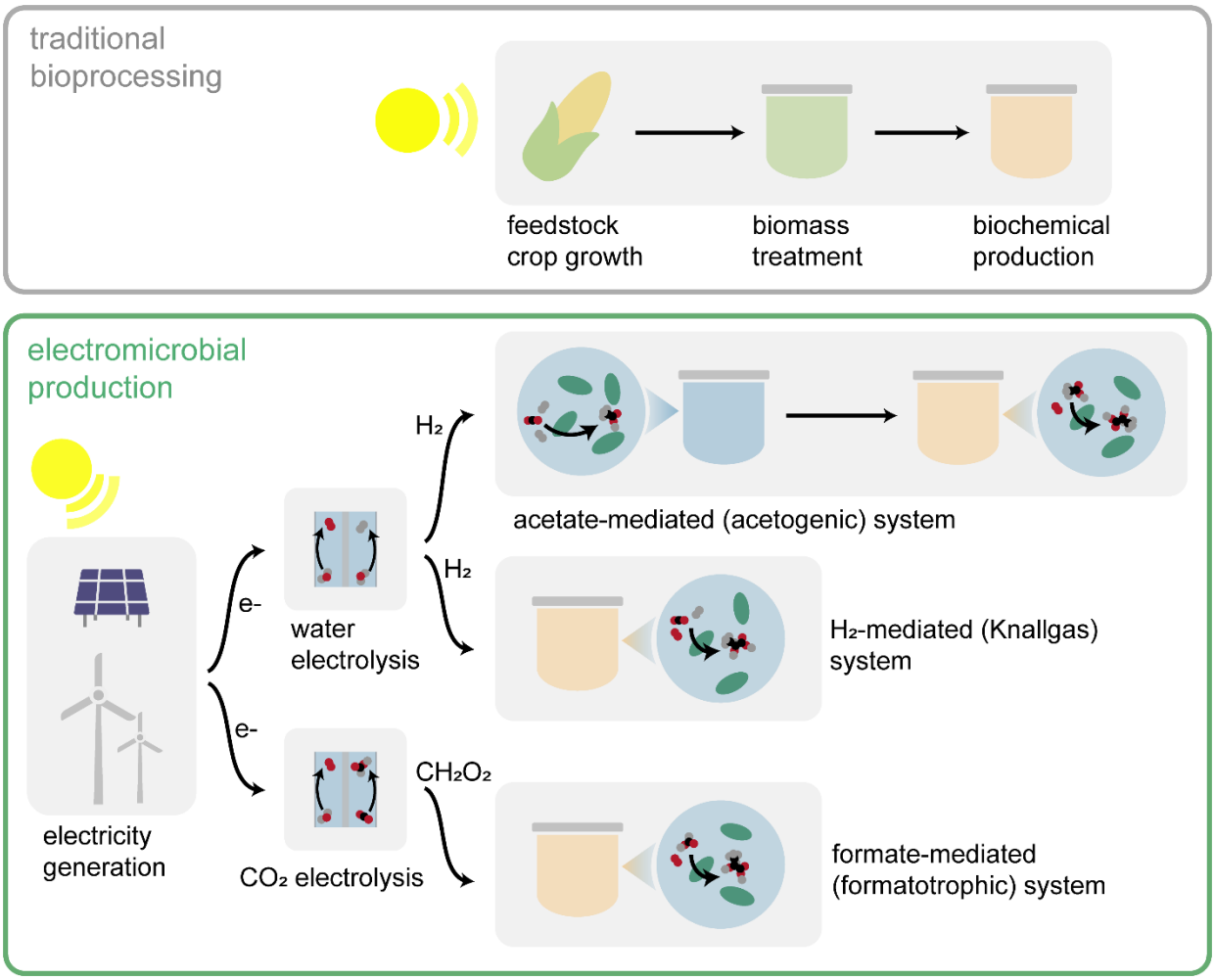

Figure 2.1. Overview of traditional bioprocessing and electromicrobial production. Traditional bioprocessing relies on feedstock crop growth, pretreatment of the resulting biomass (typically enzymatic or chemical), and subsequent biochemical production using crop-derived sugars as the feedstock. Electromicrobial production uses electricity (ideally renewable) to produce energy substrates (*e.g.,* H_2) for biochemical production from CO_2.

2.3 Computational Methods

All bioreactor models (Fig. 2.2a) assume well-mixed gas and liquid phases that are exchanged at fixed liquid- and gas-phase dilution rates. In the liquid phase, we consider, where relevant, dissolved CO_2, dissolved H_2, dissolved O_2, bicarbonate anions (HCO_3^-), carbonate anions (CO_3^{2-}), protons (H^+), hydroxide anions (OH^-), sodium cations (Na^+), chloride anions (Cl^-), formic acid (HCOOH), formate ($HCOO^-$), acetic acid ($H_3C_2O_2H$), acetate anions ($H_3C_2O_2^-$), lactic acid ($H_5C_3O_3H$), lactate anions ($H_5C_3O_3^-$), enzyme (E), and microbes (X). In the gas phase, the model considers CO_2, H_2, and O_2. By neglecting ammonium/a species, I have assumed they are fed in excess to the liquid phase as NH_3.

The well-mixed phases are assumed to have sufficient convective mixing such that no concentration gradients are formed. Such an open, well-mixed system must satisfy mass conservation, given generally for the liquid phase as

$$\frac{dc_i}{dt} = R_{\mathrm{X},i} + R_{\mathrm{A-B},i} + R_{\mathrm{LF},i} + R_{\mathrm{G-L},i} + R_{\mathrm{pH},i} \tag{1}$$

and for the gas phase as

$$\frac{dp_i}{dt} = RT(R_{\mathrm{GF},i} - R_{\mathrm{G-L},i}) \tag{2}$$

where c_i is the concentration, p_i is the partial pressure, R_i is the net volumetric rate of formation and consumption due to microbial growth (X), acid/base reactions (A–B), liquid or gas flow (LF/GF), gas/liquid mass transfer (G–L), and pH control (pH) for species i (Fig. 2.2a). The operating temperature is given by T, and R is the gas constant. Note that the gas phase species are assumed to follow ideal behavior and that the liquid and gas volumes in the reactor are equal.

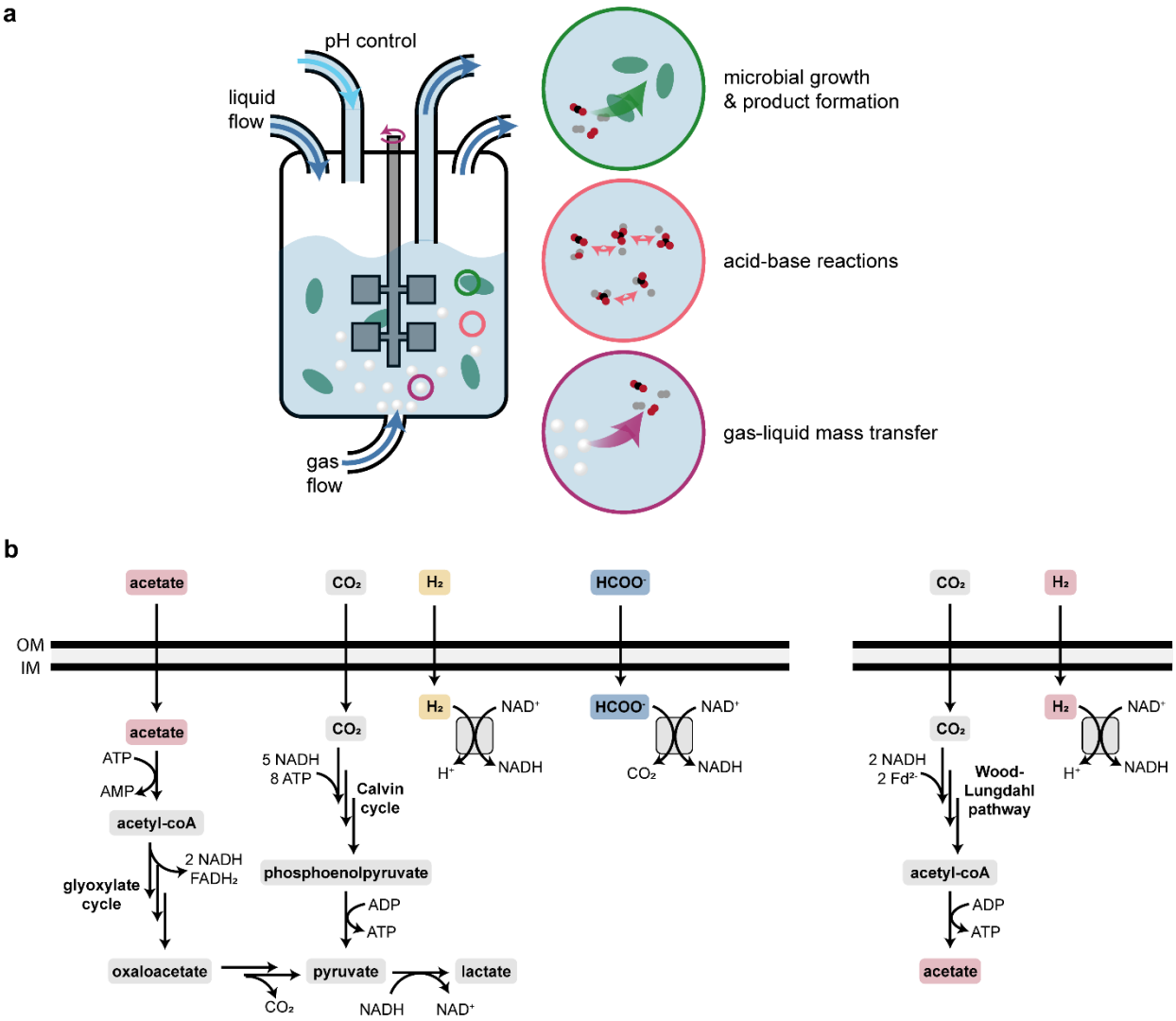

Figure 2.2. Overview of reactor model and metabolic pathways. (**a**) Bioreactor scheme. Gas and liquid media (dark blue arrows) are fed to and extracted from a two-phase, well-mixed bioreactor. The model considers gas-liquid mass transfer (purple), acid-base reactions (pink), microbial growth and product formation (green), and pH control (light blue). (**b**) Metabolic pathway map showing acetate assimilation and H_2 and formate oxidation coupled to lactate production (left), and acetate production in acetogenic microbes (right). Colors correspond to the three processes we evaluate (red: acetate-mediated; yellow: H_2-mediated; blue: formate-mediated).

Microbial growth and product formation

Microbial growth occurs in the well-mixed liquid phase and is responsible for the production of more cells and the consumption or production of several chemical species (Fig. 2.2a). These reactions are compiled in $R_{X,i}$. I assume that the kinetics of carbon fixation (or acetate uptake, in the case of acetotrophic growth) represent the upper bound on the biomass and product formation rates because all carbon-containing molecules produced by the cell are derived from the carbon-fixing metabolism. Hence, I assume that the combined rate of biomass and product (lactate

or enzyme) formation (moles carbon per volume per time) is dependent on the molar biomass carbon concentration (c_{X}) and the specific growth rate (μ). For lactate, this results in

$$R_{\mathrm{X,X}} + 3R_{\mathrm{X,L}} = \mu c_{\mathrm{X}} \tag{3}$$

where the factor of 3 precedes $R_{\mathrm{X,L}}$ because lactate is a 3-carbon molecule. For the enzyme, the analogous equation is given by

$$R_{\mathrm{X,X}} + R_{\mathrm{X,E}} = \mu c_{\mathrm{X}} \tag{4}$$

I define the fraction of carbon diverted to biomass as

$$\begin{aligned} x &= \frac{1}{1+3\zeta} \text{ (lactate)} \\ x &= \frac{1}{1+\zeta} \text{ (enzyme)} \end{aligned} \tag{5}$$

where ζ is the stoichiometric ratio of products to cells in, for example, the generic biomass equation given by

$$\sum_i \alpha_i \mathrm{S}_i = \mathrm{X} + \zeta \mathrm{P} \tag{6}$$

where S is a generic substrate and P is a generic product. I assume x is an engineerable parameter (*e.g.* by tuning the expression levels of different enzymes) and calculate ζ according to

$$\begin{aligned} \zeta &= \frac{1-x}{3x} \text{ (lactate)} \\ \zeta &= \frac{1-x}{x} \text{ (enzyme)} \end{aligned} \tag{7}$$

Hence, the biomass growth rate ($R_{\mathrm{X,X}}$) and product formation rate ($R_{\mathrm{X,L}}$, $R_{\mathrm{X,E}}$) are given by

$$\begin{aligned} R_{\mathrm{X,X}} &= x\mu c_{\mathrm{X}} \\ R_{\mathrm{X,L/E}} &= \zeta x\mu c_{\mathrm{X}} \end{aligned} \tag{8}$$

and consumption or production of other molecules (*e.g.* O_2, H_2, CO_2, *etc.*) is written as

$$R_{\mathrm{X},i} = \alpha_{\mathrm{X},i} R_{\mathrm{X,X}} + \alpha_{\mathrm{L/E},i} R_{\mathrm{X,L/E}} \tag{9}$$

where $\alpha_i < 0$ if the species is consumed in the reaction following standard convention.[31]

Microbial growth kinetics are defined using the Monod model with dependencies on each potentially growth-limiting substrate. The equations for aerobic formatotrophic (F), aerobic hydrogenotrophic (H_2), anaerobic acetogenic (A), and aerobic acetotrophic growth (Ac) are given as

$$\mu_{\mathrm{F}} = \mu_{\max,\mathrm{F}} \left(\frac{c_{\mathrm{F}}}{K_{\mathrm{F}} + c_{\mathrm{F}}}\right)\left(\frac{c_{\mathrm{O_2}}}{K_{\mathrm{O_2}} + c_{\mathrm{O_2}}}\right) \tag{10}$$

$$\mu_{\mathrm{H_2}} = \mu_{\max,\mathrm{H_2}} \left(\frac{c_{\mathrm{H_2}}}{K_{\mathrm{H_2}} + c_{\mathrm{H_2}}}\right)\left(\frac{c_{\mathrm{O_2}}}{K_{\mathrm{O_2}} + c_{\mathrm{O_2}}}\right)\left(\frac{c_{\mathrm{CO_2}}}{K_{\mathrm{CO_2}} + c_{\mathrm{CO_2}}}\right) \tag{11}$$

$$\mu_{\mathrm{A}} = \mu_{\max,\mathrm{A}} \left(\frac{c_{\mathrm{H_2}}}{K_{\mathrm{H_2}} + c_{\mathrm{H_2}}}\right)\left(\frac{c_{\mathrm{CO_2}}}{K_{\mathrm{CO_2}} + c_{\mathrm{CO_2}}}\right) \tag{12}$$

$$\mu_{\mathrm{Ac}} = \mu_{\max,\mathrm{Ac}} \left(\frac{c_{\mathrm{Ac}}}{K_{\mathrm{Ac}} + c_{\mathrm{Ac}} + \frac{c_{\mathrm{Ac}}^2}{K_{\mathrm{I,Ac}}}}\right)\left(\frac{c_{\mathrm{O_2}}}{K_{\mathrm{O_2}} + c_{\mathrm{O_2}}}\right) \tag{13}$$

where $\mu_{\max}$ is the maximum specific growth rate of the organism when all fixed carbon is diverted to biomass and K_i is the Monod constant for substrate i. Note that acetotrophic growth includes an Andrews/Haldane inhibition term ($K_{\mathrm{I,Ac}}$) to account for growth defects associated with high acetate concentrations reported previously.[32]

Biomass and product yield

A combination of experimental values and stoichiometric and energetic calculations is used to determine the yields of biomass and products on different carbon and energy sources (Fig. 2.2b). In all cases I assume that enzyme yield ($Y'_{\mathrm{E}/i}$) is equivalent to biomass yield ($Y'_{\mathrm{X}/i}$) and that enzymes have approximately the same chemical composition as biomass.

Formatotrophic (aerobic) growth

For formatotrophic growth with O_2 as the terminal electron acceptor and formate as the energy and carbon source (note that formate is completely oxidized and CO_2 is fixed via the Calvin cycle in *C. necator*), the biomass reaction is written as

$$\begin{aligned}\alpha_{\mathrm{X,F}}\mathrm{HCOO^-} + \alpha_{\mathrm{X,F}}\mathrm{H^+} + \beta_{\mathrm{X,F}}\mathrm{NH_3} + \gamma_{\mathrm{X,F}}\mathrm{O_2} \\ \rightarrow \mathrm{CH_{1.77}O_{0.49}N_{0.24}} + \kappa_{\mathrm{X,F}}\mathrm{CO_2} + \epsilon_{\mathrm{X,F}}\mathrm{H_2O}\end{aligned} \tag{14}$$

where $\mathrm{CH_{1.77}O_{0.49}N_{0.24}}$ represents cell mass (molar mass ~25 g mol^{-1}). From stoichiometry,

$$\begin{aligned}\alpha_{\mathrm{X,F}} &= \frac{1}{Y'_{\mathrm{X/F}}} \\ \beta_{\mathrm{X,F}} &= 0.24\end{aligned} \tag{15}$$

$$\gamma_{\mathrm{X,F}} = \frac{1}{2}\left(0.49 + 2\kappa_{\mathrm{X,F}} + \epsilon_{\mathrm{X,F}} - 2\alpha_{\mathrm{X,F}}\right)$$

$$\kappa_{\mathrm{X,F}} = \alpha_{\mathrm{X,F}} - 1$$

$$\epsilon_{\mathrm{X,F}} = \frac{1}{2}\left(2\alpha_{\mathrm{X,F}} + 3\beta_{\mathrm{X,F}} - 1.77\right)$$

where $Y'_{\mathrm{X/F}}$ is the molar yield of biomass on formate, which I define according to a previously described empirical relationship,[16,17]

$$Y'_{\mathrm{X/F}} = Y'_{\mathrm{X/F,max}}\left(1 - \frac{c_{\mathrm{F}} + c_{\mathrm{FA}}}{\theta_{\mathrm{F}}}\right) \tag{16}$$

where θ_{F} is a fitting parameter that represents the maximum formate/ic acid concentration at which cells can grow.

The lactate formation reaction is written as

$$\begin{aligned}\alpha_{\mathrm{L,F}}\mathrm{HCOO^-} + (\alpha_{\mathrm{L,F}} - 1)\mathrm{H^+} + \beta_{\mathrm{L,F}}\mathrm{NH_3} + \gamma_{\mathrm{L,F}}\mathrm{O_2} \\ \rightarrow \mathrm{C_3H_5O_3^-} + \kappa_{\mathrm{L,F}}\mathrm{CO_2} + \epsilon_{\mathrm{L,F}}\mathrm{H_2O}\end{aligned} \tag{17}$$

Relying on stoichiometry,

$$\begin{aligned}\alpha_{\mathrm{L,F}} &= \frac{1}{Y'_{\mathrm{L/F}}} \\ \beta_{\mathrm{L,F}} &= 0 \\ \gamma_{\mathrm{L,F}} &= \frac{\alpha_{\mathrm{L,F}}}{2} - 3 \\ \kappa_{\mathrm{L,F}} &= \alpha_{\mathrm{L,F}} - 3 \\ \epsilon_{\mathrm{L,F}} &= \alpha_{\mathrm{L,F}} - 3\end{aligned} \tag{18}$$

where $Y'_{\mathrm{L/F}}$ is the molar yield of lactate on formate. To determine this value, we follow the stoichiometry and energetics of carbon fixation via the Calvin cycle to lactate as follows (Fig. 2.2b). Microbes support energy carrier (NADH and ATP) regeneration by using $\mathrm{NAD^+}$-dependent formate dehydrogenases to catalyze the reaction

$$\mathrm{HCOO^-} + \mathrm{NAD^+} \rightarrow \mathrm{CO_2} + \mathrm{NADH} \tag{19}$$

NADH is then used to regenerate ATP following aerobic respiration (oxidative phosphorylation):

$$\mathrm{NADH} + \mathrm{H^+} + \frac{1}{2}\mathrm{O_2} + \left(\frac{\mathrm{P}}{\mathrm{O}}\right)(\mathrm{ADP} + \mathrm{P_i}) \rightarrow \mathrm{NAD^+} + \mathrm{H_2O} + \left(\frac{\mathrm{P}}{\mathrm{O}}\right)\mathrm{ATP} \tag{20}$$

where P/O is the oxidative phosphorylation ratio (typically 2–3). When using the Calvin cycle to fix CO_2, seven ATP and five NADH are consumed to fix three CO_2 molecules into one pyruvate molecule:

$$3CO_2 + 5NADH + 7ATP + 4H^+ \rightarrow C_3H_3O_3^- + 5NAD^+ + 7(ADP + P_i) + 3H_2O \quad (21)$$

Pyruvate is then converted to lactate via lactate dehydrogenase according to

$$C_3H_3O_3^- + NADH + H^+ \rightarrow C_3H_5O_3^- + NAD^+ \quad (22)$$

The resulting overall reaction for lactate production (using a P/O ratio of 2.5) is given by

$$8.8HCOO^- + 7.8H^+ + 1.4O_2 \rightarrow C_3H_5O_3^- + 5.8CO_2 + 5.8H_2O \quad (23)$$

Hence, the maximum theoretical molar yield of lactate on formate is ~0.11 mol mol^{-1}. Because the molar cell yield ($Y'_{X,F}$) is influenced by the formate concentration due to a variety of toxicity effects in *C. necator*, I include this dependency for lactate as well:

$$Y'_{L/F} = Y'_{L/F,max}\left(1 - \frac{c_F + c_{FA}}{\theta_F}\right) \quad (24)$$

Hydrogenotrophic aerobic (Knallgas) growth

I use the same formulation as that for formatotrophy to describe biomass growth and product formation, but the stoichiometry is modified to account for the different energy source. The biomass equation is written as

$$\alpha_{X,H}H_2 + \beta_{X,H}NH_3 + \gamma_{X,H}O_2 + \kappa_{X,H}CO_2 \rightarrow CH_{1.77}O_{0.49}N_{0.24} + \epsilon_{X,H}H_2O \quad (25)$$

resulting in the stoichiometric relationships given by

$$\alpha_{X,H} = \frac{1}{Y'_{X/H}}$$

$$\beta_{X,H} = 0.24$$

$$\gamma_{X,H} = \frac{1}{2}\left(0.49 + \epsilon_{X,H} - 2\kappa_{X,H}\right) \quad (26)$$

$$\kappa_{X,H} = 1$$

$$\epsilon_{X,H} = \frac{1}{2}\left(2\alpha_{X,H} + 3\beta_{X,H} - 1.77\right)$$

The lactic acid production reaction is written as

$$\alpha_{L,H}H_2 + \beta_{L,H}NH_3 + \gamma_{L,H}O_2 + \kappa_{L,H}CO_2 \rightarrow C_3H_6O_3 + \epsilon_{L,H}H_2O \quad (27)$$

with stoichiometry given by

$$\alpha_{\mathrm{L,H}} = \frac{1}{Y'_{\mathrm{L,H}}}$$

$$\beta_{\mathrm{L,H}} = 0$$

$$\gamma_{\mathrm{L,H}} = \frac{\alpha_{\mathrm{L,H}}}{2} - 3 \tag{28}$$

$$\kappa_{\mathrm{L,H}} = 3$$

$$\epsilon_{\mathrm{L,H}} = \alpha_{\mathrm{L,H}} - 3$$

We determine the lactic acid production yield on H_2 ($Y'_{\mathrm{L/H}}$) following the same method as for formate, resulting in:

$$8.8\mathrm{H_2} + 3\mathrm{CO_2} + 1.4\mathrm{O_2} \rightarrow \mathrm{C_3H_6O_3} + 5.8\mathrm{H_2O} \tag{29}$$

The equivalent theoretical molar yield of lactate on H_2 and formate is because H_2 and formate oxidation both result in the reduction of one molecule of NAD^+ to NADH (Fig. 2.2b).

Acetogenic (anaerobic) growth

Acetogenic growth relies on the energy derived from acetate generation to drive biomass formation. Following Fast and Papoutsakis,[33] H_2 oxidation drives acetyl-CoA formation from CO_2 given by

$$\begin{aligned} 4\mathrm{H_2} + 2\mathrm{CO_2} + (1-n)\mathrm{ATP} + \mathrm{HSCoA} \\ \rightarrow \mathrm{C_2H_3OSCoA} + 3\mathrm{H_2O} + (1-n)(\mathrm{ADP} + \mathrm{P_i}) \end{aligned} \tag{30}$$

where n is the ATP conservation coefficient, representing ATP regeneration driven by the conservation of energy from proton or sodium gradients.[33,34] A simple equation for biomass formation from acetyl-CoA is also derived by Fast and Papoutsakis,[33] written as

$$0.5\mathrm{C_2H_3OSCoA} + 4\mathrm{ATP} + \frac{\Delta\gamma}{2}\mathrm{NADH} \rightarrow \mathrm{CH_{1.77}O_{0.49}N_{0.24}} \tag{31}$$

where $\Delta\gamma$ is the difference in the degree of reduction between acetyl-CoA ($\gamma = 4$) and biomass ($\gamma = 0.07$). This equation, as written, is neither atomically nor charge balanced, so it should be taken to only represent the energy carrier demand of biomass formation. To generate the necessary energy, acetyl-CoA can be oxidized to acetic acid, resulting in the generation of an ATP:

$$\mathrm{C_2H_3OSCoA} + (\mathrm{ADP} + \mathrm{P_i}) + \mathrm{H_2O} \rightarrow \mathrm{C_2H_4O_2} + \mathrm{HSCoA} + \mathrm{ATP} \tag{32}$$

A linear combination of these equations to balance ATP results in

$$\frac{18}{n}\mathrm{H_2} + \frac{9}{n}\mathrm{CO_2} + \frac{\Delta\gamma}{2}\mathrm{NADH} \rightarrow \mathrm{CH_{1.77}O_{0.49}N_{0.24}} + \left(\frac{4.5}{n} - \frac{1}{2}\right)\mathrm{C_2H_4O_2} + \left(\frac{9}{n} - 1\right)\mathrm{H_2O} \quad (33)$$

NADH is readily generated by the oxidation of H_2 using hydrogenases, and I assume the nitrogen content in biomass is supplied by ammonia. Hence, a balanced overall acetogenic growth equation is given by

$$\left(\frac{18}{n} + \frac{\Delta\gamma}{2}\right)\mathrm{H_2} + \frac{9}{n}\mathrm{CO_2} + 0.24\mathrm{NH_3} \rightarrow C\mathrm{H_{1.77}O_{0.49}N_{0.24}} + \left(\frac{4.5}{n} - \frac{1}{2}\right)\mathrm{C_2H_4O_2} + \left(\frac{9}{n} + (1-b)\right)\mathrm{H_2O} \quad (34)$$

where b is the oxygen content in the biomass equation (0.49 in this case).

Acetotrophic (aerobic) growth

The biomass equation is written as

$$\alpha_{\mathrm{X,A}}\mathrm{C_2H_3O_2^-} + \alpha_{\mathrm{X,A}}\mathrm{H^+} + \beta_{\mathrm{X,A}}\mathrm{NH_3} + \gamma_{\mathrm{X,A}}\mathrm{O_2} \rightarrow \mathrm{CH_{1.77}O_{0.49}N_{0.24}} + \kappa_{\mathrm{X,A}}\mathrm{CO_2} + \epsilon_{\mathrm{X,A}}\mathrm{H_2O} \quad (35)$$

with stoichiometry given by

$$\alpha_{\mathrm{X,A}} = \frac{1}{Y'_{\mathrm{X/A}}}$$

$$\beta_{\mathrm{X,A}} = 0.24$$

$$\gamma_{\mathrm{X,A}} = \frac{1}{2}\left(0.49 + 2\kappa_{\mathrm{X,A}} + \epsilon_{\mathrm{X,A}} - 2\alpha_{\mathrm{X,A}}\right) \quad (36)$$

$$\kappa_{\mathrm{X,A}} = 2\alpha_{\mathrm{X,A}} - 1$$

$$\epsilon_{\mathrm{X,H}} = \frac{1}{2}\left(4\alpha_{\mathrm{X,A}} + 3\beta_{\mathrm{X,A}} - 1.77\right)$$

The lactate-forming reaction is written similarly,

$$\alpha_{\mathrm{L,A}}\mathrm{C_2H_3O_2^-} + \left(\alpha_{\mathrm{L,A}} - 1\right)\mathrm{H^+} + \beta_{\mathrm{L,A}}\mathrm{NH_3} + \gamma_{\mathrm{L,A}}\mathrm{O_2} \rightarrow \mathrm{C_3H_5O_3^-} + \kappa_{\mathrm{L,A}}\mathrm{CO_2} + \epsilon_{L,\mathrm{A}}\mathrm{H_2O} \quad (37)$$

resulting in stoichiometry given by:

$$\alpha_{\mathrm{L,A}} = \frac{1}{Y'_{\mathrm{L/A}}} \quad (38)$$

$$\beta_{\mathrm{L,A}} = 0$$

$$\gamma_{\mathrm{L,A}} = 2\alpha_{\mathrm{L,A}} - 3$$

$$\kappa_{\mathrm{L,A}} = 2\alpha_{\mathrm{L,A}} - 3$$

$$\epsilon_{\mathrm{L,H}} = 2\alpha_{\mathrm{L,A}} - 3$$

To determine the yield of lactate on acetate ($Y'_{\mathrm{L/A}}$), we follow the stoichiometry and energetics of acetate assimilation and oxidation through the glyoxylate shunt (Fig. 2.2b). Acetate is first activated to acetyl-CoA according to

$$\mathrm{C_2H_3O_2^-} + 2\mathrm{ATP} + \mathrm{HSCoA} + \mathrm{H^+} \rightarrow \mathrm{C_2H_3OSCoA} + 2(\mathrm{ADP} + \mathrm{P_i}) + \mathrm{H_2O} \qquad (39)$$

Note that this formulation combines equations for ATP hydrolysis due to acetyl-CoA synthetase (resulting in AMP) and due to recombination with AMP resulting in 2 ADP. Acetyl-CoA is passed through the glyoxylate shunt to produce oxaloacetate and regenerate energy carriers, resulting in the net reaction given by

$$2\mathrm{C_2H_3OSCoA} + 3\mathrm{H_2O} + 2\mathrm{NAD^+} + \mathrm{FAD} \rightarrow \mathrm{C_4H_3O_5^-} + 3\mathrm{H^+} + 2\mathrm{NADH} + \mathrm{FADH_2} + 2\mathrm{HSCoA} \qquad (40)$$

I assume oxaloacetate is converted to lactate via phosphoenolpyruvate and pyruvate with the net reaction

$$\mathrm{C_4H_3O_5^-} + \mathrm{NADH} + \mathrm{H^+} \rightarrow \mathrm{C_3H_5O_3^-} + \mathrm{CO_2} + \mathrm{NAD^+} \qquad (41)$$

Using the $\mathrm{P/O}$ ratio of 2.5 for NADH (as above) and 1.5 for $\mathrm{FADH_2}$, the resulting net reaction for acetate conversion to lactate is given as

$$2\mathrm{C_2H_3O_2^-} + \mathrm{O_2} + \mathrm{H^+} \rightarrow \mathrm{C_3H_5O_3^-} + \mathrm{CO_2} + \mathrm{H_2O} \qquad (42)$$

Hence, I use a theoretical molar yield of lactate on acetate ($Y'_{\mathrm{L/A}}$) of 0.5 mol mol^{-1}.

Growth rate dependence on pH and salinity

A simple model is used to describe the effects of pH and salinity on microbial growth:

$$\mu_{\max} = \mu_{\mathrm{opt}}\rho(\mathrm{pH})\nu(c_{\mathrm{Na}}) \qquad (43)$$

where μ_{opt} is the specific growth rate at optimal conditions and $\rho(\mathrm{pH})$ and $\nu(c_{\mathrm{Na}})$ are functions describing the impacts of pH and $\mathrm{Na^+}$ concentration on the growth rate.

Following Rosso *et al.*,[35] I write $\rho(\mathrm{pH})$ as

$$\rho(\mathrm{pH}) = \begin{cases} 0 & \mathrm{pH} < \mathrm{pH_{min}} \\ f(\mathrm{pH}) & \mathrm{pH_{min}} \leq \mathrm{pH} \leq \mathrm{pH_{max}} \\ 0 & \mathrm{pH} > \mathrm{pH_{max}} \end{cases} \tag{44}$$

Here, $pH_{\mathrm{min/max}}$ is the range of pH over which microbial growth is observed, and the function $f(\mathrm{pH})$ is

$$f(\mathrm{pH}) = \frac{(\mathrm{pH} - \mathrm{pH_{min}})(\mathrm{pH} - \mathrm{pH_{max}})}{(\mathrm{pH} - \mathrm{pH_{min}})(\mathrm{pH} - \mathrm{pH_{max}}) - \left(\mathrm{pH} - \mathrm{pH_{opt}}\right)^2} \tag{45}$$

where $\mathrm{pH_{opt}}$ is the optimal pH for growth.

Microbial growth is strongly dependent on the salinity of the medium. In an effort to adapt *E. coli* to high salt concentrations necessary for high lactic acid titers, Wu *et al.* demonstrated that the effect is determined primarily by the Na^+ concentration, and that the maximum growth rate decreases approximately linearly with increasing Na^+ concentration.[36] I use data from Wu *et al.* to fit this dependence according to

$$\nu(c_{\mathrm{Na}}) = \begin{cases} 1 & c_{\mathrm{Na}} < c_{\mathrm{Na,min}} \\ f(c_{\mathrm{Na}}) & c_{\mathrm{Na,min}} < c_{\mathrm{Na}} < c_{\mathrm{Na,max}} \\ 0 & c_{\mathrm{Na}} > c_{\mathrm{Na,max}} \end{cases} \tag{46}$$

where $c_{\mathrm{Na,min/max}}$ is the range of Na^+ concentration over which growth is impacted, and the function $f(c_{\mathrm{Na}})$ is given by

$$f(c_{\mathrm{Na}}) = 1 - \frac{c_{\mathrm{Na}}}{c_{\mathrm{Na,max}} - c_{\mathrm{Na,min}}} \tag{47}$$

To ensure a fair comparison across processes, we assume that Na^+ concentration has the same impact on each organism in the models.

Acid/base reactions

The acid/base bicarbonate/carbonate, formic acid/formate, acetic acid/acetate, lactic acid/lactate, and water dissociation reactions shown below occur in the liquid phase (Fig. 2.2a) and are treated as kinetic expressions without assuming equilibrium:

$$\mathrm{CO_{2(aq)}} + \mathrm{H_2O} \overset{k_{+1},k_{-1}}{\Longleftrightarrow} \mathrm{H^+} + \mathrm{HCO_3^-} \qquad K_1 \tag{48}$$

$$\mathrm{HCO_3^-} \overset{k_{+2},k_{-2}}{\Longleftrightarrow} \mathrm{H^+} + \mathrm{CO_3^{2-}} \qquad K_2 \tag{49}$$

$$\mathrm{CO_{2(aq)}} + \mathrm{OH^-} \overset{k_{+3},k_{-3}}{\Longleftrightarrow} \mathrm{HCO_3^-} \qquad K_3 = K_1/K_{\mathrm{W}} \tag{50}$$

$$\mathrm{HCO_3^-} + \mathrm{OH^-} \overset{k_{+4},k_{-4}}{\Longleftrightarrow} \mathrm{CO_3^{2-}} + \mathrm{H_2O} \qquad K_4 = K_2/K_{\mathrm{W}} \tag{51}$$

$$\mathrm{HCOOH} \overset{k_{+5},k_{-5}}{\Longleftrightarrow} \mathrm{H^+} + \mathrm{HCOO^-} \qquad K_5 \qquad (52)$$

$$\mathrm{H_3C_2OOH} \overset{k_{+6},k_{-6}}{\Longleftrightarrow} \mathrm{H^+} + \mathrm{H_3C_2OO^-} \qquad K_6 \qquad (53)$$

$$\mathrm{H_5C_3O_2OH} \overset{k_{+7},k_{-7}}{\Longleftrightarrow} \mathrm{H^+} + \mathrm{H_5C_3O_2O^-} \qquad K_7 \qquad (54)$$

$$\mathrm{H_2O} \overset{k_{+w},k_{-w}}{\Longleftrightarrow} \mathrm{H^+} + \mathrm{OH^-} \qquad K_\mathrm{W} \qquad (55)$$

where k_{+n} and k_{-n} are the forward and reverse rate constants, respectively, and K_n is the equilibrium constant for the nth reaction. For formic acid, acetic acid, lactic acid, and water, I calculate K_n from the van't Hoff equation using the change of entropy, ΔS_n, and the heat of reaction, ΔH_n, given by

$$K_n = \exp\left(\frac{\Delta S_n}{R}\right)\exp\left(-\frac{\Delta H_n}{RT}\right) \qquad (56)$$

For CO_2/HCO_3^- and HCO_3^-/CO_3^{2-} equilibria, K_n is calculated using the empirical relationships compiled by W.G. Mook that account for salinity-induced impacts on the equilibrium constant:[37]

$$pK_1 = \frac{3670.7}{T} - 62.008 + 9.7944\ln(T) - 0.0118S + 0.000116S^2 \qquad (57)$$

$$pK_2 = \frac{1394.7}{T} + 4.777 - 0.0184S + 0.000118S^2 \qquad (58)$$

where S is the medium salinity (in units g/kg water).

Source and sink terms resulting from these reactions are compiled in $R_{\mathrm{A-B},i}$, written as:

$$R_{\mathrm{A-B},i} = \sum_i \nu_i \left(k_{+n} \prod_{\nu_i<0} c_i - k_{-n} \prod_{\nu_i>0} c_i \right) \qquad (59)$$

where ν_i is the stoichiometric coefficient of species i for the nth reaction and reverse rate constants (k_{-n}) are calculated from

$$k_{-n} = \frac{k_{+n}}{K_n} \qquad (60)$$

Liquid and gas flow

Liquid media is fed to and extracted from the well-mixed liquid phase at a constant dilution rate (Fig. 2.2a), resulting in a feed term written as

$$R_{\mathrm{LF},i} = D_\mathrm{liq}\left(c_{\mathrm{f},i} - c_i\right) \qquad (61)$$

where D_{liq} is the liquid dilution rate (defined as the inverse space time, or volumetric flow rate divided by reactor volume). We assume the feed stream is free of microbes. I similarly define a feed term for the gas phase according to

$$R_{\mathrm{GF},i} = \frac{D_{\mathrm{gas}}}{RT}\left(p_{\mathrm{f},i} - p_i\right) \tag{62}$$

where D_{gas} is the gas dilution rate.

Gas-liquid mass transfer

Gas fed to the reactor results in mass transfer to the liquid phase according to

$$R_{\mathrm{G-L},i} = k_{\mathrm{L}}a_i(\beta_i p_i - c_i) \tag{63}$$

where $k_{\mathrm{L}}a_i$ is the volumetric mass-transfer coefficient on the liquid side of the gas/liquid interface, and β_i is the Bunsen solubility coefficient (Fig. 2.2a). Volumetric gas/liquid mass transfer coefficients can be calculated from first principles[31] or by using correlations that depend on the system geometry. For O_2, I use the correlation developed by Vasconcelos *et al.* for stirred tank reactors with a height that is twice the diameter,

$$k_{\mathrm{L}}a_{\mathrm{O_2}} = 22.3(P_{\mathrm{G}})^{0.66}(u_{\mathrm{G}})^{0.51} \tag{64}$$

where P_{G} is the specific power input (in units W m^{-3}) and u_{G} is the superficial gas velocity (in units m s^{-1}). I relate u_{G} to the gas phase dilution rate using

$$u_{\mathrm{G}} = \frac{D_{\mathrm{gas}}}{A_{\mathrm{S}}} \tag{65}$$

where A_{S} is the specific surface area of sparging holes in the reactor (units m^{-1}). In our model, I assume a value of 5.6 m^{-1} to make a gas dilution rate of 100 hr^{-1} correspond to a superficial gas velocity of 0.05 m s^{-1}, and the correlation above is used to determine the power demand necessary to achieve a given gas/liquid mass transfer rate.

To calculate the $k_{\mathrm{L}}a$ value for CO_2 and H_2, I use

$$k_{\mathrm{L}}a_{i\neq\mathrm{O_2}} = \sqrt{\frac{D_i}{D_{\mathrm{O_2}}}}\,k_{\mathrm{L}}a_{\mathrm{O_2}} \tag{66}$$

where D_i is the diffusivity of species i following Meraz *et al.* to account for differences in the mass transfer coefficient (k_{L}).[38]

The equilibrium solubility of CO_2, O_2, and H_2 is calculated according to the empirical relationship for the Bunsen solubility coefficient (β),

$$\ln \beta = A_1 + A_2 \left(\frac{100}{T}\right) + A_3 \ln\left(\frac{T}{100}\right) + S\left[B_1 + B_2\left(\frac{T}{100}\right) + B_3\left(\frac{T}{100}\right)^2\right] \quad (67)$$

where A_n and B_n are fitting parameters and S is the medium salinity (in units g kg^{-1} water).

pH control

A feedback control loop is included in the reactor to maintain an optimal pH for microbial growth by adding 1 M hydrochloric acid or 1 M sodium hydroxide solutions where appropriate (Fig. 2.2a). The manipulated flow rate variable (units hr^{-1}) is defined as

$$r_{\mathrm{M}} = 0 + K_{\mathrm{C}}\left(E + \frac{1}{\tau}\int E dt\right) \quad (68)$$

where K_{C} is the controller gain, E is the error, and τ is the controller reset time. The error (E) is defined according to

$$E = \mathrm{pH}^{\mathrm{set}} - \mathrm{pH} \quad (69)$$

where $\mathrm{pH}^{\mathrm{set}}$ is equivalent to $\mathrm{pH}_{\mathrm{opt}}$. The resulting pH control flow is given by

$$R_{\mathrm{pH},i} = r_{\mathrm{M}} c_{\mathrm{pH},i} \quad (70)$$

where $c_{\mathrm{pH},i}$ is 1 M for H^+/Cl^- (acid addition) or 1 M for OH^-/Na^+ (base addition).

Reactor model analysis

Reactor productivity

I defined a normalized dilution rate (δ) according to

$$\delta = \frac{D_{\mathrm{liq}}}{x\mu_{\max}} \quad (71)$$

to account for the fact that the maximum growth rate is reduced by diversion of carbon to the product. The reactor productivity can then be calculated as

$$\dot{m}_{j,n} = Z_j \delta_{j,n} x_j \mu_{\max,n} c_j \quad (72)$$

where Z_j is the molar mass of product j and the subscript n refers to a particular process. For the acetogenic system, we calculated the full-system productivity by accounting for flow through both reactors using

$$\dot{m}_{j,\mathrm{AA}} = \frac{\dot{m}_{j,\mathrm{Ac}}}{1 + \frac{\delta_{j,\mathrm{Ac}} x_j \mu_{\max,\mathrm{Ac}}}{\delta_{\mathrm{A}} \mu_{\max,\mathrm{A}}}} \quad (73)$$

where the subscripts "Ac" and "A" refer to the acetotrophic and acetogenic reactors, respectively, and the subscript "AA" refers to the full acetate-mediated system.

Reactor energy efficiency

The energy efficiency of each reactor system is calculated according to

$$\eta_{\mathrm{E},j,n} = \frac{P_{\mathrm{C},j,n}}{P_{\mathrm{C},n} + P_{\mathrm{G},j,n} + P_{\mathrm{th},j,n}} \tag{74}$$

where P_{C}, P_{G}, and P_{th} are the powers per unit volume embodied in the formation of product j or the substrate in process n, the demand from mixing and gas/liquid mass transfer (calculated using eq. 64), and due to heating the liquid feed from room temperature to the operating temperature, respectively. I define the power of formation of a chemical species as the Gibbs free energy change per volume per time associated with the complete combustion of the chemical species following Claassens *et al.*[21]:

$$P_{\mathrm{C},i,n} = \left| R_{\mathrm{LF},i,n} \Delta_{\mathrm{r}} G_i^0 \right| \tag{75}$$

for liquid-phase species and

$$P_{\mathrm{C},i,n} = \left| R_{\mathrm{GF},i,n} \Delta_{\mathrm{r}} G_i^0 \right| \tag{76}$$

for gas-phase species. I note that these formulations mean that I have assumed residual substrate can be perfectly recycled and therefore represent upper bounds on the efficiency of the systems. The power necessary to heat the liquid feed, P_{th}, is given by

$$P_{\mathrm{th},j,n} = \frac{\delta_{j,n} x_j \mu_{\max,n} C_{\mathrm{P,W}} \rho_{\mathrm{W}} (T - T_0)}{\mathrm{COP}} \tag{77}$$

where $C_{\mathrm{P,W}}$ and ρ_{W} are the heat capacity and density of water, respectively, and COP is the coefficient of performance of the heat transfer unit. Overall efficiency for the acetate-mediated process is calculated by accounting for the power demands of each individual reactor with H_2 as the sole energy substrate.

In the formate-mediated system, the productivity of lactic acid is enhanced by concentrating the formate/ic acid effluent from the CO_2 electrolysis system (see Results and Discussion). To account for the energy demand associated with this, I assume formate is concentrated using electrodialysis and calculate the power demand according to

$$P_{\mathrm{conc,LLA,F}} = \frac{\delta_{\mathrm{LLA,F}} x_{\mathrm{LLA}} \mu_{\max,\mathrm{F}} c_{\mathrm{FFA,f}} RT}{\eta_{\mathrm{ED,F}}} \ln\left(\frac{c_{\mathrm{FFA,f}}}{c_{\mathrm{FFA,eff}}}\right) \tag{78}$$

where $c_{\mathrm{FFA,f}}$ is the total concentration of formate and formic acid in the feed stream for the system, $\eta_{\mathrm{ED,F}}$ is the energy efficiency of the electrodialysis system concentrating formate/ic acid, and

$c_{\mathrm{FFA,eff}}$ is the total concentration of formate/ic acid in the effluent stream of the CO_2 electrolyzer. This power demand is then included in the reactor efficiency calculation (eq. 74).

CO_2 demand

For each reactor, we assume that all fed CO_2 (in the gas phase) that is not transferred to the liquid phase is recycled perfectly such that the net CO_2 demand for the reactor producing product j is given directly by the net gas phase CO_2 feed rate:

$$\dot{n}_{\mathrm{CO_2},j,n} = R_{\mathrm{GF,CO_2},j,n} \tag{79}$$

This balance accounts for the fact that CO_2 is generated by microbes oxidizing formate (in the formate-mediated system) and acetate (in the acetate-mediated system). In these reactors, $\dot{n}_{\mathrm{CO_2}} < 0$ because CO_2 is generated. In the formate-mediated system, CO_2 is consumed to produce formate by the CO_2 electrolyzer. Hence, the full-system net consumption of CO_2 is given by

$$\dot{N}_{\mathrm{CO_2},j,\mathrm{F}} = R_{\mathrm{LF,FFA},j,\mathrm{F}} + \dot{n}_{\mathrm{CO_2},j,\mathrm{F}} \tag{80}$$

where $R_{\mathrm{LF,FFF},j,\mathrm{F}}$ is the liquid-phase net feed rate of formate/ic acid (which is produced on a 1:1 molar basis from CO_2 in the upstream electrolyzer). In the acetate-mediated system, CO_2 is consumed in the acetogenic reactor and consumed in the acetotrophic reactor. Hence, the full-system net consumption of CO_2 is written as

$$\dot{N}_{\mathrm{CO_2},j,\mathrm{AA}} = R_{\mathrm{GF,CO_2},j,\mathrm{Ac}} + \left(\frac{\delta_{j,\mathrm{Ac}} x_j \mu_{\mathrm{max,Ac}}}{\delta_{\mathrm{A}} \mu_{\mathrm{max,A}}}\right) R_{\mathrm{GF,CO_2,A}} \tag{81}$$

where the subscript "AA" refers to the full acetate-mediated system.

Reactor model implementation

All equations are solved using the MUMPS general solver in COMSOL Multiphysics 5.4. Model parameters are listed in Table S1.

Life Cycle Analysis Goal and Scope Definition‡

This life cycle assessment was carried out according to the standards in ISO 14044.[24] The open source life cycle assessment software openLCA version 1.10.3 (https://www.openlca.org/)[39] was used to aggregate life cycle inventory data and apply impact assessment methods. The Product Environmental Footprints Dataset[40] was used to obtain most background life cycle inventories while others were aggregated from literature as needed. Unless otherwise stated, the analysis was made indifferent to the exact location of the process. MATLAB was used to develop an impact model sensitive to changes of various variables and parameters studied.

‡The methods described in this and the following subsections within Section 2.3 were led by Jeremy Adams, the co-lead author of the paper on which this chapter is based.

The primary goal of this LCA is to predict the performance of three electromicrobial production systems (labelled as the Knallgas bacteria-based system, the formatotrophic system, and the acetogenic system) with regard to two sustainability metrics: global warming potential and land occupation. The LCA compares these systems to each other as well as to a traditional bioprocess using corn-derived glucose as a feedstock for a heterotrophic bacterium. A secondary goal of this analysis is to determine the specific limitations, bottlenecks, and environmental hotspots of each proposed EMP system. The final goal of this analysis is to integrate the life cycle impact model with the bioreactor models developed to create a tool enabling the eco-design of EMP processes.

Functional Unit and System Boundaries

The production of three products is considered: biomass, industrial enzymes, lactic acid. The life cycle impact analysis ends at the production of each product in unprocessed form. Downstream processing is not considered, as the processing of a given product would be identical for each system studied. For the production of biomass, the functional unit is 1 kg biomass. For industrial enzyme production, the functional unit is 1 kg of enzyme unpurified from the cell pellet. For lactic acid, the functional unit is 1 kg of lactic acid at a concentration of 100 g/L.[41] Despite not considering end of life processing of the products, biogenic carbon is not considered as sequestered carbon, and all biogenic carbon is assumed to decompose to carbon dioxide.

Process Modelling and Life Cycle Inventory

Material and energy requirements for the process are obtained from the results of the EMP reactor models and are sub-divided into the following categories: electricity generation for the EMP system; carbon dioxide direct air capture; ammonia production; other required nutrients and pH control agents; electrolyzer materials; electrodialysis materials; and plant and bioreactor construction. In addition, a corn-derived glucose-fed *E. coli* process is modelled, in which glucose production is added as a process category. Carbon dioxide flows are explicitly considered in the EMP models (see eq. 79–81). For all other non-substrate nutrient requirements, the medium is assumed to be recycled such that 95% of input materials are consumed by cells in the bioreactor (*i.e.* the nutrient utilization ratio is 0.95). We assume a C:P ratio of 50:1 and base calcium, magnesium, and sulfur requirements on the elemental composition of *E. coli*.[42]

The model assumes that each major process in the system draws electricity from a grid composed of coal, natural gas, hydropower, nuclear, photovoltaic, and wind-derived energy. The composition of the grid is treated as a variable in the impact assessment model. The life cycle inventories of these six electricity sources are obtained from the Product Environmental Footprints (PEF) dataset. Direct air capture of carbon dioxide via temperature-vacuum swing adsorption is modelled based on Duetz and Bardow's analysis of industrial-scale plants operated by Climeworks.[43] Two possible routes for ammonia synthesis are considered, both involving the Haber-Bosch process. In one route, hydrogen for ammonia synthesis is obtained from steam methane reforming (SMR). In an alternative route, hydrogen is obtained from electrolysis of water drawing electricity from the grid (green ammonia). In both cases, the energy requirements and life cycle impacts are adapted from Singh *et al*.[44] A mix of ammonium phosphate (from phosphoric acid) and ammonium chloride (from hydrochloric acid) is supplied to the bioreactor to maintain the assumed C:N:P ratio. Life cycle inventories for phosphoric acid, magnesium sulfate, and calcium chloride are obtained from the PEF dataset. The pH is controlled in the bioreactor by

addition of hydrochloric acid and sodium hydroxide, which are obtained through the chlor-alkali process and rely on electricity from the grid. Energy requirements and life cycle impacts are derived from Garcia-Herrero *et al*.[45]

Power demand for electrolytic H_2 production in the Knallgas system is given by

$$P_{\mathrm{E},j,\mathrm{H}} = \frac{V_{\mathrm{H_2}} n_{\mathrm{H_2}} F}{\eta_{\mathrm{F,H_2}}} R_{\mathrm{GF,H_2},j,\mathrm{H}} \tag{82}$$

where $V_{\mathrm{H_2}}$ is the operating voltage of the electrolyzer, $n_{\mathrm{H_2}}$ is the stoichiometric ratio of electrons to product, F is Faraday's constant, and $\eta_{\mathrm{F,H_2}}$ is the Faradaic efficiency of the electrolyzer producing H_2. Power demand for formate production in the formatotrophic system is calculated similarly, resulting in

$$P_{\mathrm{E},j,\mathrm{F}} = \frac{V_{\mathrm{F}} n_{\mathrm{F}} F}{\eta_{\mathrm{F,F}}} R_{\mathrm{LF,FFA},j,\mathrm{F}} \tag{83}$$

Power demand for H_2 production in the acetate-mediated system is calculated using

$$P_{\mathrm{E},j,\mathrm{AA}} = \frac{V_{\mathrm{H_2}} n_{\mathrm{H_2}} F}{\eta_{\mathrm{H_2}}} \left(\frac{\delta_{j,\mathrm{Ac}} x_j \mu_{\mathrm{max,Ac}}}{\delta_{\mathrm{A}} \mu_{\mathrm{max,A}}} \right) R_{\mathrm{GF,H_2,A}} \tag{84}$$

to account for the two-step conversion of H_2 into products with acetate as the intermediate. Electrolyzer material requirements are adapted from previous literature[46–48] and the life cycle inventories associated with each component are obtained from the PEF database. The lifetime of the electrolyzers is assumed to be three years.

Because none of the processes achieve a lactic acid titer of 100 g/L, the power demand necessary to concentrate lactate is modeled using an electrodialysis system. Using data from Hábová *et al.*,[49] I fit an empirical relationship (see Supplementary Note 5 in Appendix A) between the lactate titer fed to the electrodialysis system and the energy demand for separation and concentration, resulting in

$$P_{\mathrm{conc,LLA,n}} = \dot{m}_{\mathrm{LLA},n} \left(a_{\mathrm{ED}} - b_{\mathrm{ED}} c_{\mathrm{LLA},n} \right) \tag{85}$$

where a_{ED} and b_{ED} are fitting parameters. To determine material demands of electrodialysis, we fit an empirical equation (see Supplementary Note 5 in Appendix A) of the form

$$\Gamma_{\mathrm{LLA},n} = \Gamma_{\mathrm{max}} \left(\frac{c_{\mathrm{LLA},n}}{\kappa_{\mathrm{M}} + c_{\mathrm{LLA},n}} \right) \tag{86}$$

to relate the rate of lactic acid flux ($\Gamma_{\mathrm{LLA},n}$) through the membrane to the titer of lactic acid effluent from the reactor. Here, both Γ_{max} and κ_{M} are fitting parameters meant to represent the maximum rate of lactic acid flux and the concentration at half the maximum rate, respectively. Using this

calculated flux, an assumed lifetime (t_{M}) of three years, and an assumed diluate concentration ($c_{\mathrm{LLA,d}}$) of 1 g/L, the membrane material requirements are given by

$$M_{\mathrm{M,LLA},n} = \left(\frac{\delta_{\mathrm{LLA},n} x_{\mathrm{LLA}} \mu_{\mathrm{max},n} \left(c_{\mathrm{LLA},n} - c_{\mathrm{LLA,d}}\right) d_{\mathrm{M}} \rho_{\mathrm{M}}}{\Gamma_{\mathrm{LLA},n}}\right)\left(\frac{1}{t_{\mathrm{M}} \dot{m}_{\mathrm{LLA},n}}\right) \tag{87}$$

The same calculations are used to determine the material demands for concentrating the formate feed stream in the formate-mediated system in the case of lactic acid production, and the life cycle inventory associated with the electrodialysis membrane (Nafion 324 is used as a stand-in) is obtained from the Stropnik *et. al*.[50]

The process productivities obtained from the reactor models are used to determine the total bioreactor volumes required to produce the functional unit of a given product. Stainless steel bioreactors are used, with material requirements calculated based on the design of Mobius Bioreactors from EMD Millipore. The impacts of the bioreactor and the plant facility are due primarily to producing the required construction materials—stainless steel for the bioreactor and concrete and steel for the plant, assuming a constant amount of concrete and steel per square meter of facility area.[51] The area of facility space required per aggregate volume of the bioreactors is based on the Natureworks lactic acid production facility in Blair, NE. Steel, stainless steel, and concrete life cycle inventories are all obtained from the PEF database. The analysis assumes a reactor lifetime of eight years and a plant lifetime of thirty years.

Glucose for the heterotrophic process is obtained from the hydrolysis of corn starch, and life cycle inventories of glucose production are obtained from the PEF dataset. Ammonia requirements for corn production are obtained from Ma *et al*.[52] and the life cycle inventories for glucose production are adjusted to account for reduced carbon emissions in the case of green ammonia production.

Life Cycle Impact Assessment

Global warming potentials were calculated according to the 2013 IPCC model for 100-year global warming potential and are expressed in kilograms of CO_2-equivalents [kg CO_2-e].[53] The land use footprint is calculated using the ReCiPe (H) 2016 method, which weights the impact of various types of land use by their impact on biodiversity.[54] The units of land use are expressed as m^2·year crop equivalents, representing the weighted land use needed to produce a given functional unit of product per year.

Sensitivity Analysis

All parameters used in the development of the bioreactor models and life cycle analysis (*e.g.*, growth rates, reactor lifetimes, solar electricity GWP) other than physical properties (molecular weights, heat capacities, *etc.*) were independently altered by +/-30% and the global warming potential of each process was recalculated. The ratio of the global warming potential of each EMP process (formatotrophic, Knallgas, and acetogenic) and the global warming potential of the heterotrophic process in each scenario was taken to be the metric of interest to evaluate the sensitivity of each parameter. The parameters that caused the largest deviation of this ratio from the equivalent ratio for the base case value of all parameters were taken to be the most critical

parameters in the study (a 10% deviation of this ratio from the base case value was used as a cutoff). A list of all parameters studied can be found in the paper on which this chapter is based.[61]

2.4 Results and Discussion

Reactor models reveal trade-offs in productivity and efficiency across processes

I first describe trends in the productivity (Fig. 2.3a-c), titer (Fig. 2.3d-f), and efficiency (Fig. 2.3g-i) of the three EMP processes producing biomass, enzyme, and lactic acid, and second make comparisons between base case conditions for the three processes.

The productivity, titer, and efficiency of biomass and enzyme production for each system have nearly identical dynamics. Because formate is fed in the liquid phase, the formatotrophic system follows the standard trend of initially increasing productivity as a function of the dilution rate, followed by a rapid decline as cell washout occurs (Fig. 3a, b). Complete washout (*i.e.*, a productivity and titer of ~0) occurs well before the dilution rate exceeds the maximum growth rate (at a normalized dilution rate of 1). This is due to the limitation on productivity imposed by O_2 gas-liquid mass transfer. As the dilution rate increases, the formate feed rate exceeds the consumption rate limit imposed by O_2 mass transfer, causing toxic build-up of formate in the reactor. Formate build-up prevents cell growth, which results in cell washout. Mass transfer limit-induced washout dynamics are also observed in the acetogenic system (Fig. 2.3a, b; d, e), although the behavior for acetate is slightly different from that for the formate case due to the different strategies for modeling acetate and formate toxicity. The productivity of biomass (Fig. 3a) and enzymes (Fig. 2.3b) in the H_2 mediated system does not follow the typical trend because all substrates necessary for growth are fed via the gas phase. Hence, productivity is only slightly dependent on the liquid phase dilution rate until washout begins to occur at a normalized dilution rate of ~0.85 (Fig. 2.3a, b). Instead, for the H_2-mediated system, product titer is controlled by the liquid dilution rate, enabling a wide range of achievable product titers (Fig. 2.3d, e). For each system, the optimal efficiency occurs at the same dilution rate at which the productivity is maximized.

In each system, lactic acid production is significantly influenced by the toxicity induced by high salinity (Fig. 2.3c, f, i). In the formatotrophic system, the productivity initially increases as the dilution rate increases, reaching a maximum at a normalized dilution rate of 0.55 (Fig. 2.3c). In contrast to biomass and enzyme production, this maximum is not due to the gas-liquid mass transfer limit of O_2. Instead, lactic acid production (resulting in a lactic acid titer of ~42 g/L, Fig. 3f), requires pH control to maintain an optimal pH for microbial growth. This results in a high Na^+ concentration due to NaOH addition, reducing the maximum growth rate of cells (eqs. 46 and 47). In this case, the lactic acid titer of ~42 g/L reduces the growth rate to ~56% of its maximum value, causing cell washout to begin to occur at a normalized dilution rate of ~0.56 (Fig. 2.3c, f). Cell washout also reduces the titer of lactic acid (Fig. 2.3f). These effects, in addition to the incomplete utilization of formate feed as cell washout occurs, combine to reduce the efficiency of formatotrophic lactic acid production as the normalized dilution rate exceeds ~0.56 (Fig. 2.3i).

In the acetate-mediated system, the toxicity effect of high salinity also causes cell washout near ~56% of the maximum growth rate (Fig. 2.3c, f). The decline in productivity, titer, and efficiency is much more rapid than in the formatotrophic case. This is because the Na^+

concentration in the feed stream is much higher than in the formate case. Acetic acid production in the upstream reactor requires NaOH addition to maintain a neutral pH for acetogenesis, so the acetotrophic reactor cannot avoid a high Na^+ concentration by reducing the lactic acid titer. Hence, even though the acetotrophic reactor requires acid addition to maintain a near-neutral pH (resulting in no additional Na^+ supplied to the reactor), the residual Na^+ fed from the acetogenic reactor is sufficient to result in cell washout above a normalized dilution rate of ~0.56.

In the H_2-mediated system, Na^+ toxicity limits the productivity and titer of lactic acid, although this limitation occurs at lower dilution rates ($\delta < 0.55$) rather than high dilution rates. This effect is because the lactic acid titer (and therefore, the Na^+ concentration) increases as the dilution rate decreases (Fig. 2.3f), which in turn is a result of the fact that all substrates for growth and lactic acid formation (H_2, CO_2, O_2) are fed via the gas phase (similar to the biomass and enzyme production cases).

The efficiency of lactic acid production, in addition to that of biomass and enzyme production, is optimized at the maximum productivity. Base-case operating conditions were therefore selected by maximizing the productivity for each system (Table 2.1). A minimum normalized dilution rate of 0.1 was arbitrarily set for the H_2-mediated system producing biomass and enzymes because it has a wide dilution rate range at which the productivity is roughly equal. In the acetate-mediated system, the dilution rate in the acetogenic (*S. ovata*) reactor was set by maximizing the full-system productivity (see Supplementary Note 1 in Appendix A). For lactic acid production in the formate-mediated system, we used a concentrated (5.1 M) formate feed stream to maximize productivity (see Supplementary Note 2 in Appendix A).

Considering biomass first, the achievable productivity is highest for the H_2-mediated system at ~0.65 g/L/h, ~11% and ~225% higher than the productivities of the formatotrophic and acetogenic systems, respectively (Fig. 2.3a). The former difference is due to the ~13% higher biomass yield on O_2 with H_2 as the energy substrate than with formate and the fact that the H_2 gas/liquid mass transfer limit is slightly lower than the O_2-imposed limit. The acetogenic system, in contrast, is primarily limited by the acetate production rate of the acetogen, which grows ~4-fold slower than Knallgas and formatotrophic bacteria.

The Knallgas system also achieves the highest biomass titer (~36 g/L vs. ~8.8 g/L and ~11 g/L) because the titer is fully controllable by the liquid-phase dilution rate for this system (Fig. 2.3d). These trends also hold for the enzyme production case, although the productivity, titer, and efficiency are all ~10-fold lower than for biomass because we assume only 10% of the fixed carbon is diverted to enzyme production (Fig. 2.3b, e). For both biomass and enzyme formation, the efficiency of each EMP process is remarkably similar (~32-35% for biomass production, Fig. 3g). These efficiencies are dominated by the metabolic efficiency, defined as the ratio of energy embodied in the product to energy embodied in the main substrate. That these efficiencies are nearly equal is surprising given the remarkably different metabolic strategies for biomass (or enzyme) production.

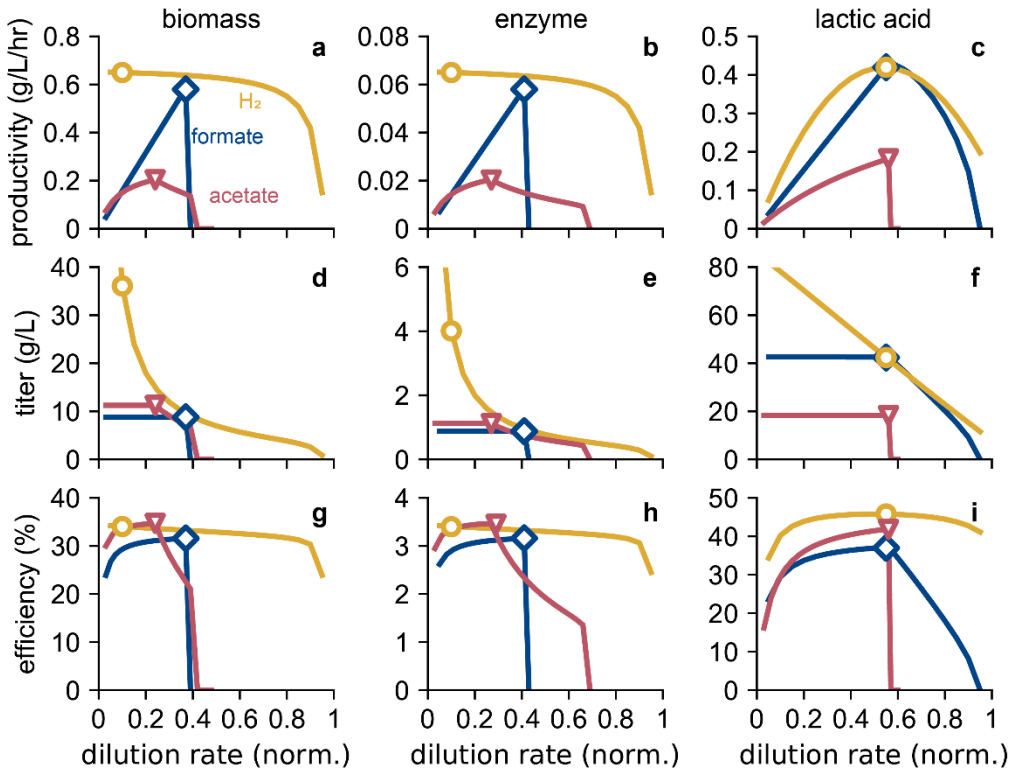

Figure 2.3. EMP reactor performance. Productivity (**a**, **b**, **c**), titer (**d**, **e**, **f**), and energy efficiency (**g**, **h**, **i**) as a function of normalized dilution rate (δ) for the three EMP systems producing biomass (**a**, **d**, **g**), enzyme (**b**, **e**, **h**), and lactic acid (**c**, **f**, **i**). Base case conditions (see Table 2.1) are indicated by blue diamonds (formate-mediated), yellow circles (H_2-mediated), and red triangles (acetate-mediated). The color scheme in all panels follows that in (**a**).

Table 2.1. Base case operating conditions

Parameter *Description*	*Variable*	**Value** *Formatotrophic*	*Knallgas*	*Acetogenic*	**Units**
Biomass					
Normalized dilution rate (liquid phase)	δ	0.37	0.1	0.55 (*S. ovata*) 0.24 (*E. coli*)	--
H_2 feed pressure	P_{H_2}	--	1	1 (*S. ovata*) -- (*E. coli*)	atm
O_2 feed pressure	P_{O_2}	0.21	0.21	-- (*S. ovata*) 0.21 (*E. coli*)	atm
Formate feed concentration	$c_{FFA,f}$	2.08	--	--	M
Titer	c_X	8.8	36.1	11.25	g L^{-1}
Productivity	$\dot{m}_X$	0.585	0.65	0.20	g L^{-1} hr^{-1}
Efficiency	η_X	31.6	34.0	34.7	%
Enzyme					
Normalized dilution rate (liquid phase)	δ	0.41	0.1	0.55 (*S. ovata*) 0.27 (*E. coli*)	--

H_2 feed pressure	P_{H_2}	--	1	1 (*S. ovata*) -- (*E. coli*)	atm
O_2 feed pressure	P_{O_2}	0.21	0.21	-- (*S. ovata*) 0.21 (*E. coli*)	atm
Formate feed concentration	$c_{FFA,f}$	2.08	--	--	M
Carbon fraction to biomass	x	0.9	0.9	-- (*S. ovata*) 0.9 (*E. coli*)	--
Titer	c_E	0.88	4.0	1.1	g L^{-1}
Productivity	$\dot{m}_E$	0.058	0.065	0.020	g L^{-1} hr^{-1}
Efficiency	η_E	3.16	3.40	3.45	%
Lactic Acid					
Normalized dilution rate (liquid phase)	δ	0.55	0.55	0.55 (*S. ovata*) 0.56 (*E. coli*)	--
H_2 feed pressure	P_{H_2}	--	1	1 (*S. ovata*) -- (*E. coli*)	atm
O_2 feed pressure	P_{O_2}	0.21	0.21	-- (*S. ovata*) 0.21 (*E. coli*)	atm
Formate feed concentration	$c_{FFA,f}$	5.1	--	--	M
Carbon fraction to biomass	x	0.1	0.1	-- (*S. ovata*) 0.1 (*E. coli*)	--
Titer	c_{LLA}	42.4	42.4	18.3	g L^{-1}
Productivity	$\dot{m}_{LLA}$	0.42	0.42	0.18	g L^{-1} hr^{-1}
Efficiency	η_{LLA}	37.0	45.8	41.8	%

In contrast to the case for biomass and enzyme formation, the formate-mediated and H_2-mediated lactic acid productivity is equal at ~0.42 g/L/h, ~130% higher than the acetogenic system (Fig. 2.3c). Each system is limited by the Na^+ concentration-induced toxicity; in the acetate-mediated system, each of the two bioreactors experience this limitation, which is responsible for the substantially lower productivity. The H_2-mediated system achieves the highest efficiency of the three EMP options; the efficiency of the formate-mediated system is hindered by the requirement that the formate effluent from the CO_2 electrolyzer must be concentrated by a factor of ~2.5 to achieve high productivity (eq. 78, Supplementary Note 2 in Appendix A).

Several initial conclusions can be drawn from this analysis. First, both the Knallgas and formatotrophic systems can achieve higher productivities than the acetogenic system. The acetogen-based system does maintain advantages not captured in this analysis, including that a wider range of industrial microorganisms (*e.g.*, *E. coli*, *Bacillus licheniformis*, and some oleaginous yeasts) grow naturally on acetate, but bioengineering efforts could obviate this advantage in the future. Second, the solubility advantage of formate as a growth substrate is only relevant in cases where the O_2 gas-liquid mass transport is a less stringent limit on productivity than H_2 transport. This depends both on the ratio of H_2 to O_2 in the gas phase and the ratio of H_2 to O_2 consumed per unit of product. In the production cases explored here, the formatotrophic system never achieves a higher productivity than the Knallgas system. In the biomass and enzyme

production cases, the O_2 mass transport limit is rate-determining. In principle, the formatotrophic system could achieve a higher lactic acid productivity than the Knallgas system, but salinity effects prevent this (Fig. 2.3c). Third, the necessity of concentrating formate from the effluent of a CO_2 electrolyzer to achieve high formatotrophic productivity when O_2 gas liquid mass transfer is not rate-limiting represents a non-negligible energy penalty, reducing energy efficiency (Fig. 3i). Improvements in CO_2 electrolysis reactor operation may overcome this challenge, as we discuss later.

The gas mixture assumed for the Knallgas system is flammable.[55] A nonflammable gas mixture would either require significantly less air (~0.27 atm vs. the assumed 1 atm), reducing productivity by decreasing O_2 solubility, or significantly more H_2 (~3.62 atm vs. the assumed 1 atm), increasing safety concerns associated with pressurized gases and likely increasing reactor and control systems complexity.

These results indicate trade-offs in productivity, titer, and efficiency such that reactor models alone cannot identify a clearly-best EMP strategy. Moreover, upstream processes including energy substrate generation (via either water of CO_2 electrolysis), CO_2 capture, ammonia production, NaOH and HCl production for pH control, and other considerations, require explicit attention as important drivers of material and energy demand for EMP processes. I therefore developed a complete process model (diagrammed in Fig. 2.4) for the EMP processes to understand material and energy flows for the full system, which is discussed next.

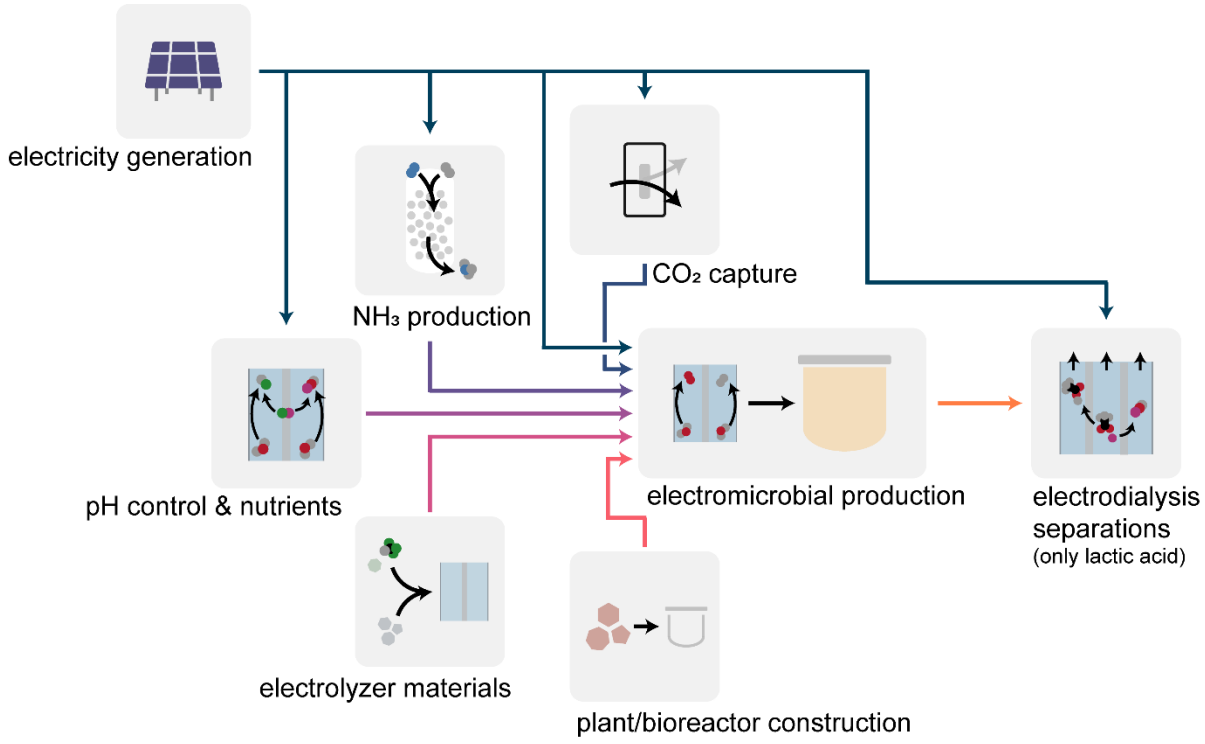

Figure 2.4. Schematic representation of the EMP system. Grid electricity (midnight blue) supplies electricity to the EMP reactors and supporting processes, including direct air capture of CO_2 (blue), ammonia production via the Haber-Bosch process (royal purple), the chlor-alkali process producing pH control agents (purple), and downstream electrodialysis-based separations for lactic acid (orange). Mining and production of electrolyzer materials (magenta) and materials for reactor and plant construction (bright pink) are also considered within the impact model.

Global Warming Potential

The global warming impacts of all components shown in Fig. 2.4 were calculated as outlined in the methods section for each of the three EMP systems and the traditional glucose-fed process. For the case of a wind-powered process, the global warming potential broken down by process categories is shown in Fig. 2.5. It should be noted that other means of clean electricity production (such as thin-film photovoltaics and hydropower) have roughly equivalent life cycle emissions per kWh produced, and therefore would lead to similar results. To study general trends regarding the potential of each process alternative, 1 kg of biomass is chosen as the product and functional unit for a baseline comparison.

Our impact model shows that all three proposed EMP systems have the potential to have a lower global warming potential than that of the corn-based glucose-fed bioprocess, given a clean electricity source. Our analysis indicates the Knallgas bacteria system has a lower overall global warming potential (0.68 kg CO_2-eq./kg biomass) than both the formatotrophic system and acetogenic system (1.16 and 1.35 kg CO_2-eq./kg biomass respectively). The reduction in greenhouse gas emissions associated with the electromicrobial production system compared to the heterotrophic system stems from the low emissions of the individual components of the EMP systems when drawing energy from a low-impact energy grid. The high-impact agricultural production of corn and other crops as feedstocks in bioprocesses contributes the largest share of the global warming potential of these systems. While the carbon emissions associated with fertilizer production can be reduced with increased clean energy (as calculated in the impact model), the large amount of nitrous oxide emissions due to fertilizer application will not be affected by this change, leading to a relatively large global warming potential of traditional bioprocesses. Therefore, in a clean-electricity dominated scenario, the Knallgas bacteria-based EMP system will have a GWP 64% lower than a glucose-fed process (Fig. 2.5).

Although both rely on the same microorganism in the model (*C. necator*), the formate-mediated electromicrobial system will have a larger global warming potential than a hydrogen-mediated system. CO_2 electrolysis to formate occurs at lower current densities (140 mA/cm^2 vs. 1 A/cm^2) and with higher overpotentials (>2 V vs. ~0.8 V) compared to water electrolysis, resulting in an increased carbon footprint due to an increased demand for electrolyzer materials (*e.g.* Ir, Pt, Nafion, *etc.*) and increased energy consumption. The effects of potential improvements to this system are further described later.

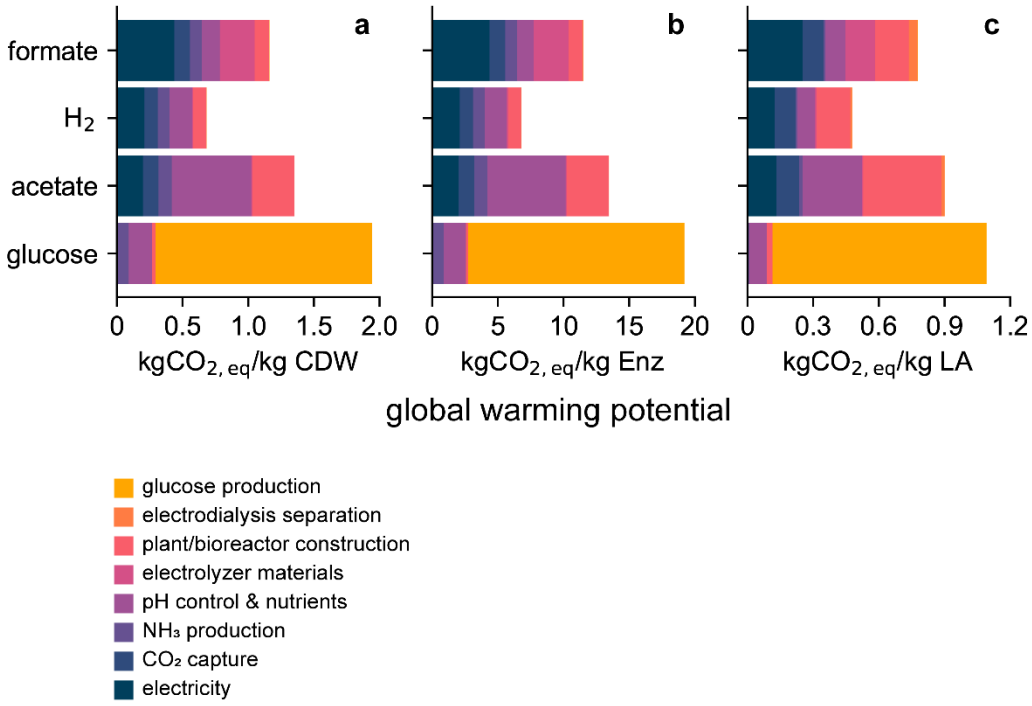

Figure 2.5. Global warming potential of EMP and traditional bioprocesses. Global warming potential for the three EMP systems and traditional heterotrophic system for the production of (**a**) biomass, (**b**) enzymes, and (**c**) lactic acid, broken down by process category. Data shown here assume base-case conditions as described in Table 2.1.

The greatest environmental hotspot of the acetogen-based system compared to the others is due to the production of NaOH and HCl for pH control (Fig. 2.5). The chlor-alkali process that produces NaOH and HCl is an energy-intensive electrolytic process, and therefore contributes a substantial carbon footprint. Even when running the chlor-alkali process with clean electricity, NaCl production and other processing steps still contribute to the carbon footprint of pH control.[45] However, there are options to help alleviate this constraint. For example, engineering the acetogen-based process to take place in a single reactor could address the problem of pH control because the combined biochemical reactions result in no net generation or consumption of protons. The key impediment to this solution is the strict oxygen sensitivity of acetogens such as *S. ovata*[56] and the requirement for oxygen in assimilation of acetate as a sole carbon source.[57] However, for certain applications, this may be achievable. *S. ovata* has recently been evolved to tolerate low concentrations of oxygen.[58] If paired with a heterotroph producing a product traditionally produced by fermentation such as butanol,[59] microaerobic conditions would be suitable to achieve high yields. Therefore, the aeration conditions of the two organisms could be similar enough to warrant their co-culture in a single reactor.

Further transitions to a clean energy grid will likely reduce the carbon footprint of EMP processes due to a combination of effects too granular to be captured in our model. The life cycle carbon footprint of solar energy production, for example, will likely fall as silicon production and purification processes begin to use cleaner energy. Emissions due to transportation along the

supply chain will likely fall due to increased use of electric vehicles. As such changes continue to occur, it is in principle feasible for electromicrobial production processes to achieve full carbon neutrality. The carbon footprint of glucose-based bioprocesses, however, is unlikely to achieve full carbon neutrality. Cleaner methods of fertilizer production and electrified processes for farming machinery and glucose processing will indeed lower the carbon footprint of conventional bioprocesses. However, the primary source of greenhouse gas emissions in corn production is due to the application of fertilizers, as nitrogenous fertilizers are partially degraded to nitrous oxide, a greenhouse gas with 298-fold higher global warming potential than of CO_2.[52,53] Further transitions to a clean electric grid and electrified processing, then, are more likely to decrease the global warming potential of EMP processes than of heterotroph-based processes.

In the case of an industrial enzyme as the product of interest, the trends largely follow that of biomass (Fig. 2.5b). Assuming the industrial enzyme product is intracellular, effects of titer do not impact the energy demand as low-energy separation methods (*e.g.*, settling, filtering, centrifuging) are possible. Therefore, the similar trends for GWP in enzyme production and biomass production, scaled due to the relative yields of each, are expected. In the case of lactic acid production, the trends between EMP systems are similar to those of biomass production, with Knallgas bacteria-based production of lactic acid exhibiting the lowest global warming potential of the systems studied. I note that the lactic acid effluent must be concentrated (the model assumes electrodialysis, see Methods) in all three EMP systems studied in order to achieve the desired 100 g/L titer. However, due to the relatively low material and energy demands of the electrodialysis process, this does not significantly impact the global warming potential (Fig. 2.5c).

Importantly, the data shown in Fig. 2.5 assume 90% of the fixed carbon is converted to lactic acid (see Table 2.1), which matches the yield commonly achieved by lactic acid fermentation from glucose.[60] This high yield of lactic acid, achievable due to the high yield of fermentation products during anaerobic growth, may not be achievable in EMP systems. All three EMP systems considered (based on hydrogen-oxidizing, formatotrophic, or acetotrophic metabolism) require respiration, suggesting the high yield of lactic acid may not be achievable. Further analysis indicates that the electricity grid must be composed of at least ~90% renewable energy sources in order for EMP systems to break even with traditional bioprocessing approaches in terms of global warming potential.[61] Moreover, the product yield of lactic acid must reach ~50% of its theoretical maximum.[61]

Intrinsically safer operation of the H_2-mediated Knallgas system

Despite the lower GWP associated with the H_2-mediated system, the flammable gas mixture fed to the reactor under base case operating conditions (1 atm H_2 and 0.21 atm O_2) may pose a significant barrier to adoption of this EMP strategy. I therefore evaluated intrinsically safer operation (ISO) of the H_2-mediated system by adjusting the H_2:O_2 ratio in the gas phase such that the gas mixture was inherently non-flammable (defined as comprising an H_2:O_2 ratio of >10:1).[55] Under these conditions, O_2 gas/liquid mass transfer limits the productivity for each product (Fig. S3 in Appendix A). However, reactor productivities equivalent to that of the base case scenario can be achieved simply by increasing the total gas pressure while maintaining the inherently non-flammable gas ratio, so the GWP of the H_2-mediated EMP process is not negatively impacted by ensuring intrinsically safer operating conditions (Fig. S3). For biomass, enzymes, and lactic acid, the partial pressure of H_2 must be 3.62 atm, 3.62 atm, and ~1.8 atm, respectively, to match the

GWP of the base case scenario, pressures that are readily achievable with existing water electrolysis and bioreactor technology.[62,63]

LCA as an ecodesign tool: engineering targets for formate electrolysis

The formate-mediated EMP system is associated with a significantly higher GWP than the H_2-mediated system due primarily to differences in electrolyzer performance with currently achievable efficiencies and current densities. Because electrochemical reduction of CO_2 is an active area of research, this technology may improve in coming years, making the formate-mediated system more competitive with the H_2-mediated system. To identify engineering targets that must be met by CO_2 electrolysis systems, I calculated the GWP of biomass production as a function of electrolyzer parameters (current density, j; energy efficiency, η; formate titer, c_{FFA}), and compared these results to the H_2-mediated system operated under intrinsically safe conditions (Fig. 2.6).

Base-case electrolysis operation ($j = 140\ \mathrm{mA/cm^2}$, $\eta = 32.5\%$) results in a significantly higher GWP than the H_2-mediated system (Fig 2.6). A current density of >~250 mA/cm^2 and η >~40% is necessary to outcompete the H_2-mediated system operating at an H_2 partial pressure of 1 atm, while a current density in excess of ~750 mA/cm^2 with η >75% is necessary to reach parity with an H_2-mediated system operating at 3.62 atm of H_2 (Fig. 2.6). Despite significant progress towards improving CO_2 electrolysis performance in the past decade,[64] these metrics represent extremely challenging targets that may be infeasible. Hence, H_2-mediated EMP systems based on Knallgas bacteria appear to be better-suited for industrial adoption.

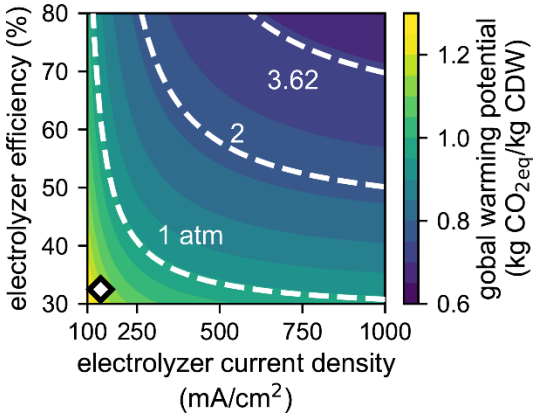

Figure 2.6. Effects of CO_2 electrolysis operating parameters. Global warming potential of biomass production with the formate-mediated system as a function of electrolyzer current density and electrolyzer efficiency. Overlaid white dashed lines correspond to the global warming potential of the intrinsically-safer H_2-mediated system (as described in the text) operating at different H_2 partial pressures (1 atm, 2 atm, 3.62 atm). Point highlighted by the diamond (white fill, black outline) denotes the base case CO_2 electrolysis operation using current technology.

Parameter sensitivity analysis

To investigate the impact of uncertainty on our model and conclusions, I performed a sensitivity analysis on the 96 individual parameters in our model. I identified the most important parameters for biomass production, defined as those for which a 30% change in the parameter value induced a significant change in the results of the analysis as defined in the Computational Methods (Fig. 2.7). Of these, three (global warming potential of glucose, biomass yield on glucose, and global warming potential of wind-produced renewable energy) are outside the scope of reactor models and therefore do not affect the productivities or efficiencies of any of the electromicrobial production systems, although they are important considerations for evaluating the trade-offs with implementing EMP systems.[61]

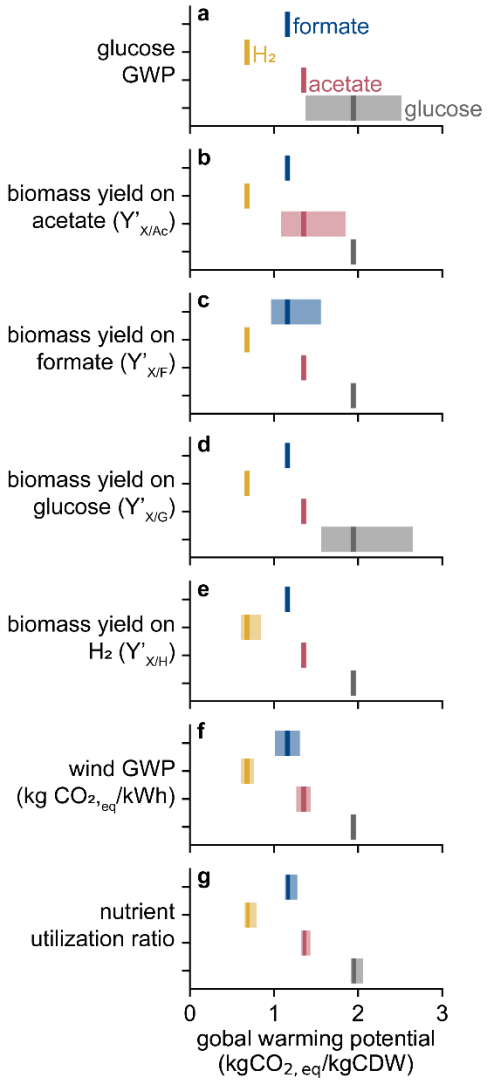

Figure 2.7. Parameter sensitivity analysis. Global warming potential dependence of producing biomass on +/-30% variation in (**a**) glucose production global warming potential, (**b**) biomass yield on acetate, (**c**) biomass yield on formate, (**d**) biomass yield on glucose, (**e**) biomass yield on H_2, (**f**) wind-based energy production global warming potential, and (**g**) the nutrient utilization ratio for each process. Dark bars represent base case values, shaded bars represent the range in global warming potential induced by variation.

Biomass yields on acetate, formate, and H_2 can all significantly impact the global warming potential of the relevant processes; however, the Knallgas bacteria system still outperforms the others even if the biomass yield on H_2 is 30% lower than expected while the biomass yields on formate and acetate are 30% higher (Fig. 2.7). Notably, microbial growth rates do not significantly impact global warming potential mainly because gas/liquid mass transfer rates impose an upper bound on productivity (see discussion around Fig. 2.3). Because the electricity demand associated with achieving high k_La values is small compared to energy substrate generation via electrolysis (Table S2 in Appendix A), productivity improvements via increased agitation or other strategies to enhance gas/liquid mass transfer rates are a straightforward strategy to reduce the carbon footprint of a given process. The final significantly impactful parameter is the nutrient utilization ratio, indicating that efforts to recycle unconsumed nutrients (especially ammonia) are also important for the viability of EMP (and traditional) bioprocesses.

The sensitivity analysis demonstrates that neither 30% variability in any single parameter nor any pair of parameters is sufficient to dislodge Knallgas bacteria-based EMP systems as the process with the lowest global warming potential, although variation in some single parameters can result in re-ordering EMP processes: for example, a 30% higher yield on acetate enables the acetate-mediated system to outperform the formate-mediated system. However, all EMP processes outcompete glucose-based bioprocessing given 30% uncertainty in any single parameter, and concomitant variation in multiple parameters in particular directions is required for glucose-based systems to achieve parity with any of the EMP processes. This analysis indicates that the conclusions presented here are robust to significant uncertainties in parameters used in the reactor, process, and life cycle impact models.

Analysis Limitations

This study employed a three-part framework, relying on physics-based bioreactor models, process models, and life cycle assessment, to analyze three proposed electromicrobial production systems. This framework predicted achievable productivity, energy use, and life cycle global warming potential. General trends regarding system performance, as well as specific engineering targets, were determined in this analysis. However, several limitations and opportunities for future work regarding the analysis of EMP systems remain. First, the three EMP systems considered here do not represent an exhaustive list of proposed or possible EMP systems. Although these three systems are prominent in the literature, several other systems that meet the criteria for electromicrobial production described in the introduction are possible. For example, methanotrophs have also been proposed for the production of bioproducts including PHB.[65,66] Methane and methanol, both potential feedstocks for methanotrophic bacteria, can be produced from CO_2 through a variety of means using renewable electricity.[67–69] Furthermore, in an attempt to obviate the need for an electrochemically-derived mediator molecule, electroautotrophic systems have been proposed in which carbon fixation is driven by direct electron transfer via reversible electron conduit proteins such as those found in *Shewanella oneidensis*.[70,71] Future work (see Chapters 4 and 5) will involve applying the framework developed here for the analysis of such systems.

Second, the current analysis predicted three key metrics regarding the potential performance of EMP systems (productivity, energy use, and life cycle GWP). These metrics each give valuable insight to the capacities and environmental impacts of EMP processes. However, this is not an exhaustive list of possible social and environmental impacts of such processes. For example, land use, eutrophication effects of unused ammonia in EMP processes, as well as the ecotoxicity of by-products (such as chlorine gas and sodium hypochlorite from the chlor-alkili process) are important environmental considerations. However, such impacts do not affect the energy demand or carbon footprint of EMP processes and are therefore outside the stated scope of this current life cycle assessment. Targeted analysis of these environmental impacts of EMP should be performed prior to large-scale industrial adoption.

2.5 Conclusion

I have described a tripartite framework for analyzing EMP systems that relies on physics-based bioreactor modelling, process design and modelling, and life cycle assessment. While life cycle assessments are typically done using industrial data from an existing process, the three-part

framework allows proactive assessments of the potential environmental impacts of EMP despite its relative immaturity compared to existing industrial biotechnology. Specifically, our methodology predicts vital metrics such as bioreactor productivity, electricity consumption, global warming potential, and land occupation footprint of hypothetical scaled-up EMP technologies based on limited bench-scale empirical data. This analysis not only demonstrates the promise of EMP for industrial application, but also identifies important hurdles that must be addressed for successful and environmentally sustainable implementation.

In brief, the bioreactor models predict productivities up to ~0.7 g/L/h with current technology, which are reasonably close to common targets for industrial commodity chemical bioproduction (~1 g/L/h).[72,73] In general, gas-liquid mass transfer is shown to be one of the limiting factors for each system's productivity, indicating that reactor designs that enable high pressure operation and/or high gas-liquid interfacial contact areas can enhance the performance of EMP systems. In some cases, the salinity tolerance of microbes limited the productivity, signaling that efforts to improve halotolerance of industrial strains or employing native halophiles for industrial applications could play an important role in the development of EMP processes.

The life cycle impact assessment of biomass production shows that each of the three analyzed EMP (formate-mediated, H_2-mediated, and acetate-mediated) systems can potentially reduce greenhouse gas emissions compared to traditional heterotroph-based processes provided the electric grid is composed of at least ~90% renewable energy sources. The carbon footprint of each EMP process is very sensitive to the composition of the electricity grid, indicating that substantial progress towards decarbonizing the grid must occur before EMP becomes environmentally advantageous. Based on our analysis, assuming current technology, the hydrogen-mediated system has the lowest global warming potential. For the acetate-mediated process to have a carbon footprint comparable to the hydrogen-mediated process, either the need for pH control must be obviated or the pH control elements (HCl and NaOH) must be obtained through a more sustainable process than currently exists industrially. For the formate-mediated process to have a global warming potential as low as the hydrogen-mediated system, improvements must be made to the energy efficiency and/or current density of formate electrolysis (see Fig. 2.6). Because formate-mediated EMP does have several advantages over hydrogen-mediated (*e.g.*, reduced safety concerns, less challenging transportation and storage), research in the field of electrochemistry to improve the performance of CO_2 reduction to formate has the potential to greatly improve EMP systems. However, in the current modelling and analysis, hydrogen-mediated EMP has the lowest global warming potential and is currently most suitable for industrial application.

Sensitivity analysis revealed that the most important engineering parameter for the global warming potential of the hydrogen-mediated system is the yield of product on hydrogen. Utilization of carbon fixation pathways other than the Calvin cycle with higher thermodynamic efficiency could improve this yield and therefore improve the environmental (and economic) viability of EMP. Efforts to improve the yield through more efficient carbon fixation pathways, as has been done with the reductive glycine pathway in *C. necator*,[74] represent a promising research direction for the field. Likewise, the carbon efficiency (which affects the overall hydrogen-to-product yield) for commodity chemical products such as lactic acid strongly influences the global warming potential of the process. Therefore, metabolic engineering efforts should prioritize

engineering strains capable of maximizing carbon flux towards the product of interest while minimizing the production of unnecessary byproducts. As individual components of EMP systems continue to improve, our framework will be able to evaluate these changes in terms of productivity, energy demand, and global warming potential. The methodology is therefore a useful tool for iteratively assessing the status of this technology and identifying obstacles to its implementation.

Electromicrobial production has the potential to "electrify" the biotechnology industry. However, my analysis indicates that, due to the abundance of fossil energy sources in the current electric grid, EMP would lead to higher greenhouse gas emissions compared to traditional bioprocesses if implemented in the United States today. Nonetheless, as the grid is decarbonized in the coming decades, EMP will become an attractive alternative method of bioproduction. Pilot-scale EMP of various value-added products should be thus developed in the near term such that further scaling and distribution can be accomplished in the coming decades as the electricity grid becomes fully decarbonized.

2.6 References

1 S. Huffer, C. M. Roche, H. W. Blanch and D. S. Clark, *Trends Biotechnol.*, 2012, **30**, 538–545.

2 A. M. Brandon and C. S. Criddle, *Curr. Opin. Biotechnol.*, 2019, **57**, 160–166.

3 T. Werpy and G. Petersen, *Top Value Added Chemicals from Biomass Volume I-Results of Screening for Potential Candidates from Sugars and Synthesis Gas*, 2004.

4 R. Singh, M. Kumar, A. Mittal, • Praveen and K. Mehta, *3 Biotech*, , DOI:10.1007/s13205-016-0485-8.

5 J. D. Adams, J. J. Røise, D. S. Lee and N. Murthy, *Chem. Commun.*, 2020, **56**, 3175–3178.

6 J. Puetz and F. M. Wurm, *Processes*, 2019, **7**, 476.

7 L. M. L. Laurens, J. Markham, D. W. Templeton, E. D. Christensen, S. Van Wychen, E. W. Vadelius, M. Chen-Glasser, T. Dong, R. Davis and P. T. Pienkos, *Energy Environ. Sci.*, 2017, **10**, 1716–1738.

8 R. E. Blankenship, D. M. Blankenship, J. Tiede, G. W. Barber, G. Brudvig, M. Fleming, M. R. Ghirardi, W. Gunner, D. M. Junge, A. Kramer, T. A. Melis, C. C. Moore, D. G. Moser, A. J. Nocera, D. R. Nozik, W. W. Ort, R. C. Parson, R. T. Prince and Sayre, *Science (80-.).*, 2011, **332**, 805–809.

9 K. Tanaka and A. Ishizaki, *J. Ferment. Bioeng.*, 1994, **77**, 425–427.

10 B. Kunasundari, V. Murugaiyah, G. Kaur, F. H. J. Maurer and K. Sudesh, *PLoS One*, 2013, **8**, 78528.

11 E. Grousseau, J. Lu, N. Gorret, S. E. Guillouet and A. J. Sinskey, *Appl. Microbiol. Biotechnol.*, 2014, **98**, 4277–4290.

12 C. Windhorst and J. Gescher, *Biotechnol. Biofuels*, 2019, **12**, 163.

13 L. Crépin, E. Lombard and S. E. Guillouet, *Metab. Eng.*, 2016, **37**, 92–101.

14 O. Yishai, S. N. Lindner, J. Gonzalez de la Cruz, H. Tenenboim and A. Bar-Even, *Curr. Opin. Chem. Biol.*, 2016, **35**, 1–9.

15 H. Li, P. H. Opgenorth, D. G. Wernick, S. Rogers, T. Wu, W. Higashide, P. Malati, Y. Huo, K. M. Cho and J. C. Liao, *Science (80-.).*, 2012, **335**, 1596.

16 A. J. Abel and D. S. Clark, *ChemSusChem*, 2021, **14**, 344–355.

17 S. Grunwald, A. Mottet, E. Grousseau, J. K. Plassmeier, M. K. Popović, J. L. Uribelarrea, N. Gorret, S. E. Guillouet and A. Sinskey, *Microb. Biotechnol.*, 2015, **8**, 155–163.
18 S. Kim, S. N. Lindner, S. Aslan, O. Yishai, S. Wenk, K. Schann and A. Bar-Even, *Nat. Chem. Biol.*, 2020, **16**, 538–545.
19 C. Liu, J. J. Gallagher, K. K. Sakimoto, E. M. Nichols, C. J. Chang, M. C. Y. Chang and P. Yang, *Nano Lett.*, 2015, **15**, 3634–3639.
20 S. Cestellos-Blanco, S. Friedline, K. B. Sander, A. J. Abel, J. M. Kim, D. S. Clark, A. P. Arkin and P. Yang, *Front. Microbiol.*, 2021, **12**, 1–12.
21 N. J. Claassens, C. A. R. Cotton, D. Kopljar and A. Bar-Even, *Nat. Catal.*, 2019, **2**, 437–447.
22 F. Salimijazi, J. Kim, A. M. Schmitz, R. Grenville, A. Bocarsly and B. Barstow, *Joule*, 2020, **4**, 2101–2130.
23 D. Leger, S. Matassa, E. Noor, A. Shepon, R. Milo and A. Bar-Even, *Proc. Natl. Acad. Sci.*, 2021, **118**, e2015025118.
24 International Organization for Standardization (ISO), *ISO 14044*.
25 International organization for standarization, *ISO 14040*.
26 T. E. McKone, W. W. Nazaroff, P. Berck, M. Auffhammer, T. Lipman, M. S. Torn, E. Masanet, A. Lobscheid, N. Santero, U. Mishra, A. Barrett, M. Bomberg, K. Fingerman, C. Scown, B. Strogen and A. Horvath, *Environ. Sci. Technol.*, 2011, **45**, 1751–1756.
27 J. Izursa, E. A. Hanlon, N. Y. Amponsah and J. C. Capece, *Carbon Footprint of Biofuel Sugarcane Produced in Mineral and Organic Soils in Florida - Manuscript submitted for publication*, LaBelle, FL, 2013.
28 S. N. Nangle, M. Ziesack, S. Buckley, D. Trivedi, D. M. Loh, D. G. Nocera and P. A. Silver, *Metab. Eng.*, 2020, **62**, 207–220.
29 J. Sillman, L. Nygren, H. Kahiluoto, V. Ruuskanen, A. Tamminen, C. Bajamundi, M. Nappa, M. Wuokko, T. Lindh, P. Vainikka, J.-P. Pitkänen and J. Ahola, *Glob. Food Sec.*, 2019, **22**, 25–32.
30 T. Cumberlege, T. Blenkinsopp and J. Clark, 2016, 1–26.
31 H. W. Blanch and D. S. Clark, *Biochemical Engineering*, CRC Press, 2nd edn., 1997.
32 Y. Xiao, X. Feng, A. M. Varman, L. He, H. Yu and Y. J. Tang, *Ind. Eng. Chem. Res.*, 2012, **51**, 15855–15863.
33 A. G. Fast and E. T. Papoutsakis, *Curr. Opin. Chem. Eng.*, 2012, **1**, 380–395.
34 K. Schuchmann and V. Müller, *Nat. Rev. Microbiol.*, 2014, **12**, 809–821.
35 L. Rosso, J. R. Lobry, S. Bajard and J. P. Flandrois, *Appl. Environ. Microbiol.*, 1995, **61**, 610–616.
36 X. Wu, R. Altman, M. A. Eiteman and E. Altman, *Appl. Environ. Microbiol.*, 2014, **80**, 2880–2888.
37 W. G. Mook, *Environmental isotopes in the hydrological cycle: Principles and applications, Volume I: Introduction: Theory, Methods, Review*, 2001, vol. 1.
38 J. L. Meraz, K. L. Dubrawski, S. H. El Abbadi, K. H. Choo and C. S. Criddle, *J. Environ. Eng.*, , DOI:10.1061/(ASCE)EE.1943-7870.0001703.
39 A. Ciroth, *Int. J. Life Cycle Assess.*, 2007, **12**, 209.
40 D. M. de S. Simone Manfredi, Karen Allacker, Kirana Chomkhamsri, Nathan Pelletier, *Product Environmental Footprint (PEF) Guide*, 2012.
41 M. R. Subramanian, S. Talluri and L. P. Christopher, *Microb. Biotechnol.*, 2015, **8**, 221–229.

42 M. Heldal, S. Norland and O. Tumyr, *Appl. Environ. Microbiol.*, 1985, **50**, 1251 LP – 1257.
43 S. Deutz and A. Bardow, *Nat. Energy*, 2021, **6**, 203–213.
44 V. Singh, I. Dincer and M. A. Rosen, eds. I. Dincer, C. O. Colpan and O. B. T.-E. Kizilkan Energetic and Environmental Dimensions, Academic Press, 2018, pp. 935–959.
45 I. Garcia-Herrero, M. Margallo, R. Onandía, R. Aldaco and A. Irabien, *Sci. Total Environ.*, 2017, **580**, 147–157.
46 A. Buttler and H. Spliethoff, *Renew. Sustain. Energy Rev.*, 2018, 82, 2440–2454.
47 J. Xu, G. Liu, J. Li and X. Wang, *Electrochim. Acta*, 2012, **59**, 105–112.
48 H. Yang, J. J. Kaczur, S. D. Sajjad and R. I. Masel, *J. CO2 Util.*, 2017, **20**, 208–217.
49 V. Hábová, K. Melzoch, M. Rychtera and B. Sekavová, *Desalination*, 2004, **162**, 361–372.
50 R. Stropnik, A. Lotrič, A. Bernad Montenegro, M. Sekavčnik and M. Mori, *Energy Sci. Eng.*, 2019, **7**, 2519–2539.
51 A. Stadel, P. Gursel and E. Masanet, , DOI:10.2172/1223003.
52 B. L. Ma, B. C. Liang, D. K. Biswas, M. J. Morrison and N. B. McLaughlin, *Nutr. Cycl. Agroecosystems*, 2012, **94**, 15–31.
53 J. Huang, B. Mendoza, J. S. Daniel, C. J. Nielsen, L. Rotstayn and O. Wild, *Clim. Chang. 2013 Phys. Sci. Basis Work. Gr. I Contrib. to Fifth Assess. Rep. Intergov. Panel Clim. Chang.*, 2013, **9781107057**, 659–740.
54 M. Huijbregts, Z. J. N. Steinmann, P. M. F. M. Elshout, G. Stam, F. Verones, M. D. M. Vieira, M. Zijp and R. van Zelm, *ReCiPe 2016 - A harmonized life cycle impact assessment method at midpoint and endpoint level. Report I: Characterization*, 2016.
55 M. A. Terpstra, University of Calgary, 2012.
56 B. Möller, R. Oßmer, B. H. Howard, G. Gottschalk and H. Hippe, *Arch. Microbiol.*, 1984, **139**, 388–396.
57 R. Kutscha and S. Pflügl, *Int. J. Mol. Sci.*, 2020, **21**, 1–30.
58 X. C. Shi, P. L. Tremblay, L. Wan and T. Zhang, *Sci. Total Environ.*, 2021, **754**, 142440.
59 E. M. Nichols, J. J. Gallagher, C. Liu, Y. Su, J. Resasco, Y. Yu, Y. Sun, P. Yang, M. C. Y. Chang, C. J. Chang, C. J. C. Designed, Y. Su and Y. Sun, *PNAS*, 2015, **112**, 11461–11466.
60 B. P. Upadhyaya, L. C. DeVeaux and L. P. Christopher, *Trends Biotechnol.*, 2014, **32**, 637–644.
61 A. J. Abel, J. D. Adams and D. S. Clark, *bioRxiv*, 2021, 2021.07.01.450744.
62 M. Carmo, D. L. Fritz, J. Mergel and D. Stolten, *Int. J. Hydrogen Energy*, 2013, **38**, 4901–4934.
63 W. Van Hecke, R. Bockrath and H. De Wever, *Bioresour. Technol.*, 2019, **293**, 122129.
64 M. Y. Lee, K. T. Park, W. Lee, H. Lim, Y. Kwon and S. Kang, *Crit. Rev. Environ. Sci. Technol.*, 2020, **50**, 769–815.
65 E. R. Sundstrom and C. S. Criddle, *Appl. Environ. Microbiol.*, 2015, **81**, 4767–4773.
66 S. N. Nangle, M. Y. Wolfson, L. Hartsough, N. J. Ma, C. E. Mason, M. Merighi, V. Nathan, P. A. Silver, M. Simon, J. Swett, D. B. Thompson and M. Ziesack, *Nat. Biotechnol.*, 2020, **38**, 401–407.
67 M. Götz, J. Lefebvre, F. Mörs, A. McDaniel Koch, F. Graf, S. Bajohr, R. Reimert and T. Kolb, *Renew. Energy*, 2016, **85**, 1371–1390.
68 J. C. Fornaciari, D. Primc, K. Kawashima, B. R. Wygant, S. Verma, L. Spanu, C. B.

Mullins, A. T. Bell and A. Z. Weber, , DOI:10.1021/acsenergylett.0c01508.
69 M. Umeda, Y. Niitsuma, T. Horikawa, S. Matsuda and M. Osawa, *ACS Appl. Energy Mater.*, 2020, **3**, 1119–1127.
70 A. Prévoteau, J. M. Carvajal-Arroyo, R. Ganigué and K. Rabaey, *Curr. Opin. Biotechnol.*, 2020, **62**, 48–57.
71 A. J. Abel, J. M. Hilzinger, A. P. Arkin and D. S. Clark, *Bioelectrochemistry*, 2022, 108054.
72 R. Davis, L. Tao, E. C. D. Tan, M. J. Biddy, G. T. Beckham, C. Scarlata, J. Jacobson, K. Cafferty, J. Ross, J. Lukas, D. Knorr and P. Schoen, *Natl. Renew. Energy Lab.*, 2013, 147.
73 Y. Li, S. S. Bhagwat, Y. R. Cortés-Peña, D. Ki, C. V Rao, Y.-S. Jin and J. S. Guest, *ACS Sustain. Chem. Eng.*, 2021, **9**, 1341–1351.
74 N. J. Claassens, G. Bordanaba-Florit, C. A. R. Cotton, A. De Maria, M. Finger-Bou, L. Friedeheim, N. Giner-Laguarda, M. Munar-Palmer, W. Newell, G. Scarinci, J. Verbunt, S. T. de Vries, S. Yilmaz and A. Bar-Even, *Metab. Eng.*, 2020, **62**, 30–41.

Chapter 3: Modeling analysis of formate-mediated electromicrobial production systems[†]

3.1 Abstract

In Chapter 2, I analyzed three mediated EMP systems with formate, H_2, and acetate as the mediator molecules. In all systems, I assumed that the electrochemical reactions (*e.g.*, CO_2 electroreduction to formate) occurred in a separate reactor from the biochemical reactions. This type of mediated process relies on existing technologies, and therefore represents the most "industrially ready" version of EMP processes. However, as discussed in Chapter 1, EMP processes have also been proposed wherein the electrochemical and biochemical reactions occur in the same reactor. This strategy could reduce the materials demand for the overall system if it is able to achieve high productivities. In this chapter, I describe the development and application of a comprehensive multiphysics model to analyze a formate-mediated EMP reactor in which electrochemical and biochemical reactions occur simultaneously. The model shows that this system can achieve a biomass productivity of ~1.7 g/L/h but is limited by a competitive trade-off between O_2 gas-liquid mass transfer and CO_2 transport to the cathode. Synthetic metabolic strategies are evaluated for formatotrophic growth, which can enable an energy efficiency of ~21%, a 30% improvement over the Calvin cycle. However, carbon utilization efficiency is only ~10% in the best cases due to a futile CO_2 cycle, so gas recycle will be necessary for greater efficiency. Finally, I show that the two-reactor (one electrolyzer, one bioreactor) system enables a higher biomass productivity of ~2.4 g/L/hr, indicating that the integrated system would likely result in higher materials demands than those described in Chapter 2.

3.2 Introduction

The capture and conversion of CO_2 is a promising strategy for the production of carbon-based chemicals and could help to close the anthropogenic carbon cycle.[1] Among the many strategies to fix CO_2 using renewable energy, so-called "mediated" or "coupled" electromicrobial production (EMP) has received significant attention.[2–5] In this scheme, electrons (ideally from a renewable source) are used to electrochemically reduce a mediator molecule that is then oxidized by planktonic microbes as a growth substrate.

[†]This chapter was originally published in *ChemSusChem* and has been adapted with permission from the coauthors

Several groups have developed prototypical systems for mediated EMP, relying on various redox mediators including H_2,[6–9] inorganic ions (*e.g.* ferrous ions or ammonia),[10,11] simple organic molecules (*e.g.* carbon monoxide, formate, and methanol),[12–15] and complex organic molecules such as the dye neutral red.[16,17] Although these prototype systems have been able to achieve high efficiencies (~10% in the case of Wang *et al.*[8]), the scalability and potential productivity of these systems remain unclear. The choice of redox mediator requires careful consideration: the ideal one should be abundantly available or easily produced electrochemically (eliminating complex organic molecules and inorganic ions), and electropositive enough to directly reduce NAD(P)H for efficient energy transfer to cellular metabolism.[3,5] Moreover, many authors suggest that high solubility is beneficial,[3,18] although these benefits may not be easy to realize (see Chapter 2). Formate/ic acid stands out as an especially promising redox mediator because it is readily and specifically produced from CO_2[19–21] and multiple natural and engineered formatotrophic growth mechanisms exist in workhorse bacteria.[22–26]

Initial scale-up,[27] component integration,[28] and media optimization[29] studies have been performed for EMP systems, demonstrating the need for careful attention to process parameters including the gas/liquid mass transfer coefficient (k_La). However, progress towards scaled, optimized systems has been limited, in part due to the complex nature of coupled bio-electrochemical systems. Because many physical processes occur simultaneously (diffusion and migration of species in fluid boundary layers, electrochemical and acid/base reactions, microbial growth and consumption and production of species, gas/liquid mass transfer, *etc.*), understanding the impact or potential of a given process or engineering strategy is difficult without a detailed, comprehensive model that accounts for all of the relevant physics. Moreover, such a model is necessary to quantify design and operation strategies that optimize efficiency and to identify process parameters that limit productivity.

To that end, several models of EMP or related systems have been developed.[30–35] Picioreanu *et al.* developed models for microbial fuel cells with planktonic microbes and biofilms using a generic redox mediator to shuttle electrons between the anode and microbes, both of which were able to accurately fit data from fed-batch experimental systems.[33,34] Kazemi *et al*. developed one of the first EMP models based on a conductive biofilm performing direct electron transfer, and using the model were able to relate applied potential to acetate production for the acetogenic bacterium *Sporomusa ovata* in a batch system.[32] Recently, Gadkari *et al.* modeled microbial communities driving electrode reactions at both the anode and the cathode using a generic redox mediator, and predicted limiting production rates as a function of initial substrate concentration in a fed-batch system.[30] Despite these successes, modeling studies have so far not focused on mediated EMP systems or continuous operation schemes that will be necessary for processing at industrial scales. Moreover, previous models have focused on batch or fed-batch systems without considering physical phenomena such as gas/liquid mass transfer that are critical to scaled-up operation. Additionally, formate/ic acid requires explicit attention as a redox mediator because of its potential toxicity and participation in acid/base reactions that must be considered in reactor design and operation.

In this chapter, I present a comprehensive multiphysics modeling framework that describes mass transport; electrochemical, acid/base, and microbial reaction kinetics; temperature effects, and gas/liquid mass transfer for an EMP system generating formate and H_2 (as a secondary

product) at an abiotic cathode for consumption by planktonic cells (Fig. 3.1). The model is used to evaluate the effects of reactor design and operating parameters on critical performance metrics including biomass productivity, cell density, and carbon utilization and energy efficiency; and to compare the performance of microbes using different formatotrophic growth strategies under different optimal growth conditions. A key finding is that for integrated systems the tradeoff between O_2 availability for microbial respiration and CO_2 transport to the cathode surface for electrochemical reduction limits formate-mediated EMP productivity and that separating electrochemical and microbial processes into two reactors avoids this fundamental limitation. The presented model, methodology, and analysis provide a complete framework for analyzing mediated EMP reactor systems and identify promising research strategies for scale-up and process optimization that can advance EMP systems from basic science to technological practice.

3.3 Computational Methods

System overview and governing equations

The model considers a one-dimensional bio-electrochemical reactor for conversion of CO_2 into biomass via formate (Fig. 3.1A). The reactor has a well-mixed region that is exchanged at a fixed dilution rate and to which a CO_2/O_2 gas mix is constantly supplied at a fixed pressure. Fluid boundary layers (BLs) separate the well-mixed liquid phase from the anode and cathode surfaces, where electrochemical reactions are driven by an applied voltage to oxidize water (at the anode surface) and reduce CO_2 to $HCOO^-$ or reduce protons to H_2 (both at the cathode surface). Microbes at an initial concentration of $c_{X,0}$ grow in the well-mixed phase by consuming $HCOO^-$, H^+, H_2, CO_2, and O_2. The chemical species considered in the reactor system are dissolved CO_2, dissolved O_2, dissolved H_2, bicarbonate anions (HCO_3^-), carbonate anions (CO_3^{2-}), formic acid (HCOOH), formate anions ($HCOO^-$), protons (H^+), hydroxide anions (OH^-), sodium cations (Na^+), nitrate anions (NO_3^-), and microbes (X). NO_3^- was selected as a representative anion for sodium salt to avoid the use of chloride ions (Cl^-), which are known to produce deleterious and toxic side reactions at the cathode surface in EMP systems.[29] By neglecting ammonium/a species, I have assumed that they are fed in excess to the system as NH_3. The growth of two different model organisms is considered: *Cupriavidus necator*, a well-studied chemolithoautotrophic organism in EMP systems that is capable of growth on both formate and H_2 as energy sources, and *Escherichia coli*, the biotechnology workhorse bacterium that has been recently engineered to support formatotrophic growth.[23]

Well-mixed phase balance equations

The well-mixed electrolyte regions are assumed to have sufficient convective mixing such that no concentration gradients are formed. Such an open, well-mixed system must satisfy mass conservation, given generally for the reactor model by

$$\frac{dc_i}{dt} = R_{\mathrm{X},i} + R_{\mathrm{A-B},i} + R_{\mathrm{F},i} + S_{\mathrm{A}}\left(N_i|_{\mathrm{BL_A}} - N_i|_{\mathrm{BL_C}}\right) \quad (1)$$

where c_i is the concentration, R_i is the net volumetric rate of formation and consumption due to microbial growth (X), acid/base reactions (A–B), and feed terms (F), and N_i is the flux of species i. The electrode surface area-to-volume ratio is given by S_{A}. By convention, the positive x-

direction is defined to the right of the page such that species flux from the cathode boundary layer phase (BL_C) to the well-mixed phase will have a negative value.

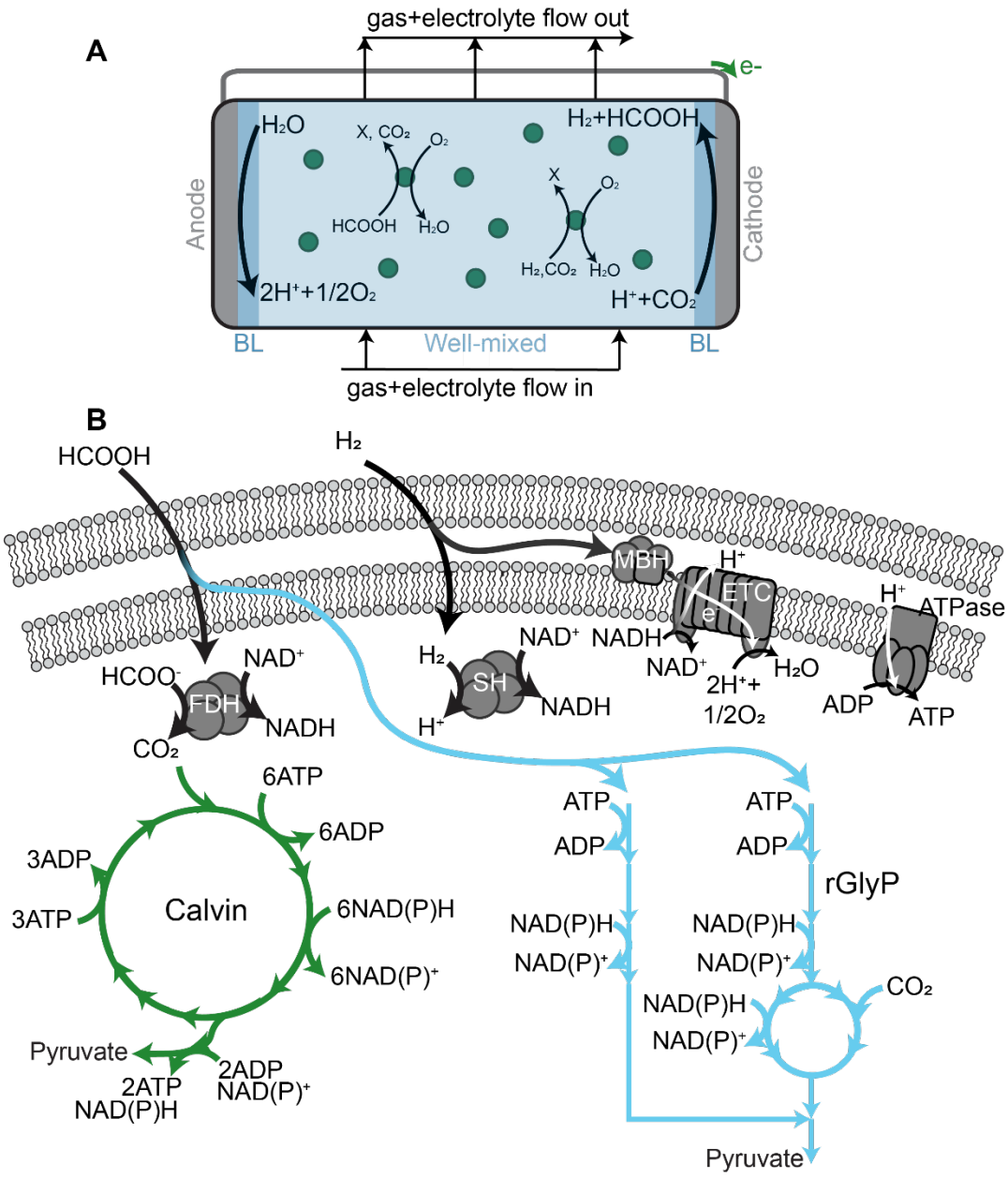

Figure 3.1. Reactor overview and formatotrophic growth strategies. (**A**) Reactor scheme. Carbon dioxide (CO_2) and oxygen (O_2) gas and electrolyte media are fed into a well-mixed bioelectrochemical reactor with hydrodynamic boundary layers separating the well-mixed phase from the electrode surfaces. (**B**) Energy metabolism (black, gray) and carbon fixation pathways (Calvin cycle: green, reductive glycine pathway (rGlyP): blue). X: biomass; FDH: formate dehydrogenase; SH: soluble hydrogenase; MBH: membrane-bound hydrogenase; ETC: electron transport chain.

Species transport in the electrolyte boundary layers

The molar flux of species (assuming no net fluid velocity) in dilute electrolyte solutions is written as the sum of diffusive and migrative fluxes:

$$N_i = -D_i \frac{\partial c_i}{\partial x} - z_i u_i F c_i \frac{\partial \phi_\mathrm{l}}{\partial x} \tag{2}$$

where D_i and u_i are the diffusivity and mobility (related by the Nernst-Einstein relationship, $u_i = D_i/RT$ for dilute solutions) and z_i is the charge number for species i, F is Faraday's constant, and ϕ_l is the local electrolyte potential. Flux boundary conditions at the anode and cathode surfaces are described below.

Charge conservation and electroneutrality

Charge conservation in the system requires that

$$i_\mathrm{s} = i_\mathrm{l} = i_\mathrm{R} \tag{3}$$

where i_n is the current density in the solid electrode (s), electrolyte media (l), and at the electrode/electrolyte interface (R, *i.e.* the electrochemical reaction current density). The net ionic current density (i_l) can be calculated from the total ionic flux,

$$i_\mathrm{l} = F \sum_i z_i N_i \tag{4}$$

following electroneutrality, given by

$$\sum_i z_i c_i = 0 \tag{5}$$

Note that the equilibrium distribution of species in gas-saturated electrolyte media is constrained by the electroneutrality requirement, the four independent acid/base reactions, the three gas solubility relationships, and the requirement that mole fractions sum to unity. Therefore, this system has two degrees of freedom (excluding microbes), and is fully constrained by setting the concentrations of, for example, CO_2 and H^+ (or the pH). To better replicate experimental procedures, I fix the pH and the $NaNO_3$ concentration and use the equilibrium, solubility, and electroneutrality relationships to determine all other values.

Microbial growth

Microbial growth occurs in the well-mixed phase and is responsible for the production of more cells and the consumption or production of several chemical species. These reactions are compiled in $R_{X,i}$, which is written as

$$R_{\mathrm{X,X}} = \mu X \tag{6}$$

for microbes, and as:

$$R_{\mathrm{X},i} = -\alpha_i \mu X \tag{7}$$

for all other species. Here, μ is the specific growth rate and α_i is a stoichiometric coefficient, which will be defined for different species as $\alpha, \beta, \gamma, \kappa, \epsilon$, and ζ, following convention from Blanch and Clark,[36] in the following sections.

Microbial growth kinetics are defined using the Monod model. For formatotrophic growth, I consider the growth rate dependence on both formate and oxygen:

$$\mu_{\mathrm{F}} = \mu_{\max}\left(\frac{c_{\mathrm{F}}}{K_{\mathrm{S,F}} + c_{\mathrm{F}}}\right)\left(\frac{c_{\mathrm{O_2}}}{K_{\mathrm{S,O_2}} + c_{\mathrm{O_2}}}\right) \tag{8}$$

where μ_F refers to growth on formate, $\mu_{\max}$ is the maximum specific growth rate, and $K_{S,i}$ is the Monod constant or half-saturation constant for substrate i. For hydrogenotrophic growth, I consider the concentrations of H_2, O_2, CO_2, and $HCOO^-$ (only for growth using the reductive Glycine pathway) following the same method:

$$\mu_{H_2} = \mu_{\max}\left(\frac{c_{\mathrm{H_2}}}{K_{\mathrm{S,H_2}} + c_{H_2}}\right)\left(\frac{c_{\mathrm{O_2}}}{K_{\mathrm{S,O_2}} + c_{\mathrm{O_2}}}\right)\left(\frac{c_{\mathrm{CO_2}}}{K_{\mathrm{S,CO_2}} + c_{CO_2}}\right)\left(\frac{c_{\mathrm{F}}}{K_{\mathrm{S,F}} + c_{\mathrm{F}}}\right) \tag{9}$$

In the case of *C. necator* growth, the growth on formate and H_2 is summed:

$$\mu = \mu_{\mathrm{F}} + \mu_{\mathrm{H_2}} \tag{10}$$

Formatotrophic growth yield

I use a simple, generic equation to describe both complete formate oxidation coupled with CO_2 fixation and partial formate oxidation coupled to partial formate assimilation (Fig. 3.1B):

$$\frac{1}{Y'_{\mathrm{X/S}}}(\mathrm{HCOO^-} + \mathrm{H^+}) + \beta\mathrm{NH_3} + \gamma\mathrm{O_2} \rightarrow X + \kappa\mathrm{CO_2} + \epsilon\mathrm{H_2O} \tag{11}$$

The molar cell yield, $Y'_{X/S}$, is influenced by formate concentration due to a range of toxicity effects in *C. necator*, and is given by an empirical equation[24]:

$$Y'_{\mathrm{X/S}} = Y'_{\mathrm{X/S,max}}\left(1 - \frac{c_{\mathrm{F}} + c_{\mathrm{FA}}}{\theta_{\mathrm{F}}}\right) \tag{12}$$

where θ_F is a fitting parameter that represents the maximum formate/ic acid concentration at which cells can grow. By mole balance, the stoichiometric coefficients are

$$\begin{gathered} \beta = 0.25 \\ \gamma = \frac{1}{2}\left(0.44 + 2\kappa + \epsilon - \frac{2}{Y'_{\mathrm{X/S}}}\right) \\ \kappa = \frac{1}{Y'_{\mathrm{X/S}}} - 1 \end{gathered} \tag{13}$$

$$\epsilon = \frac{1}{2}\left(\frac{2}{Y'_{\mathrm{X/S}}} + 3\beta - 1.77\right)$$

for biomass with the composition $\mathrm{C_1H_{1.77}O_{0.44}N_{0.25}}$.[24]

The reductive glycine pathway (rGlyP), recently engineered in both *C. necator*[22] and *E. coli*[23] and discovered in wild-type phosphite-oxidizing organisms,[37] is predicted to enable higher biomass yield using formate as a growth substrate than the Calvin cycle (Fig. 3.1B).[25] To evaluate the promise of this alternate formatotrophic growth strategy, I modeled the improved growth by increasing $Y'_{\mathrm{X/S,max}}$ 27% relative to its value for the Calvin cycle based on the predicted theoretical improvement (see supplementary note 1 for additional details).

I used the same equations (11 – 13) to describe formatotrophic growth of *E. coli* using the rGlyP, and adjusted θ_{F} to reflect the maximum formate concentration that enabled growth reported by Kim *et al*.[23] I used $Y'_{\mathrm{X/S,max}}$ and μ_{max} values equivalent to the theoretical values for *C. necator* using the rGlyP to reflect an optimistic outlook on the promise of further engineering to improve formatotrophic *E. coli* growth (the strain reported by Kim *et al.* achieves ~42% of this yield value and ~50% of the maximum growth rate).

Hydrogenotrophic growth yield

A simple equation for hydrogenotrophic growth of *C. necator* using the Calvin cycle is given by Ishizaki *et al.*[38]:

$$5.22\mathrm{H_2} + 1.52\mathrm{O_2} + \mathrm{CO_2} + 0.186\mathrm{NH_3} \rightarrow \mathrm{C_1H_{1.74}O_{0.46}N_{0.186}} + 4.57\ \mathrm{H_2O} \qquad (14)$$

Note that the cell stoichiometry measured by Ishizaki *et al.* is slightly different from that used by Grunwald *et al.*[24] In the model, cell mass is a single species that is not broken into its constitutive elements, so this difference is not accounted for in the model.

To compare hydrogenotrophic growth using the Calvin cycle and the rGlyP, eq. (14) is generalized according to

$$\alpha\mathrm{H_2} + \beta\mathrm{NH_3} + \gamma\mathrm{O_2} + \kappa\mathrm{CO_2} + \zeta\mathrm{HCOOH} \rightarrow \mathrm{X} + \epsilon\mathrm{H_2O} \qquad (15)$$

where $\zeta = 0$ for growth with the Calvin cycle and $\zeta = 2\kappa$ for growth on the rGlyP (see supplementary note 1 in Appendix B for additional details). The stoichiometric coefficients are determined by a mole balance using the cell stoichiometry given by Ishizaki *et al*.[38]:

$$\begin{gathered} \alpha = \frac{1}{Y'_{X/H}} \\ \beta = 0.186 \\ \kappa + \zeta = 1 \\ \epsilon = \alpha + \zeta - 0.591 \\ \gamma = \frac{0.46 + \epsilon}{2} - 1 \end{gathered} \qquad (16)$$

Because the rGlyP makes more efficient use of reducing equivalents, I increase the biomass yield ($Y'_{\mathrm{X/H}}$) by ~82% as predicted by the theoretical calculations (Supplementary note 1).

2.2.3 Growth rate dependence on temperature and pH

A simple model is used to describe the effects of temperature and pH on microbial growth following Rosso *et al.*[39]:

$$\mu_{\max} = \mu_{\mathrm{opt}} \tau(\mathrm{T}) \rho(\mathrm{pH}) \tag{17}$$

where μ_{opt} is the growth rate at optimal conditions and $\tau(\mathrm{T})$ and $\rho(\mathrm{pH})$ are written as

$$\begin{gathered} \tau(\mathrm{T}) = \begin{cases} 0, & T < T_{\min} \\ f(\mathrm{T}), & T_{\min} \le T \le T_{\max} \\ 0, & T > T_{\max} \end{cases} \\ \rho(\mathrm{pH}) = \begin{cases} 0, & pH < pH_{\min} \\ f(\mathrm{pH}), & pH_{\min} \le pH \le pH_{\max} \\ 0, & pH > pH_{\max} \end{cases} \end{gathered} \tag{18}$$

Here, $T_{\min/\max}$ and $pH_{\min/\max}$ are the ranges of temperature and pH over which microbial growth is observed, and the functions $f(T)$ and $f(pH)$ are

$$\begin{aligned} f(T) &= \frac{(T - T_{\max})(T - T_{\min})^2}{(T_{\mathrm{opt}} - T_{\min})\left[(T_{\mathrm{opt}} - T_{\min})(T - T_{\mathrm{opt}}) - (T_{\mathrm{opt}} - T_{\max})(T_{\mathrm{opt}} + T_{\min} - 2T)\right]} \\ f(\mathrm{pH}) &= \frac{(pH - pH_{\min})(pH - pH_{\max})}{(pH - pH_{\min})(pH - pH_{\max}) - \left(pH - pH_{\mathrm{opt}}\right)^2} \end{aligned} \tag{19}$$

where T_{opt} and $\mathrm{pH_{opt}}$ are the optimal temperature and pH for growth, respectively.

Acid/base reactions

The acid/base bicarbonate/carbonate, formic acid/formate, and water dissociation reactions shown below occur in all phases and are treated as kinetic expressions without assuming equilibrium (eq. (26)):

$$\mathrm{CO_{2(aq)}} + \mathrm{H_2O} \overset{k_{+1},k_{-1}}{\longleftrightarrow} \mathrm{H^+} + \mathrm{HCO_3^-} \qquad K_1 \tag{20}$$

$$\mathrm{HCO_3^-} \overset{k_{+2},k_{-2}}{\longleftrightarrow} \mathrm{H^+} + \mathrm{CO_3^{2-}} \qquad K_2 \tag{21}$$

$$\mathrm{CO_{2(aq)}} + \mathrm{OH^-} \overset{k_{+3},k_{-3}}{\longleftrightarrow} \mathrm{HCO_3^-} \qquad K_3 = K_1/K_{\mathrm{w}} \tag{22}$$

$$\mathrm{HCO_3^-} + \mathrm{OH^-} \overset{k_{+4},k_{-4}}{\longleftrightarrow} \mathrm{CO_3^{2-}} + \mathrm{H_2O} \qquad K_4 = K_2/K_{\mathrm{w}} \tag{23}$$

$$\mathrm{HCOOH} \overset{k_{+5},k_{-5}}{\longleftrightarrow} \mathrm{HCOO^-} + \mathrm{H^+} \qquad K_5 \qquad (24)$$

$$\mathrm{H_2O} \overset{k_{\mathrm{w}},k_{-\mathrm{w}}}{\longleftrightarrow} \mathrm{H^+} + \mathrm{OH^-} \qquad K_{\mathrm{W}} \qquad (25)$$

where k_{+n} and k_{-n} are the forward and reverse rate constants, respectively, and K_n is the equilibrium constant for the nth reaction, given by

$$K_n = \exp\left(\frac{\Delta S_n}{R}\right)\exp\left(-\frac{\Delta H_n}{RT}\right) \qquad (26)$$

Source and sink terms resulting from these reactions are compiled in $R_{\mathrm{A-B},i}$, written as

$$R_{\mathrm{A-B},i} = \sum_n \nu_i \left(k_{+n} \prod_{\nu_i<0} c_i - k_{-n} \prod_{\nu_i>0} c_i \right) \qquad (27)$$

where ν_i is the stoichiometric coefficient of species i for the nth reaction and reverse rate constants (k_{-n}) are calculated from:

$$k_{-n} = \frac{k_{+n}}{K_n} \qquad (28)$$

Electrochemical reactions and electron transport

The surface reaction at the anode is the oxidation of water:

$$\mathrm{H_2O} \rightarrow \frac{1}{2}\mathrm{O_2} + 2\mathrm{H^+} + 2\mathrm{e^-} \qquad (29)$$

which I write in its acidic form to reflect the fact that acidic conditions are observed at the anode surface. At the cathode, two reduction reactions are considered:

$$2\mathrm{H_2O} + 2\mathrm{e^-} \rightarrow \mathrm{H_2} + 2\mathrm{OH^-} \qquad (30)$$

and

$$\mathrm{CO_2} + \mathrm{H_2O} + 2\mathrm{e^-} \rightarrow \mathrm{HCOO^-} + \mathrm{OH^-} \qquad (31)$$

which are both described under the basic conditions observed at the cathode. The surface reactions relate current density to species generation, consumption, and transport by flux boundary conditions given by

$$N_k = -\frac{\nu_{i,k} i_k}{n_k F} \qquad (32)$$

where i_k is the current density, $\nu_{i,k}$ is the stoichiometric coefficient of species i, and n_k is the number of participating electrons for electrochemical reaction k.

Electrochemical kinetics

Charge transfer reactions occur at the electrode/electrolyte interface and can be described by the Butler-Volmer equation:

$$i_k = i_{0,k}\left[\left(\frac{c_{\mathrm{red}}}{c_{\mathrm{red}}^{\mathrm{ref}}}\right)^{\gamma_{\mathrm{red}}} \exp\left(\frac{\alpha_{\mathrm{a}}F}{RT}\eta_k\right) - \left(\frac{c_{\mathrm{ox}}}{c_{\mathrm{ox}}^{\mathrm{ref}}}\right)^{\gamma_{ox}} \exp\left(\frac{\alpha_{\mathrm{c}}F}{RT}\eta_k\right)\right] \tag{33}$$

where $i_{0,k}$ is the exchange current density for reaction k, $\gamma_{red/ox}$ is the reaction order with respect to some reactant $c_{\mathrm{red/ox}}$, $\alpha_{\mathrm{a/c}}$ is the anodic/cathodic transfer coefficient, and η_k is the overpotential for reaction k. The exchange current density, $i_{0,k}$ depends on a pre-exponential factor (A_k) and an apparent activation energy ($E_{a,k}$) that can be pH-dependent according to the Arrhenius equation,

$$i_{0,k} = A_k \exp\left(-\frac{E_{a,k}}{RT}\right) \tag{34}$$

The overpotential, η_k, is defined according to

$$\eta = \phi_{\mathrm{s}} - \phi_{\mathrm{l}} - E \tag{35}$$

where ϕ_s is the electrode potential, ϕ_{l} is the electrolyte potential, and E is the half-cell equilibrium potential.

Electron transport in the solid electrodes

Electron transport in the solid electrode regions is governed by charge conservation (eq. (3)) and Ohm's law:

$$i_{\mathrm{s}} = \kappa_{\mathrm{s}}\frac{\partial \phi_s}{\partial x} \tag{36}$$

where κ_{s} is the anode or cathode conductivity.

Gas feed and electrolyte flow

Gas feed

A CO_2/O_2 gas mixture at a pressure P is fed to the reactor, resulting in mass transfer into the liquid phase according to

$$R_{\mathrm{F,CO_2}} = k_{\mathrm{L,CO_2}}a\left(P\beta_{\mathrm{CO_2}}y_{\mathrm{F,CO_2}} - c_{\mathrm{CO_2}}\right) \tag{37}$$

$$R_{F,O_2} = k_{\mathrm{L,O_2}}a\left[P\beta_{\mathrm{O_2}}\left(1 - y_{\mathrm{F,CO_2}}\right) - c_{\mathrm{O_2}}\right] \tag{38}$$

where $k_{\mathrm{L},i}a$ is the volumetric mass-transfer coefficient on the liquid side of the gas/liquid interface, β_i is the Bunsen solubility coefficient, and $y_{\mathrm{F},i}$ is the mole fraction of species i in the gas phase.

Equilibrium solubility of CO_2, O_2, and H_2 in electrolyte

I calculate the equilibrium solubility of CO_2, O_2, and H_2 according to the empirical relationship for the Bunsen solubility coefficient (β):

$$\ln(\beta) = A_1 + A_2\left(\frac{100}{T}\right) + A_3 \ln\left(\frac{T}{100}\right) + S\left[B_1 + B_2\left(\frac{T}{100}\right) + B_3\left(\frac{T}{100}\right)^2\right] \tag{39}$$

where A_n and B_n are fitting parameters and S is the electrolyte salinity in g/kg water. The equilibrium concentration of gaseous species in the liquid phase is then given simply by

$$c_{\mathrm{sat},i} = \beta_i P y_i \tag{40}$$

Gas/liquid mass transfer coefficients

Gas/liquid mass transfer coefficients can be calculated either from first principles[36] or by any of several correlations that are dependent on the system geometry. Here, I use the correlation first developed by Vasconcelos *et al*. for stirred tank reactors with a height that is twice the diameter[40]:

$$k_{\mathrm{L}}a = 22.3\left(\frac{P_{\mathrm{g}}}{V}\right)^{0.66}\left(u_{\mathrm{g}}\right)^{0.51} \tag{41}$$

where P_{g}/V is the specific power input (in units W m^{-3}) and u_{g} is the superficial gas velocity (in units m s^{-1}). In this model, I assume a $k_{\mathrm{L}}a$ value of 300 hr^{-1}, and an upper bound power demand of 4000 W m^{-3} with a superficial gas velocity of ~0.11 m s^{-1}. Note that the actual $k_{\mathrm{L}}a$ value in a given reactor is highly dependent on the gas feeding mechanism,[41] the reactor geometry and gas contacting strategies,[42] and components integrated into bioreactors,[28] so any model of experimental results must rely on carefully measured $k_{\mathrm{L}}a$ values before valid comparisons can be made.

Evolution of supersaturated gas at electrode surfaces

Water oxidation at the anode surface and hydrogen evolution at the cathode surface will generate O_2 and H_2 in excess of what the liquid phase can solubilize. Additionally, because water oxidation creates acidic conditions near the anode surface, bicarbonate and carbonate species will be converted to aqueous CO_2 according to Le Chatelier's principle. To avoid the unrealistic supersaturation of gases in the electrolyte media these mechanisms would cause, I describe evolution of gases as a flux boundary condition at the electrode surfaces as:

$$N_{\mathrm{evo},i} = \begin{cases} -\gamma_i S_i^2 & S \geq 1 \\ 0 & S < 1 \end{cases} \tag{42}$$

where γ_i is the releasing coefficient and S_i is the supersaturation coefficient for species i, defined as $c_i/\beta_i p_i$, where p_i is the partial pressure. The releasing coefficient, γ_i, is known to vary over at least seven orders of magnitude.[43] Lin *et al.* studied the rate of CO_2 evolution driven by electrolyte acidification in a CO_2 electrolyzer system and showed that the value of the releasing coefficient does not impact the steady-state rate of gas evolution but does change the time to reach steady-state evolution conditions.[44] In their system, gas evolution reached steady-state values in <30 min when the current density was ~10 mA cm^{-2}, so the actual value of γ_i is not expected to change the conclusions of the analysis.

2.5.5 Gaseous species concentration exiting the reactor

Only a fraction of the CO_2 (and O_2) fed to the reactor is transferred to the liquid phase; defining this fraction as δ_{CO_2} allows us to calculate the flow rate of fed gas to the reactor (f_F), given by:

$$f_F = \frac{R_{F,CO_2}}{S_A \delta_{CO_2} y_{F,CO_2}} \tag{43}$$

where S_A is the reactor electrode surface area to reactor volume ratio. Note that f_F is written in units of moles per area per time (mol l^{-2} t^{-1}); for generality, I have normalized the feed rates to the electrode surface area to more straightforwardly connect this feed rate to the rates of gas evolution from the electrode surfaces. The fraction of fed O_2 transferred to the liquid phase, δ_{O_2}, is defined as

$$\delta_{O_2} = \delta_{CO_2}\left(\frac{y_{F,CO_2}}{1 - y_{F,CO_2}}\right)\left(\frac{R_{F,O_2}}{R_{F,CO_2}}\right) \tag{44}$$

by performing a mass balance on the feed gas stream.

Gas exiting the reactor will include CO_2, O_2, and H_2. To calculate their mole fractions, I perform a mole balance on the gas phase of the reactor and assume perfect mixing. The flow rate of gas exiting the reactor is given by:

$$f_O = \left(\frac{1 - \delta_{CO_2}}{\delta_{CO_2}}\right)\frac{F_{CO_2}}{S_A} + \left(\frac{1 - \delta_{O_2}}{\delta_{O_2}}\right)\frac{F_{O_2}}{S_A} + \left(N_{evo,CO_2} + N_{evo,O_2} + N_{evo,H_2}\right) \tag{45}$$

Here, the first two terms represent CO_2 and O_2 fed to the reactor that do not dissolve into the liquid phase, and the final term represents fluxes of gas species due to evolution at electrode surfaces, as described in eq. 42.

Gaseous species mole fractions of the exiting gas stream are then calculated by component mole balances:

$$y_{H_2} = \frac{N_{evo,H_2}}{f_O} \tag{46}$$

$$y_{O_2} = \frac{N_{evo,O_2} + \left(\frac{1-\delta_{O_2}}{\delta_{O_2}}\right)\frac{F_{O_2}}{S_A}}{f_O}$$

$$y_{CO_2} = 1 - y_{H_2} - y_{O_2}$$

These equations are used to predict the saturation concentration of H_2 in the liquid phase. They could also be used to identify the operational conditions that lead to flammable gas mixtures of H_2 and O_2 in the reactor headspace. In the model, y_{H_2} was ≤5% in all cases when using $\delta_{CO_2} = 0.5$, so flammable conditions are not expected to occur under typical operation.

2.5.6 Electrolyte media flow

Electrolyte media is fed to and extracted from the well-mixed liquid phase at a constant dilution rate, resulting in a feed term written as

$$R_{F,i} = D(c_{i,f} - c_i) \quad (47)$$

where D is the dilution rate (defined as the inverse space time, or volumetric flow rate divided by reactor volume[36]). I assume the feed stream is free of microbes but otherwise equivalent to the initial conditions (*i.e.* $c_{i\neq X,f} = c_{i\neq X,0};\ c_{X,f} = 0$) and that CO_2 and O_2 are supplied by the gas feed.

Model implementation

The governing equations are solved using the MUMPS general solver in COMSOL Multiphysics 5.4 with a nonlinear controller. The modeling domain has a maximum element size of 20 μm in the well-mixed regions and 2 μm in boundary layers to capture concentration gradients; the solution was independent of increasing mesh resolution. Model parameters are listed in Table S1. The potential in the reactor is calculated relative to zero potential at the cathode base and potential is applied as a boundary condition at the anode.

3.4 Results and Discussion

CO_2 diffusion and O_2 interphase transfer determine upper bounds on productivity

I first evaluated the performance of a mediated EMP system using *C. necator* as the microbial catalyst since a wealth of formatotrophic and hydrogenotrophic growth data for this organism exists in the literature (Fig. 3.2).[22,24,38] I used experimental parameters describing electrochemical reduction towards $HCOO^-$ and H_2 on a Sn electrode because of its ability to selectively produce formate[19,45] and I compared operation with two different gas feed compositions: $y_{F,CO_2} = 0.5$, corresponding to an equal mixture of CO_2 and O_2 in the gas feed stream; and $y_{F,CO_2} = 0.833$, corresponding to a CO_2 partial pressure of 1 atm for. Current density towards CO_2 reduction or H_2 production increases exponentially as a function of voltage following Butler-Volmer kinetics (Fig. 3.2A, eq. (33)). Because the cell density and biomass productivity depend linearly on the current density (see eq. S25 in Appendix B, for example), these values also increase exponentially with the applied voltage (Fig. 3.2B, C). For the equimolar gas feed mixture (dashed curves in Fig. 3.2), the molar yield remains constant at just below its maximum value,

indicating that microbes are consuming nearly all the formate produced by the electrochemical reaction (*i.e.* there is a low residual formate concentration in the reactor) (Fig. 3.2D). In this case, the electrochemical reaction (and therefore biomass productivity) is limited to ~0.48 g L^{-1} hr^{-1} by the availability of CO_2 at the electrode surface. Above ~2.35 V, the steady-state concentration of CO_2 at the cathode surface approaches zero (Fig. 3.2E), limiting the production rate of formate and therefore biomass productivity.

In contrast, for the case of $y_{F,CO_2} = 0.833$, the steady-state concentration of CO_2 at the cathode surface remains above 4 mM for the entire voltage range considered (solid curve in Fig. 3.2E), but the cell density (Fig. 3.2B), productivity (Fig. 3.2C), and molar yield (Fig. 2D) all decrease rapidly to nearly zero above an applied voltage of ~2.35 V. This behavior can be explained by microbial consumption of O_2: above ~2.35 V, the bulk O_2 concentration drops below 5 μM (Fig. 3.2F), reducing the microbial growth rate (eqs. 8–9). When the growth rate is reduced, the residual formate concentration increases, reducing the yield (Fig. 3.2D). The combined effect of reduced growth rate and reduced cellular yield causes washout of the cells. Hence, the biomass productivity of the reactor in this case is limited to ~0.65 g L^{-1} hr^{-1} by O_2 transfer from the gas phase to the liquid phase. Interestingly, cell washout also reduces the electrode current density (Fig. 3.2A) because formate build-up reduces the pH in the reactor, increasing the Nernst potential drop at the anode surface and reducing OER kinetics because the OER exchange current density is pH-dependent (eq. 34, Table S1 in Appendix B).

These results indicate that formate-mediated EMP systems are limited either by CO_2 or O_2 transport and depend on the gas feed composition. When the O_2 partial pressure is high, CO_2 transport to the electrode surface limits formate production and therefore microbial growth; when the CO_2 partial pressure is high, the O_2 consumption rate driven by microbial respiration is limited by the gas/liquid mass transfer rate, slowing microbial growth and allowing build-up of $HCOO^-$ to toxic concentrations. The trade-off between CO_2 and O_2 availability implies the existence of an optimal gas feed composition, which is explored next.

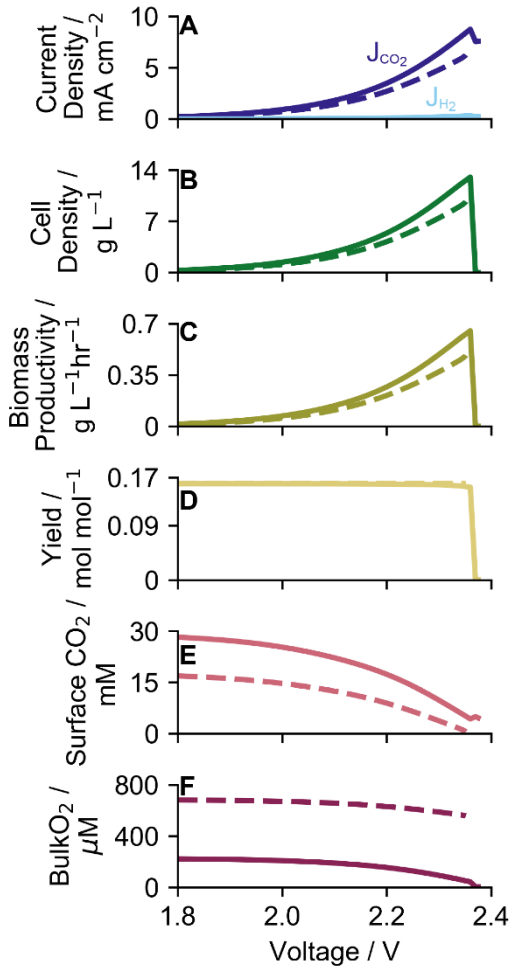

Figure 3.2. Current density and operating conditions as a function of applied voltage. Steady-state (**A**) current densities towards CO_2 (J_{CO2}) and H_2 (J_{H2}), (**B**) cell density, (**C**) biomass productivity, (**D**) molar cell yield on formate, (**E**) CO_2 liquid-phase concentration at the cathode surface, and (**F**) O_2 liquid-phase concentration in the well-mixed bulk region as a function of applied voltage for $y_{F,CO_2} = 0.5$ (dashed lines) and $y_{F,CO_2} = 0.833$ (solid lines) with S_A = 100 m^{-1} and D = 0.05 hr^{-1}.

Reactor geometry determines optimal operating conditions and productivity

The optimal gas feed composition for biomass productivity is coupled to reactor design by the electrode surface area to reactor volume ratio (S_A). This effect can be understood by considering the effective volumetric formate production rate (electrochemical CO_2 consumption rate), which is proportional to the product of current density and S_A (*i.e.* $\propto i_{CO_2} S_A$). The current density (i_{CO_2}) is limited by CO_2 transport to the cathode surface. At equivalent current densities (*e.g.* the highest that can be supported by CO_2 transport through the boundary layer), a larger S_A results in a larger volumetric formate production rate that must be matched by an increased microbial growth rate to maintain steady-state conditions. The increased microbial growth rate, then, results in a higher achievable cell density and volumetric productivity. However, microbial growth relies on O_2 consumption (*via* respiration), so the O_2 mass transfer rate from the gas phase to the liquid phase must also proportionally increase. If the k_La value is fixed, increasing the rate of O_2 mass transfer can only be achieved by increasing the partial pressure of O_2 in the gas feed, accomplished by increasing y_{F,O_2} (equivalently, decreasing y_{F,CO_2}).

To illustrate this effect, I calculated the maximum volumetric biomass productivities (g biomass per time per reactor volume) as a function of gas feed composition for different S_A values and as a function of S_A for different y_{F,CO_2} values (Fig. 3.3A, B). For an S_A of 100 m^{-1}, the maximum volumetric productivity of ~0.74 g/L/hr is reached when the gas feed is an 80/20 mixture of CO_2/O_2 (*i.e.* $y_{F,CO_2} = 0.8$) (Fig. 3.3A). CO_2 transport to the cathode surface limits productivity when the CO_2 gas fraction is <0.8, while CO_2 gas fractions >0.8 result in O_2 gas/liquid mass transfer-limited operation. Increasing S_A results in higher achievable volumetric productivities, reaching ~1.76 g/L/hr with an S_A of 333 m^{-1} at $y_{F,CO_2} = 0.6$. For a fixed gas composition, increasing S_A increases the volumetric productivity to a plateau value (~0.74 g/L/hr for $y_{F,CO_2} = 0.8$), after which further increasing the S_A has no effect (Fig. 3.3B). These plateau values correspond to the maximum microbial consumption rate that can be supported by O_2 transfer from the gas phase to the liquid phase.

Interestingly, higher areal biomass productivities (g biomass per time per cathode surface area) are achieved by decreasing S_A (Fig. 3.3C, D). This effect can also be understood by considering the volumetric production rate of formate. For a given gas composition, O_2 gas/liquid mass transfer can support a maximal volumetric productivity (Fig. 3.3B), which corresponds to a specific volumetric production rate of formate (that is $\propto i_{CO_2} S_A$). For a lower S_A, a higher current density (i_{CO_2}) is necessary to achieve that rate. Because areal productivity is proportional to i_{CO_2}, this results in an increased areal productivity as the S_A decreases (Fig. 3D). For $y_{F,CO_2} = 0.8$, the areal biomass productivity plateaus at ~7.4 $g/m^2/hr$ for S_A <100 m^{-1}, while $y_{F,CO_2} = 0.6$ can only achieve ~5.6 $g/m^2/hr$ (a ~25% decrease).

Results from this analysis have significant implications for mediated EMP system engineering. First, the competing limitations of CO_2 transport and O_2 gas/liquid mass transfer place a fundamental upper bound on the productivity of mediated EMP systems, and the optimal operating conditions (*i.e.* feed gas composition) are dependent on reactor design parameters (S_A, $k_L a$). The trade-off can be avoided by separating electrochemical formate production and biomass growth, as discussed later, or by using gas diffusion electrodes (GDEs) to minimize the transport distance for CO_2.[46,47] The latter strategy has been recently reported for bioplastic production using *C. necator*.[14] Second, volumetric and areal productivities cannot be simultaneously optimized. A higher S_A results in higher volumetric productivity and therefore a higher CO_2-fixing rate per unit volume, but also has a lower areal productivity and therefore requires more electrode material and is more resource-intensive. Hence, the optimal reactor design will be process-specific and will depend in part on the cell density or titer desired for a given product. Additionally, life-cycle assessments can inform reactor design and operation schemes that minimize energy and resource use while maximizing CO_2-fixation.[48,49]

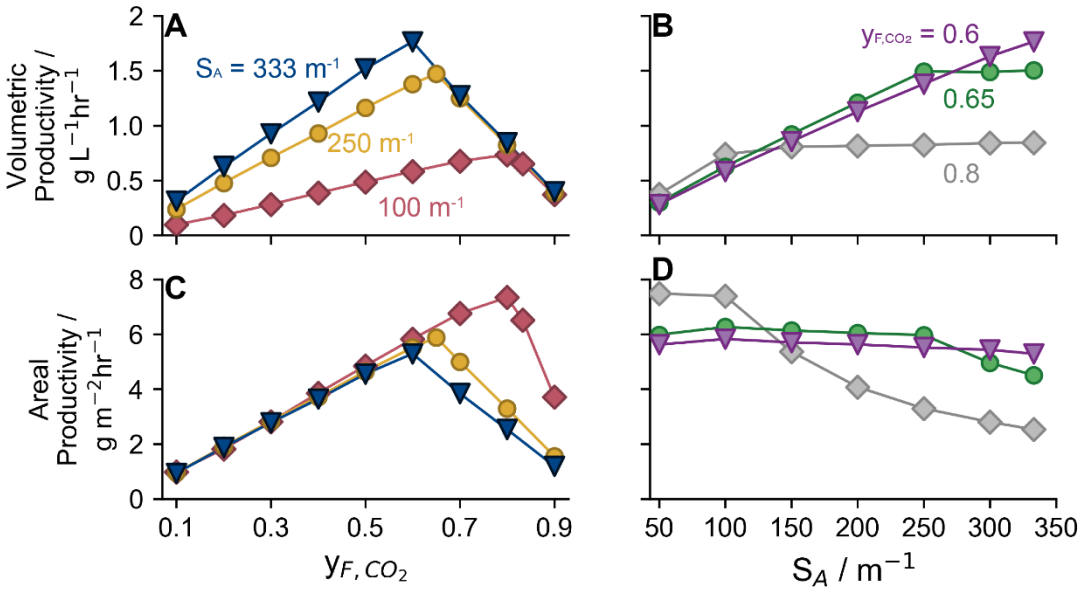

Figure 3.3. Coupled effects of gas feed composition and electrode surface area to volume ratio. Maximum volumetric productivity (**A**, **B**) and areal productivity (**C**, **D**), as a function of feed gas CO_2 fraction (y_{F,CO_2}) (**A**, **C**) and electrode surface area to volume ratio (S_A) (**B**, **D**). Feed gas compositions plotted in (**B**, **D**) correspond to the optimal compositions for the three S_A values plotted in (**A**, **C**). All points use D = 0.05 hr^{-1}.

Decreasing dilution rate increases productivity

For a standard CSTR bioreactor where the growth substrate is fed in the liquid phase, the dilution rate can be adjusted to maximize biomass productivity.[36] However, for a mediated EMP system, the growth substrate is generated electrochemically, so substrate availability is partially decoupled from the dilution rate. To evaluate this effect, I calculated the biomass productivity as a function of dilution rate (Fig. 3.4). At a dilution rate of 0.01 hr^{-1}, the volumetric productivity is ~1.9 g/L/hr for $y_{F,CO_2} = 0.6$ with an S_A of 333 m^{-1}, but decreases monotonically as the dilution rate increases. For a simplified version of the model, where growth is dependent on a single, generic substrate and boundary layers are neglected, I show analytically that the productivity approaches a maximum as the dilution rate approaches 0, and that this result holds even if the yield decreases with increasing substrate concentration, as is the case for formate (Supplementary note 2 in Appendix B).[24] This result indicates that scaling-up the reactor volume offers an intrinsic benefit to mediated EMP productivity. Increasing the reactor volume while maintaining a fixed volumetric flow rate will increase the overall productivity of the system and will result in a higher cell density (or product titer). However, a larger reactor also requires more electrode and other materials, increasing resource intensity, and more power for gas/liquid mass transfer (eq. 41). Life cycle analyses can indicate an optimal value for this trade-off and will be informed by the material and energy efficiency of the mediated EMP system, which I consider in the next section.

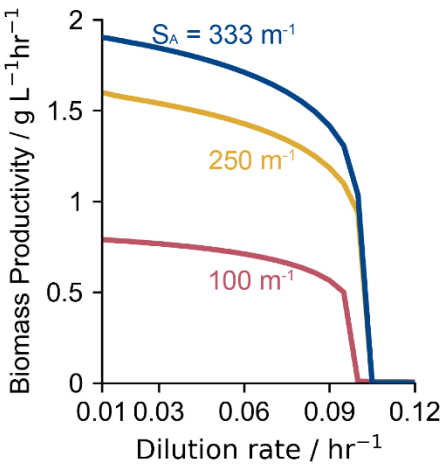

Figure 3.4. Effect of dilution rate. Steady-state volumetric biomass productivity as a function of the dilution rate for three different reactor operating configurations. Blue curve: S_A = 333 m^{-1}, y_{F,CO_2} = 0.6. Yellow curve: S_A = 250 m^{-1}, y_{F,CO_2} = 0.65. Red curve: S_A = 100 m^{-1}, y_{F,CO_2} = 0.8.

Achievable carbon, hydrogen, and energy efficiency

Material utilization and energy efficiencies need to be defined and quantified as a function of reactor design and operating conditions because they will have a significant impact on the overall efficiency and practicality of EMP systems. The carbon utilization efficiency can be written as the fraction of carbon exiting the reactor in biomass (since the total carbon fed to and exiting from the reactor must be equal):

$$\eta_C = \frac{Dc_X}{D\left(c_{CO_2} + c_{HCO_3^-} + c_{CO_3^{2-}} + c_{HCOO^-} + c_{HCOOH} + c_X\right) + S_A N_{evo,CO_2}} \quad (48)$$

and the distribution of carbon exiting the reactor can be quantified simply by adjusting the numerator in this equation. For the formate-mediated EMP system, <10% of the carbon fed to the reactor is diverted to biomass regardless of the applied potential (Fig. 3.5A). Notably, this is not due to low utilization of formate, which is nearly completely consumed prior to exiting the reactor. Instead, evolution of CO_2 at the anode surface (eq. 42) comprises >80% of the carbon exiting the reactor. Gas recycle will therefore be necessary to achieve high overall carbon utilization efficiency for scaled EMP systems.

H_2 utilization efficiency can be calculated in a similar fashion, this time using the rate of H_2 consumption by cells:

$$\eta_{H_2} = \frac{\alpha_{H_2}\mu_H c_X}{\alpha_{H_2}\mu_H c_X + Dc_{H_2} + S_A N_{evo,H_2}} \quad (49)$$

In this system, nearly all the H_2 is consumed by cells at low applied voltages (Fig. 3.5B). However, as the voltage (and therefore, the current density) increases, evolution at the cathode surface begins to dominate because H_2 is generated more rapidly than it can be solubilized by the liquid medium. This effect strongly limits the achievable biomass productivity for H_2-mediated EMP systems.

To calculate the energy efficiency, I used the estimate that autotrophic biomass production requires ~479 kJ mol^{-1},[6,50] and considered the power input from gas/liquid mass transfer and the applied current density:

$$\eta_{\mathrm{E}} = \frac{\Delta_{\mathrm{r}} G_{\mathrm{X}}^{0} D c_{\mathrm{X}}}{\left(\frac{P_{\mathrm{g}}}{V}\right) + S_{\mathrm{A}} i V_{\mathrm{appl}}} \tag{50}$$

where $\Delta_r G_{\mathrm{X}}^{0}$ = 479 kJ mol^{-1} is the Gibbs' free energy change for the biomass production reaction, i is the total current density and V_{appl} is the applied voltage. Note that this calculation should represent an upper bound on η_{E} since the power demand for pumping liquid media and for heating or cooling the reactor to maintain optimal microbial growth temperatures are not considered. In this system, the energy efficiency increases from ~5% at 1.8 V to a maximum of ~16.5% at ~2.3 V (Fig. 3.5C). Upon coupling to commercially available solar cells that have an energy efficiency of ~20–25%, the system can therefore achieve an overall solar-to-chemical (STC) efficiency ($\eta_{STC} = \eta_{solar} \times \eta_E$) of only ~3–4%.

Multiple strategies can overcome the low carbon utilization and energy efficiencies achievable for mediated EMP systems. In addition to gas recycle, microbial engineering to improve growth yield can divert a higher fraction of carbon into biomass or products, reducing the futile CO_2 cycle (CO_2 reduced to formate electrochemically, then formate oxidized back to CO_2 for metabolic energy by microbes), as evaluated in the next section. Improved growth yield can also enhance overall energy efficiency, but energy efficiency may be better improved by separating electrochemical and microbial reactions into two reactors, allowing for individual, rather than coupled, optimization.

Engineered growth strategies can significantly improve productivity and efficiency

Although formate oxidation coupled to CO_2 assimilation enables formatotrophic growth *via* the Calvin cycle, higher biomass yields are theoretically possible using the reductive glycine pathway (rGlyP; see Supplementary note 1 in Appendix B for additional details).[25] I evaluated the potential for improved productivity, carbon utilization, and energy efficiency by formatotrophic growth using the rGlyP since this pathway has recently been engineered in *C. necator* and *E. coli*.[22,23] The maximum biomass productivity for *E. coli* is ~22% higher than for wild-type *C. necator* (*i.e. C. necator* using the Calvin cycle), reaching ~2.15 g/L/hr at ~2.3 V (Fig. 3.6A). Engineered *C. necator* slightly outperforms *E. coli*, reaching ~2.23 g L/hr at 2.33 V; the difference is attributable to the fact the *C. necator* is also able to use H_2 as additional reducing power. Both the carbon utilization and energy efficiency are also significantly improved with the rGlyP, reaching ~10.2% and ~21.7% respectively for *E. coli*, representing ~30% improvements over wild-type *C. necator* (Fig. 3.6B, C). Interestingly, the difference in operating temperature (30 °C for *C. necator* and 37 °C for *E. coli*) has almost no impact on productivity or efficiency limits despite impacting gas solubility (reduced with increased temperature), diffusivity of species (increased with increased temperature), acid/base equilibria (multiple effects), electrochemical potential (reduced with increased temperature), and electrochemical reaction kinetics (multiple effects), indicating that the competing impacts effectively cancel out. These results indicate the promise of microbial engineering to improve EMP systems and can be combined with process engineering strategies to further increase productivity and efficiency.

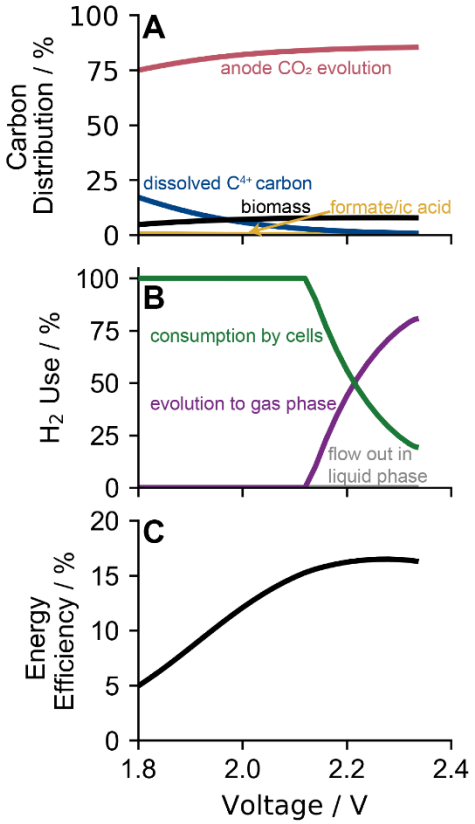

Figure 3.5. Carbon distribution, H_2 utilization, and energy efficiency. (**A**) Distribution of carbon exiting the reactor; (**B**) final destination of H_2 produced by the cathode; (**C**) energy efficiency towards cellular biomass as a function of applied voltage. All curves use D = 0.05 hr^{-1}, S_A = 333 m^{-1}, and y_{F,CO_2} = 0.6. Dissolved C^{4+} carbon corresponds to solubilized CO_2, HCO_3^-, and CO_3^{2-}.

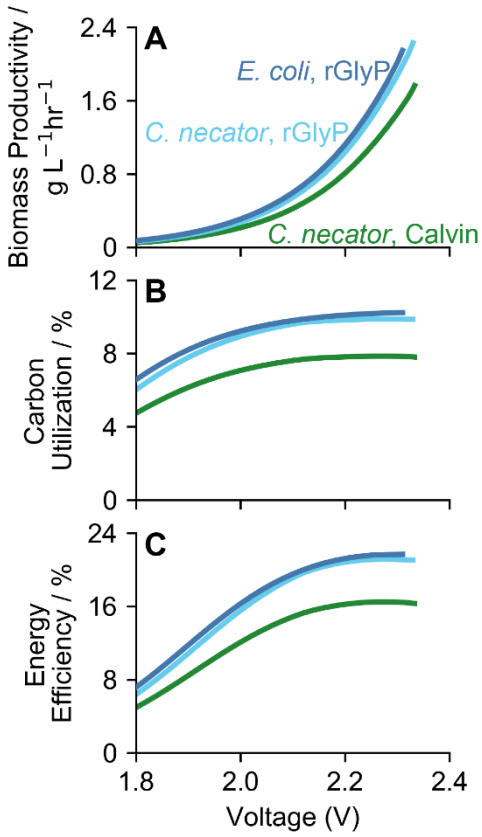

Figure 3.6. Effects of different formatotrophic growth strategies. (**A**) Productivity, (**B**) percent of fed carbon converted to biomass, and (**C**) energy efficiency towards cellular biomass for *C. necator* using the Calvin cycle (green curves) or the reductive glycine pathway (light blue curves) and *E. coli* using the reductive glycine pathway (dark blue curves) as a function of applied voltage. *C. necator* is modeled at 30 °C; *E. coli* is modeled at 37 °C. All curves use S_A = 333 m^{-1} and y_{F,CO_2} = 0.6.

Decoupled systems are likely to outcompete integrated reactors

Integrated systems for mediated EMP minimize gas and fluid pumping power demand by integrating multiple processes into a single reactor. However, the competing requirements of CO_2 and O_2 mass transport create a fundamental limit on achievable productivity (Fig. 3.3). Decoupled systems, where an electrochemical reactor produces formate/ic acid at high rates that is then fed to a bioreactor (Fig. 3.7A), can break this limit by enabling individual optimization of the two processes. To evaluate the productivity of a decoupled system, I adapted the model by eliminating the electrochemical reactions, adjusting the gas feed composition to an 80/20 O_2/CO_2 ratio (*i.e.*

$y_{F,CO_2} = 0.2$), and altering the media feed to include sodium formate (HCOONa) and formic acid (HCOOH) in equilibrium at a pH of 2 to maintain reasonable Na^+ concentrations of <3.5 g/L (note that the operating pH in the reactor remained at a pH of ~7 due to microbial consumption of protons). I then calculated biomass productivity as a function of dilution rate and total inlet formate concentration, comprised of both $HCOO^-$ and HCOOH (Fig. 3.7B). At lower inlet formate concentrations (<4.5 M), biomass productivity follows the standard trend of first increasing with increasing dilution rate up to a maximum value, then rapidly decreasing once microbial growth cannot match the dilution rate, causing washout. For this formate concentration range (<4.5 M), the maximum dilution rate that can be supported by microbes, and the achievable biomass productivity, also increase with inlet formate concentration following standard trends. However, above 4.5 M, microbial growth becomes O_2-limited at higher dilution rates, causing a decline in the maximum dilution rate microbes can support. Despite the O_2-limitation at high inlet formate concentrations, biomass productivities in excess of 2.4 g/L/hr are readily achieved with wild-type *C. necator*, outperforming the integrated EMP system by >35% (Fig. 3.7B).

A decoupled reactor system offers several benefits beyond higher biomass productivities. Higher applied current densities are achievable using GDEs or membrane-electrode assembly systems that can be optimized independently of the requirements for microbial growth (*i.e.* higher salt and buffer concentrations, higher pHs that enable higher selectivity towards carbon products).[19,46,47] Issues associated with short-lived but toxic byproducts are lessened,[12,29] but simple strategies to directly integrate electrochemical and microbial media with minimal intermediate processing are still necessary. Recently, Stöckl *et al.* developed a prototype system coupling a GDE-based CO_2 electrolysis cell to formatotrophic growth and bioplastic production, and demonstrated production directly from the electrolyte used in the electrolysis cell.[14] In general, a two-reactor system does have some challenges, however, including increased gas and liquid pumping requirements and the increased number of failure or contamination points. Life-cycle analyses comparing these reactor systems on the basis of material utilization, energy efficiency, and productivity should clarify these trade-offs and are enabled by the quantitative evaluation of mediated EMP systems provided in this chapter.

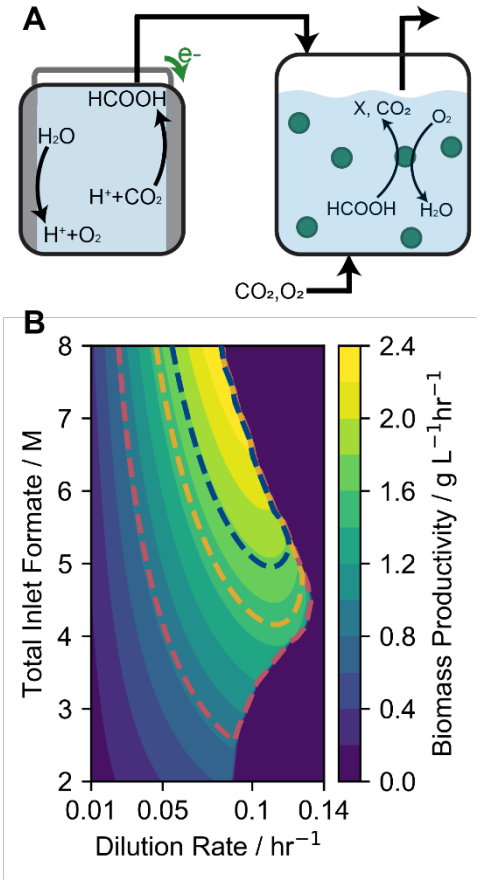

Figure 3.7. Higher productivity with decoupled systems. (**A**) Decoupled reactor scheme. Electrochemically-produced formate/ic acid is fed to a bioreactor along with CO_2 and O_2, which cells consume for growth. (**B**) Volumetric productivity as a function of dilution rate and total inlet formate concentration (comprised of sodium formate and formic acid) for a formate-fed bioreactor as described in the text with y_{F,CO_2} = 0.2. Overlaid dashed curves correspond to the maximum volumetric productivities of the integrated system reported in Fig. 3A (red: S_A = 100 m^{-1}, yellow: 250 m^{-1}, blue: 333 m^{-1}).

3.5 Conclusion

Formate-mediated EMP represents a promising avenue for the production of multi-carbon molecules from CO_2. In this chapter, I developed a comprehensive modeling framework for integrated, mediated EMP systems that captures species transport, electrochemical, acid/base, and microbial reaction thermodynamics and kinetics, temperature effects, and gas/liquid mass transfer. I show that formate-mediated EMP reactors are fundamentally limited by the trade-off between O_2 gas/liquid mass transfer and CO_2 transport to the cathode surface, and that decoupling electrochemical and microbial processes into separate reactors (see Chapter 2) overcomes this limitation. I additionally evaluated the promise of synthetic formatotrophic growth via the reductive glycine pathway and showed that this strategy can significantly enhance carbon utilization and energy efficiency once the theoretical growth yields are realized. However, single-pass carbon utilization efficiency remains at ~10% in the best case, indicating that gas recycle will be necessary for high overall CO_2 utilization in scaled-up systems.

Future modeling efforts built on the framework developed here could include the effects of ionic strength on growth rate (especially for microbes such as *C. necator* that are sensitive to high salinity, see Chapter 2) and explicitly consider microbial product synthesis and its effects on growth yields and rates.

3.6 References

1 S. Perathoner and G. Centi, *ChemSusChem*, 2014, **7**, 1274–1282.
2 N. J. Claassens, D. Z. Sousa, V. A. P. M. Dos Santos, W. M. De Vos and J. Van Der Oost, *Nat. Rev. Microbiol.*, 2016, **14**, 692–706.
3 N. J. Claassens, I. Sánchez-Andrea, D. Z. Sousa and A. Bar-Even, *Curr. Opin. Biotechnol.*, 2018, **50**, 195–205.
4 A. Prévoteau, J. M. Carvajal-Arroyo, R. Ganigué and K. Rabaey, *Curr. Opin. Biotechnol.*, 2020, **62**, 48–57.
5 N. J. Claassens, C. A. R. Cotton, D. Kopljar and A. Bar-Even, *Nat. Catal.*, 2019, **2**, 437–447.
6 C. Liu, B. C. Colón, M. Ziesack, P. A. Silver and D. G. Nocera, *Science (80-.).*, 2016, **352**, 1210–1213.
7 M. Soundararajan, R. Ledbetter, P. Kusuma, S. Zhen, P. Ludden, B. Bugbee, S. A. Ensign and L. C. Seefeldt, *Front. Microbiol.*, , DOI:10.3389/fmicb.2019.01817.
8 M. Wang, W. Zhong, S. Zhang, R. Liu, J. Xing and G. Zhang, *J. Mater. Chem. A*, 2018, **6**, 9915–9921.
9 T. Krieg, A. Sydow, S. Faust, I. Huth and D. Holtmann, *Angew. Chemie - Int. Ed.*, 2018, **57**, 1879–1882.
10 J. Guan, S. A. Berlinger, X. Li, Z. Chao, V. Sousa e Silva, S. Banta and A. C. West, *J. Biotechnol.*, 2017, **245**, 21–27.
11 W. O. Khunjar, A. Sahin, A. C. West, K. Chandran and S. Banta, *PLoS One*, 2012, **7**, 44846.
12 H. Li, P. H. Opgenorth, D. G. Wernick, S. Rogers, T. Wu, W. Higashide, P. Malati, Y. Huo, K. M. Cho and J. C. Liao, *Science (80-.).*, 2012, **335**, 1596.
13 Y. Tashiro, S. Hirano, M. M. Matson, S. Atsumi and A. Kondo, *Metab. Eng.*, 2018, **47**, 211–218.
14 M. Stöckl, S. Harms, I. Dinges, S. Dimitrova and D. Holtmann, *ChemSusChem*, 2020, **13**, 4086–4093.
15 R. Hegner, K. Neubert, C. Kroner, D. Holtmann and F. Harnisch, *ChemSusChem*, 2020, **13**, 5295–5300.
16 T. D. Harrington, V. N. Tran, A. Mohamed, R. Renslow, S. Biria, L. Orfe, D. R. Call and H. Beyenal, *Bioresour. Technol.*, 2015, **192**, 689–695.
17 T. D. Harrington, A. Mohamed, V. N. Tran, S. Biria, M. Gargouri, J. J. Park, D. R. Gang and H. Beyenal, *Bioresour. Technol.*, 2015, **195**, 57–65.
18 O. Yishai, S. N. Lindner, J. Gonzalez de la Cruz, H. Tenenboim and A. Bar-Even, *Curr. Opin. Chem. Biol.*, 2016, **35**, 1–9.
19 Y. Chen, A. Vise, W. E. Klein, F. C. Cetinbas, D. J. Myers, W. A. Smith, T. G. Deutsch and K. C. Neyerlin, *ACS Energy Lett.*, 2020, **5**, 1825–1833.
20 R. Hegner, L. F. M. Rosa and F. Harnisch, *Appl. Catal. B Environ.*, 2018, **238**, 546–556.
21 G. Wen, D. U. Lee, B. Ren, F. M. Hassan, G. Jiang, Z. P. Cano, J. Gostick, E. Croiset, Z. Bai, L. Yang and Z. Chen, *Adv. Energy Mater.*, 2018, **8**, 1802427.
22 N. J. Claassens, G. Bordanaba-Florit, C. A. R. Cotton, A. De Maria, M. Finger-Bou, L.

Friedeheim, N. Giner-Laguarda, M. Munar-Palmer, W. Newell, G. Scarinci, J. Verbunt, S. T. de Vries, S. Yilmaz and A. Bar-Even, *bioRxiv*, 2020, 2020.03.11.987487.
23 S. Kim, S. N. Lindner, S. Aslan, O. Yishai, S. Wenk, K. Schann and A. Bar-Even, *Nat. Chem. Biol.*, 2020, **16**, 538–545.
24 S. Grunwald, A. Mottet, E. Grousseau, J. K. Plassmeier, M. K. Popović, J. L. Uribelarrea, N. Gorret, S. E. Guillouet and A. Sinskey, *Microb. Biotechnol.*, 2015, **8**, 155–163.
25 A. Bar-Even, E. Noor, A. Flamholz and R. Milo, *Biochim. Biophys. Acta - Bioenerg.*, 2013, **1827**, 1039–1047.
26 C. A. Cotton, N. J. Claassens, S. Benito-Vaquerizo and A. Bar-Even, *Curr. Opin. Biotechnol.*, 2020, **62**, 168–180.
27 F. Enzmann, F. Mayer, M. Stöckl, K. M. Mangold, R. Hommel and D. Holtmann, *Chem. Eng. Sci.*, 2019, **193**, 133–143.
28 L. F. M. Rosa, S. Hunger, T. Zschernitz, B. Strehlitz and F. Harnisch, *Front. Energy Res.*, 2019, **7**, 98.
29 A. Sydow, T. Krieg, R. Ulber and D. Holtmann, *Eng. Life Sci.*, 2017, **17**, 781–791.
30 S. Gadkari, M. Shemfe, J. A. Modestra, S. V. Mohan and J. Sadhukhan, *Phys. Chem. Chem. Phys.*, 2019, **21**, 10761–10772.
31 S. Gadkari, J. M. Fontmorin, E. Yu and J. Sadhukhan, *Chem. Eng. J.*, 2020, **388**, 124176.
32 M. Kazemi, D. Biria and H. Rismani-Yazdi, *Phys. Chem. Chem. Phys.*, 2015, **17**, 12561–12574.
33 C. Picioreanu, K. P. Katuri, M. C. M. Van Loosdrecht, I. M. Head and K. Scott, *J. Appl. Electrochem.*, 2010, **40**, 151–162.
34 C. Picioreanu, I. M. Head, K. P. Katuri, M. C. M. van Loosdrecht and K. Scott, *Water Res.*, 2007, **41**, 2921–2940.
35 C. Moß, N. Jarmatz, J. Heinze, S. Scholl and U. Schröder, *ChemSusChem*, 2020, cssc.202001232.
36 H. W. Blanch and D. S. Clark, *Biochemical Engineering*, CRC Press, 2nd edn., 1997.
37 I. A. Figueroa, T. P. Barnum, P. Y. Somasekhar, C. I. Carlström, A. L. Engelbrektson and J. D. Coates, *Proc. Natl. Acad. Sci. U. S. A.*, 2018, **115**, E92–E101.
38 A. Ishizaki and K. Tanaka, *J. Ferment. Bioeng.*, 1990, **69**, 170–174.
39 L. Rosso, J. R. Lobry, S. Bajard and J. P. Flandrois, *Appl. Environ. Microbiol.*, 1995, **61**, 610–616.
40 J. M. T. Vasconcelos, S. C. P. Orvalho, A. M. A. F. Rodrigues and S. S. Alves, *Ind. Eng. Chem. Res.*, 2000, **39**, 203–213.
41 L. A. H. Petersen, J. Villadsen, S. B. Jørgensen and K. V. Gernaey, *Biotechnol. Bioeng.*, 2017, **114**, 344–354.
42 J. L. Meraz, K. L. Dubrawski, S. H. El Abbadi, K. H. Choo and C. S. Criddle, *J. Environ. Eng.*, , DOI:10.1061/(ASCE)EE.1943-7870.0001703.
43 P. M. Wilt, *J. Colloid Interface Sci.*, 1986, **112**, 530–538.
44 M. Lin, L. Han, M. R. Singh and C. Xiang, *ACS Appl. Energy Mater.*, 2019, **2**, 5843–5850.
45 H. Li and C. Oloman, *J. Appl. Electrochem.*, 2007, **37**, 1107–1117.
46 L. C. Weng, A. T. Bell and A. Z. Weber, *Energy Environ. Sci.*, 2019, **12**, 1950–1968.
47 L. C. Weng, A. T. Bell and A. Z. Weber, *Phys. Chem. Chem. Phys.*, 2018, **20**, 16973–16984.
48 D. Helmdach, P. Yaseneva, P. K. Heer, A. M. Schweidtmann and A. A. Lapkin,

ChemSusChem, 2017, **10**, 3632–3643.
49 M. Shemfe, S. Gadkari, E. Yu, S. Rasul, K. Scott, I. M. Head, S. Gu and J. Sadhukhan, *Bioresour. Technol.*, 2018, **255**, 39–49.
50 R. O. N. Grosz and G. Stephanopoulos, *Biotechnol. Bioeng.*, 1983, **25**, 2149–2163.

Chapter 4: Process-informed biocatalyst discovery for direct electron transfer-based electromicrobial production[†]

4.1 Abstract

In Chapter 2, I analyzed mediated electromicrobial production (EMP) systems that rely on standard electrolyzers and bioreactors to accomplish overall CO_2 fixation driven by electricity. This strategy represents the most "industrially ready" version of EMP systems. In Chapter 3, I analyzed an emerging alternative EMP system in which the electrochemical and biochemical reactions occur simultaneously in the same reactor. Although this strategy has the potential to reduce materials demand relative to the EMP systems considered in Chapter 2, its productivity was limited by trade-offs associated with gas delivery demands for electrochemical and biochemical reactions. In this chapter and the following one, I analyze a second major alternative EMP strategy in which electrons are transferred directly into the microbe *via* direct electron uptake. Here, I develop a multiphysics model to investigate the fundamental and practical limits of EMP enabled by direct electron uptake. I also identify potential electroautotrophic organisms and metabolic engineering strategies to enable electroautotrophy in organisms lacking the native capability. Systematic model comparisons of microbial respiration and carbon fixation strategies revealed that, under aerobic conditions, the CO_2 fixation rate is limited to <6 μmol/cm^2/hr by O_2 mass transport despite efficient electron utilization. In contrast, anaerobic nitrate respiration enables CO_2 fixation rates >50 μmol/cm^2/hr for microbes using the reductive tricarboxylic acid cycle. Phylogenetic analysis, validated by recapitulating experimental demonstrations of electroautotrophy, predicted multiple probable electroautotrophic organisms and a significant number of genetically tractable strains that require heterologous expression of <5 proteins to gain electroautotrophic function.

4.2 Introduction

The capture and conversion of CO_2 to fuels, commodity chemicals, and pharmaceutical precursors can help close the anthropogenic carbon cycle. Biological CO_2 fixation using plants, algae and cyanobacteria occurs naturally at scale, but biotechnological application of photosynthetic carbon fixation is challenging for several reasons including low conversion rates, low efficiencies, and difficulties with downstream separations.[1] Physicochemical strategies to fix CO_2 by generating syngas have also been considered, but extreme operating conditions and low product selectivity for complex hydrocarbons have hindered adaptation.[2–4]

[†]This chapter was originally published in *Bioelectrochemistry* and has been adapted with permission from the coauthors

Recently, electromicrobial approaches have been proposed in which electrochemical and bioelectrochemical reactions are combined to produce a wide array of chemicals.[5,6] Although naming conventions for such bioelectrochemical systems vary in the literature,[6–8] I define electromicrobial production (EMP) processes as any process that converts CO_2 into a value-added product, uses electricity as the primary source of energy driving that transformation, and uses microbes to produce the final product. Mediated EMP systems, relying, for example, on electrochemically-derived H_2 or CO_2-reduction products,[9–11] have made substantial progress in recent years. This strategy is particularly promising because it benefits from extensive system modeling and abiotic catalyst discovery efforts.[12–15] However, poor catalyst stability, reliance on rare elements, and potential catalyst toxicity could inhibit the scalability of this method.[16–18] EMP systems based on direct electron transfer (DET) may overcome these issues because they avoid an electrocatalyst by using so-called electroautotrophic microbes that accept electrons from a cathode.[6,19] The inherent regenerative capacity of microbes also makes DET-based EMP (dEMP) an attractive option for chemical production during space exploration missions because carry-along mass and materials resupply challenges are key constraints on long-term or deep-space expeditions.[20]

Despite the promise of dEMP systems, product spectrum and production rate bottlenecks have prevented technological realization[21]. Systems developed to date primarily use acetogenic or methanogenic microbes that divert most of their fixed carbon into low-value acetate and methane.[22] Although genetic tools have recently become available for some of these organisms,[23,24] microbial energy conservation strategies severely restrict the achievable product spectrum and selectivity. Microbes supporting electroautotrophy via the Calvin cycle have recently been discovered and are likely to alleviate product spectrum issues.[25,26] However, high throughput platforms for discovery and engineering of novel microbial chassis are in their nascent stages and distinguishing between more and less promising candidates and identifying engineering targets that enable high production rates is challenging.[27,28]

Computational models can address this challenge by comparing microbial respiration and carbon fixation strategies. To that end, several models of dEMP systems have been developed, but these have assumed electron uptake interfaces directly with the intracellular NAD^+/NADH pool, in contrast to known electron transfer mechanisms.[29,30] Recent energetic calculations to determine the limiting efficiency of EMP systems have addressed this issue, but assumed that aerobic respiration is equally available for all carbon fixation pathways (CFPs).[31] Moreover, considerations of physiological mechanisms of electron transfer, respiration, and carbon fixation in models that capture relevant physical phenomena remains an outstanding challenge.

Here, I incorporate a physiological, mechanistic understanding of extracellular electron uptake into a comprehensive multiphysics model of dEMP that describes mass transport, electrochemical and acid-base thermodynamics and kinetics, and gas-liquid mass transfer (Fig. 1). In the proposed mechanism, based on the reversible electron conduit in *Shewanella oneidensis*,[32] electrons supplied by the cathode are deposited into the quinone pool. A fraction of these electrons is used to produce a proton motive force (PMF) via aerobic or anaerobic nitrate respiration, while the remainder is used along with the PMF to regenerate cellular energy carriers (ATP, NAD(P)H, reduced ferredoxin) consumed in the CFPs. This picture of the electron transfer mechanism is nearly identical to that of Salimijazi *et al.*[31] I compare the productivity and efficiency of dEMP

systems with hypothetical microbes performing carbon fixation with each of four major CFPs and I identify physiological modules that enable the highest productivities. In this model, I use pyruvate as an example product molecule because it is a central metabolite common to the production of many biofuels and biochemicals.[33]

I further describe naturally occurring and/or readily engineerable microbial chassis that require the heterologous expression of only a few proteins. Finally, I identify additional microbial characteristics and reactor concepts that would be extremely beneficial to an industrial dEMP process based on direct electron uptake. Thus, this analysis provides crucial insight into microbial catalyst discovery and engineering and reactor design strategies that can advance dEMP systems from basic science to technological practice.

4.3 Computational Methods

System dimensionality

The model considers a one-dimensional bioelectrochemical reactor for CO_2 reduction (Fig. 4.1a). Three key assumptions were required to reduce the full MES system that is inherently three-dimensional to an appropriate one-dimensional representation. First, the bulk liquid electrolyte/media was assumed to be well-mixed, which avoids concentration gradients that could occur along the direction of electrolyte flow (the vertical axis in Fig. 4.1a). Second, the model assumes that the geometric area of the reactor (parallel to the plane formed by the vertical axis on the page and the axis extending into and out of the page in Fig. 4.1a) is much larger than the separation distance between the anode and biocathode layer. This avoids edge effects for ion transport and neglects potentially imperfect current distribution throughout the area of the electrodes. Third, the model assumes that there is no macro-scale variation in the biocathode layer (macro-homogeneity), which allows this layer to be described with a characteristic porosity and conductivity following porous electrode theory.[34]

Certain operating or practical conditions could cause any of these assumptions to be faulty in real systems. In such cases, two- or three-dimensional model descriptions would provide further accuracy. For example, insufficient mixing could cause concentration gradients to form in the vertical direction (in Fig. 4.1a), which would reduce the concentration of CO_2 and increase the pH along this axis. In this case, the one-dimensional description could be retained by defining an effectiveness factor related to the Damköhler number, or a complete two-dimensional description of the system could be defined following, for example, similar efforts with abiotic CO_2 electrolysis.[35] In either case, insufficient mixing would reduce the productivity of the system, and optimal operation would avoid this issue, so the additional computational expense of the two-dimensional model would provide only marginal benefits for defining the optimal productivity of dEMP systems at this stage of development.

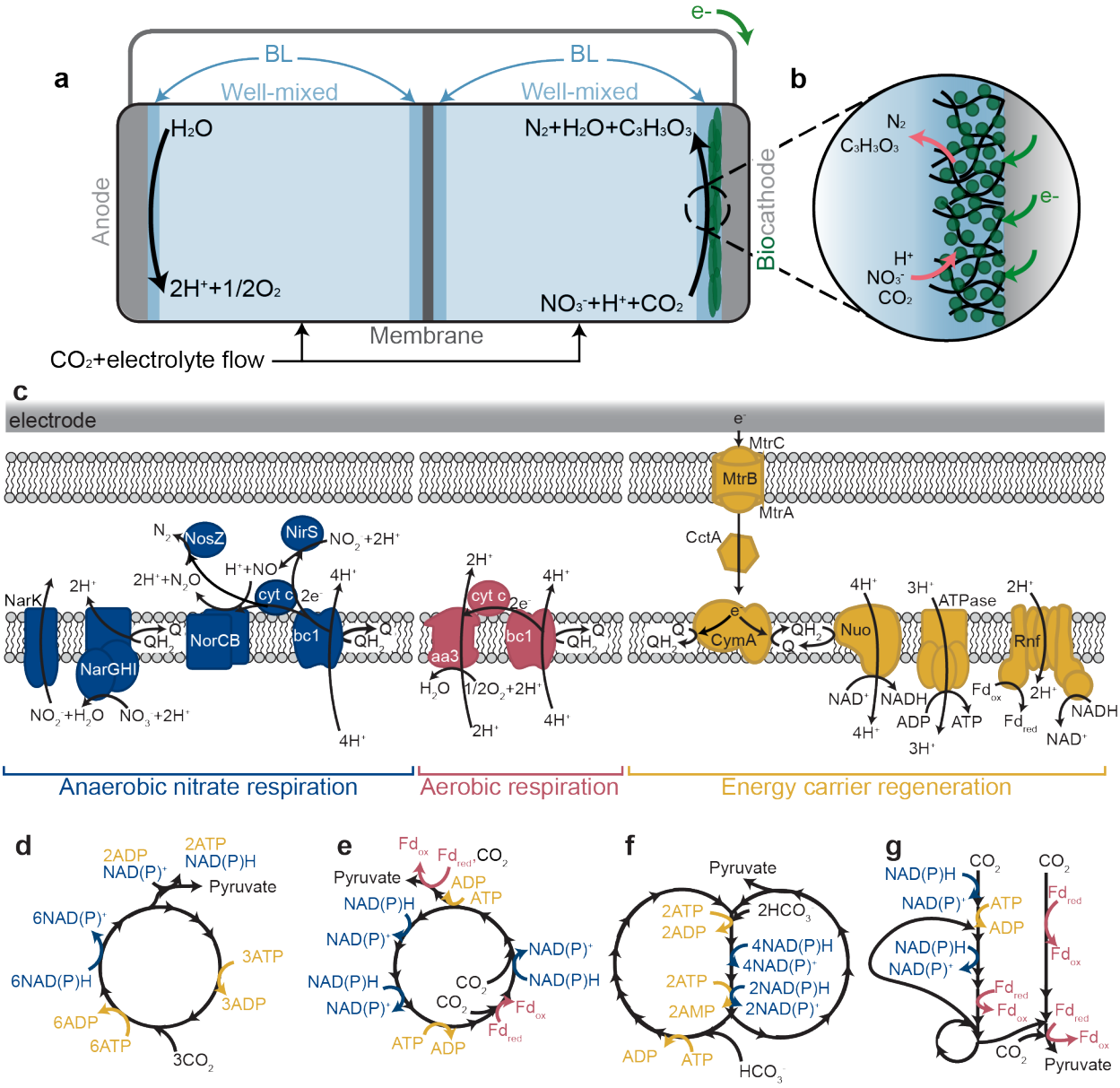

Figure 4.1. Schematic of a one-dimensional EMP reactor and direct electron transfer mechanisms for (an)aerobic carbon fixation. (**a**) Reactor scheme. Carbon dioxide (CO_2) and electrolyte media are fed into well-mixed regions separated by a membrane. (**b**) Direct electron transfer to a microbial biofilm supports carbon fixation to pyruvate using NO_3^- as the terminal electron acceptor. (**c**) Respiratory and energy carrier regeneration mechanisms using NO_3^- and O_2 as terminal electron acceptors. (**d**) The Calvin-Benson-Bassham (CBB), (**e**) reductive tricarboxylic acid (rTCA), (**f**) 3-hydroxypropionate bi-cycle (3HP), and (**g**) Wood-Ljungdahl (WL) pathway for carbon fixation to pyruvate shown with reducing equivalent consumption.

System overview

Species transport for an open electrochemical system must satisfy mass conservation:

$$\frac{\partial c_i}{\partial t} + \frac{\partial N_i}{\partial x} = R_{\mathrm{F},i} + R_{\mathrm{H},i} + R_{\mathrm{CT},i} \tag{51}$$

where c_i is the concentration, N_i is the molar flux, and $R_{\mathrm{F},i}$, $R_{\mathrm{H},i}$, and $R_{\mathrm{CT},i}$ are the net volumetric rates of formation or consumption for species i (CO_2, HCO_3^-, CO_3^{2-}, H^+, OH^-, Na^+, NO_3^-) due to gas and electrolyte (F) feed terms, homogeneous (H) chemical reactions, and electrochemical charge transfer (CT) reactions, respectively. $R_{\mathrm{F},i}$ applies only in the well-mixed electrolyte phases where gas and electrolyte feeds are introduced and $R_{\mathrm{CT},i}$ applies only in the porous biocathode layer. The biocathode layer is assumed to be comprised of a porous electrode support structure on which cells grow in a monolayer (Fig. 4.1b).

In the following sections, I formulate the equations that govern transport and reactions within the dEMP system, describe assumptions, and report the key parameter values used in the model.

2.3 Species transport in the electrolyte boundary layers, membrane, and porous biocathode

The molar flux of species (assuming no net fluid velocity) in dilute electrolyte solutions is written as the sum of diffusive and migrative fluxes:

$$N_i = -D_i \frac{\partial c_i}{\partial x} - z_i u_i F c_i \frac{\partial \phi_{\mathrm{l}}}{\partial x} \tag{52}$$

where D_i and u_i are the diffusivity and mobility (related by the Nernst-Einstein relationship, $u_i = D_i/RT$ for dilute solutions) of species i, z_i is the charge number, F is Faraday's constant, and ϕ_l is the local electrolyte potential. In the anion exchange membrane (AEM), I reduce diffusion coefficients of anions and cations by a factor of 10 and 100 respectively relative to those in the electrolyte to model a generic anion exchange membrane and assume a fixed background positive unit charge with a 0.5 M concentration, following Singh *et al.*[36] I also use effective diffusion coefficients within the biocathode layer calculated using the Bruggeman relationship,

$$D_{i,\mathrm{eff}} = {\epsilon_{\mathrm{p}}}^{3/2} D_i \tag{53}$$

where ϵ_{p} is the biofilm porosity. The net ionic current density in the electrolyte (i_{l}) can be calculated from the total ionic flux:

$$i_{\mathrm{l}} = F \sum_i z_i N_i \tag{54}$$

where F is Faraday's constant and z_i is the charge number, following electroneutrality:

$$\sum_i z_i c_i = 0 \tag{55}$$

Gas feed and electrolyte flow in the well-mixed electrolyte

The well-mixed electrolyte regions are assumed to have sufficient convective mixing such that no concentration gradients are formed. Species transport into and out of the boundary layers is considered at the interface between the well-mixed and boundary layer electrolyte phases (Fig. 4.1a, b). Constant gas feed and electrolyte flow terms in the well-mixed regions are included to describe a continuously operating system, given by

$$R_{\mathrm{F,CO_2}} = k_{\mathrm{L}}a\left(K_0 P_{\mathrm{CO_2}} - c_{\mathrm{CO_2}}\right) \tag{56}$$

$$R_{\mathrm{F},i\neq\mathrm{CO_2}} = D\left(c_{i,0} - c_i\right) \tag{57}$$

where $k_{\mathrm{L}}a$ is the volumetric mass-transfer coefficient (in units s^{-1}) on the liquid side of the gas/liquid interface, K_0 is Henry's constant for CO_2 in water, $P_{\mathrm{CO_2}}$ is the pressure of CO_2 in the gas phase, D is the dilution rate (defined as the inverse space time, or volumetric flow rate divided by reactor volume), and $c_{i,0}$ is the initial or feed concentration of the ith species. The equilibrium of CO_2 between the gas and liquid phases, $\mathrm{CO_{2(g)}} \leftrightarrow \mathrm{CO_{2(aq)}}$, is described by Henry's constant such that

$$K_0 = \frac{c_{\mathrm{CO_2}}}{P_{\mathrm{CO_2}}} \tag{58}$$

Henry's constant for CO_2 depends on the temperature and salinity of the aqueous phase and follows an empirical relationship,[37]

$$\ln(K_0) = 93.4517\left(\frac{100}{T}\right) - 60.2409 + 23.3585\ln\left(\frac{T}{100}\right) + S\left(0.023517 - 0.023656\left(\frac{T}{100}\right) + 0.0047036\left(\frac{T}{100}\right)^2\right) \tag{59}$$

where S is the salinity in units g/kg and T is the temperature.

Homogeneous chemical reactions

The acid-base bicarbonate/carbonate and water-dissociation reactions shown below occur in all phases and are treated as kinetic expressions without assuming equilibrium (eq. 15):

$$\mathrm{CO_{2(aq)}} + \mathrm{H_2O} \overset{k_{+1},k_{-1}}{\longleftrightarrow} \mathrm{H^+} + \mathrm{HCO_3^-} \qquad K_1 \tag{60}$$

$$\mathrm{HCO_3^-} \overset{k_{+2},k_{-2}}{\longleftrightarrow} \mathrm{H^+} + \mathrm{CO_3^{2-}} \qquad K_2 \tag{61}$$

$$\mathrm{CO_{2(aq)}} + \mathrm{OH^-} \overset{k_{+3},k_{-3}}{\longleftrightarrow} \mathrm{HCO_3^-} \qquad K_3 = K_1/K_{\mathrm{w}} \tag{62}$$

$$\mathrm{HCO_3^-} + OH^- \overset{k_{+4},k_{-4}}{\longleftrightarrow} \mathrm{CO_3^{2-}} + \mathrm{H_2O} \qquad K_4 = K_2/K_{\mathrm{w}} \tag{63}$$

$$\mathrm{H_2O} \overset{k_{\mathrm{w}},k_{-\mathrm{w}}}{\longleftrightarrow} \mathrm{H^+} + \mathrm{OH^-} \qquad K_{\mathrm{W}} \tag{64}$$

where k_{+n} and k_{-n} are the forward and reverse rate constants, respectively, and K_n is the equilibrium constant for the nth reaction. Source and sink terms resulting from these reactions are compiled in $R_{\mathrm{H},i}$, written as

$$R_{\mathrm{H},i} = \sum_n \nu_i \left(k_{+n} \prod_{\nu_i<0} c_i - k_{-n} \prod_{\nu_i>0} c_i \right) \tag{65}$$

where ν_i is the stoichiometric coefficient of species i for the nth reaction and reverse rate constants are calculated from

$$k_{-n} = \frac{k_{+n}}{K_n} \tag{66}$$

Electrode reactions – anode

The surface reaction at the anode is the oxidation of water:

$$\mathrm{H_2O} \longrightarrow \frac{1}{2}\mathrm{O_2} + 2\mathrm{H^+} + 2\mathrm{e^-} \qquad E^0_{\mathrm{OER}} \tag{67}$$

where E^0_{OER} is the equilibrium potential of the oxygen evolution half-cell reaction (OER) at standard state. The anode reaction is related to species transport by a flux boundary condition at the electrode surface,

$$N_i = \frac{-\nu_i i_{\mathrm{R}}}{nF} \tag{68}$$

where i_{R} is the reaction current density and n is the number of electrons participating in the electrode reaction. I model charge transfer kinetics at the anode using Butler-Volmer kinetics:

$$i_{\mathrm{R}} = i_0 \left[\left(\frac{c_{\mathrm{red}}}{c_{\mathrm{red},0}} \right)^{\gamma_{\mathrm{red}}} \exp\left(\frac{\alpha_{\mathrm{a}} F \eta}{RT} \right) - \left(\frac{c_{\mathrm{ox}}}{c_{\mathrm{ox},0}} \right)^{\gamma_{\mathrm{ox}}} \exp\left(\frac{\alpha_{\mathrm{c}} F \eta}{RT} \right) \right] \tag{69}$$

where i_0 is the constant exchange current density, $\gamma_{\mathrm{red/ox}}$ is the reaction order with respect to a reactant, $\alpha_{\mathrm{a/c}}$ is the anodic/cathodic transfer coefficient, and η is the overpotential. Kinetic parameters for the OER are sourced from Haussener *et al.*[38] The overpotential is defined according to

$$\eta = \phi_{\mathrm{s}} - \phi_{\mathrm{l}} - E \tag{70}$$

where ϕ_{s} is the electrode potential, ϕ_{l} is the electrolyte potential, and E is the half-cell equilibrium potential.

Because water oxidation creates acidic conditions near the anode surface, bicarbonate and carbonate species will be converted to aqueous CO_2 according to Le Chatelier's principle. To avoid the unrealistic supersaturation of CO_2 in the electrolyte this would cause, I describe evolution of CO_2 in the electrolyte as

$$R_{\mathrm{CO_2,evolution}} = \begin{cases} -\gamma\left(\frac{c_{\mathrm{CO_2}}}{K_0 f_{\mathrm{CO_2}}}\right)^2 & \frac{c_{\mathrm{CO_2}}}{K_0 P_{\mathrm{CO_2}}} > 1 \\ 0 & \frac{c_{\mathrm{CO_2}}}{K_0 P_{\mathrm{CO_2}}} \leq 1 \end{cases} \tag{71}$$

where γ is the releasing coefficient and $c_{\mathrm{CO_2}}/K_0 P_{\mathrm{CO_2}}$ is the supersaturation ratio. This formulation was originally reported by Wilt, and was utilized to describe CO_2 evolution in abiotic electrochemical systems previously.[15,36,39,40]

Electrode reactions – biocathode

Electrons supplied from the solid electrode support Fig. 4.1b) must be energetic enough to reduce heme groups in the exterior electron conduit protein, MtrC (corresponding to a redox potential below ~-100 mV *vs.* SHE, see supplementary note 7 in Appendix C). These electrons are passed through the MtrCAB conduit and ultimately to CymA or similar inner membrane proteins, where they are used to reduce the quinone pool at a redox potential between -80 and +100 mV *vs.* SHE (Fig. 4.1c).[32,41] Electrons in the quinone pool are not energetic enough to drive NAD^+ reduction by themselves, so reverse electron flow is required for (re-)generation of energy carriers (reducing equivalents) such as NADH, ATP, and ferredoxins.[42] In the proposed scheme, which is experimentally supported by the analysis of Rowe *et al.*[32] and analogous to a similar process in *Acidithiobacillus ferrooxidans*,[25] a portion of the electrons deposited into the quinone pool travel energetically downhill to reduce a terminal electron acceptor (*e.g.*, NO_3^-, +740 mV *vs.* SHE). The released energy from this process is conserved by a proton motive force, which is used to drive the thermodynamically uphill energy carrier (re-)generation reactions (Fig. 1c). Once these energy carriers are generated, carbon fixation processes function as normal. By tracking the electrons through each step of this process, I derive the overall electron demand per fixed CO_2 molecule and use this as the overall (bio)electrochemical reaction occurring throughout the biocathode layer (R_{CT}).

I begin with the physiology of direct electron transfer through the MtrCAB electron conduit (Fig. 4.1c) to determine the stoichiometry of CO_2 reduction to pyruvate for four major carbon fixation pathways (Fig. 4.1d–g) using either aerobic or anaerobic nitrate respiration. All processes start with quinone (Q) reduction,

$$\mathrm{Q} + 2\mathrm{H^+_{in}} + 2\mathrm{e^-} \rightarrow \mathrm{QH_2} \tag{72}$$

using the MtrCAB/CctA/CymA electron conduit native to *S. oneidensis*.[32,42–44] Thermodynamically downhill electron transfer processes (respiration) are used to generate a proton motive force necessary to drive regeneration of energy carriers (*e.g.*, NADH). For aerobic respiration, the respiratory complex III (*e.g.* the *bc1* complex) oxidizes a quinol, pumping protons across the inner membrane:[45,46]

$$QH_2 + 2H^+_{in} \rightarrow Q + 4H^+_{out} + 2e^- \quad (73)$$

where the subscripts "in" and "out" refer to ion locations in the intracellular space and periplasm, respectively. The two electrons liberated in this process are transported by *c*-type cytochromes to respiratory complex IV (*e.g.* the *aa3* complex), which transports two additional protons across the inner membrane and reduces O_2 to H_2O:[45,47]

$$\frac{1}{2}O_2 + 2H^+ + 2e^- + 2H^+_{in} \rightarrow H_2O + 2H^+_{out} \quad (74)$$

For anaerobic nitrate respiration, quinols are consumed both to pump protons via respiratory complex III, eq. (23), and to reduce NO_3^- to nitrite (NO_2^-) using, *e.g.* the Nar complex:[48]

$$NO_3^- + 2H^+ + QH_2 \rightarrow NO_2^- + H_2O + Q + 2H^+_{out} \quad (75)$$

Further reactions consume electrons liberated by quinol oxidation to complete the reduction of NO_2^- to N_2:[48]

$$NO_2^- + 2H^+ + e^- \rightarrow NO + H_2O \quad (76)$$

$$NO + H^+ + e^- \rightarrow \frac{1}{2}N_2O + \frac{1}{2}H_2O \quad (77)$$

$$N_2O + 2H^+ + 2e^- \rightarrow N_2 + H_2O \quad (78)$$

Carbon fixation pathways require NAD(P)H, ATP, and/or reduced ferredoxins (Fd_{red}) as reducing equivalents.[49] Cells can regenerate these reducing equivalents by translocating protons (PMF consumption) using, *e.g.*, the Nuo complex for NADH,[50] ATP synthase for ATP,[51] and the Rnf complex for ferredoxins[52–54] according to

$$NAD^+ + 4H^+_{out} + QH_2 \rightarrow NADH + 4H^+_{in} + Q \quad (79)$$

$$ADP + 3H^+_{out} \rightarrow ATP + 3H^+_{in} \quad (80)$$

$$Fd_{ox} + NADH + 2H^+_{out} \rightarrow Fd_{red} + NAD^+ + 2H^+_{in} \quad (81)$$

I use these regeneration mechanisms to determine the stoichiometry (number of reduced molecules produced per number of electrons consumed) for aerobic or anaerobic nitrate respiration (Table S1 in Appendix C). Because carbon fixation pathways have different energy carrier requirements, I also derive the overall stoichiometry for CO_2 reduction to pyruvic acid (pyruvate) (Table S2 in Appendix C). For the aero-tolerant carbon fixation pathways (Calvin cycle, eq. (32), Fuchs-Holo bi-cycle, eq. (33)), the cathodic half-cell reactions using aerobic respiration are

$$3CO_2 + 3\frac{5}{12}O_2 + 23\frac{2}{3}H^+ + 23\frac{2}{3}e^- \rightarrow C_3H_4O_3 + 9\frac{5}{6}H_2O \quad (82)$$

$$3CO_2 + 3\frac{3}{4}O_2 + 25H^+ + 25e^- \rightarrow C_3H_4O_3 + 10\frac{1}{2}H_2O \tag{83}$$

For carbon fixation pathways using NO_3^- as the terminal electron acceptor, the half-cell reactions are

$$3CO_2 + 10\frac{1}{4}NO_3^- + 71\frac{1}{2}H^+ + 61\frac{1}{4}e^- \rightarrow C_3H_4O_3 + 5\frac{1}{8}N_2 + 33\frac{3}{4}H_2O \tag{84}$$

$$3CO_2 + 7\frac{1}{2}NO_3^- + 55H^+ + 47\frac{1}{2}e^- \rightarrow C_3H_4O_3 + 3\frac{1}{4}N_2 + 25\frac{1}{2}H_2O \tag{85}$$

$$3CO_2 + 11\frac{1}{4}NO_3^- + 77\frac{1}{2}H^+ + 66\frac{1}{4}e^- \rightarrow C_3H_4O_3 + 5\frac{5}{8}N_2 + 36\frac{3}{4}H_2O \tag{86}$$

$$3CO_2 + 7\frac{1}{4}NO_3^- + 53\frac{1}{2}H^+ + 46\frac{1}{4}e^- \rightarrow C_3H_4O_3 + 3\frac{1}{8}N_2 + 24\frac{3}{4}H_2O \tag{87}$$

where eq. (34) is for the Calvin cycle, eq. (35) is for the rTCA cycle, eq. (36) is for the Fuchs-Holo bicycle (F-H), and eq. (37) is for the Wood-Ljungdahl (WL) pathway.

Biocathode reactions, eq. (32–37), relate CO_2-fixing reactions to species transport in the biocathode layer by

$$R_{\mathrm{CT},i} = \frac{\nu_i a_{\mathrm{v}} i_{\mathrm{B}}}{nF} \tag{88}$$

where a_{v} is the active specific surface area of the biocathode and i_{B} is the current density on the biocathode surfaces. The active specific surface area is calculated based on the geometric assumptions described above, resulting in

$$a_{\mathrm{v}} = \frac{3\left(1-\epsilon_{\mathrm{p}}\right)}{r_{\mathrm{cell}}} \tag{89}$$

where r_{cell} is the radius of the spherical microbe.

The current density, and therefore the CO_2-fixation rate, can be limited by any of three factors comprising several processes. First, the CO_2-fixation rate could be limited by the enzyme kinetics of carbon fixation. Second, this rate could be limited by the kinetics of electron transfer, including electron uptake by cells, passage through the electron conduit (MtrCAB), or regeneration of reducing equivalents (*e.g.*, NADH). Third, it could be limited by the availability of a necessary substrate (*e.g.*, CO_2). Of these processes, this analysis indicates three could limit the CO_2 fixation rate: the enzyme kinetics of carbon fixation, the electron uptake charge transfer reaction, and the availability of CO_2 (see Supplementary Note 9 in Appendix C for a detailed description).

To account for the rate limit set by the enzyme kinetics, which depends on the turnover number of the rate-limiting enzyme in the carbon fixation pathway, I impose a limit on i_{B} via

$$i_{\mathrm{B}} = \frac{i_{\mathrm{R}}}{1 + \left|\frac{i_{\mathrm{R}}}{i_{\mathrm{lim}}}\right|} \tag{90}$$

Where i_{lim} is the biomass-limited current density. I calculate the biomass-limited current density by projecting the enzymatic rate limit to the total cell surface:

$$i_{\mathrm{lim}} = nFk_{\mathrm{cat}}\left(\frac{n_{\mathrm{E}}}{N_{\mathrm{Av}}V_{\mathrm{cell}}}\right)\left(\frac{1-\epsilon_{\mathrm{p}}}{a_{\mathrm{v}}}\right) \tag{91}$$

where k_{cat} is the enzyme turnover number (units s^{-1}), n_{E} is the enzyme amount in each cell (units $cell^{-1}$) N_{Av} is Avogadro's number, and V_{cell} is the microbe volume. This formulation for the limiting current density relies on the fact that the rate of intracellular diffusion of substrates is much faster than the rate-limiting reaction step in carbon fixation pathways (see supplementary note 1 in Appendix C for calculations that validate this description), indicating that energy carriers and CO_2 have complete and effectively immediate access to intracellular enzymes once generated at or delivered to the cell surface.

The charge transfer reaction current density limit, i_{R} in eq. (40), is defined using Butler-Volmer kinetics, eq. (19), which describes the rate limit set by electron transfer from the solid electrode support to the electron conduit proteins. The Butler-Volmer equation also accounts for the availability of CO_2 based on the pre-exponential factor $\left(\frac{c_{\mathrm{ox}}}{c_{\mathrm{ox,0}}}\right)^{\gamma_{\mathrm{ox}}}$.

Electron transport in the solid electrode

Electron transport in the solid electrode regions is governed by charge conservation and Ohm's law, given by

$$\nabla i_{\mathrm{s}} = -\nabla i_{\mathrm{l}} = -a_{\mathrm{v}} i_{\mathrm{B}} \tag{92}$$

$$i_{\mathrm{s}} = \kappa_{\mathrm{s}} \frac{\partial \phi_{\mathrm{s}}}{\partial x} \tag{93}$$

where i_s is the electrode current density and κ_s is the anode/biocathode conductivity. The conductivity in the biocathode is modified by a Bruggeman correction:

$$\kappa_{s,\text{eff}} = (1 - \epsilon_p)^{1.5}\kappa_s \quad (94)$$

Numerical method

The governing equations are solved using the MUMPS general solver in COMSOL Multiphysics 5.4. The modeling domain has a maximum element size of 10 μm in the well-mixed regions and 0.5 μm near boundaries to capture steep concentration gradients; the solution was independent of increasing mesh resolution. Model parameters are listed in Table S3 in Appendix C. The potential in the reactor is calculated relative to zero potential at the cathode base and potential or current density is applied as a boundary condition at the anode.

Reactor model analysis

The total system voltage (V_{system}) is calculated according to[55]

$$V_{\text{system}} = \Delta E^0 + V^{\text{Ohmic}} + U^{\text{Nernst}} + \eta_A + \eta_{BC} \quad (95)$$

where ΔE^0 is the standard state potential difference between the anode and biocathode reactions ($\Delta E^0 = E^0_{\text{OER}} - E^0_{\text{CO}_2\text{RR}}$), V^{Ohmic} is the total ohmic overpotential due to liquid and solid phase resistivity, U^{Nernst} is the Nernst potential that accounts for deviations away from standard state concentrations of reacting species, and η_A and η_{BC} are the kinetic (activation) overpotentials associated with the anode (A) and biocathode layer (BC) charge transfer reactions as defined in eq. (20).

4.4 Results and Discussion

System overview

The model (see Methods for additional detail) considers a one-dimensional bioelectrochemical reactor for CO_2 reduction (Fig. 4.1a). The reactor has well-mixed anolyte and catholyte regions that are replenished at a fixed dilution rate and to which CO_2 is constantly supplied at a fixed partial pressure. These regions are separated by an anion exchange membrane (AEM) and fluid boundary layers, which also separate the well-mixed phases from the anode surface and the biocathode layer. The chemical species in each chamber are dissolved CO_2, dissolved O_2 (in the case of aerobic operation), bicarbonate anions (HCO_3^-), carbonate anions (CO_3^{2-}), protons (H^+), hydroxide anions (OH^-), sodium cations (Na^+), and nitrate anions (NO_3^-). The biocathode is assumed to be comprised of a porous electrode support with a characteristic porosity and electrical (Ohmic) conductivity, supporting an active biomass density of 1 cell per μm^3 (roughly equivalent to a biomass density of 0.4 gCDW/cm^3, Fig. 1b).

I use the physiology of direct electron transfer through the MtrCAB electron conduit (Fig. 4.1c) to determine the stoichiometry of CO_2 reduction to pyruvate for four major CFPs (Fig. 4.1d-g) using either aerobic or anaerobic nitrate respiration (see Methods for additional detail). Although this particular physiology is not found in any known organisms, several factors justify this choice as a representative system for modeling. First, the MtrCAB electron conduit has been

shown to be reversible, resulting in electron uptake and deposition into the quinone pool.[32,41] Second, known electron conduit proteins interact primarily with the quinone pool and not with other cellular energy carriers (*e.g.*, NADH).[56] Third, the quinone pool is less energetic than other energy carriers (redox potential of ~-80 mV vs. SHE as compared to ~-320 mV vs. SHE for the NAD^+/NADH redox couple), so this assumption is more likely to underestimate the efficiency of cellular energy acquisition *via* electron uptake than to overestimate it. I also assume that the high pH (resulting from the microbial consumption of protons associated with respiration and carbon fixation) will have no effect on cellular activity, which allows us to calculate productivity limits imposed by enzymatic activity or chemical species transport. I note that this is realizable only by alkaliphiles or organisms that have been adapted to alkaline environments. I consider this, and other, microbial engineering targets in the discussion below and in Chapter 5.

Comparing microbial respiration and carbon fixation pathways

The terminal electron acceptor and CFP constrain the efficiency and productivity of dEMP systems. Because O_2 is more electronegative than NO_3^-, aerobic respiration allows microbes to divert a higher fraction of electrons to energy carrier regeneration and therefore carbon fixation (Tables S1 and S2 in Appendix C). For microbes using the Calvin-Benson-Bassham (CBB) cycle, aerobic respiration uses only 23.67 electrons per pyruvate molecule, while anaerobic nitrate respiration requires 61.25 electrons for the equivalent reaction. Under anaerobic conditions, obligately anaerobic CFPs use electrons more efficiently than aero-tolerant pathways: the reductive tricarboxylic acid (rTCA) cycle and the Wood-Ljungdahl pathway (WLP) require 47.5 and 46.25 electrons per pyruvate, respectively, while the CBB cycle and the 3-hydroxypropionate (3-HP) bi-cycle need 61.25 and 66.25 electrons. The rate-limiting step in carbon-fixing reactions must also be considered when evaluating productivity. While the WLP uses electrons most efficiently, the enzymatic processes are rate-limited compared to other CFPs (Table S3, Supplementary note 2 in Appendix C), so more biomass would be needed to fix carbon at equal rates.

To determine the impacts these competing constraints have on dEMP systems, I calculated the pyruvate production rate as a function of O_2 partial pressure for microbes using the CBB cycle to fix carbon with O_2 as the terminal electron acceptor (Fig. 4.2a) and pyruvate production versus applied voltage for microbes using NO_3^- as the terminal electron acceptor and different CFPs (Fig. 4.2b). For aerobic respiration, pyruvate production remains <2 μmol/cm^2/hr even at O_2 partial pressures 5-fold greater than in the atmosphere (P_{O_2} = 1 atm) due mainly to the low solubility and corresponding transport limitations of O_2 in aqueous solutions (Supplementary note 3 in Appendix C). In contrast, pyruvate production using anaerobic nitrate respiration reaches ~16.9 μmol/cm^2/hr at ~2.3 V for microbes using the rTCA cycle before the system becomes CO_2 transport limited, defined as the point at which the CO_2 concentration reaches ~0 mM at the base of the biofilm (current collector). It is worth noting that the applied voltage reported in Fig. 4.2b corresponds to the total system voltage, including the thermodynamic voltage, kinetic overpotentials associated with both the water oxidation reaction (at the anode) and the CO_2-fixation reaction (throughout the biocathode), the Nernst overpotential, and solid and liquid Ohmic overpotentials. Maximum pyruvate production rates for microbes using the CBB cycle (~7.0 μmol/cm^2/hr), 3-HP cycle (~4.4 μmol/cm^2/hr), and WLP (~1.9 μmol/cm^2/hr) are limited by the biomass available to fix carbon in 50 μm biofilms well before CO_2 transport becomes rate limiting.

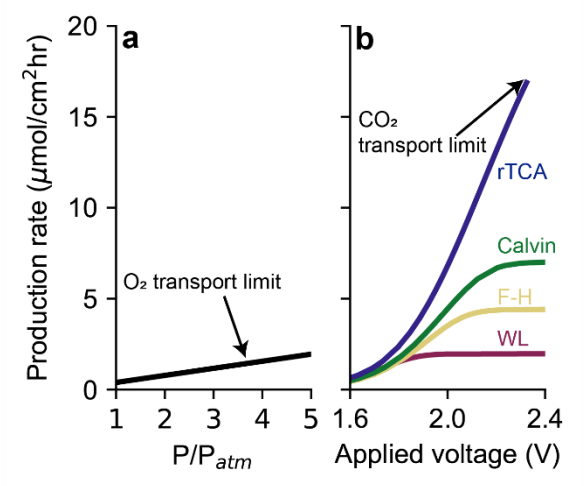

Figure 4.2. Effects of terminal electron acceptor and carbon fixation pathway on reactor operation. Pyruvate production rate at equivalent biofilm thickness (50 μm) as a function of (**a**) O_2 pressure supplied to the reactor headspace relative to atmospheric O_2 for microbes using the Calvin cycle with O_2 as the terminal electron acceptor, and (**b**) applied voltage for each carbon fixation pathway with NO_3^- as the terminal electron acceptor. Reactor conditions: initial pH=7.4, 0.25 M $NaNO_3$, D=5 hr^{-1}

Biofilm thickness effects on productivity

Because electroautotrophic biofilms are typically only a few monolayers thick, 3D electrodes of varying geometries have been used to increase the effective biofilm thickness by orders of magnitude.[57,58] For example, Jourdin *et al.* was able to grow a ~5–10 μm-thick biofilm throughout a 3D electrode with an active surface area of ~2600 m^{-1} and a total thickness of ~1 cm.[59] To simplify the modeling domain, I treat this complex structure as a porous electrode with a characteristic porosity, conductivity, and biomass density, following similar approaches to modeling gas diffusion electrodes.[13] Because the carbon fixation reaction can be treated as occurring on the cell surface (Supplementary note 1 in Appendix C), this approach does not result in any loss in model validity or generality. This effective biofilm thickness plays an important and complex role in determining both the total carbon fixation rate and the energy efficiency of the system. Increasing the biofilm thickness increases the biomass available to fix carbon, enabling a higher total electron uptake rate by increasing the biomass-limited production rate. However, CO_2 (and/or NO_3^-) transport through the biofilm will eventually impose an upper bound on the reaction rate. I plot the voltage necessary to achieve selected pyruvate production rates as a function of biofilm thickness for microbes using the rTCA cycle (Fig. 4.3a) or CBB cycle (Fig. 4.3b). For microbes using the CBB cycle, ~3.5-fold thicker biofilms are needed to achieve equivalent production rates because of the lower turnover number for the rate-limiting enzyme, RuBisCo, and the ~29% less efficient use of electrons. These factors also limit the achievable productivity of microbes using the CBB cycle to <12 μmol/cm^2/hr because thicker biofilms present a longer distance for CO_2 diffusion.

For both CFPs, increasing the biofilm thickness has a non-linear effect on the applied voltage necessary to achieve a fixed production rate (Fig. 4.3a, b). The initial rapid decline, and the following plateau over a wide thickness range, is due to the competing impacts of the activation overpotential for the CO_2 reduction reaction (CO_2RR) and transport-associated (Nernst and Ohmic) overpotentials (Supplementary note 4 in Appendix C). To describe these trends, I show the applied voltage breakdown for microbes using the rTCA (Fig. 4.3c, d) or CBB (Fig. 4.3e, f) cycles at representative biofilm thicknesses. For microbes using the rTCA cycle, increasing the effective biofilm thickness from 35 μm (Fig. 4.3c) to 50 μm (Fig. 4.3d) increases the maximum current density the biofilm can support from ~21.5 mA/cm^2 to ~31 mA/cm^2, but CO_2 transport

restricts the current density to 21.5 mA/cm^2 for the 50-µm biofilm. Increasing the effective biofilm thickness reduces the applied voltage necessary to achieve a given production rate (Fig. 4.3a). The difference is slight at lower rates because increased Ohmic loss (due to electron conduction through a thicker biofilm) mostly balances the reduced activation overpotential associated with the CO_2RR (Fig. 4.3c, d). However, as the production rate approaches the biomass-limited rate for the 35-µm film, the difference increases significantly, reaching ~200 mV at 21.5 mA/cm^2 (~16.9 µmol/cm^2/hr) because the activation overpotential for the 35-µm film rises sharply (Fig. 4.3c). Similar behavior is observed when comparing 50 µm (Fig. 4.3e) and 80 µm (Fig. 4.3f) biofilms using the CBB cycle to fix CO_2.

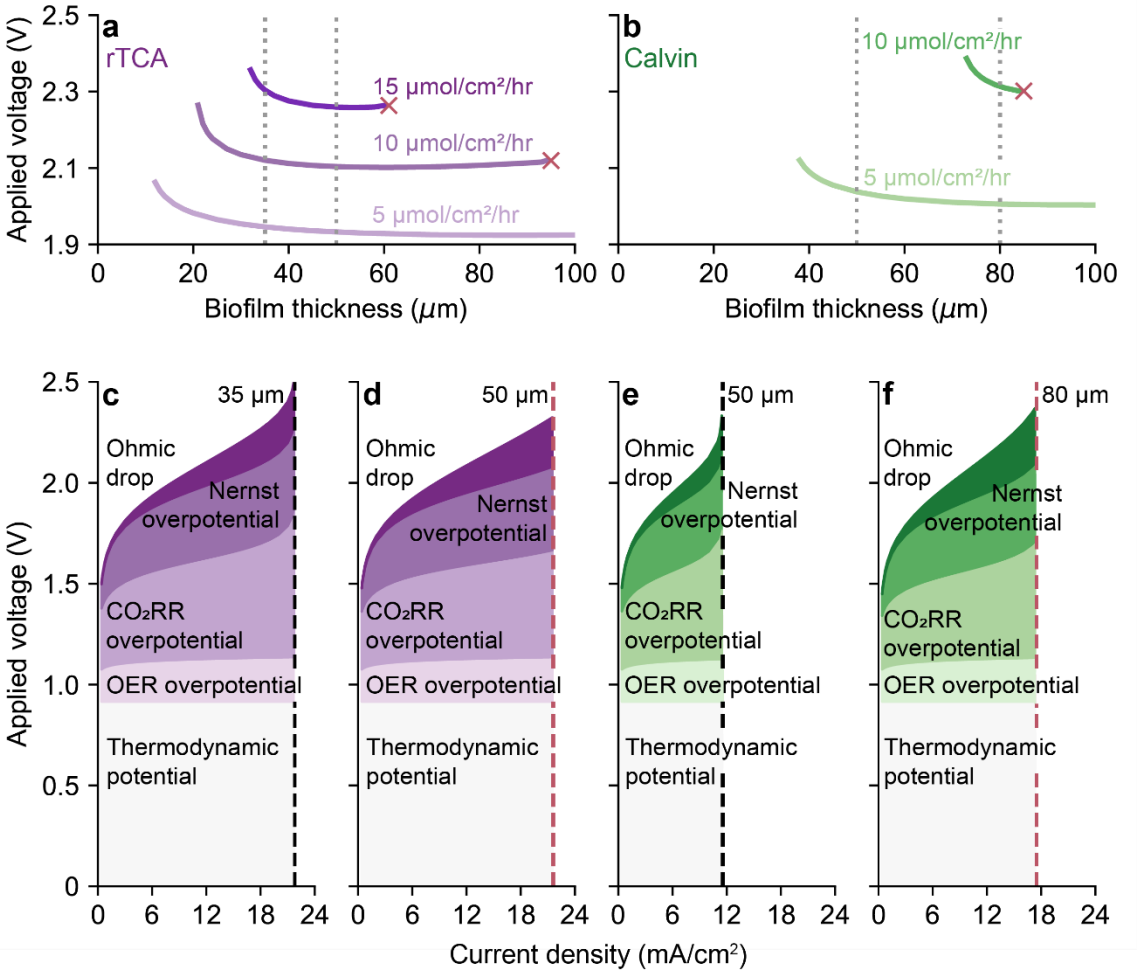

Figure 4.3. Effect of biofilm thickness on reactor operation. Applied voltage necessary to achieve a specific pyruvate production rate as a function of biofilm thickness for microbes fixing carbon using (**a**) the rTCA cycle and (**b**) the Calvin cycle. Applied voltage breakdown for (**c**) 35 µm, (**d**) 50 µm, (**e**) 50 µm, (**f**) 80 µm biofilms for microbes using the rTCA cycle (**c**, **d**) or Calvin cycle (**e**, **f**). Gray dotted lines in (**a**) and (**b**) correspond to biofilm thicknesses in (**c**–**f**) and were chosen to be representative of different production limits (biomass, CO_2 transport). Red crosses in (**a**, **b**) correspond to the CO_2 transport limit. Black dashed lines in (**c**, **e**) correspond to biomass-limited current density; red dashed lines in (**d**, **f**) correspond to the CO_2 transport-limited current density. Reactor conditions: initial pH=7.4, 0.25 M $NaNO_3$, D=5 hr^{-1}.

Implications for engineering dEMP systems

This analysis has significant implications for dEMP systems. The model demonstrates that although O_2 is a more efficient terminal electron acceptor than NO_3^-, low O_2 solubility limits the productivity of microbes using aerobic respiration. In principle, this issue can be overcome with a carefully designed gas diffusion electrode (GDE). Several criteria must be met simultaneously in this architecture: the GDE would need to be sufficiently hydrophilic to maintain complete wetting with a water film thick enough to support at least a monolayer of cells (>1 μm). However, flooding would displace the vapor phase, so the porosity would have to be high enough to prevent flooding and allow vapor channels for rapid CO_2 and O_2 diffusion. Future modeling and experimental efforts could identify optimal characteristics for this GDE architecture, which I note would also significantly enhance the CO_2-limited productivity described here for standard electrode architectures.

For current designs, NO_3^- respiration is substantially more productive than O_2 respiration. In general, soluble terminal electron acceptors such as perchlorate or sulfate should enable higher productivities than O_2. However, soluble terminal electron acceptors present two main challenges. First, production of these molecules is typically either energy intensive (in the case of nitrate and perchlorate) or can emit potent greenhouse gases (*e.g.*, nitrous oxide in the case of NO_3^- production). Hence, a comprehensive life cycle analysis of these impacts would be necessary to determine the viability of this production strategy compared to, for example, H_2- or formate-mediated electromicrobial production. However, nitrate, perchlorate, and sulfate remediation are all attractive applications of electromicrobial systems independent of commodity chemical production. Second, because NO_3^- (or other soluble terminal electron acceptors) is supplied via the liquid phase, the product titer is restricted by the feed concentration and the stoichiometry of carbon fixation. For example, this model assumed an NO_3^- feed concentration of 250 mM. For carbon fixation with the rTCA cycle, this would limit the pyruvate titer to ~33 mM (~3 g/L) because 7.5 NO_3^- molecules are consumed per pyruvate produced (eq. 35 in Methods). This limitation may be partially overcome by enhancing the nitrate tolerance of organisms via adaptive laboratory evolution strategies that have been successful in similar scenarios.[60] Nitrate is expected to minimize this challenge because it is the most thermodynamically favorable soluble terminal electron acceptor.

Regardless of the terminal electron acceptor, the CO_2 transport limit eventually imposes an upper bound on productivity, so increasing biofilm thicknesses cannot enable arbitrarily high production rates. For microbes with a lower enzymatic reaction rate limit (lower turnover number), the steady-state CO_2 transport limit is also lower, so microbes using the 3-HP bi-cycle and WLP cannot match the productivity achievable by microbes using the rTCA or CBB cycle regardless of the biofilm thickness. A lower turnover number for the rate-limiting enzyme also increases transport- or activation-associated overpotentials for a given CO_2-fixation rate, reducing energy efficiency. Combined, these results indicate that microbes using the rTCA cycle are likely to be both the most productive and most efficient biocatalysts for dEMP systems. Microbes that use the CBB cycle are the second-best option because the biomass-limited reaction rate is much higher even though the cycle's electron utilization efficiency is lower than that for the WLP. Thus, the CO_2 transport-limited production rate is higher and transport-associated inefficiencies are lower.

In the paper on which this chapter is based,[61] co-lead author Jacob Hilzinger developed a marker protein phylogeny-driven bioinformatics approach to identify organisms capable of electroautotrophy by coupling electron uptake to either O_2 or NO_3^- respiration and using either the CBB or rTCA cycles to fix carbon. In this dataset, 72 organisms have complete CBB cycles, NarG and/or *aa*$_3$/*bo*$_3$-type cytochrome *c* oxidases, and at least one electron conduit.[61] Of these, 19 encode NarG. This analysis accurately "predicted" four of the six known electroautotrophic bacteria: *A. ferrooxidans*,[25] *Rhodopseudomonas palustris*,[26] *Candidatus Tenderia electrophaga*,[62,63] and *Desulfovibrio ferrophilus.*[64] One of the bacteria the analysis missed, *Kyrpidia spormannii*,[65] was not cultured at the time of our analysis and therefore was not included in the Reference Proteomes Database. The second, *Prosthecochloris aestuarii*,[66] was predicted to be autotrophic (it encodes the rTCA cycle), but was not predicted to encode an electron conduit. This indicates that there may be to-date uncharacterized electron conduit proteins. Interestingly, this analysis also indicated that electroautotrophic capacity could be engineered in *Geobacter sulfurreducens* simply by the introduction of a citrate lyase (aclB/ccsA) gene, a task that was accomplished by Ueki *et al.* with the predicted effect of enabling electroautotrophic growth.[67]

Most of the organisms this analysis identified have not been previously characterized as electroautotrophs. Hence, physiological confirmation of the remaining organisms plus development of genetic tools would significantly expand the available CBB-based electroautotrophs for industrial applications. In contrast, only *Geobacter metallireducens* encodes the rTCA cycle, NarG, and at least one electron conduit. As genetic tools have been developed for *G. metallireducens*,[68] this organism represents an especially promising catalyst for industrial dEMP. Because the phylogenetic analysis identified only a small number of organisms that have all the desired modules, most of which do not have genetic tools, organisms that have potential as synthetic chassis for dEMP are also identified, which I discuss here in the context of several possible synthetic biology strategies for engineering electroautotrophy.

First, an organism may have a partial CFP that can be completed by heterologous expression of the missing components. Several recent demonstrations make this an attractive strategy: the CBB cycle has been engineered into heterotrophs by the addition of key enzymes,[69–71] and the rTCA cycle was completed in *G. sulfurreducens* to enable electroautotrophy using both rational engineering[67] and directed evolution strategies.[72] An alternate CFP, the reductive glycine pathway,[73,74] is a third option since its modularity has recently been confirmed by functional expression in both *Escherichia coli*[75] and *Cupriavidus necator*.[76] The dataset revealed several organisms in which completion of a partial CFP may be viable.[61] Four of five *Shewanella* species identified in this study encode Prk, three encode partial rTCA cycle markers, and two encode NarG. Given the prevalence of genetic tools available to this genus, the well-characterized use of *Shewanella oneidensis* in bioelectrochemical systems, and facultative anaerobic metabolism, engineering a complete CFP in *Shewanella* could lead to readily-engineerable electroautotrophs. All *Shewanella* species encode the Rnf marker gene, indicating that they can support the efficient reverse-electron transport-driven ferredoxin reduction that may be required for the rTCA cycle.

Second, an organism encoding a complete CFP may be engineered to directly uptake electrons from a cathode. The electron conduit native to *S. oneidensis*, MtrCAB/CymA, has been functionally expressed in *E. coli*,[77–79] which is a promising host for this strategy since multiple CFPs have been successfully engineered and it naturally respires NO_3^- and O_2. Alternatively,

Cupriavidus spp. encode both a complete CBB cycle, NO_3^- and O_2 respiratory modules, and have genetic tools available,[80] making these species an attractive option for expressing an electron conduit. Because only two organisms that encode a full rTCA cycle with at least one electron conduit have genetic methods available, the green sulfur bacterium *Chlorobaculum tepidum*, which encodes the full rTCA and has genetic tools, may be another suitable host for electron conduit expression.

Finally, an organism with a complete CFP and a functional electron conduit may be engineered to use an alternate electron acceptor. I use NO_3^- respiration in this model because it is the most thermodynamically favorable soluble electron acceptor; NO_3^- respiration could be introduced into organisms by expressing the NarGHI complex. However, 5 molybdopterin cofactor biosynthesis enzymes are also necessary for proper functioning of this complex, so an appropriate chassis would benefit significantly from natural expression of these supporting proteins. *R. palustris* is an excellent candidate for this strategy since it has a well-characterized electron conduit[26], a complete CBB cycle, and encodes the molybdopterin biosynthesis genes. This organism has been engineered for *poly*-hydroxybutyrate[81] and *n*-butanol[82] production in dEMP systems, so heterologous expression of NarGHI may enable higher yields and productivities. *Azoarcus* sp. KH32C has complete CBB and rTCA cycles and encodes NosZ, while lacking NarG. A genetic system was developed in the related *Azoarcus* sp. strain BH72,[83] which may open up KH32C for heterologous expression of NarGHI, further increasing the potential of this species for dEMP.

The multiheme cytochrome phylogeny developed in this analysis indicates that a significant number of undiscovered cytochromes that support electron exchange with an electrode may exist.[61] This hypothesis is supported by reports of direct electron uptake independent of the four biochemically characterized families of outer membrane cytochromes used in our study; for example, both the methanogenic archaeon *Methanosarcina barkeri*[84] and the green sulfur bacterium *P. aestuarii*[66] have been shown to directly accept electrons from a cathode. Cytochromes involved in direct electron transfer may therefore be more widespread and diverse than currently realized, opening the possibility of a significant number of additional chassis for dEMP.

4.5 Conclusion

This analysis identified several microbial chassis that have potential as industrial dEMP strains (Table 4.1), and I have outlined a series of Technology Readiness Levels (TRLs) to evaluate industrial relevance of microbial catalysts (Table S4 in Appendix C). Beyond the genetic modules that enable electroautotrophy, additional factors constrain the productivity achievable by a given organism. For current densities >10 mA/cm^2, which are likely necessary for viable production capacity, the model predicts alkaline conditions throughout the biofilm, indicating that (facultative) alkalophilicity is a desirable trait in the ideal strain. A higher salinity reduces Ohmic overpotential and an increased bicarbonate concentration can enhance productivity by aiding CO_2 transport, so halophilicity or halotolerance is similarly advantageous. Unfortunately, the pH- and halo-tolerance of the identified organisms is unclear, so future studies, in addition to confirming electroautotrophic capacity, should also characterize these traits. A suitable microbial catalyst could also be engineered to tolerate alkaline or saline conditions using rational engineering or directed evolution strategies.[60,85] Because the turnover number of the rate-limiting enzyme plays a

key role in setting productivity and efficiency limits for dEMP, these values should also be characterized in the organism(s) of interest. Strain engineering can then focus on increasing the rate limit either by increasing the enzyme turnover number or overexpressing the rate-limiting enzyme.

Table 4.1. Promising microbial chassis for dEMP

Organism	TRL†	Complete CFP	Engineered CFP
Geobacter metallireducens	1	rTCA	-
Geobacter sulfurreducens	3	-	*rTCA[67,72]
Escherichia coli	1	-	*CBB[69] and *rGly[75]
Cupriavidus necator	1	CBB	*rGly[76]
Shewanella oneidensis	1	-	rTCA or CBB
Shewanella sediminis	1	-	rTCA or CBB
Shewanella woodii	1	-	rTCA or CBB
Vibrio natriegens	1	-	CBB
Chlorobaculum tepidum	1	rTCA	-
Rhodopseudomonas palustris	4	CBB	-
Azoarcus sp. KH32C	1	rTCA and CBB	-
Methanosarcina barkeri	1	WL	rTCA or CBB
Methanosarcina acetivorans	1	WL	rTCA or CBB

†Scale: 1, least ready; 5 most ready (Table S7)
*Denotes experimental demonstration of engineered CFP

Strain selection and engineering should also be guided by the desired product. For example, the CBB cycle is well-suited for the production of sugars such as sucrose because its end product is glyceraldehyde-3-phosphate, while the rTCA cycle may be better suited to fatty acid production since the end product, acetyl-CoA, is used directly by fatty acid biosynthesis pathways.

4.6 References

1 R. E. Blankenship, D. M. Blankenship, J. Tiede, G. W. Barber, G. Brudvig, M. Fleming, M. R. Ghirardi, W. Gunner, D. M. Junge, A. Kramer, T. A. Melis, C. C. Moore, D. G. Moser, A. J. Nocera, D. R. Nozik, W. W. Ort, R. C. Parson, R. T. Prince and Sayre, *Science (80-.).*, 2011, **332**, 805–809.

2 J. M. Spurgeon and B. Kumar, *Energy Environ. Sci.*, 2018, **11**, 1536–1551.

3 W. Sheng, S. Kattel, S. Yao, B. Yan, Z. Liang, C. J. Hawxhurst, Q. Wu and J. G. Chen, *Energy Environ. Sci.*, 2017, **10**, 1180–1185.

4 P. De Luna, C. Hahn, D. Higgins, S. A. Jaffer, T. F. Jaramillo and E. H. Sargent, *Science (80-.).*, , DOI:10.1126/science.aav3506.

5 Z. Liu, K. Wang, Y. Chen, T. Tan and J. Nielsen, *Nat. Catal.*, 2020, **3**, 274–288.

6 N. J. Claassens, D. Z. Sousa, V. A. P. M. Dos Santos, W. M. De Vos and J. Van Der Oost, *Nat. Rev. Microbiol.*, 2016, **14**, 692–706.

7 N. J. Claassens, C. A. R. Cotton, D. Kopljar and A. Bar-Even, *Nat. Catal.*, 2019, **2**, 437–447.
8 U. Schröder, F. Harnisch and L. T. Angenent, *Energy Environ. Sci.*, 2015, **8**, 513–519.
9 C. Liu, B. C. Colón, M. Ziesack, P. A. Silver and D. G. Nocera, *Science (80-.).*, 2016, **352**, 1210–1213.
10 H. Li, P. H. Opgenorth, D. G. Wernick, S. Rogers, T. Wu, W. Higashide, P. Malati, Y. Huo, K. M. Cho and J. C. Liao, *Science (80-.).*, 2012, **335**, 1596.
11 N. J. Claassens, I. Sánchez-Andrea, D. Z. Sousa and A. Bar-Even, *Curr. Opin. Biotechnol.*, 2018, **50**, 195–205.
12 L. C. Weng, A. T. Bell and A. Z. Weber, *Energy Environ. Sci.*, 2019, **12**, 1950–1968.
13 L. C. Weng, A. T. Bell and A. Z. Weber, *Phys. Chem. Chem. Phys.*, 2018, **20**, 16973–16984.
14 K. Tran and Z. W. Ulissi, *Nat. Catal.*, 2018, **1**, 696–703.
15 A. J. Abel and D. S. Clark, *ChemSusChem*, 2021, **14**, 344–355.
16 Y. Chen, A. Vise, W. E. Klein, F. C. Cetinbas, D. J. Myers, W. A. Smith, T. G. Deutsch and K. C. Neyerlin, *ACS Energy Lett.*, 2020, **5**, 1825–1833.
17 R. Hegner, K. Neubert, C. Kroner, D. Holtmann and F. Harnisch, *ChemSusChem*, 2020, **13**, 5295–5300.
18 A. Tanaka, M. Hirata, Y. Kiyohara, M. Nakano, K. Omae, M. Shiratani and K. Koga, *Thin Solid Films*, 2010, **518**, 2934–2936.
19 R. G. Grim, Z. Huang, M. T. Guarnieri, J. R. Ferrell, L. Tao and J. A. Schaidle, *Energy Environ. Sci.*, 2020, **13**, 472–494.
20 A. A. Menezes, J. Cumbers, J. A. Hogan and A. P. Arkin, *J. R. Soc. Interface*, , DOI:10.1098/rsif.2014.0715.
21 L. Jourdin, J. Sousa, N. van Stralen and D. P. B. T. B. Strik, *Appl. Energy*, 2020, **279**, 115775.
22 A. Prévoteau, J. M. Carvajal-Arroyo, R. Ganigué and K. Rabaey, *Curr. Opin. Biotechnol.*, 2020, **62**, 48–57.
23 D. D. Nayak and W. W. Metcalf, *Proc. Natl. Acad. Sci. U. S. A.*, 2017, **114**, 2976–2981.
24 C. Leang, T. Ueki, K. P. Nevin and D. R. Lovley, *Appl. Environ. Microbiol.*, 2013, **79**, 1102–1109.
25 T. Ishii, S. Kawaichi, H. Nakagawa, K. Hashimoto and R. Nakamura, *Front. Microbiol.*, 2015, **6**, 994.
26 D. Gupta, M. C. Sutherland, K. Rengasamy, J. Mark Meacham, R. G. Kranz and A. Bose, *MBio*, 2019, **10**, 1659–1677.
27 M. D. Yates, L. J. Bird, B. J. Eddie, E. L. Onderko, C. A. Voigt and S. M. Glaven, *Bioelectrochemistry*, , DOI:10.1016/j.bioelechem.2020.107644.
28 M. Tahernia, M. Mohammadifar, Y. Gao, W. Panmanee, D. J. Hassett and S. Choi, *Biosens. Bioelectron.*, 2020, **162**, 112259.
29 B. Korth, L. F. M. Rosa, F. Harnisch and C. Picioreanu, *Bioelectrochemistry*, 2015, **106**, 194–206.
30 A. C. L. De Lichtervelde, A. Ter Heijne, H. V. M. Hamelers, P. M. Biesheuvel and J. E. Dykstra, *Phys. Rev. Appl.*, 2019, **12**, 14018.
31 F. Salimijazi, J. Kim, A. M. Schmitz, R. Grenville, A. Bocarsly and B. Barstow, *Joule*, 2020, **4**, 2101–2130.
32 A. R. Rowe, P. Rajeev, A. Jain, S. Pirbadian, A. Okamoto, J. A. Gralnick, M. Y. El-

Naggar and K. H. Nealson, *MBio*, 2018, **9**, 1–19.
33 A. G. Fast and E. T. Papoutsakis, *Curr. Opin. Chem. Eng.*, 2012, **1**, 380–395.
34 J. S. Newman and C. W. Tobias, *J. Electrochem. Soc.*, 1962, **109**, 1183.
35 Z. Yang, D. Li, L. Xing, H. Xiang, J. Xuan, S. Cheng, E. H. Yu and A. Yang, *ACS Sustain. Chem. Eng.*, 2021, **9**, 351–361.
36 M. R. Singh, E. L. Clark and A. T. Bell, *Phys. Chem. Chem. Phys.*, 2015, **17**, 18924–18936.
37 Ulf Riebesell, Victoria J. Fabry, Lina Hansson and Jean-Pierre Gattuso, *Guide to best practices for ocean acidification research and data reporting*, 2011.
38 S. Haussener, C. Xiang, J. M. Spurgeon, S. Ardo, N. S. Lewis and A. Z. Weber, *Energy Environ. Sci.*, 2012, **5**, 9922–9935.
39 P. M. Wilt, *J. Colloid Interface Sci.*, 1986, **112**, 530–538.
40 M. Lin, L. Han, M. R. Singh and C. Xiang, *ACS Appl. Energy Mater.*, 2019, **2**, 5843–5850.
41 A. R. Rowe, F. Salimijazi, L. Trutschel, J. Sackett, O. Adesina, I. Anzai, L. H. Kugelmass, M. H. Baym and B. Barstow, *Commun. Biol.*, 2021, **4**, 957.
42 D. E. Ross, J. M. Flynn, D. B. Baron, J. A. Gralnick and D. R. Bond, *PLoS One*, , DOI:10.1371/journal.pone.0016649.
43 M. N. Alves, S. E. Neto, A. S. Alves, B. M. Fonseca, A. Carrêlo, I. Pacheco, C. M. Paquete, C. M. Soares and R. O. Louro, *Front. Microbiol.*, 2015, **6**, 665.
44 F. Kracke, I. Vassilev and J. O. Krömer, *Front. Microbiol.*, 2015, **6**, 1–18.
45 P. Mitchell, *J. Theor. Biol.*, 1976, **62**, 327–367.
46 C. Lange and C. Hunte, *Proc. Natl. Acad. Sci. U. S. A.*, 2002, **99**, 2800–2805.
47 M. Saraste, *Science (80-.).*, 1999, **283**, 1488–1493.
48 C. Moreno-Vivián, P. Cabello, M. Martínez-Luque, R. Blasco and F. Castillo, *J. Bacteriol.*, 1999, **181**, 6573–6584.
49 I. A. Berg, *Appl. Environ. Microbiol.*, 2011, **77**, 1925–1936.
50 T. Yagi, *Biochim. Biophys. Acta - Bioenerg.*, 1993, **1141**, 1–17.
51 P. Mitchell, *Biol. Rev. Camb. Philos. Soc.*, 1966, **41**, 445–502.
52 E. Biegel, S. Schmidt, J. M. González and V. Müller, *Cell. Mol. Life Sci.*, 2011, **68**, 613–634.
53 P. L. Tremblay, T. Zhang, S. A. Dar, C. Leang and D. R. Lovley, *MBio*, , DOI:10.1128/mBio.00406-12.
54 M. Rubin-Blum, N. Dubilier and M. Kleiner, *mSphere*, , DOI:10.1128/mSphere.00394-18.
55 J. Newman and K. E. Thomas-Alyea, *Electrochemical Systems*, Wiley, Hoboken, N. J., 3rd edn., 2004.
56 D. Gupta, M. S. Guzman and A. Bose, *J. Ind. Microbiol. Biotechnol.*, 2020, **47**, 863–876.
57 T. Zhang, H. Nie, T. S. Bain, H. Lu, M. Cui, O. L. Snoeyenbos-West, A. E. Franks, K. P. Nevin, T. P. Russell and D. R. Lovley, *Energy Environ. Sci.*, 2013, **6**, 217–224.
58 M. Cui, H. Nie, T. Zhang, D. Lovley and T. P. Russell, *Sustain. Energy Fuels*, 2017, **1**, 1171–1176.
59 L. Jourdin, T. Grieger, J. Monetti, V. Flexer, S. Freguia, Y. Lu, J. Chen, M. Romano, G. G. Wallace and J. Keller, *Environ. Sci. Technol.*, 2015, **49**, 13566–13574.
60 X. Wu, R. Altman, M. A. Eiteman and E. Altman, *Appl. Environ. Microbiol.*, 2014, **80**, 2880–2888.
61 A. J. Abel, J. M. Hilzinger, A. P. Arkin and D. S. Clark, *Bioelectrochemistry*, 2022,

108054.
62 A. P. Malanoski, B. Lin, B. J. Eddie, Z. Wang, W. J. Hervey and S. M. Glaven, *Microb. Biotechnol.*, 2018, **11**, 98–111.
63 B. J. Eddie, Z. Wang, W. J. Hervey, D. H. Leary, A. P. Malanoski, L. M. Tender, B. Lin and S. M. Strycharz-Glaven, *mSystems*, , DOI:10.1128/mSystems.00002-17.
64 X. Deng, N. Dohmae, K. H. Nealson, K. Hashimoto and A. Okamoto, *Sci. Adv.*, , DOI:10.1126/sciadv.aao5682.
65 J. E. Reiner, K. Geiger, M. Hackbarth, M. Fink, C. J. Lapp, T. Jung, A. Dötsch, M. Hügler, M. Wagner, A. Hille-Reichel, W. Wilcke, S. Kerzenmacher, H. Horn and J. Gescher, *ISME J.*, 2020, **14**, 1125–1140.
66 P. T. Ha, S. R. Lindemann, L. Shi, A. C. Dohnalkova, J. K. Fredrickson, M. T. Madigan and H. Beyenal, *Nat. Commun.*, 2017, **8**, 1–7.
67 T. Ueki, K. P. Nevin, T. L. Woodard, M. A. Aklujkar, D. E. Holmes and D. R. Lovley, *Front. Microbiol.*, 2018, **9**, 1512.
68 P. L. Tremblay, M. Aklujkar, C. Leang, K. P. Nevin and D. Lovley, *Environ. Microbiol. Rep.*, 2012, **4**, 82–88.
69 S. Gleizer, R. Ben-Nissan, Y. M. Bar-On, N. Antonovsky, E. Noor, Y. Zohar, G. Jona, E. Krieger, M. Shamshoum, A. Bar-Even and R. Milo, *Cell*, 2019, **179**, 1255-1263.e12.
70 A. I. Flamholz, E. Dugan, C. Blikstad, S. Gleizer, R. Ben-Nissan, S. Amram, N. Antonovsky, S. Ravishankar, E. Noor, A. Bar-Even, R. Milo and D. F. Savage, *Elife*, , DOI:10.7554/eLife.59882.
71 T. Gassler, M. Sauer, B. Gasser, M. Egermeier, C. Troyer, T. Causon, S. Hann, D. Mattanovich and M. G. Steiger, *Nat. Biotechnol.*, 2020, **38**, 210–216.
72 T. Zhang, X. C. Shi, R. Ding, K. Xu and P. L. Tremblay, *ISME J.*, 2020, **14**, 2078–2089.
73 A. Bar-Even, E. Noor, A. Flamholz and R. Milo, *Biochim. Biophys. Acta - Bioenerg.*, 2013, **1827**, 1039–1047.
74 I. Sánchez-Andrea, I. A. Guedes, B. Hornung, S. Boeren, C. Lawson, D. Z. Sousa, A. Bar-Even, N. J. Claassens and A. J. Stams, *Nat. Commun.*, 2020, 1–12.
75 S. Kim, S. N. Lindner, S. Aslan, O. Yishai, S. Wenk, K. Schann and A. Bar-Even, *Nat. Chem. Biol.*, 2020, **16**, 538–545.
76 N. J. Claassens, G. Bordanaba-Florit, C. A. R. Cotton, A. De Maria, M. Finger-Bou, L. Friedeheim, N. Giner-Laguarda, M. Munar-Palmer, W. Newell, G. Scarinci, J. Verbunt, S. T. de Vries, S. Yilmaz and A. Bar-Even, *Metab. Eng.*, 2020, **62**, 30–41.
77 H. M. Jensen, A. E. Albers, K. R. Malley, Y. Y. Londer, B. E. Cohen, B. A. Helms, P. Weigele, J. T. Groves and C. M. Ajo-Franklin, *Proc. Natl. Acad. Sci.*, 2010, **107**, 19213–19218.
78 H. M. Jensen, M. A. TerAvest, M. G. Kokish and C. M. Ajo-Franklin, *ACS Synth. Biol.*, 2016, **5**, 679–688.
79 D. Coursolle and J. A. Gralnick, *Mol. Microbiol.*, 2010, **77**, 995–1008.
80 C. Bi, P. Su, J. Müller, Y. Yeh, S. R. Chhabra, H. R. Beller, S. W. Singer and N. J. Hillson, *Microb. Cell Fact.*, 2013, **12**, 1–10.
81 T. O. Ranaivoarisoa, R. Singh, K. Rengasamy, M. S. Guzman and A. Bose, *J. Ind. Microbiol. Biotechnol.*, 2019, **46**, 1401–1417.
82 W. Bai, T. O. Ranaivoarisoa, R. Singh, K. Rengasamy and A. Bose, *bioRxiv*, , DOI:10.1101/2020.10.13.336636.
83 M. Böhm, T. Hurek and B. Reinhold-Hurek, *Mol. Plant-Microbe Interact.*, 2007, **20**, 526–

533.
84 A. R. Rowe, S. Xu, E. Gardel, A. Bose, P. Girguis, J. P. Amend and M. Y. El-Naggar, *MBio*, 2019, **10**, 1659–1677.
85 I. Hamdallah, N. Torok, K. M. Bischof, N. Majdalani, S. Chadalavada, N. Mdluli, K. E. Creamer, M. Clark, C. Holdener, P. J. Basting, S. Gottesman and J. L. Slonczewski, *Appl. Environ. Microbiol.*, , DOI:10.1128/AEM.00520-18.

Chapter 5: Charting a narrow course for direct electron uptake-facilitated electromicrobial production[†]

5.1 Abstract

In the preceding chapter, I analyzed which physiological modules could enable the highest productivity in electromicrobial production (EMP) systems relying on direct electron uptake, and I described a phylogenetics-based pipeline for discovering microbes that are capable of electroautotrophic growth. However, fundamental questions about the performance limits and viability of this strategy remain unanswered. Here, I sought to determine what would be necessary for such a system to compete with alternative sustainable production technologies based on H_2-mediated EMP (the highest-performing mediated strategy from Chapter 2) and traditional bioprocessing with crop feedstocks. Using global warming potential as the metric for comparison, I show that each EMP process can outperform sugarcane-based sucrose production. Following a stoichiometric and energetic analysis, direct electron uptake-based EMP would need to achieve a current density >48 mA/cm^2 to reach parity with the H_2-mediated system. Because this is currently only practical with a gas diffusion electrode (GDE) architecture, I developed a physical model of the proposed bio-GDE and used it to determine the conditions that a microbial catalyst would experience in a reactor. My analysis demonstrates that unavoidable inefficiencies in the reactor (e.g., kinetic overpotentials and Ohmic losses) require additional energy input, increasing the breakeven current density to ~91 mA/cm^2. At this current density, the microbial catalyst would need to withstand a pH >10.4 and a total salinity >18.8%. Because currently-known electroautotrophs are not adapted to such extreme conditions, I discuss potential improvements to reactor design that may alleviate these challenges, and consider the implications these results have on the engineerability and feasibility of direct electron uptake-based EMP.

5.2 Introduction

Electromicrobial production (EMP) has received significant attention as a sustainable alternative to fossil fuel-based commodity chemical production.[1–5] In this strategy, electricity or electrochemically-derived mediator molecules act as the primary energy source for microbial transformation of CO_2 into value-added products. EMP processes encompass a wide variety of systems based on both mediated and direct transfer of reducing power to microorganisms. In mediated systems, an electrochemically-reduced molecule, such as hydrogen (H_2), carbon monoxide (CO), or formate ($HCOO^-$) is fed to microbes as an energy source driving microbial growth and product formation.[6–9] In direct systems, electrons are passed directly into cellular energy pools (*e.g.*, the quinone pool or NADH pool) by electron conduit proteins that traverse the cell wall and/or outer membrane and make direct electrical contact with the cathode.[10–12]

[†]This chapter was originally submitted as a preprint to *bioRxiv* and has been adapted with permission from the coauthors

This latter strategy, direct electron uptake-based EMP (dEMP), has generated significant excitement because it avoids relying on transfer of sparingly soluble gases (H_2, CO) into liquid phases for microbial growth. Moreover, by transferring electrons directly through conductive proteins, it may obviate expensive and rare catalyst materials that are typically used in abiotic electrochemistry.

Despite this excitement, progress towards practical dEMP systems has remained limited. The original systems relied on acetogens[13] and methanogens[14] to fix CO_2, although it was later determined that much, if not all, of the reducing power supplied to these organisms was mediated by electrochemical H_2 generation.[15,16] Recently, direct electron transfer mechanisms in some methanogens have been confirmed,[17] but a crucial feature of acetogens and methanogens is that a large fraction of the fixed carbon is diverted to acetate or methane as a consequence of their metabolism.[18,19] Hence, even if genetic tools are rapidly developed for these organisms, high selectivity towards an arbitrary product in a single reactor is unlikely.

Product spectrum and selectivity problems may be addressed by recent discoveries of a significant number of alternative electroautotrophs.[20–23] Perhaps most notably, Bose and coworkers have engineered *Rhodopseudomonas palustris* to produce the bioplastic *poly*-hydroxybutyrate[24] and the biofuel *n*-butanol[25] during cathode-associated growth. In addition, Abel and Hilzinger *et al.* have recently developed a phylogenetic-driven discovery pipeline for putative electroautotrophs, which identified >70 potential electroautotrophic organisms.[23]

Proteins involved in extracellular electron transfer are also increasingly well-characterized,[10,26] suggesting that strategies to engineer electroautotrophy in suitable microbial chassis may be possible in the near future. However, known and characterized electron conduits are not exhaustive of the myriad ecological mechanisms for electron transfer.[10,11,26] For example, the most well-studied electron conduits (*e.g.*, the Mtr proteins in *Shewanella* spp.) interface with the quinone pool in the inner membrane.[27–29] Electron uptake based on this mechanism cannot support acetogenesis-, methanogenesis-, and sulfate reduction-based metabolisms because these terminal electron acceptors are thermodynamically uphill of the quinone pool. This suggests that these organisms use some strategy for direct electron uptake that interfaces directly with the NAD^+/NADH pool, a hypothesis that is supported by the redox potential of electron uptake in these organisms,[17,30] although the specific mechanisms remain unclear.

Recently, uncertainty has grown about the promise of dEMP.[31,32] Mediated systems continue to make gains in scale-up,[33–35] product spectrum diversity,[36–38] and process modelling;[9,39] they rely on well-characterized metabolic pathways (*i.e.*, those of Knallgas, formatotrophic, or aceto-/methanogenic microbes); and, in the case of H_2- and CO-mediated systems, they avoid challenges associated with incompatible electrolyte/medium requirements by transferring reducing power through the gas phase.[40] Moreover, questions about the pH and salt tolerance, in addition to the productive capacity of cathodic biofilms, have also raised serious questions about the viability of dEMP.[31,32,41]

Here, I take a systematic approach to determine the feasibility of dEMP processes. I use a life cycle assessment (LCA) framework to quantify the carbon footprint (global warming potential) of this process in comparison to a well-established alternative EMP strategy, H_2-mediated

production, and a legacy process, sugarcane growth. I follow the LCA standards set by ISO 14040[42] and 14044[43] to quantify greenhouse gasses (in kg CO_2-equivalents) emitted during the production of all materials and the generation of all energy necessary for a given process. I use sucrose as an example product in this analysis for three reasons. First, sucrose has a well-defined and portable secretion mechanism,[36,44] which is necessary for direct electron uptake-based systems since microbes are immobilized on the cathode surface. Second, sucrose is a useful substrate for downstream production of a wide variety of biomolecules via workhorse heterotrophic microbes such as *E. coli* and *S. cerevisiae*. Third, sucrose production from traditional crops (*e.g.*, sugarcane) has well-defined life cycle impacts,[45] which provides a solid benchmark for comparison with the EMP processes modeled here.

Based on a stoichiometric and energetic approach, I first calculated the metabolic efficiency of carbon fixation to sucrose relying on direct electron uptake. I considered electron uptake into the quinone pool or the NAD^+/NADH pool, five different carbon fixation pathways, and four different terminal electron acceptors (Fig. 5.1a). Next, I developed a process model for the EMP scheme that, together with energy demand calculations, enabled me to calculate the global warming potential (GWP) associated with sucrose production for the direct electron uptake-based system (Fig. 5.1b). This analysis demonstrated that electron uptake into the NADH pool coupled to carbon fixation with the reductive glycine pathway and O_2 reduction as the terminal electron acceptor could result in the lowest GWP but needs to achieve a current density >48 mA/cm^2 (>88 mA/cm^2 when electrons are deposited into the QH_2 pool) to reach parity with H_2-mediated sucrose production with Knallgas bacteria.

Because the previous analyses (Chapters 3 and 4) showed that O_2 and CO_2 gas-liquid mass transfer prevents current densities >~20 mA/cm^2 in standard EMP reactors,[9,23] I developed a multiphysics model of a gas diffusion electrode (GDE) architecture that enables an extremely high interfacial area between the gas and liquid phases, overcoming the mass transfer limits of standard direct electron transfer-based EMP reactor designs (Fig. 5.1c). I then used this model to calculate both the electrochemical kinetics- and transport-associated inefficiencies inherent to the direct electron uptake system as well as relevant operating conditions (pH and salinity) that microbes would experience in such a reactor.

The additional energy needed to overcome reactor inefficiency increases the current density necessary to break even with an H_2-mediated system from ~48 mA/cm^2 to ~91 mA/cm^2. At this current density, the microbial catalyst within the bio-GDE would experience an average pH of ~10.45 and an average salinity of ~18.8%. Although some microbes exist that can tolerate such extreme conditions, enabling electroautotrophy would require complex metabolic rewiring in organisms with limited genetic tractability, and engineering extreme pH and salinity tolerance into currently-known electroactive microbes may also prove challenging. I therefore evaluate reactor improvements that could alleviate pH and salinity extremes experienced by the microbe. In contrast to the substantial hurdles facing dEMP systems, H_2-mediated sucrose production has been demonstrated already (albeit at a modest carbon efficiency),[36] and strategies to enhance the product yield can rely on insight gained from decades of equivalent study in cyanobacteria.[44] Hence, this comprehensive analysis charts a narrow course for the viability of dEMP systems.

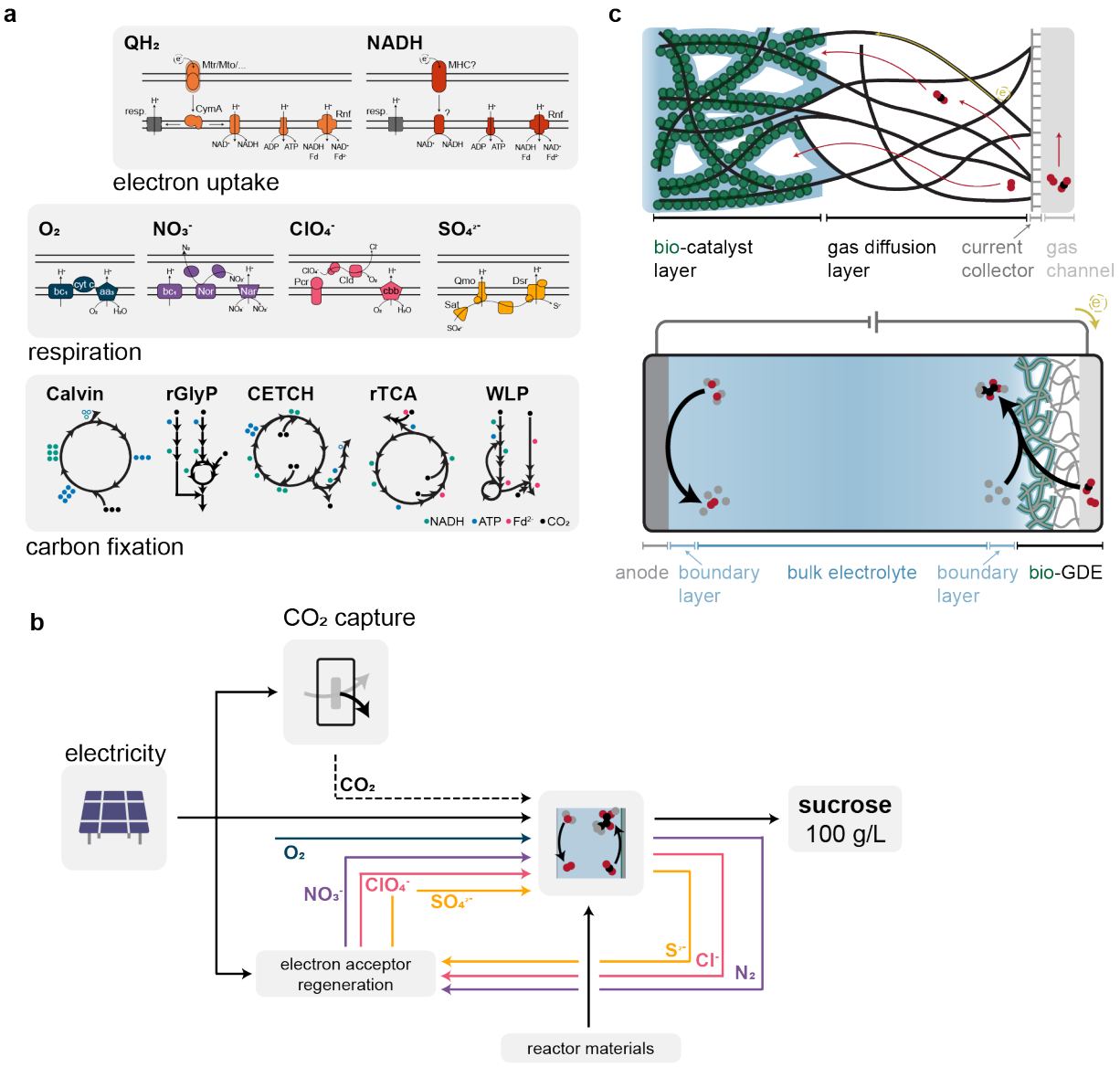

Figure 5.1. Overview of direct electron uptake-based metabolism and processes. (**a**) The three metabolic modules (electron uptake, respiration, and carbon fixation) necessary to support electroautotrophic growth and biochemical production. NADH, ATP, and ferredoxin (Fd^{2-}) demands for each carbon fixation pathway are shown for pyruvate as the end product. (**b**) Schematic of the modeled electromicrobial production process. (**c**) Diagram of the modeled gas diffusion bioelectrode (bio-GDE) and the CO_2-electrolyzer using a bio-GDE to fix carbon. Distances in (**c**) are not to scale.

5.3 Computational Methods

Stoichiometry and energetic analysis of electroautotrophic metabolisms
Carbon fixation pathways
Different carbon fixation pathways (CFPs) generate different molecules as the primary product; I normalized each CFP to pyruvate as a common molecular intermediate, resulting in

Calvin cycle:[18,46]

$$3CO_2 + 5NADH + 7ATP + 4H^+ \rightarrow C_3H_3O_3^- + 5NAD^+ + 7(ADP + P_i) + 3H_2O \quad (88)$$

Reductive tricarboxylic acid (rTCA) cycle:[18,46]

$$3CO_2 + 3NADH + 2ATP + 2Fd^{2-} + 6H^+ \rightarrow C_3H_3O_3^- + 3NAD^+ + 2(ADP + P_i) + 2Fd + 3H_2O \quad (89)$$

Reductive glycine pathway (rGlyP):[47,48]

$$3CO_2 + 5NADH + 2ATP + 4H^+ \rightarrow C_3H_3O_3^- + 5NAD^+ + 2(ADP + P_i) + 3H_2O \quad (90)$$

Crotonyl-CoA/ethylmalonyl-CoA/hydroxybutyryl-CoA (CETCH) cycle:[49]

$$3CO_2 + 7NADH + 4ATP + 2FAD + 6H^+ \rightarrow C_3H_3O_3^- + 7NAD^+ + 2FADH_2 + 4(ADP + P_i) + 3H_2O \quad (91)$$

Wood-Ljungdahl pathway (WLP):[18,46]

$$3CO_2 + 2NADH + 1ATP + 3Fd^{2-} + 7H^+ \rightarrow C_3H_3O_3^- + 2NAD^+ + 1(ADP + P_i) + 3Fd + 3H_2O \quad (92)$$

Sucrose production
Sucrose is generated by the conversion of primary products from CFPs via gluconeogenesis. Using pyruvate as a basis,

$$4C_3H_3O_3^- + 4NADH + 13ATP + 8H^+ \rightarrow C_{12}H_{22}O_{11} + 4NAD^+ + 13(ADP + P_i) + 1H_2O \quad (93)$$

Note that here I have assumed ATP, GTP, and UTP are interchangeable.

Direct electron uptake
I consider two potential mechanisms by which electrons are transferred from the cathode into energy carrier pools in the cell. In the first, based on the MtrCAB/CctA/CymA conduit from *Shewanella oneidensis*,[27–29] electrons are transferred into the quinone pool according to

$$Q + 2H_{in}^+ + 2e^- \rightarrow QH_2 \quad (94)$$

Most characterized mechanisms for electron uptake rely on the quinone pool as an electron sink.[10,21] Still, some sulfate-reducing microbes (SRMs),[11] methanogens,[17,50] and acetogens[16] may be able to grow on electrons directly without H_2 (or an equivalent) as a mediator. This metabolism would not be thermodynamically possible if electrons were deposited into the quinone pool:

quinone oxidation cannot drive proton motive force generation with sulfate as the terminal electron acceptor and energy conservation in acetogens and methanogens requires direct NADH generation. Therefore, these bacteria must rely on some mechanism for electron uptake that follows the net reaction

$$NAD^+ + H^+_{in} + 2e^- \rightarrow NADH \quad (95)$$

These reactions require electrons at different potentials. For electron uptake into the quinone pool, I assume electrons are supplied at -100 mV *vs.* SHE because this is roughly the midpoint redox potential of MtrC[51] and is sufficiently electropositive to reduce the quinone pool (midpoint redox potential of >-80 mV *vs.* SHE). Following a similar strategy, I use -350 mV *vs.* SHE for electrons deposited into the NAD^+/NADH pool because the midpoint redox potential is ~-320 mV *vs.* SHE, and because -350 mV represents a rough average of the range of putative electron uptake mechanisms linked to SRMs and methanogens.[11,17]

Energy carrier regeneration

When electrons are deposited into the quinone pool, NADH is (re)generated by reverse operation of complex I in the electron transport chain (ETC):

$$NAD^+ + 4H^+_{out} + QH_2 \rightarrow NADH + 5H^+_{in} + Q \quad (96)$$

ATP is (re)generated by the action of ATP synthase according to

$$ADP + P_i + 3H^+_{out} \rightarrow ATP + 3H^+_{in} \quad (97)$$

I use the stoichiometry of the Rnf complex in, for example, *Clostridium ljungdahlii* to calculate ferredoxin regeneration:[19,52]

$$Fd + NADH + 2H^+_{out} \rightarrow Fd^{2-} + NAD^+ + 3H^+_{in} \quad (98)$$

Respiration

O_2 as the terminal electron acceptor

In the case where electrons taken up from the cathode are deposited into the quinone pool, complex III in the ETC releases 4 protons into the periplasmic space and liberates two electrons for later O_2 reduction according to

$$QH_2 + 2H^+_{in} \rightarrow Q + 4H^+_{out} + 2e^- \quad (99)$$

The two liberated electrons are transported by *c*-type cytochromes to ETC complex IV, transporting two additional protons across the inner membrane:

$$\frac{1}{2}O_2 + 4H^+_{in} + 2e^- \rightarrow H_2O + 2H^+_{out} \quad (100)$$

Hence, the overall reaction for quinol oxidation coupled to O_2 reduction is written as

$$QH_2 + \frac{1}{2}O_2 + 6H^+_{in} \rightarrow Q + H_2O + 6H^+_{out} \quad (101)$$

When electrons are deposited into the NADH pool, I use the standard description of oxidative phosphorylation assuming a P/O ratio of 3 (*i.e.,* assuming the best-possible energy conservation):

$$NADH + H^+_{in} + \frac{1}{2}O_2 + 3ADP + 3P_i \rightarrow NAD^+ + H_2O + 3ATP \quad (102)$$

NO_3^- as the terminal electron acceptor
Nitrate is reduced first to nitrite by quinol oxidation via the NarGHI complex:[53,54]

$$NO_3^- + 2H^+_{in} + QH_2 \rightarrow NO_2^- + H_2O + 2H^+_{out} + Q \quad (103)$$

Quinol is also oxidized to liberate electrons necessary for reducing nitrite all the way to N_2 following

$$\begin{gathered} 1.5QH_2 + 3H^+_{in} \rightarrow 1.5Q + 6H^+_{out} + 3e^- \\ NO_2^- + 2H^+_{out} + e^- \rightarrow NO + H_2O \\ NO + H^+_{out} + e^- \rightarrow \frac{1}{2}N_2O + \frac{1}{2}H_2O \\ \frac{1}{2}N_2O + H^+_{out} + e^- \rightarrow \frac{1}{2}N_2 + \frac{1}{2}H_2O \end{gathered} \quad (104)$$

Partial denitrification (*e.g.*, to nitrite) is also possible, but I neglect this possibility for two reasons related to the resulting build-up of the denitrification product. First, high nitrite concentration is typically toxic to cells.[55] Second, build-up of nitrite or other soluble terminal electron acceptors can negatively affect the thermodynamics of the terminal electron acceptor process. Hence, the overall reaction for quinol oxidation coupled to complete denitrification from nitrate is given by

$$2.5QH_2 + NO_3^- + 5H^+_{in} \rightarrow 2.5Q + 0.5N_2 + 3H_2O + 4H^+_{out} \quad (105)$$

When electrons taken up from the cathode are deposited into the NAD^+/NADH pool, complex I in the ETC transfers electrons from NADH into the quinone pool, written as

$$NADH + 5H^+_{in} + Q \rightarrow NAD^+ + 4H^+_{out} + QH_2 \quad (106)$$

Hence, the overall proton motive force-generating reaction associated with NO_3^- reduction in this case is given by

$$2.5NADH + NO_3^- + 17.5H^+_{in} \rightarrow 2.5\ NAD^+ + 0.5N_2 + 3H_2O + 14H^+_{out} \quad (107)$$

ClO_4^- as the terminal electron acceptor
Perchlorate is first reduced to chlorite by the action of PcrQ/O/C/B/A according to[56,57]

$$2QH_2 + ClO_4^- \rightarrow 2Q + 2H_2O + ClO_2^- \quad (108)$$

Chlorite dismutase splits ClO_2^- into Cl^- and O_2 without energy conservation. The O_2 is then reduced by complex IV of the ETC,

$$O_2 + 8H_{in}^+ + 4e^- \rightarrow 2H_2O + 4H_{out}^+ \quad (109)$$

using electrons liberated by the oxidation of two extra quinols in complex III of the ETC:

$$2QH_2 + 4H_{in}^+ \rightarrow 2Q + 8H_{out}^+ + 4e^- \quad (110)$$

Hence, the overall reaction for quinol oxidation coupled to perchlorate reduction is given by

$$4QH_2 + ClO_4^- + 12H_{in}^+ \rightarrow 4Q + Cl^- + 4H_2O + 12H_{out}^+ \quad (111)$$

When electrons from the cathode are deposited into the NAD^+/NADH pool, complex I in the ETC transfers electrons from NADH into the quinone pool, written as

$$NADH + 5H_{in}^+ + Q \rightarrow NAD^+ + 4H_{out}^+ + QH_2 \quad (112)$$

The remainder of the respiratory system is the same as written above, resulting in an overall reaction given by

$$4NADH + ClO_4^- + 32H_{in}^+ \rightarrow 4NAD^+ + Cl^- + 4H_2O + 28H_{out}^+ \quad (113)$$

SO_4^- as the terminal electron acceptor

Electrons taken up from a cathode that are deposited into the quinone pool cannot be used to generate a proton motive force when quinol oxidation is coupled to sulfate reduction because the quinone pool (~-80 mV *vs.* SHE) is more electronegative than the SO_4^{2-}/H_2S redox couple (~-220 mV *vs.* SHE). Hence, carbon fixation can only proceed in this case with electrons deposited into the NAD^+/NADH pool. Sulfate reduction begins by the activation of sulfate with ATP forming adenylyl sulfate (APS):[58–60]

$$SO_4^{2-} + ATP + 2H^+ \rightarrow APS + PP_i \quad (114)$$

Pyrophosphate (PP_i) is hydrolyzed to regenerated phosphate according to

$$PP_i + H_2O \rightarrow 2P_i \quad (115)$$

APS reduction to sulfite is coupled to quinol oxidation, resulting in

$$APS + QH_2 \rightarrow HSO_3^- + AMP + H_{out}^+ \quad (116)$$

Finally, sulfite is converted to sulfide via a two-step process involving the formation of a trisulfide bond with the protein DsrC with the supply of 4 electrons from the quinone pool and additional

two electrons from a cytoplasmic source I assume is NADH.[59] The overall reaction for sulfate reduction is then given by

$$\mathrm{SO_4^{2-} + ATP + 3QH_2 + NADH + 2H_{in}^+ \rightarrow S^{2-} + AMP + 2P_i + 2Q + NAD^+ + 3H_2O + 3H_{out}^+} \quad (117)$$

I assume complex I of the ETC forms reduced quinol from NADH,

$$\mathrm{NADH + 5H_{in}^+ + Q \rightarrow NAD^+ + 4H_{out}^+ + QH_2} \quad (118)$$

Then, the overall reaction for sulfate reduction is written as

$$\mathrm{4NADH + SO_4^{2-} + ATP + 17H_{in}^+ \rightarrow 4NAD^+ + S^{2-} + AMP + 2P_i + 3H_2O + 15H_{out}^+} \quad (119)$$

Assuming AMP reacts with a second ATP to generate two ADP, both of which are regenerated to ATP, I rewrite the overall reaction for sulfate reduction as

$$\mathrm{4NADH + SO_4^{2-} + 11H_{in}^+ \rightarrow 4NAD^+ + S^{2-} + 3H_2O + 9H_{out}^+} \quad (120)$$

Overall stoichiometry

The preceding analysis allows me to derive the overall stoichiometry of electron-driven CO_2-fixation to sucrose for each carbon-fixation pathway (Calvin, rTCA, rGlyP, CETCH, WLP), electron sink (quinone pool, NADH pool), and terminal electron acceptor (O_2, NO_3^-, ClO_4^-, SO_4^{2-}), summarized below.

Calvin cycle

$\underline{QH_2 \text{ pool, } O_2}$

$$\mathrm{12CO_2 + 121e^- + 18.25O_2 + 121H^+ \rightarrow C_{12}H_{22}O_{11} + 49.5H_2O} \quad (121)$$

$\underline{NADH \text{ pool, } O_2}$

$$\mathrm{12CO_2 + 75.33e^- + 6.83O_2 + 75.33H^+ \rightarrow C_{12}H_{22}O_{11} + 26.66H_2O} \quad (122)$$

$\underline{QH_2 \text{ pool, } NO_3^-}$

$$\mathrm{12CO_2 + 321.75e^- + 54.75NO_3^- + 376.5H^+ \rightarrow C_{12}H_{22}O_{11} + 23.375N_2 + 177.25H_2O} \quad (123)$$

$\underline{NADH \text{ pool, } NO_3^-}$

$$\mathrm{12CO_2 + 91.93e^- + 8.79NO_3^- + 100.72H^+ \rightarrow C_{12}H_{22}O_{11} + 4.395N_2 + 39.37H_2O} \quad (124)$$

$\underline{QH_2 \text{ pool, } ClO_4^-}$

$$12CO_2 + 194e^- + 18.25ClO_4^- + 194H^+ \rightarrow C_{12}H_{22}O_{11} + 18.25Cl^- + 86H_2O \quad (125)$$

NADH pool, ClO_4^-

$$12CO_2 + 83.14e^- + 4.39ClO_4^- + 83.14H^+ \rightarrow C_{12}H_{22}O_{11} + 4.39Cl^- + 30.56H_2O \quad (126)$$

NADH pool, SO_4^{2-}

$$12CO_2 + 157.33e^- + 13.66SO_4^{2-} + 157.33H^+ \rightarrow C_{12}H_{22}O_{11} + 13.66S^{2-} + 67.64H_2O \quad (127)$$

---

rTCA cycle

QH_2 pool, NO_3^-

$$12CO_2 + 266.76e^- + 43.75NO_3^- + 310.5H^+ \rightarrow C_{12}H_{22}O_{11} + 21.875N_2 + 144.25H_2O \quad (128)$$

NADH pool, NO_3^-

$$12CO_2 + 76.21e^- + 5.64NO_3^- + 81.84H^+ \rightarrow C_{12}H_{22}O_{11} + 2.82N_2 + 29.92H_2O \quad (129)$$

QH_2 pool, ClO_4^-

$$12CO_2 + 164.66e^- + 14.58ClO_4^- + 164.66H^+ \rightarrow C_{12}H_{22}O_{11} + 14.58Cl^- + 71.32H_2O \quad (130)$$

NADH pool, ClO_4^-

$$12CO_2 + 70.57e^- + 2.82ClO_4^- + 70.57H^+ \rightarrow C_{12}H_{22}O_{11} + 2.82Cl^- + 24.28H_2O \quad (131)$$

NADH pool, SO_4^{2-}

$$12CO_2 + 118.22e^- + 8.78SO_4^{2-} + 118.22H^+ \rightarrow C_{12}H_{22}O_{11} + 8.78S^{2-} + 48.12H_2O \quad (132)$$

---

rGlyP

QH_2 pool, O_2

$$12CO_2 + 101e^- + 13.25O_2 + 101H^+ \rightarrow C_{12}H_{22}O_{11} + 39.5H_2O \quad (133)$$

NADH pool, O_2

$$12CO_2 + 62e^- + 3.5O_2 + 62H^+ \rightarrow C_{12}H_{22}O_{11} + 20H_2O \quad (134)$$

QH_2 pool, NO_3^-

$$12CO_2 + 246.75e^- + 39.75NO_3^- + 286.5H^+ \rightarrow C_{12}H_{22}O_{11} + 19.875N_2 + 132.25H_2O \quad (135)$$

NADH pool, NO_3^-

$$12CO_2 + 70.5e^- + 4.5NO_3^- + 75H^+ \rightarrow C_{12}H_{22}O_{11} + 2.25N_2 + 26.5H_2O \quad (136)$$

QH_2 pool, ClO_4^-

$$12CO_2 + 154e^- + 13.25ClO_4^- + 154H^+ \rightarrow C_{12}H_{22}O_{11} + 13.25Cl^- + 66H_2O \quad (137)$$

NADH pool, ClO_4^-

$$12CO_2 + 66e^- + 2.25ClO_4^- + 66H^+ \rightarrow C_{12}H_{22}O_{11} + 2.25Cl^- + 22H_2O \quad (138)$$

NADH pool, SO_4^{2-}

$$12CO_2 + 104e^- + 7SO_4^{2-} + 104H^+ \rightarrow C_{12}H_{22}O_{11} + 7S^{2-} + 41H_2O \quad (139)$$

CETCH cycle

QH_2 pool, O_2

$$12CO_2 + 119.66e^- + 17.92O_2 + 119.66H^+ \rightarrow C_{12}H_{22}O_{11} + 48.84H_2O \quad (140)$$

NADH pool, O_2

$$12CO_2 + 72.66e^- + 6.17O_2 + 72.66H^+ \rightarrow C_{12}H_{22}O_{11} + 25.33H_2O \quad (141)$$

QH_2 pool, NO_3^-

$$12CO_2 + 316.75e^- + 53.75NO_3^- + 370.5H^+ \rightarrow C_{12}H_{22}O_{11} + 26.875N_2 + 174.25H_2O \quad (142)$$

NADH pool, NO_3^-

$$12CO_2 + 90.5e^- + 8.5NO_3^- + 99H^+ \rightarrow C_{12}H_{22}O_{11} + 4.25N_2 + 38.5H_2O \quad (143)$$

QH_2 pool, ClO_4^-

$$12CO_2 + 191.33e^- + 17.92ClO_4^- + 191.33H^+ \rightarrow C_{12}H_{22}O_{11} + 17.92Cl^- + 84.67H_2O \quad (144)$$

NADH pool, ClO_4^-

$$12CO_2 + 82e^- + 4.25ClO_4^- + 82H^+ \rightarrow C_{12}H_{22}O_{11} + 4.25Cl^- + 30H_2O \quad (145)$$

NADH pool, SO_4^{2-}

$$12CO_2 + 141.33e^- + 9.67SO_4^{2-} + 141.33H^+ + 8FAD \rightarrow C_{12}H_{22}O_{11} + 9.67S^{2-} + 51.68H_2O + 8FADH_2 \quad (146)$$

WLP

QH_2 pool, NO_3^-

$$12CO_2 + 261.75e^- + 42.75NO_3^- + 304.5H^+ \rightarrow C_{12}H_{22}O_{11} + 21.375N_2 + 141.25H_2O \quad (147)$$

NADH pool, NO_3^-

$$12CO_2 + 74.78e^- + 5.36NO_3^- + 80.14H^+ \rightarrow C_{12}H_{22}O_{11} + 2.68N_2 + 29.07H_2O \quad (148)$$

QH_2 pool, ClO_4^-

$$12CO_2 + 162e^- + 14.25ClO_4^- + 162H^+ \rightarrow C_{12}H_{22}O_{11} + 14.25Cl^- + 70H_2O \quad (149)$$

NADH pool, ClO_4^-

$$12CO_2 + 69.43e^- + 2.68ClO_4^- + 69.43H^+ \rightarrow C_{12}H_{22}O_{11} + 2.68Cl^- + 23.72H_2O \quad (150)$$

NADH pool, SO_4^{2-}

$$12CO_2 + 114.66e^- + 8.33SO_4^{2-} + 114.66H^+ \rightarrow C_{12}H_{22}O_{11} + 8.33S^{2-} + 46.33H_2O \quad (151)$$

Energy demand and efficiency calculations

Prior to a more detailed modeling assessment (see section below), preliminary energy demand and efficiency calculations (Table 5.1) can be determined directly from the stoichiometry. The energy demand e is given by

$$e_k = \frac{n_{e,k} F \Delta V_{0,k}}{M_S} \quad (152)$$

where $n_{e,k}$ is the electron demand per sucrose, F is Faraday's constant, $\Delta V_{0,k}$ is the voltage difference between the anode reaction (water oxidation) and cathode reaction (electron deposition into the quinone pool or NADH pool), and M_S is the molar mass of sucrose for a given physiological mechanism for electron uptake and carbon fixation (k). When electrons are deposited into the quinone pool, $\Delta V_0 = 0.918$ V corresponding to the difference between the redox potential of water oxidation (818 mV *vs.* SHE) and electron deposition into electron conduit proteins that interface with the quinone pool (~-100 mV *vs.* SHE). Similarly, $\Delta V_0 = 1.168$ V when electrons are deposited into the NADH pool following the assumption that the electron conduit must accept electrons at a voltage of ~-350 mV *vs.* SHE to reduce NAD^+ directly (see eq. 8). The full electrochemical model (see below) accounts for overpotentials associated with electron and chemical species transport and electrochemical kinetics; the energy demand is modified to include these by exchanging ΔV_0 with the ΔV calculated by the model.

Efficiency is calculated straightforwardly from the combustion energy of sucrose and the energy demand following the method of Claassens *et al.*:[41]

$$\eta_k = \frac{\Delta H^\circ}{M_S e_k} \quad (153)$$

Sucrose production from H_2

I rely on the previously described (see Chapter 2) framework for analyzing the production of sucrose from aerobic autotrophic growth on H_2.[5] H_2 is first oxidized to H^+ by soluble and membrane-bound hydrogenases, resulting in

$$H_2 + NAD^+ \rightarrow NADH + H^+ \quad (154)$$

I use the Calvin cycle for carbon fixation and O_2 as the terminal electron acceptor. Following my previous analysis of electromicrobial production system (see Chapter 2),[5] I assume the P/O ratio is 2.5 here. Hence, the overall reaction for sucrose production from H_2 is given by

$$12CO_2 + 40.4H_2 + 8.2O_2 \rightarrow C_{12}H_{22}O_{11} + 29.4H_2O \tag{155}$$

Life Cycle Impact Assessment

ISO standards 14040 and 14044 were used as guides for the life cycle impact assessments.[42,43] Unless otherwise stated, background life cycle inventories were obtained from the Product Environmental Footprints dataset.[61] Global warming potentials are calculated using the IPCC 2013 100-year model.[62] The functional unit is 1 kg of sucrose at a titer of 100 g/L. The analysis is cradle-to-gate, ending with an unpurified 100 g/L solution of sucrose. However, biologically-sequestered carbon does not count as "negative" emissions at the 100-year time scale. As an example, the overall global warming potential (C_k) of the bio-GDE system is given by

$$C_k = e_k c_{\mathrm{P}} + n_{\mathrm{CO_2}} \frac{M_{\mathrm{CO_2}}}{M_{\mathrm{S}}} c_{\mathrm{DAC}} + n_{\mathrm{TEA},k} \frac{M_{\mathrm{TEA},k}}{M_{\mathrm{S}}} c_{\mathrm{TEA}} + a_{\mathrm{E},k} \ddot{c}_{\mathrm{E}} \tag{156}$$

where c_{P}, c_{DAC}, and c_{TEA} are the carbon footprints of power generation, direct air capture of CO_2, and terminal electron acceptor, respectively; $n_{\mathrm{CO_2}}$ and n_{TEA} are the demands of CO_2 and the terminal electron acceptor per sucrose molecule from stoichiometry; $a_{\mathrm{E},k}$ is the effective area of electrolyzer necessary to produce a unit of product, given by

$$a_{\mathrm{E},k} = \frac{1}{M_{\mathrm{S}} \gamma t} \left(\frac{n_{\mathrm{e},k} F}{i} \right) \tag{157}$$

and $\ddot{c}_{\mathrm{E}}$ is the carbon footprint of electrolyzer materials normalized to the electrolyzer area:

$$\ddot{c}_{\mathrm{E}} = \sum_n c_n \ddot{m}_n \tag{158}$$

Here, γ is the operation uptime, t is the electrolyzer lifetime, i is the bio-GDE current density, c_n is the carbon footprint of electrolyzer material n, and $\ddot{m}_n$ is the areal mass (mass per unit area of electrolyzer) of electrolyzer material n. Carbon footprints are calculated as described below.

Terminal Electron Acceptor (Re-generation)

Upstream production was modeled for four terminal electron acceptors: oxygen, nitrate, sulfate, and perchlorate. Mass and energy balances, along with data from industrial and academic literature, were used to determine material and energy flows for upstream production of each terminal electron acceptor. Oxygen is assumed to be abundant and readily available, so no additional energy or greenhouse gas emissions were included to produce oxygen. In the process model, nitrate is produced from atmospheric nitrogen gas through a combination of the Haber Bosch process and the Ostwald Process.[63] Hydrogen gas for the Haber Bosch process is produced through electrolysis of water driven by wind power; both energy and life cycle greenhouse gas emissions for production of ammonia through this process are obtained from Singh et al.[64] Nitric acid is produced from the combustion of this ammonia through the Ostwald process. As this

process is exothermic, no additional energy is required, though nitrous oxide as a byproduct is produced (8 kg N_2O/ton HNO_3).[65] The model assumes 95% captured and the balance emitted to the atmosphere.[65] Nitric acid is neutralized by the addition of sodium hydroxide, producing neutral sodium nitrate for the MES process. Perchlorate is produced using the chloride ions generated through perchlorate respiration, forming a chlorine cycle for the process. Sodium chloride is first converted to sodium chlorate by electrolysis.[66] Sodium chlorate is further converted to sodium perchlorate, again by electrolysis.[66] Sulfur is likewise recycled in the process. Hydrogen sulfide gas produced by the sulfate-reducing bacteria is converted to sulfuric acid through the wet sulfuric acid process, an exothermic process which requires no additional energy.[67] Sulfuric acid is neutralized to sodium sulfate by the addition of sodium hydroxide. Sodium hydroxide (in both sodium nitrate and sodium sulfate production) is produced from the electrolysis of sodium chloride and water in the chlor-alkali process, with mass allocation used to determine the impacts associated with NaOH production. Electricity demand is assumed to be the major contributor of the global warming potential of the chlor-alkali process.[68]

Other LCA Components

All electricity in the process is assumed to be from wind energy, with life cycle impacts drawn from the PEF dataset. It should be noted other decarbonized electricity sources such as thin-film photovoltaics and hydropower have similar global warming potentials and would therefore lead to similar results. Carbon dioxide in the modelled process is provided via direct air capture, with energy requirements and life cycle impacts obtained from Duetz and Bardow.[69] Impacts for most of electrolyzer materials (IrO_2, SnO_2, carbon paper, and PMMA) are obtained from the PEF database while impacts for Nafion are obtained from Stropnik et al.[70] Electrolyzer material requirements are calculated using the system described by Xu *et al.*[71] as a basis assuming a geometric area of 1 m^2, an electrode separation distance of 1 cm, and an electrolyzer lifetime of three years assumed. In the case of direct electroautotrophy, the bio-GDE uses the geometry and density of a Sigracet 35BC gas diffusion electrode for the cathode and makes the same assumptions regarding geometric area, electrode separation, and lifetime.

Electroautotrophic production of sucrose is compared to two alternative sucrose production methods: from sugarcane and in a metabolically engineered Knallgas bacterium. Life cycle global warming potential of sugarcane is derived from Izursa *et al*.,[45] while that of sucrose production in Knallgas bacterium is determined by adapting the process model from my previous work (see Chapter 2).[5]

Mass transport in a bio-GDE

Governing equations

Following Weng *et al.*[72], I describe the gas diffusion electrode with a microbial catalyst layer (bio-GDE) using a one-dimensional, macro-homogeneous model assuming isothermal conditions. I explicitly consider both gas and liquid phases, species transport within each phase, and mass transfer between the two phases. With this model, I was attempting only to determine if gas-liquid mass transfer or gas-phase transport could limit the productivity of a bio-GDE. Therefore, I considered only two species: CO_2 and O_2, although N_2 was included in the gas phase at a small concentration (1000 ppm) for numerical stability. The mole balance within the liquid phase of the bio-GDE can be written as

$$\frac{\partial c_i^{\mathrm{L}}}{\partial t} = -\frac{\partial n_i^{\mathrm{L}}}{\partial x} - R_{\mathrm{X},i} + R_{\mathrm{GL},i} \tag{159}$$

where c_i^{L} is the liquid phase concentration, n_i^{L} is the molar flux in the liquid phase, $R_{\mathrm{X},i}$ and $R_{\mathrm{GL},i}$ are the microbial reaction (carbon fixation) and gas-liquid mass transfer source terms, respectively. The subscript i refers to the chemical species. In the gas phase, the mole balance is given by

$$\frac{\partial c_i^{\mathrm{G}}}{\partial t} = -\frac{\partial n_i^{\mathrm{G}}}{\partial x} - \frac{\theta^{\mathrm{L}}}{\theta^{\mathrm{G}}} R_{\mathrm{GL},i} \tag{160}$$

Where θ^{L} and θ^{G} are the liquid- and gas-phase volume fractions, respectively. Note that the gas-liquid mass transfer term, $R_{\mathrm{GL},i}$ is written as positive for the liquid phase (*i.e.,* a source term) and negative for the gas-phase (*i.e.,* a sink term).

Geometry

I assume that the biocatalyst layer (bCL) within the bio-GDE has a defined volume fraction for the conductive support material (θ^{CM}) with a defined specific surface area ($a_{\mathrm{v}}^{\mathrm{CM}}$). If the biomass is distributed evenly throughout the bCL, the volume fraction of biomass is given by

$$\theta^{\mathrm{X}} = \gamma t^{\mathrm{X}} a_{\mathrm{v}}^{\mathrm{CM}} \tag{161}$$

where θ^{X} is the biomass volume fraction, γ is the packing factor, and t^{X} is the biofilm thickness. I assume $\gamma \approx 0.52$, equivalent to a square lattice of spheres with equal diameter. The surface area of the biomass is written as

$$a_{\mathrm{v}}^{\mathrm{X}} = 6\gamma a_{\mathrm{v}}^{\mathrm{CM}} \tag{162}$$

To determine the volume fraction of liquid and gas phases in the bCL, I define a saturation fraction (S) such that

$$\theta^{\mathrm{L}} = S\left(1 - \theta^{\mathrm{CM}} - \theta^{\mathrm{X}}\right) \tag{163}$$

and

$$\theta^{\mathrm{G}} = 1 - \theta^{\mathrm{CM}} - \theta^{\mathrm{X}} - \theta^{\mathrm{L}} \tag{164}$$

I use $S = 0.64$ following the "ideally wetted" case in Weng *et al.*[72] To calculate the liquid film thickness (which is relevant for gas-liquid mass transfer as discussed later), I use

$$t^{\mathrm{L}} = \frac{\theta^{\mathrm{L}}}{a_{\mathrm{v}}^{\mathrm{X}}} \tag{165}$$

Finally, the specific surface area of the liquid phase is given by

$$a_{\mathrm{v}}^{\mathrm{L}} = \frac{6\theta^{\mathrm{X}}}{t^{\mathrm{X}} + t^{\mathrm{L}}} \tag{166}$$

following geometric arguments.

Liquid-phase transport

Flux of aqueous species is given simply by

$$n_i^{\mathrm{L}} = -D_i^{\mathrm{L,eff}} \frac{\partial c_i^{\mathrm{L}}}{\partial x} \tag{167}$$

where $D_i^{\mathrm{L,eff}}$ is the effective diffusion coefficient of species i in the liquid phase. Because species transport is occurring through the porous bCL, I use effective diffusion coefficients following the Bruggeman relationship,

$$D_i^{\mathrm{L,eff}} = \frac{\theta^{\mathrm{L}}}{\tau^{\mathrm{L}}} D_i^{\mathrm{L}} = \left(\theta^{\mathrm{L}}\right)^{3/2} D_i^{\mathrm{L}} \tag{168}$$

where τ^{L} is the tortuosity of the medium. The full electrochemical model, as described in the next section, uses the Nernst-Planck relationship to describe both diffusion and migration in the liquid phase. I neglect migration here because none of the species considered (CO_2, O_2, N_2) are charged.

Gas-phase transport

Gaseous species flux consists of both diffusive and convective terms,

$$n_i^{\mathrm{G}} = M_i j_i^{\mathrm{G}} + M_i \rho_i u_{\mathrm{g}} \tag{169}$$

where M_i is the molar mass, j_i is the diffusive mass flux, ρ_i is the mass density, and u_{g} is the mass-averaged fluid velocity. Following Weng *et al.*,[72] the diffusive flux is calculated using a mixture-averaged diffusion model,

$$j_i^{\mathrm{G}} = -\rho_{\mathrm{g}} D_i^{\mathrm{G,eff}} \frac{\partial \omega_i}{\partial x} - \rho_{\mathrm{g}} D_i^{\mathrm{G,eff}} \omega_i \frac{\partial M_n}{M_n \partial x} \tag{170}$$

where ω_i is the mass fraction of species i, ρ_{g} is the gaseous mixture density, M_{n} is the average molar mass of the mixture, $M_{\mathrm{n}} = \left(\sum_i \frac{\omega_i}{M_i}\right)^{-1}$, and $D_i^{\mathrm{G,eff}}$ is the effective gas-phase diffusion coefficient for species i. The gas-phase diffusion coefficient includes a mass-averaged Stefan-Maxwell diffusivity (D_i^{m}) and Knudsen diffusivity (D_i^{K}) occurring in parallel:

$$D_i^{\mathrm{G}} = \left(\frac{1}{D_i^{\mathrm{m}}} + \frac{1}{D_I^{\mathrm{K}}}\right)^{-1} \tag{171}$$

with

$$D_i^{\mathrm{m}} = \frac{1 - \omega_i}{\sum_{n \neq i} \frac{y_n}{D_{i,n}}} \tag{172}$$

and

$$D_i^{\mathrm{K}} = \frac{2r_{\mathrm{p}}}{3}\sqrt{\frac{8RT}{\pi M_i}} \tag{173}$$

Here, r_{p} is the pore radius of the porous medium, y_i is the molar fraction of species i, R is the gas constant and T is the temperature. I also correct the diffusivity in the gas phase to account for porosity and tortuosity:

$$D_i^{\mathrm{G,eff}} = \frac{\theta^{\mathrm{G}}}{\tau^{\mathrm{G}}} D_i^{\mathrm{G}} = \left(\theta^{\mathrm{G}}\right)^{3/2} D_i^{\mathrm{G}} \tag{174}$$

The mass-averaged velocity field (u_{g}) is described using Darcy's law,

$$u_g = -\frac{\kappa^{\mathrm{G}}}{\mu^{\mathrm{G}}}\frac{\partial p}{\partial x} \tag{175}$$

Where κ^{G} is the permeability, μ^{G} is the gas-phase viscosity, and p is the total gas pressure. The Nth gas species mass fraction is determined by a mass balance:

$$\sum_i \omega_i = 1 \tag{176}$$

Carbon fixation reaction

Carbon fixation relies on the enzymatic conversion of CO_2 into metabolites (*e.g.*, pyruvate, acetyl-CoA, *etc.*) and requires energy in the form of ATP, NADH, and/or Fd^{2-}, which are produced by electron uptake and (in the case considered in this model) aerobic respiration. Hence, either the carbon fixation pathway or aerobic respiration can set a limit on the overall rate of carbon fixation. I calculated the enzymatic rate limits using Michaelis-Menten kinetics:

$$\begin{aligned} r_{\mathrm{CO_2}} &= k_{\mathrm{cat,CO_2}} E_{\mathrm{CO_2}} \left(\frac{c^{\mathrm{L}}_{\mathrm{CO_2}}}{K_{\mathrm{M,CO_2}} + c^{\mathrm{L}}_{\mathrm{CO_2}}}\right) \\ r_{\mathrm{O_2}} &= \alpha_n k_{\mathrm{cat,O_2}} E_{\mathrm{O_2}} \left(\frac{c^{\mathrm{L}}_{\mathrm{O_2}}}{K_{\mathrm{M,O_2}} + c^{\mathrm{L}}_{\mathrm{O_2}}}\right) \end{aligned} \tag{177}$$

where α_n is a stoichiometric coefficient depending on the ratio of O_2 to CO_2 consumed during carbon-fixing metabolism, $k_{\mathrm{cat},i}$ is the turnover number of the relevant enzyme, E_i is the intracellular enzyme concentration, and $K_{\mathrm{M},i}$ is the Michaelis constant. I set $k_{\mathrm{cat,CO_2}}$ equal to 100 s^{-1} for carbon fixation using the reductive glycine pathway (rGlyP) to represent an upper bound in accordance with the maximum rate of formate dehydrogenases in *Cupriavidus necator* that would be responsible for the first carbon fixation step in the rGlyP,[73] and used an intracellular enzyme concentration of ~220 mM based on the estimate that RuBisCo comprises 3% of the enzymes in carbon-fixing organisms using the Calvin cycle.[74,75] For O_2 respiration, I calculated the product

$k_{\mathrm{cat},\mathrm{O}_2}E_{\mathrm{O}_2}$ based on estimates of cellular respiration rates in *E. coli*.[76] In all cases considered in the bio-GDE model, the carbon fixation pathway set a more stringent bound on the rate of carbon fixation than the aerobic respiration pathway (*i.e.*, $r_{\mathrm{CO}_2} < r_{\mathrm{O}_2}$). Hence, the microbial carbon fixation reaction is written as

$$R_{\mathrm{X},i} = \alpha_i \theta^{\mathrm{X}} r_{\mathrm{CO}_2} \tag{178}$$

where α_i is a stoichiometric coefficient (α_{CO_2} is always equal to 1, but α_{O_2} varies depending on the electron sink and carbon fixation pathway, as discussed in the section on the metabolism of carbon fixation).

Gas-liquid mass transfer

Gas-phase CO_2 and O_2 dissolves into the liquid at the gas/liquid interface. Following Weng *et al.*,[72] the gas-liquid mass transfer coefficient ($k_{\mathrm{GL},i}$) is calculated according to

$$k_{\mathrm{GL},i} = \frac{D_i^{\mathrm{L}}}{t^{\mathrm{L}}} \tag{179}$$

Then, the rate of gas-liquid mass transfer is given by

$$R_{\mathrm{GL},i} = a_{\mathrm{v}}^{\mathrm{L}} k_{\mathrm{GL},i}\left(H_i p_{\mathrm{G}} y_i - c_i^{\mathrm{L}}\right) \tag{180}$$

where H_i is Henry's constant for species i.

Boundary conditions

In the liquid phase, I use no-flux boundary conditions at the electrolyte-bCL and bCL-gas diffusion layer (GDL) interfaces. In the latter case, this is because the liquid phase ends at the bCL-GDL interface, so no liquid-phase flux is possible. In the former case, this is because the rate of diffusion of sparingly soluble gases from the bulk electrolyte, through the fluid boundary layer, to the electrolyte-bCL boundary is several orders of magnitude lower than the rate of gas-liquid mass transfer within the bCL such that this diffusive contribution to the liquid-phase concentration of CO_2 and O_2 can be neglected.

For the gas-phase, I use a no-flux boundary condition at the electrolyte-bCL interface because, although gas-liquid mass transfer would occur, the surface area of the bCL-electrolyte interface is several orders of magnitude smaller than the gas-liquid interfacial area within the bCL. At the bCL-GDL interface, the gas feed composition is set to 50 mol% CO_2, 49.9 mol% O_2, and 0.1 mol% N_2.

Model analysis

I calculated the projected surface area current density as

$$i = \int_0^{l_{\mathrm{bCL}}} n_{\mathrm{e}} F R_{\mathrm{X},\mathrm{CO}_2} \partial x \tag{181}$$

where l_{bCL} is the biocatalyst layer thickness, n_{e} is the stoichiometric ratio of electrons consumed per CO_2 fixed, and F is Faraday's constant.

Full electrochemical bio-GDE model

System overview

The model considers a one-dimension bio-electrochemical reactor for the conversion of CO_2 into sucrose via direct electron transfer in a bio-GDE. The reactor has a well-mixed region that is exchanged at a fixed dilution rate and to which a CO_2-containing gas mixture is constantly supplied at a fixed pressure. Fluid boundary layers (BLs) separate the well-mixed liquid phase from the anode surface and the bio-GDE. Electrochemical reactions at the anode surface (water oxidation) and throughout the biocatalyst layer (bCL) within the bio-GDE (direct electron transfer coupled to CO_2-fixation) are driven by an applied voltage. Microbes attached to the conductive support material (CM) are assumed to accept electrons into the quinone or NADH pool, use O_2 as the terminal electron acceptor, and use the reductive glycine pathway (rGlyP) to fix CO_2. The chemical species considered in the reactor system are dissolved CO_2, bicarbonate anions (HCO_3^-), carbonate anions (CO_3^{2-}), protons (H^+), hydroxide anions (OH^-), sodium cations (Na^+), and nitrate anions (NO_3^-). NO_3^- was selected as a representative anion for sodium salt to avoid the use of chloride ions (Cl^-), which are known to produce deleterious and toxic side reactions at the cathode surface in MES systems.[40] I don't consider dissolved O_2 in the model because the previous bio-GDE model (see Fig. S2 in Appendix D) demonstrated that the bio-GDE enables saturated O_2 throughout the liquid phase even at current densities >170 mA/cm^2 with NADH as the electron sink and >280 mA/cm^2 with QH_2 as the electron sink.

I assume that the microbes within the bCL are not actively growing and are instead acting as a compartment for enzymatic processes. Hence, I assume that all fixed carbon is diverted to sucrose, and that additional nutrients (*e.g.*, ammonia, phosphates, *etc*.) are unnecessary. I emphasize that these assumptions do not correspond to any experimentally-realized system; rather, the goal here is to determine the best-case productivity and efficiency of a DET-based electromicrobial production system and the operating conditions of such a system. I also neglect cellular maintenance requirements, which have been previously shown to be negligible for calculations of this type.[77]

Well-mixed phase balance equations

The well-mixed electrolyte region is assumed to have sufficient convective mixing such that no concentration gradients are formed. The well-mixed phase mole balance is given for the reactor model by

$$\frac{dc_i}{dt} = R_{\mathrm{A-B},i} + R_{\mathrm{F},i} + R_{\mathrm{GL},i} + S_{\mathrm{A}}\left(n_i|_{\mathrm{BL_A}} - n_i|_{\mathrm{BL_C}}\right) \tag{182}$$

where c_i is the concentration, R_i is the net volumetric rate of formation and consumption due to acid-base reactions (A-B), electrolyte flow (F), and gas-liquid mass transfer (GL), and n_i is the flux of species i. The projected electrode surface area-to-volume ratio is given by S_{A}. By convention, the positive x-direction is defined from left to right such that species flux from the cathode boundary layer phase ($\mathrm{BL_C}$) to the well-mixed phase will have a negative value.

Anode and cathode boundary layer balance equations

Fluid in the boundary layers is approximately stagnant. Hence, species transport in these regions occurs via by diffusion and migration driven by electrochemical potential gradients. The mole balances in both the anode and cathode BL phases are given by

$$\frac{\partial c_i}{\partial t} = -\frac{\partial n_i}{\partial x} + R_{\mathrm{A-B},i} \tag{183}$$

since neither electrolyte flow nor gas-liquid mass transfer occurs here.

Biocatalyst layer balance equation

In the biocatalyst layer, the CO_2-fixation reaction and gas-liquid mass transfer provide additional sink/source terms for species in the liquid phase. Hence, the balance equation is written as

$$\frac{\partial c_i}{\partial t} = -\frac{\partial n_i}{\partial x} + R_{\mathrm{A-B},i} + R_{\mathrm{GL},i}^{\mathrm{bCL}} + R_{\mathrm{X},i} \tag{184}$$

where $R_{\mathrm{GL},i}^{\mathrm{bCL}}$ is the gas-liquid mass transfer term in the bCL phase and $R_{\mathrm{X},i}$ accounts for the CO_2-fixation reaction.

Species transport in the boundary layers and biocatalyst layer

The molar flux of species in dilute electrolyte solutions is written as the sum of diffusive and migrative fluxes:

$$n_i = -D_i^{\mathrm{eff}} \frac{\partial c_i}{\partial x} - z_i u_i F c_i \frac{\partial \phi_{\mathrm{l}}}{\partial x} \tag{185}$$

where D_i^{eff} and u_i are the diffusivity and mobility (related by the Nernst-Einstein relationship, $u_i = D_i/RT$ for dilute solutions) of species i, z_i is the charge number, F is Faraday's constant, and ϕ_{l} is the local electrolyte potential. Effective diffusion coefficients are used in the bCL according to the Bruggeman relationship as described for the bio-GDE in the preceding section. The net ionic current density in the electrolyte (i_{l}) can be calculated from the total ionic flux:

$$i_{\mathrm{l}} = F \sum_i z_i n_i \tag{186}$$

following electroneutrality,

$$\sum_i z_i c_i = 0 \tag{187}$$

Acid-base reactions

The acid-base carbon dioxide/bicarbonate/carbonate and water dissociation reactions occur in each liquid phase and are treated as kinetic expressions without assuming equilibrium:

$$\mathrm{CO_{2(aq)}} + \mathrm{H_2O} \overset{k_{+1},k_{-1}}{\longleftrightarrow} \mathrm{H^+} + \mathrm{HCO_3^-} \qquad K_1 \qquad (188)$$

$$\mathrm{HCO_3^-} \overset{k_{+2},k_{-2}}{\longleftrightarrow} \mathrm{H^+} + \mathrm{CO_3^{2-}} \qquad K_2 \qquad (189)$$

$$\mathrm{CO_{2(aq)}} + \mathrm{OH^-} \overset{k_{+3},k_{-3}}{\longleftrightarrow} \mathrm{HCO_3^-} \qquad K_3 = K_1/K_\mathrm{W} \qquad (190)$$

$$\mathrm{HCO_3^-} + \mathrm{OH^-} \overset{k_{+4},k_{-4}}{\longleftrightarrow} \mathrm{CO_3^{2-}} + \mathrm{H_2O} \qquad K_4 = K_2/K_\mathrm{W} \qquad (191)$$

$$\mathrm{H_2O} \overset{k_\mathrm{W},k_{-\mathrm{W}}}{\longleftrightarrow} \mathrm{H^+} + \mathrm{OH^-} \qquad K_\mathrm{W} \qquad (192)$$

where k_{+n} and k_{-n} are the forward and reverse rate constants, respectively, and K_n is the equilibrium constant for the nth reaction, given by

$$K_n = \exp\left(\frac{\Delta S_n}{R}\right)\exp\left(-\frac{\Delta H_n}{RT}\right) \qquad (193)$$

where ΔS_n and ΔH_n are the molar entropy change and heat of reaction, respectively, for reaction n. Source and sink terms resulting from these reactions are compiled in $R_{\mathrm{A-B},i}$, written as

$$R_{\mathrm{A-B},i} = \sum_n \nu_i \left(k_{+n} \prod_{\nu_i<0} c_i - k_{-n} \prod_{\nu_i>0} c_i \right) \qquad (194)$$

where ν_i is the stoichiometric coefficient of species i for the nth reaction and reverse rate constants are calculated from:

$$k_{-n} = \frac{k_{+n}}{K_n} \qquad (195)$$

Electrolyte flow

Liquid electrolyte is fed to and extracted from the well-mixed liquid phase at a constant dilution rate, resulting in a feed term written as

$$R_{\mathrm{F},i} = D_\mathrm{liq}(c_{\mathrm{F},i} - c_i) \qquad (196)$$

where D_liq is the liquid dilution rate and $c_{\mathrm{F},i}$ is the feed concentration of species i. For the life cycle analysis, I defined the functional unit of analysis to be sucrose at 100 g/L. I therefore defined the dilution rate as a function of the projected surface area current density to maintain a sucrose titer of 100 g/L in the well-mixed phase, given by:

$$D_{\mathrm{liq}} = \frac{iS_{\mathrm{A}}M_{\mathrm{S}}}{n_{\mathrm{e}}Fc'_{\mathrm{S}}} \tag{197}$$

where i is the projected surface area current density, M_{S} is the molar mass of sucrose (342.3 g/mol), n_{e} is the number of electrons consumed per sucrose molecule, and c'_{S} is the desired sucrose mass concentration (100 g/L in this case).

Gas feed

A CO_2-containing gas mixture is fed into the well-mixed liquid phase at a total pressure P, resulting in mass transfer according to

$$R_{\mathrm{GL,CO_2}} = k_{\mathrm{L,CO_2}}a\left(P\beta_{\mathrm{CO_2}}y_{\mathrm{F,CO_2}} - c_{\mathrm{CO_2}}\right) \tag{198}$$

where $k_{\mathrm{L,CO_2}}a$ is the volumetric mass transfer coefficient on the liquid side of the gas/liquid interface, $\beta_{\mathrm{CO_2}}$ is the Bunsen solubility coefficient, and $y_{\mathrm{F,CO_2}}$ is the mole fraction of CO_2 in the gas phase. The Bunsen solubility coefficient, $\beta_{\mathrm{CO_2}}$, is calculated according to

$$\ln\beta = A_1 + A_2\left(\frac{100}{T}\right) + A_3\ln\left(\frac{T}{100}\right) + S\left[B_1 + B_2\left(\frac{T}{100}\right) + B_3\left(\frac{T}{100}\right)^2\right] \tag{199}$$

where A_n and B_n are fitting parameters and S is the salinity (in g/kg). The gas-liquid mass transfer in the bCL is conceptually similar, but the mass transfer coefficient is adjusted to reflect the gas-liquid interfacial area as described in the preceding section:

$$R^{\mathrm{bCL}}_{\mathrm{GL,CO_2}} = a_{\mathrm{v}}^{\mathrm{L}}k_{\mathrm{GL,CO_2}}\left(P\beta_{\mathrm{CO_2}}y_{\mathrm{F,CO_2}} - c_{\mathrm{CO_2}}\right) \tag{200}$$

Electrode reactions – anode

The surface reaction at the anode is the oxidation of water:

$$\mathrm{H_2O} \longrightarrow \frac{1}{2}\mathrm{O_2} + 2\mathrm{H^+} + 2\mathrm{e^-} \qquad E^0_{\mathrm{OER}} \tag{201}$$

where E^0_{OER} is the equilibrium potential of the oxygen evolution half-cell reaction (OER) at standard state. The anode reaction is related to species transport by a flux boundary condition at the electrode surface,

$$n_i|_{\mathrm{A}} = \frac{\nu_i i_{\mathrm{R}}}{nF} \tag{202}$$

where i_{R} is the reaction current density and n is the number of electrons participating in the electrode reaction. I model charge transfer kinetics at the anode using Butler-Volmer kinetics:

$$i_{\mathrm{R}} = i_0\left[\left(\frac{c_{\mathrm{red}}}{c_{\mathrm{red,0}}}\right)^{\gamma_{\mathrm{red}}}\exp\left(\frac{\alpha_{\mathrm{a}}F\eta}{RT}\right) - \left(\frac{c_{\mathrm{ox}}}{c_{\mathrm{ox,0}}}\right)^{\gamma_{\mathrm{ox}}}\exp\left(\frac{\alpha_{\mathrm{c}}F\eta}{RT}\right)\right] \tag{203}$$

where i_0 is the exchange current density, $\gamma_{\mathrm{red/ox}}$ is the reaction order with respect to a reactant, $\alpha_{\mathrm{a/c}}$ is the anodic/cathodic transfer coefficient, and η is the overpotential. The overpotential is defined according to

$$\eta = \phi_{\mathrm{s}} - \phi_{\mathrm{l}} - E \tag{204}$$

where ϕ_{s} is the electrode potential, ϕ_{l} is the electrolyte potential, and E is the half-cell equilibrium potential.

Because water oxidation creates acidic conditions near the anode surface, bicarbonate and carbonate species will be converted to aqueous CO_2 according to Le Chatelier's principle. To avoid the unrealistic supersaturation this would cause, I describe the evolution of CO_2 as an additional sink term for CO_2 in the electrolyte as

$$R_{\mathrm{evo,CO_2}} = \begin{cases} -\gamma_{\mathrm{CO_2}} S_{\mathrm{CO_2}}^2 & S \geq 1 \\ 0 & S < 1 \end{cases} \tag{205}$$

where $\gamma_{\mathrm{CO_2}}$ is the releasing coefficient and $S_{\mathrm{CO_2}}$ is the supersaturation coefficient, defined as $c_{\mathrm{CO_2}}/\beta_{\mathrm{CO_2}} p_{\mathrm{CO_2}}$, where $p_{\mathrm{CO_2}}$ is the partial pressure.[9,23,78,79]

Electrode reactions – biocatalyst layer

The CO_2-fixation reaction ($R_{\mathrm{X},i}$) is related to the current density in the bCL by

$$R_{\mathrm{X},i} = \frac{\nu_i a_{\mathrm{v}}^{\mathrm{X}} i_{\mathrm{X}}}{n_{\mathrm{e}} F} \tag{206}$$

where $a_{\mathrm{v}}^{\mathrm{X}}$ is the active specific surface area of the microbes in the bCL and i_{X} is the current density on the microbial surfaces. The active specific surface area was calculated in the preceding section. The current density, and therefore the CO_2-fixation rate, can be limited either by the kinetics of electron transfer or by the enzymatic rate limit of CO_2 fixation. To account for this, I describe i_{X} as

$$i_{\mathrm{X}} = \frac{i_{\mathrm{R}}}{1 + \left| \frac{i_{\mathrm{R}}}{i_{\mathrm{lim}}} \right|} \tag{207}$$

where i_{R} is the reaction current density limit described by Butler-Volmer kinetics,

$$i_{\mathrm{R}} = i_0 \left[\left(\frac{c_{\mathrm{red}}}{c_{\mathrm{red},0}} \right)^{\gamma_{\mathrm{red}}} \exp\left(\frac{\alpha_{\mathrm{a}} F \eta}{RT} \right) - \left(\frac{c_{\mathrm{ox}}}{c_{\mathrm{ox},0}} \right)^{\gamma_{\mathrm{ox}}} \exp\left(\frac{\alpha_{\mathrm{c}} F \eta}{RT} \right) \right] \tag{208}$$

and i_{lim} is the biomass-limited current density. I calculate the biomass-limited current density by projecting the enzymatic CO_2-fixation rate limit to the total cell surface:

$$i_{\mathrm{lim}} = n_{\mathrm{e}} F k_{\mathrm{cat}} E_{\mathrm{CO_2}} \frac{\theta^{\mathrm{X}}}{a_{\mathrm{v}}^{\mathrm{X}}} \tag{209}$$

where k_{cat} is the enzyme turnover number and $E_{\mathrm{CO_2}}$ is the intracellular concentration of the rate-limiting enzyme in the CO_2-fixation pathway. This formulation relies on the fact that intracellular substrate diffusion is much faster than rate-limiting enzymatic reaction steps in carbon fixation pathways.[23]

Electron transport in solid electrodes

Electron transport in the solid electrode (the anode and the conductive support material within the bCL) is governed by charge conservation and Ohm's law, given by:

$$\nabla i_{\mathrm{s}} = -\nabla i_{\mathrm{l}} = -a_{\mathrm{v}}^{\mathrm{X}} i_{\mathrm{X}} \tag{210}$$

$$i_{\mathrm{s}} = \kappa_{\mathrm{s}} \frac{\partial \phi_{\mathrm{s}}}{\partial x} \tag{211}$$

where i_{s} is the electrode current density and κ_{s} is the conductivity. I modify the conductivity in the bCL with a Bruggeman correction factor:

$$\kappa_{\mathrm{s}}^{\mathrm{eff}} = \left(\theta^{\mathrm{CM}}\right)^{1.5} \kappa_{\mathrm{s}} \tag{212}$$

Numerical method

The equations for both the bio-GDE model and the electrochemical system model are solved using the MUMPS general solver in COMSOL Multiphysics 5.4. For the bio-GDE, the modeling domain has a maximum element size of 0.02 μm. For the electrochemical system, the modeling domain has a maximum element size of 10 μm in the well-mixed regions and 0.5 μm in the boundary layers and bCL to capture steep concentration gradients. Model parameters for the bio-GDE and electrochemical system are listed in Tables S1 and S2 in Appendix D, respectively.

5.4 Results and Discussion

Physiology, stoichiometry, and energy efficiency

I first sought to determine the metabolic efficiency of direct electron uptake-facilitated carbon fixation to sucrose. I employed a stoichiometric and energetic analysis based on the three metabolic modules necessary for electroautotrophy (Fig. 5.1a) as described in detail in the Methods section. Briefly, I determined the ATP, NAD(P)H, and reduced ferredoxin (Fd^{2-}) demand for sucrose production for each of five natural or synthetic carbon fixation pathways (CFPs): the Calvin cycle,[80] the reductive glycine pathway (rGlyP),[47,48] the crotonyl-CoA/ethylmalonyl-CoA/hydroxybutyryl-CoA (CETCH) cycle,[49] the reductive tricarboxylic acid (rTCA) cycle,[81] and the Wood-Ljungdahl pathway (WLP).[82] Next, I calculated the stoichiometry of ATP, NAD(P)H, and Fd^{2-} regeneration via respiration using oxygen (O_2), nitrate (NO_3^-), perchlorate (ClO_4^-), and sulfate (SO_4^{2-}) as terminal electron acceptors. I used QH_2 and NADH as the original source of electrons for these calculations based on two possible electron transfer mechanisms: electron deposition into the quinone pool, and electron deposition into the NADH pool. Finally, I

determined the electron demand (mol e^- per mol sucrose) required to support energy carrier regeneration. The results of this analysis are compiled in Table 5.1.

For a given electron sink and terminal electron acceptor (excepting O_2 in the case of the rTCA cycle and WLP, which are oxygen-sensitive), the electron demand for the five CFPs I consider is ordered rGlyP<WLP<rTCA<CETCH<Calvin. Accordingly, the energy efficiency of carbon fixation is highest for the rGlyP, and the energy demand per unit of sucrose produced is lowest (Table 5.1). Using NADH as the electron sink results in a lower electron demand and higher energy efficiency than QH_2. The former result is unsurprising since electrons deposited into the NADH pool are more energetic (have a lower redox potential) than those in the QH_2 pool, and the latter indicates that reverse electron flow cannot overcome the efficiency challenge presented by starting with a low-energy electron donor. Using QH_2 as the electron sink cannot support CO_2-fixation with sulfate as the terminal electron acceptor because the sulfate redox couple (SO_4^{2-}/S^{2-}, E^0 = -0.22 V vs. SHE) is energetically uphill of the quinone pool (Q/QH_2, E^0 = -0.08 V vs. SHE). Of the four terminal electron acceptors I consider, O_2 results in the smallest electron demand and the highest energy efficiency; the electron demand for each is ordered $O_2<ClO_4^-<NO_3^-<SO_4^{2-}$. Although this analysis suggests that perchlorate would be the preferred electron acceptor over nitrate, nitrate is typically preferred by organisms that can respire each, possibly due to the risk of toxic intermediate buildup during the respiratory process.[56]

The highest energy efficiency (84%) and the lowest energy demand (5.67 kWh/kg) can be achieved by an organism that uses the NADH pool as a sink for cathode-derived electrons, O_2 as a terminal electron acceptor, and the rGlyP to fix carbon (Table 5.1). However, metabolic energy efficiency alone is not enough to determine if a process is viable from a life cycle perspective. Upstream processes including electricity generation, CO_2 capture, and electron acceptor (re-)generation all require explicit attention as drivers of life cycle impacts. Moreover, the productivity of the EMP system is extremely important since a lower productivity results in a higher demand for electrolyzer materials per unit product over the process lifetime. I therefore developed a complete process model for dEMP processes (diagrammed in Fig. 5.1b) to understand full-system life cycle impacts, which is discussed next.

Table 5.1. Electron demand, energetic efficiency, and energy demand for sucrose production

Terminal electron acceptor	Electron sink	Carbon fixation pathway	Electron demand (mol e^-/mol)*	Energy efficiency (%)	Energy demand (kWh/kg)*
O_2	QH_2	Calvin	121	55	8.70
		rGlyP	101	66	7.26
		CETCH†	120	55	8.60
		rTCA‡	--	--	--
		WLP‡	--	--	--
	NADH	Calvin	75.3	69	6.89
		rGlyP	62.0	84	5.67
		CETCH†	72.7	72	6.65
		rTCA‡	--	--	--
		WLP‡	--	--	--
NO_3^-	QH_2	Calvin	322	21	23.1
		rGlyP	247	27	17.7

		CETCH†	317	21	22.8
		rTCA‡	267	25	19.1
		WLP‡	262	25	18.8
	NADH	Calvin	91.9	57	8.41
		rGlyP	70.5	74	6.45
		CETCH†	90.5	58	8.28
		rTCA‡	76.2	68	6.97
		WLP‡	74.8	70	6.84
ClO_4^-	QH_2	Calvin	194	34	13.9
		rGlyP	154	44	11.0
		CETCH†	191	35	13.8
		rTCA‡	165	41	11.8
		WLP‡	162	42	11.6
	NADH	Calvin	83.1	63	7.60
		rGlyP	66.0	79	6.04
		CETCH†	82.0	64	7.50
		rTCA‡	70.6	74	6.45
		WLP‡	69.4	75	6.35
SO_4^{2-}	NADH	Calvin	157	33	14.4
		rGlyP	104	50	9.51
		CETCH†	141	37	12.9
		rTCA‡	118	44	10.8
		WLP‡	115	45	10.5

†CETCH cycle has only been demonstrated *in vitro*
‡rTCA cycle and WLP require anoxic conditions
*Values are derived from whole-number calculations so 3 significant figures are reported here arbitrarily

Global warming potential calculations reveal target productivity

Four major factors contribute to the global warming potential (GWP) of sucrose production using dEMP (Fig. 5.1b): (1) direct air capture of CO_2; (2) electron acceptor regeneration, which converts the reduced electron acceptor (*e.g.*, N_2) back into the oxidized form necessary for microbial respiration (*e.g.*, NO_3^-); (3) electricity production, which supports direct air capture and electron acceptor regeneration processes in addition to driving the EMP reactor; and (4) reactor materials production, including the plastic reactor body, carbon paper electrodes supporting the anode metal catalyst and cathode biocatalyst, and the anode metal catalyst.

I calculated the GWP of these process components for each combination of electron sink, CFP, and terminal electron acceptor, as detailed in the Computational Methods section. I assume all energy is supplied by wind power and note that other forms of clean energy production (*e.g.*, thin film photovoltaics) have roughly equal life cycle emissions and would therefore lead to similar results.[61] In all cases, the GWP of direct air capture for the process is equivalent because I assume that all of the fixed carbon is diverted to sucrose production. The GWP of each terminal electron acceptor is different based on the specifics of the regeneration process, and is ordered O_2 (0 kg $CO_{2,e}$/kg O_2) < SO_4^{2-} (0.0056 kg $CO_{2,e}$/kg Na_2SO_4) < ClO_4^- (0.063 kg $CO_{2,e}$/kg $NaClO_4^-$) < NO_3^- (0.192 kg $CO_{2,e}$/kg $NaNO_3$). For the full process, the GWP contribution by the terminal electron acceptor also depends on the CFP, since less efficient CFPs (*e.g.*, the Calvin cycle) require more ATP and NAD(P)H and therefore more of the terminal electron acceptor. Hence, microbes using

the rGlyP not only consume less energy during the sucrose production process, but also consume less energy during terminal electron acceptor regeneration because they require a smaller amount of the terminal electron acceptor per unit sucrose.

The GWP contribution by reactor materials depends on the productivity of the EMP reactor because a higher productivity over the lifetime of the reactor results in more sucrose produced per unit of reactor materials. I therefore calculated the full-system GWP as a function of current density using the rGlyP to fix carbon and for each terminal electron acceptor and electron sink (Fig. 5.2). As the current density increases, the GWP decreases for each system considered until eventually approaching a plateau around 1000 mA/cm^2 as the GWP contribution of reactor materials production becomes small with respect to that of energy demands to drive the reactor and terminal electron acceptor regeneration (Fig. 5.2).

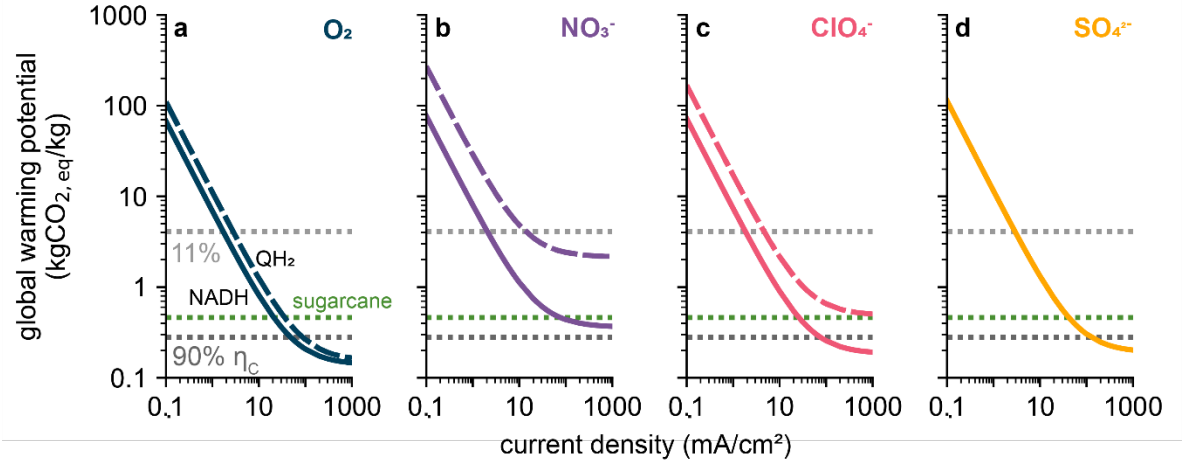

Figure 5.2. Global warming potential of direct electron transfer-based processes. Global warming potential of the production of sucrose as a function of current density for direct electron uptake using the reductive glycine pathway to fix carbon, the NADH (solid lines) or QH_2 (dashed lines) pool as the electron sink, and (**a**) O_2, (**b**) NO_3^-, (**c**) ClO_4^-, or (**d**) SO_4^- as the terminal electron acceptor. Gray dotted lines in each panel correspond to the global warming potential of sucrose production for H_2-mediated Knallgas bacteria operating at 11% (light gray) and 90% (dark gray) carbon efficiency. Green dotted line corresponds to the global warming potential of sucrose production from sugarcane. Panel (**d**) includes only electron uptake into the NADH pool (solid line) because the QH_2 pool cannot support growth with SO_4^- as the terminal electron acceptor, as discussed in the main text.

Differences in the terminal electron acceptor drive large differences in the overall GWP: at 100 mA/cm^2, the GWP of each process using NADH as the electron sink and the rGlyP to fix carbon is ordered (in units kg $CO_{2,e}$/kg sucrose) O_2 (0.21) < ClO_4^- (0.26) < SO_4^- (0.30) < NO_3^- (0.44). Hence, although NO_3^- enables more efficient carbon fixation than SO_4^{2-}(74% vs. 50%), the large GWP of nitrate regeneration causes this strategy to have a higher life cycle impact. Using QH_2 as the electron sink instead of NADH further reinforces the importance of the terminal electron acceptor. Because deposition of electrons into the quinone pool requires reverse electron flow to generate NADH and ATP, significantly more terminal electron acceptor is required per unit sucrose (*e.g.*, 1.12 kg $NaNO_3$/kg sucrose for the NADH pool vs. 9.87 kg $NaNO_3$/kg sucrose

for the QH_2 pool, using the rGlyP to fix carbon). Hence, the GWP of the full process is significantly higher if electrons are deposited into the quinone pool; at 100 mA/cm^2, these values are (in units kg $CO_{2,e}$/kg sucrose) 2.41 (vs. 0.44) for nitrate, and 0.65 (vs. 0.26) for perchlorate (Fig. 5.2). The difference between the QH_2 and NADH pools as the electron sink is smaller when O_2 is the terminal electron acceptor because O_2 is regenerated naturally by the EMP process (via water oxidation at the anode), so the slight improvement (0.26 (QH_2) vs. 0.21 (NADH)) is due to the increased efficiency of electron uptake and reduced electron demand through the NADH pool (Table 5.1).

Beyond considering differences between dEMP processes, I also wanted to benchmark this process strategy against alternative EMP options and traditional bioprocesses (*i.e.*, those based on sugarcane). My previous analysis demonstrated that H_2-mediated EMP could be more effective (induce a lower GWP) than traditional bioprocesses for the production of microbial biomass (*e.g.* for use as single cell protein), industrial enzymes, and lactic acid (see Chapter 2).[39] Here, I expanded that analysis to consider sucrose production from H_2 with microbes using the Calvin cycle to fix CO_2. I evaluated two different carbon efficiencies (fraction of fixed carbon diverted to sucrose): 11%, based on the reported value by Nangle *et al.*,[36] and 90%, representing an optimistic, but feasible, upper bound set by cyanobacterial sucrose production.[44] I also used sucrose production via sugarcane as an additional reference value, since this represents a dominant mode of sucrose production worldwide.

The results demonstrate that H_2-mediated EMP of sucrose can achieve a lower GWP than that of sugarcane-derived sucrose if the carbon efficiency is 90%. The lower carbon efficiency I considered, 11%, has a higher GWP than sugarcane-based production, although it would result in a reduced land occupation footprint.[36] To break even (in terms of GWP) with the H_2-mediated system, sucrose production based on direct electron uptake with O_2 as the terminal electron acceptor, rGlyP as the carbon fixation pathway, and NADH as the electron sink would need to achieve a current density of ~48.4 mA/cm^2 (Fig. 5.2). With QH_2 as the electron sink, the breakeven value is ~88 mA/cm^2 (Fig. 5.2, supplementary Fig. S1 in Appendix D). Regardless of the electron sink, nitrate use as the terminal electron acceptor would prevent direct electron uptake-based systems from reaching parity with H_2-mediated ones; this is due to the large GWP associated with nitrate regeneration. Although both perchlorate- and sulfate-reducing systems can achieve parity with H_2-mediated sucrose production, this requires the use of NADH as the electron sink and current densities >76 mA/cm^2 (ClO_4^-) and >128 mA/cm^2 (SO_4^{2-}). Hence, this analysis suggests that microbes using the rGlyP to fix carbon, O_2 as the terminal electron acceptor, and NADH as the electron sink represent the best option for dEMP, and that production based on this metabolic strategy may be able to outcompete alternative options.

However, this preliminary conclusion is troubled by three significant points of caution. First, I previously showed that standard dEMP systems are limited to <~1.5 mA/cm^2 by O_2 diffusion through a fluid boundary layer and to <~30 mA/cm^2 by CO_2 diffusion (see Chapter 4).[23] Hence, architectures such as gas diffusion electrodes (GDEs), which enable an extremely high gas/liquid interfacial area,[72] are necessary to achieve the high current density required for dEMP systems to compete with alternative options. Second, unavoidable efficiency losses within the EMP reactor, including kinetic overpotentials and ohmic losses in the electrolyte, will increase the energy demand per unit of sucrose produced, which will in turn increase the GWP of the overall

process. Hence, a current density higher than 48 mA/cm^2 is almost certainly necessary. Third, this high current density will cause significant pH and salinity increases in the reactor, so the microbial catalyst performing CO_2-fixation must be able to not only withstand, but function optimally, in an extreme environment. I explore each of these considerations in detail in the following sections.

Gas-phase transport and gas-liquid mass transfer in GDE architectures

Originally developed for fuel cells, GDEs have been successfully adopted for CO_2 electroreduction.[83] These systems can achieve current densities in excess of 300 mA/cm^2 for the abiotic reduction of CO_2 to formate, carbon monoxide, and ethylene, and have also been employed to enhance the gas-liquid mass transfer rate in microbial electrosynthesis reactors.[83–85] Comprehensive physical modeling of GDEs and their application in membrane electrode assemblies have been carried out for abiotic catalysts,[72,86,87] demonstrating that CO_2 gas-liquid mass transfer does not limit the productivity of these systems. However, in abiotic GDE architectures, the catalyst layer is typically only ~5 μm thick.[72,86] In contrast, for a bio-GDE with a microbial volume fraction of 0.52, a rate-limiting enzymatic turnover of 100 s^{-1}, and an electron demand of 62 mol e$^-$/mol sucrose (corresponding to carbon fixation through the rGlyP with formate dehydrogenase as the rate-limiting enzyme,[88] electron uptake into the NADH pool, and O_2 reduction as the terminal electron acceptor), the biocatalyst layer (bCL) would need to be >170 μm thick to enable a current density >100 mA/cm^2. This >30-fold difference in catalyst layer thickness could induce significant differences in the transport behavior of bio-GDE systems. I therefore wanted to confirm that gas phase transport and gas liquid mass transfer would not limit the current density of a dEMP system (diagrammed in Fig. 5.1c).

I considered two relevant cases for this system: one with an extremely high surface area (1×10^6 m^2/m^3) with a monolayer of cells distributed evenly along the carbon support, and one with a much lower surface area (5.6×10^5 m^2/m^3) and a substantially thicker biofilm (10 μm). The former case approximates the biotic analogue of GDEs designed for CO_2 electrolysis with a thin catalyst layer and ultra-high specific surface area, while the latter is similar to the architecture proposed previously for biological systems.[31]

For both bio-GDE architectures, the liquid-phase concentration of CO_2 and O_2 retain >98% of their initial values throughout the length of a 325 μm-thick biocatalyst layer operating at its limiting current density (Fig. S2 in Appendix D). Both the total pressure and individual partial pressure decrease by <0.1% for each architecture (data not shown). Hence, neither gas phase transport nor gas-liquid mass transfer limit the achievable current density in bio-GDEs. I continue the analysis here with the first case (high surface area, monolayer of cells) because the high surface area support enables a higher biomass density throughout the electrode, reducing the total bio-GDE thickness necessary to achieve a given productivity. In addition, restricting biofilm formation to a monolayer of cells minimizes the electron transport distance and relaxes demands on the conductivity of the extracellular matrix or conductive membrane extrusions or pili, which together may enable a higher fraction of cells to be metabolically active.[89]

Chemical species transport, pH, and salinity

Because gas-liquid mass transfer limitations can be overcome by employing a bio-GDE architecture, I continued my analysis by developing a comprehensive bio-electrochemical model of the bio-GDE EMP system. Since carbon fixation with the rGlyP coupled to aerobic respiration

can achieve the highest efficiency and lowest GWP (Table 5.1, Fig. 5.2), this analysis focuses on this system.

I used the model, which describes mass transport, (bio)electrochemical and acid-base thermodynamics and kinetics, and gas-liquid mass transfer (see the Computational Methods section for complete modeling details), to calculate the total system voltage necessary to achieve a given current density. In addition, because CO_2 fixation results in the net consumption of protons, the pH throughout the biocatalyst layer (bCL) will increase as the current density increases. An increased pH will promote the formation of bicarbonate and carbonate species throughout the bCL, both of which are negatively charged, so positive ions (I used Na^+ in the model) will be drawn into the liquid phase in the bCL to maintain charge neutrality. The net effect will be a substantial increase in the salinity throughout the bCL. Because microbes are sensitive to both pH and salinity extremes, I calculated the average pH and salinity developed throughout the bCL during steady-state operation.

When NADH is used as the electron sink, the total system voltage necessary to drive the reaction (which includes the thermodynamic potential, kinetic overpotentials, and Nernst and ohmic losses) increases from <1.8 V to ~2.8 V as the current density is increased from <5 mA/cm^2 to 150 mA/cm^2 (Fig. 5.3a). The total voltage is slightly lower when electrons are deposited into the QH_2 pool; this is mostly due to the difference between the thermodynamic potential necessary for quinone reduction and that for NAD^+ reduction (Fig. 5.3a). However, an equal current density for the two systems does not result in an equal sucrose productivity because more electrons are required per sucrose when electrons are deposited into the quinone pool (Table 5.1).

Both the average pH and average salinity increase, as expected, as the current density increases (Fig. 5.3b, c). At 48 mA/cm^2, the average pH is 10.1, with an average total salinity of 11.97% (w/v). At 150 mA/cm^2, these values increase to 10.8 and 28.4%, respectively (Fig. 5.3b, c). Hence, in the current density regime that is necessary for ecologically viable production (*i.e.*, a GWP near the GWP of H_2-mediated sucrose production), the microbe would need to withstand high pHs and salinities. Because well-characterized electroautotrophs (*e.g.*, *R. palustris*) are neutrophilic and non-halophilic,[21] tolerance to extreme conditions would need to be engineered into these organisms. Alternately, known extremophiles could be tested for electroautotrophic capability or engineered to contain the necessary metabolic machinery for electroautotrophy.

A limitation to the model is that I have used dilute-solution theory to describe the transport of liquid-phase species. This assumption may break down at high current densities as concentrations of carbonate and sodium species increase to well above 1 M.[72,90] More general concentrated-solution theory would account for additional drag experienced by diffusing species arising from their interactions with other species and would correct the thermodynamic driving force for diffusion and migration to account for these terms.[90] However, the general trends I report here are not expected to change significantly with corrected parameters, and would likely operate to increase the voltage, pH, and salinity at a given current density by no greater than ~10%. I also note that other models of CO_2 electroreduction have used dilute-solution theory with reasonable accuracy at significantly higher species concentrations than what is observed here.[72]

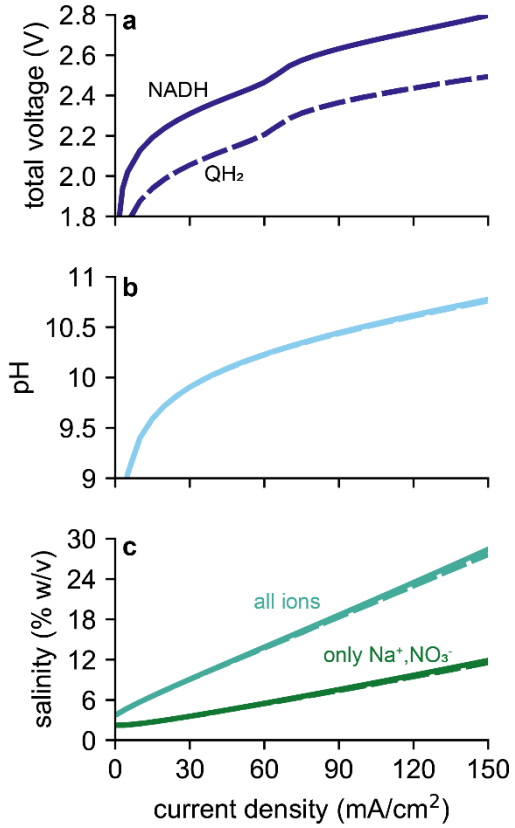

Figure 5.3. Reactor conditions. (**a**) total system voltage, (**b**) average pH in the biocatalyst layer (bCL), and (**c**) average salinity (% w/v) in the bCL as a function of current density for bacteria fixing carbon with the reductive glycine pathway, using O_2 as the terminal electron acceptor, and depositing cathode-supplied electrons into the NADH (solid lines) or QH_2 (dashed lines) pool.

Global warming potential for a highly-engineered system

Assuming that an organism with the pH- and salinity-tolerance necessary to achieve high current density can be identified or engineered, I calculated the GWP associated with sucrose production using the full electrochemical system model to predict the energy demand per unit of sucrose as a function of the current density (Fig. 5.4a). When reactor inefficiencies (due, for example, to kinetic or Ohmic overpotentials) are included, the current density necessary to match H_2-mediated sucrose production (at 90% carbon efficiency) increases from ~48 mA/cm^2 (Fig. 5.2) to 91 mA/cm^2 (Fig. 5.4a). Interestingly, the bio-GDE system using QH_2 as the electron sink cannot reach parity with the H_2-mediated case because of the higher electron demand (Fig. 5.4a).

I break down the GWP for each EMP process by subprocess category in Fig. 5.4b. The GWP associated with electrolyzer materials for direct electron uptake-based systems is significantly higher than that for H_2-mediated production (Fig. 5.4b); this is because dEMP systems operate at a significantly lower current density (here, 95 mA/cm^2 *vs.* 1000 mA/cm^2). Although the GWP associated with electricity demand for direct systems is lower when the NADH pool is used as the electron sink (because we've assumed 100% of fixed CO_2 is diverted to sucrose), the electricity demand when QH_2 is used as the electron sink is substantially higher (Fig. 5.4b). I attribute this to the higher electron demand per unit sucrose (Table 5.1). The higher electron demand also causes the GWP associated with reactor (electrolyzer) materials production to be higher at equivalent current densities because the productivity is lower (Fig. 5.4b). These twin effects prevent QH_2 use as the electron sink from reaching parity with the H_2-mediated system. At

current densities high enough to minimize GWP contribution from electrolyzer materials, the GWP associated with the power demand necessary to achieve that current density (along with the GWP from CO_2 capture) is already higher than the full-system GWP of H_2-mediated production. In addition to this practical limitation, electron uptake into the QH_2 pool has a higher energy demand (for the Calvin cycle, 8.70 kWh/kg) than H_2-mediated carbon fixation (~7.8 kWh/kg) for sucrose production when each process operates at its thermodynamic maximum efficiency (Table 5.1). Hence, only an organism that uses NADH as the electron sink can outcompete H_2-mediated production, and even then, only marginally. This presents a significant challenge to dEMP systems since electron conduits that interface with the NADH pool are uncharacterized to date.

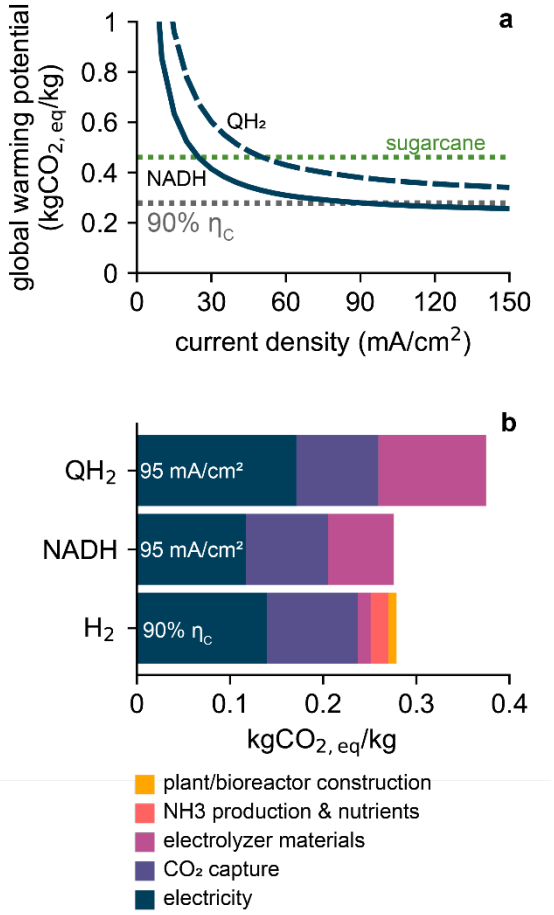

Figure 5.4. Modeled global warming potential of direct electron uptake-based processes. (**a**) Global warming potential of sucrose production for direct electron uptake as a function of current density for bacteria using the reductive glycine pathway to fix carbon, the NADH (solid lines) or QH_2 (dashed lines) as an electron sink and O_2 as the terminal electron acceptor. Gray dotted line corresponds to the global warming potential of the H_2-mediated Knallgas system operating at 90% carbon efficiency. Green dotted line corresponds to the global warming potential of sucrose production from sugarcane. (**b**) Global warming potential for the three EMP systems considered in (**a**) broken down by process category.

Charting the narrow course for direct electron uptake-based EMP

Throughout the analysis in this work, I have made a series of optimistic assumptions about the feasibility of dEMP processes. First, I assumed that an organism with the necessary metabolic components (a high-efficiency and high-rate carbon fixation pathway, an electron conduit that interfaces with the NADH pool, and aerobic respiratory capacity) could be identified or engineered wherein each physiological module functions at its maximal efficiency. Second, I assumed this organism could be effectively attached to a high-surface area gas diffusion electrode in a dense monolayer, and that this bio-GDE could be engineered to have optimal wetting characteristics to maximize liquid and gas transport. Third, I assumed that the microbe would not need to divert any

fixed carbon to maintain cellular activity (*i.e.*, that it could achieve 100% carbon efficiency to the desired product, sucrose, and that it would not need any additional elemental resources including nitrogen or phosphorous). Fourth, I assumed that this organism could function optimally at pH (>10.4) and salinity (~18.8%, composed of ~3.2 M Na^+ and ~1.87 M dissolved inorganic carbon) extremes with no loss in efficiency or productivity.

Could an organism with these characteristics be engineered? Existing or predicted electroautotrophs function optimally in near-neutral pH ranges and low salt concentrations. Although adaptive laboratory evolution strategies have enabled neutrophilic and/or non-halophilic organisms to grow at moderately alkaline or saline conditions, these efforts have so far only enabled tolerance up to pH <9.5 and <1 M Na^+.[91,92] Engineering further tolerance to extreme conditions is probably challenging since most cellular machinery would likely have to adapt to increased cytoplasmic pH and osmolarity.

A more effective solution could be to engineer an existing haloalkaliphile to use electrons accepted from a cathode as an energy source for autotrophic growth. Organisms requiring the fewest modifications to their central metabolism would be best-suited to this task. Autotrophic, aerobic haloalkaliphiles would require only the introduction of an electron conduit, a feat that has previously been accomplished in *E. coli*.[93] Among cyanobacteria, *Euhalothece* sp. ZM001 grows optimally at a pH of ~10, but requires ~0.5 M Na^+ and <1.5 M dissolved inorganic carbon.[94] Among chemolithotrophs, the alphaproteobacterial strain AHO 1 (closely related to *Roseinatronobacter thiooxidans*) grows optimally in the pH range 9.5 – 9.8 and continues H_2 oxidation up to pH 11.[95] However, the salt tolerance of this organism is <1 M Na^+, and other chemolithotrophs with higher salt tolerances are obligately anaerobic.[96] Hence, few promising cultured candidates exist based on these criteria, so expanded efforts to culture autotrophs with these desired phenotypes would be required in parallel to engineering efforts.

Moving away from known autotrophs, several extreme haloalkaliphilic chemoorganotrophs across both bacterial and archaeal domains exist that respire O_2 and grow optimally in extremely high pH and salinity regimes. Within bacteria, *Halomonas* and *Salinicoccus* genera contain obligately aerobic halophiles that can withstand Na^+ concentrations in excess of 4.2 M and pH in excess of 11. However, optimal salinities (*e.g.*, ~1.5 M Na^+ for *Halomonas cupida*) are well below the predicted conditions in the bio-GDE.[97] Within archaea, both *Halorubrum* and *Natronolimnobius* genera contain obligately aerobic halophiles that can withstand Na^+ concentrations up to 5.2 M and pH up to 11 while maintaining growth.[98] In these species, the optimal growth salinity (*e.g.*, 4.1 M Na^+ for *Halorubrum alkaliphilum*)[99] are above what is predicted in the bio-GDE, suggesting that they would be good microbial chassis candidates. None of these species, however, are known to fix CO_2 nor express characterized electron conduits,[23] although I note that archaeal electron conduits are under-characterized as compared to those of bacterial origin. This indicates that both a carbon fixation pathway (rGlyP) and an electron conduit (that interfaces with the NADH pool) would be necessary to introduce into one of these organisms. Although, in principle, this is possible, as carbon fixation pathways and an electron conduit have been functionalized in *E. coli*,[93,100,101] to my knowledge, no genetic tools for any of these extremophilic organisms currently exist. Moreover, a complete electron conduit (*e.g.*, from *Methanosarcina barkeri*)[17] that interfaces with the NADH pool would need to be elaborated prior to its functional reconstitution in a different host organism.

Could improved reactor design ease the requirements on the microbial chassis? My previous analysis demonstrated that standard reactor designs (Fig. 5.5) severely restricted the achievable current density in direct electron transfer-based EMP systems (see Chapter 4).[23] Here, I have shown that deploying a bio-GDE architecture can overcome this limitation. However, at the high current density necessary to break even with H_2-mediated systems, microbes experience pH and salinity extremes that make this strategy extremely challenging (Fig. 5.3, 5.4).

Modifying electrode materials to be less resource intensive may partially address this issue (Fig. 5.5). In this analysis, I have assumed that electrolyzers are constructed from *poly*-methyl methacrylate (PMMA), a common electrolyzer body material, and I used an IrO_2/SnO_2 anode following the methods reported in Chapter 2 on mediated EMP systems.[5] PMMA comprises ~70% of the GWP of the electrolyzer materials, and its impact could be reduced by a factor of ~3 if it was replaced with a renewable-sourced plastic such as *poly*-lactic acid.[5] This would reduce the breakeven current density (when electrons are transferred to the NADH pool) to ~50 mA/cm^2, corresponding to an average pH of ~10.1 with ~2 M Na^+ and ~1.2 M dissolved inorganic carbon in the bio-GDE (Fig. 5.3). Further replacing the IrO_2/SnO_2 anode with earth-abundant catalysts such as NiFe hydroxides[102] would decrease the breakeven current density to ~25-30 mA/cm^2, corresponding to a pH of ~9.9 with ~1.3 M Na^+ and ~0.9 M dissolved inorganic carbon (Fig. 5.3). I note, however, that earth-abundant catalysts would likely result in a higher overpotential associated with the water oxidation reaction. Some haloalkaliphilic autotrophs (*e.g.*, *Euhalothece* sp. ZM001) may be adaptable to these conditions;[94] but the native Calvin cycle would need to be replaced with the reductive glycine pathway[73] and an NADH pool-interfacing electron conduit would need to be functionally expressed, in addition to further metabolic engineering necessary to shunt carbon towards the desired product. Notably, regardless of improvements to reactor materials, electron conduits that interface with the QH_2 pool still cannot support a dEMP system that breaks-even with the H_2-mediated system.

Novel electrode designs relying on nanotube arrays have recently been proposed for EMP applications (Fig. 5.5).[103,104] In this design, the nanotube comprises the complete electrolyzer "stack", reducing the proton transport distance to tens of nanometers and potentially enabling convective transport of chemical reactants to the anode and biocathode surfaces (Fig. 5.5).[103,104] This approach could limit the pH gradient and salt buildup in the vicinity of the microbes while maintaining a high achievable current density. However, several design criteria must be met simultaneously in this system. First, the nanotube inner diameter and spacing must enable low pressure-drop transport of reacting species through the array. Second, the nanoscale membrane must conduct protons rapidly while blocking electron transport/tunneling between electrodes during operation at 1.5–2.5 V potential differences (Fig. 5.3a). Third, the array must enable robust microbial attachment even in the presence of significant local fluid velocities that could cause detachment. Fourth, nanowires are commonly deployed as antimicrobial agents,[105,106] so structure-function relationships must be determined to ensure microbe viability. Fifth, wetting characteristics must be optimized such that microbes can survive in a moist environment but without such a thick liquid film that gas exchange is inhibited and the achievable current density is limited. Finally, the nanotube arrays must be reliably synthesized at scale, and array fabrication must minimize resource intensity relative to much more easily constructed water electrolyzers. Currently, it is unclear which, if any, of these requirements are practical.

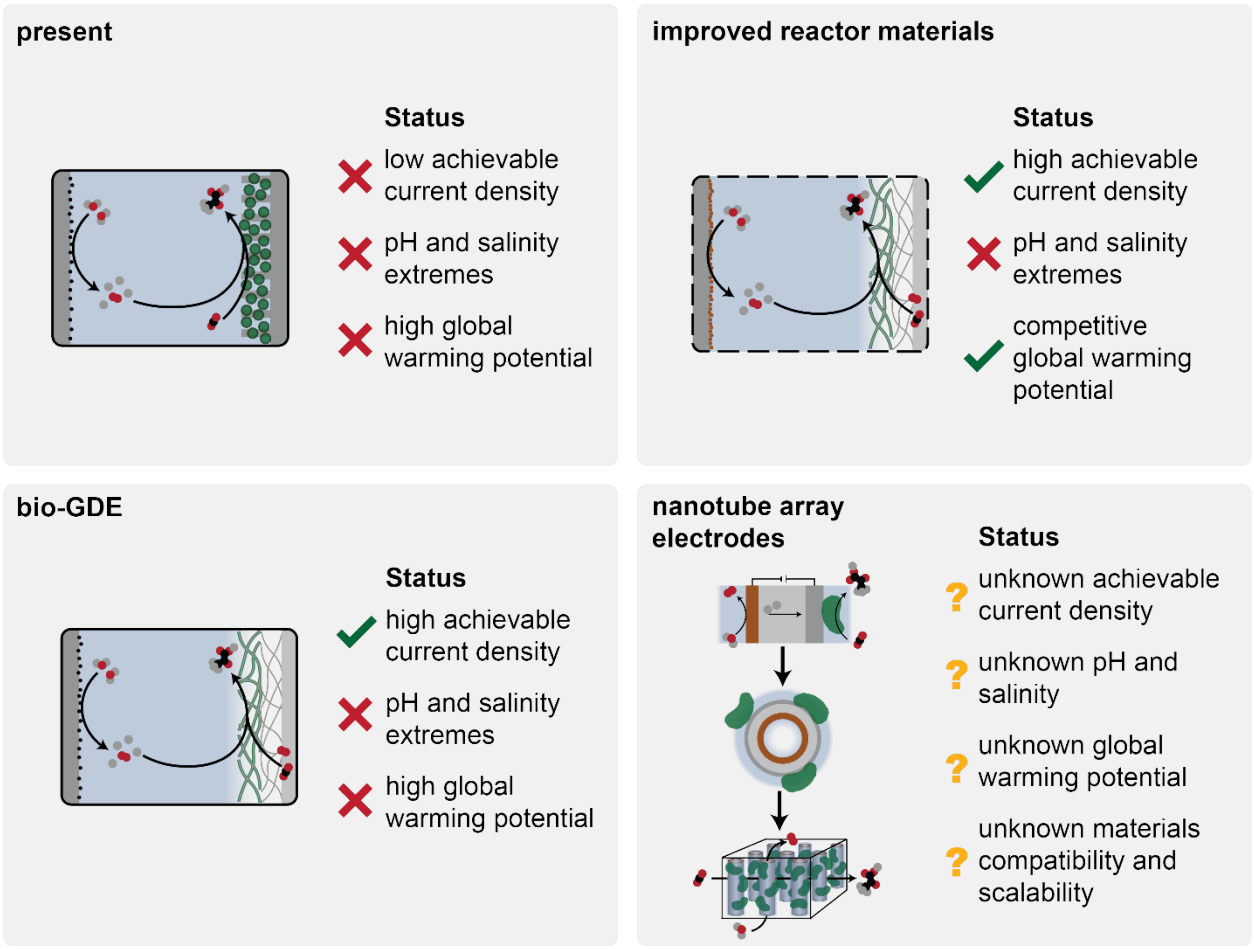

Figure 5.5. Potential reactor designs for improved performance. Current EMP reactors rely on bulk gas-liquid mass transfer, severely restricting the achievable current density. Deploying gas diffusion electrode (GDE) architectures overcome this limitation, but less resource-intensive materials are necessary, and microbes will experience pH and salinity extremes. Novel nanotube array electrodes[75,76] have been proposed to overcome these limitations, but neither their potential nor practicality are understood.

Given the significant challenges facing the design and engineering of any dEMP system, it is worth revisiting the central motivations driving the development of such systems. dEMP systems promise to achieve higher efficiency and lower resource intensity than mediated systems. Higher efficiency is predicted because NADH has a less negative redox potential than H_2 (-320 mV *vs.* -411 mV), reducing the minimum thermodynamic energy demand by ~7–8% when H_2O/O_2 (+818 mV) is the redox couple. Moreover, avoiding a mediator molecule eliminates potential losses associated with imperfect utilization of the mediator. Lower resource intensity is assumed because integrating multiple functionalities into a single reactor should reduce the overall balance-of-systems intensity. However, this analysis indicates that the resource intensity of the direct electron transfer-based EMP system is higher than that of the H_2-mediated system due to the lower

achievable current density (Fig. 5.4). The marginal potential benefit in energy efficiency, then, must act to offset the higher resource intensity.

5.5 Conclusion

The analysis presented in this chapter indicates that developing practical dEMP processes would require overcoming substantial hurdles in microbial discovery and engineering, (nano)materials synthesis, and reactor design and scale-up. In contrast, H_2-mediated systems rely on industrially-established water electrolysis[107] and gas fermentation technologies[108] that readily operate at scale with high efficiency. I suggest, therefore, that research and development towards practical applications of dEMP should be benchmarked against mediated EMP processes. This analysis, however, should not discourage efforts to study the physiology of extracellular electron transfer in microbes in general. Electron transfer mechanisms appear to be widespread in nature and of significant ecological importance.[10] Moreover, applications in toxicant biosensing,[109] wastewater treatment,[110] and environmental remediation[111] remain highly promising, but these efforts are subject to several issues beyond the technological.[112]

5.6 References

1 N. J. Claassens, I. Sánchez-Andrea, D. Z. Sousa and A. Bar-Even, *Curr. Opin. Biotechnol.*, 2018, **50**, 195–205.
2 N. J. Claassens, D. Z. Sousa, V. A. P. M. Dos Santos, W. M. De Vos and J. Van Der Oost, *Nat. Rev. Microbiol.*, 2016, **14**, 692–706.
3 X. Fang, S. Kalathil and E. Reisner, *Chem. Soc. Rev.*, 2020, 49, 4926–4952.
4 L. Su and C. M. Ajo-Franklin, *Curr. Opin. Biotechnol.*, 2019, **57**, 66–72.
5 A. J. Abel, J. D. Adams and D. S. Clark, *bioRxiv*, 2021, 2021.07.01.450744.
6 C. Liu, B. C. Colón, M. Ziesack, P. A. Silver and D. G. Nocera, *Science (80-.).*, 2016, **352**, 1210–1213.
7 J. R. Phillips, E. C. Clausen and J. L. Gaddy, *Appl. Biochem. Biotechnol.*, 1994, **45**–**46**, 145–157.
8 H. Li, P. H. Opgenorth, D. G. Wernick, S. Rogers, T. Wu, W. Higashide, P. Malati, Y. Huo, K. M. Cho and J. C. Liao, *Science (80-.).*, 2012, **335**, 1596.
9 A. J. Abel and D. S. Clark, *ChemSusChem*, 2021, **14**, 344–355.
10 D. Gupta, M. S. Guzman and A. Bose, *J. Ind. Microbiol. Biotechnol.*, 2020, **47**, 863–876.
11 V. Agostino and M. A. Rosenbaum, *Front. Energy Res.*, 2018, **6**, 1–10.
12 N. L. Costa, T. A. Clarke, L. A. Philipp, J. Gescher, R. O. Louro and C. M. Paquete, *Bioresour. Technol.*, 2018, **255**, 308–317.
13 K. P. Nevin, T. L. Woodard, A. E. Franks, Z. M. Summers and D. R. Lovley, *MBio*, 2010, **1**, 330–338.
14 S. Cheng, D. Xing, D. F. Call and B. E. Logan, *Environ. Sci. Technol.*, 2009, **43**, 3953–3958.
15 J. S. Deutzmann, M. Sahin and A. M. Spormann, *MBio*, 2015, **6**, 1–8.
16 P.-L. Tremblay, N. Faraghiparapari and T. Zhang, *Catalysts*, 2019, **9**, 166.
17 A. R. Rowe, S. Xu, E. Gardel, A. Bose, P. Girguis, J. P. Amend and M. Y. El-Naggar, *MBio*, 2019, **10**, 1659–1677.

18 A. G. Fast and E. T. Papoutsakis, *Curr. Opin. Chem. Eng.*, 2012, **1**, 380–395.
19 K. Schuchmann and V. Müller, *Nat. Rev. Microbiol.*, 2014, **12**, 809–821.
20 A. Bose, E. J. Gardel, C. Vidoudez, E. A. Parra and P. R. Girguis, *Nat. Commun.*, 2014, **5**, 3391.
21 D. Gupta, M. C. Sutherland, K. Rengasamy, J. Mark Meacham, R. G. Kranz and A. Bose, *MBio*, 2019, **10**, 1659–1677.
22 B. J. Eddie, Z. Wang, W. J. Hervey, D. H. Leary, A. P. Malanoski, L. M. Tender, B. Lin and S. M. Strycharz-Glaven, *mSystems*, , DOI:10.1128/mSystems.00002-17.
23 A. J. Abel, J. M. Hilzinger, A. P. Arkin and D. S. Clark, *Bioelectrochemistry*, 2022, 108054.
24 T. O. Ranaivoarisoa, R. Singh, K. Rengasamy, M. S. Guzman and A. Bose, *J. Ind. Microbiol. Biotechnol.*, 2019, **46**, 1401–1417.
25 W. Bai, T. O. Ranaivoarisoa, R. Singh, K. Rengasamy and A. Bose, *bioRxiv*, , DOI:10.1101/2020.10.13.336636.
26 D. R. Lovley and D. E. Holmes, *Nat. Rev. Microbiol.*, , DOI:10.1038/s41579-021-00597-6.
27 A. R. Rowe, P. Rajeev, A. Jain, S. Pirbadian, A. Okamoto, J. A. Gralnick, M. Y. El-Naggar and K. H. Nealson, *MBio*, 2018, **9**, 1–19.
28 N. M. Tefft and M. A. Teravest, *ACS Synth. Biol.*, 2019, **8**, 1590–1600.
29 D. E. Ross, J. M. Flynn, D. B. Baron, J. A. Gralnick and D. R. Bond, *PLoS One*, , DOI:10.1371/journal.pone.0016649.
30 X. Deng, N. Dohmae, K. H. Nealson, K. Hashimoto and A. Okamoto, *Sci. Adv.*, , DOI:10.1126/sciadv.aao5682.
31 L. Jourdin and T. Burdyny, *Trends Biotechnol.*, 2020, xx, 1–11.
32 A. Prévoteau, J. M. Carvajal-Arroyo, R. Ganigué and K. Rabaey, *Curr. Opin. Biotechnol.*, 2020, **62**, 48–57.
33 Turning CO2 and green energy into green chemistry, https://biooekonomie.de/en/news/turning-co2-and-green-energy-green-chemistry.
34 Carbon Engineering and LanzaTech partner to advance jet fuel made from air, https://carbonengineering.com/news-updates/ce-lanzatech-jet-fuel/.
35 F. E. Liew, R. Nogle, T. Abdalla, B. J. Rasor, C. Canter, R. O. Jensen, L. Wang, J. Strutz, P. Chirania, S. De Tissera, A. P. Mueller, Z. Ruan, A. Gao, L. Tran, N. L. Engle, J. C. Bromley, J. Daniell, R. Conrado, T. J. Tschaplinski, R. J. Giannone, R. L. Hettich, A. S. Karim, S. D. Simpson, S. D. Brown, C. Leang, M. C. Jewett and M. Köpke, *Nat. Biotechnol.*, , DOI:10.1038/s41587-021-01195-w.
36 S. N. Nangle, M. Ziesack, S. Buckley, D. Trivedi, D. M. Loh, D. G. Nocera and P. A. Silver, *Metab. Eng.*, 2020, **62**, 207–220.
37 C. Windhorst and J. Gescher, *Biotechnol. Biofuels*, 2019, **12**, 163.
38 J. L. Gascoyne, R. R. Bommareddy, S. Heeb and N. Malys, *Metab. Eng.*, 2021, **67**, 262–276.
39 A. J. Abel, J. D. Adams and D. S. Clark, *bioRxiv*, 2021, 2021.07.01.450744.
40 A. Sydow, T. Krieg, R. Ulber and D. Holtmann, *Eng. Life Sci.*, 2017, **17**, 781–791.
41 N. J. Claassens, C. A. R. Cotton, D. Kopljar and A. Bar-Even, *Nat. Catal.*, 2019, **2**, 437–447.
42 International organization for standarization, *ISO 14040*.
43 International Organization for Standardization (ISO), *ISO 14044*.

44 D. C. Ducat, J. Abraham Avelar-Rivas, J. C. Way and P. A. Silver, *Appl. Environ. Microbiol.*, 2012, **78**, 2660–2668.
45 J. Izursa, E. A. Hanlon, N. Y. Amponsah and J. C. Capece, *Carbon Footprint of Biofuel Sugarcane Produced in Mineral and Organic Soils in Florida - Manuscript submitted for publication*, LaBelle, FL, 2013.
46 I. A. Berg, *Appl. Environ. Microbiol.*, 2011, **77**, 1925–1936.
47 I. Sánchez-Andrea, I. A. Guedes, B. Hornung, S. Boeren, C. Lawson, D. Z. Sousa, A. Bar-Even, N. J. Claassens and A. J. Stams, *Nat. Commun.*, 2020, 1–12.
48 I. A. Figueroa, T. P. Barnum, P. Y. Somasekhar, C. I. Carlström, A. L. Engelbrektson and J. D. Coates, *Proc. Natl. Acad. Sci. U. S. A.*, 2018, **115**, E92–E101.
49 T. Schwander, L. S. Von Borzyskowski, S. Burgener, N. S. Cortina and T. J. Erb, *Science (80-.).*, 2016, **354**, 900–904.
50 S. T. Lohner, J. S. Deutzmann, B. E. Logan, J. Leigh and A. M. Spormann, *ISME J.*, 2014, **8**, 1673–1681.
51 M. Firer-Sherwood, G. S. Pulcu and S. J. Elliott, *J. Biol. Inorg. Chem.*, 2008, **13**, 849–854.
52 P. L. Tremblay, T. Zhang, S. A. Dar, C. Leang and D. R. Lovley, *MBio*, , DOI:10.1128/mBio.00406-12.
53 B. Kraft, M. Strous and H. E. Tegetmeyer, *J. Biotechnol.*, 2011, **155**, 104–117.
54 C. Moreno-Vivián, P. Cabello, M. Martínez-Luque, R. Blasco and F. Castillo, *J. Bacteriol.*, 1999, **181**, 6573–6584.
55 A. Tiemeyer, H. Link and D. Weuster-Botz, *Appl. Microbiol. Biotechnol.*, 2007, **76**, 75–81.
56 M. D. Youngblut, O. Wang, T. P. Barnum and J. D. Coates, *Annu. Rev. Microbiol.*, 2016, 70, 435–457.
57 J. D. Coates and L. A. Achenbach, *Nat. Rev. Microbiol.*, 2004, **2**, 569–580.
58 L. L. Barton and G. D. Fauque, in *Advances in Applied Microbiology*, Elsevier Inc., 1st edn., 2009, vol. 68, pp. 41–98.
59 A. A. Santos, S. S. Venceslau, F. Grein, W. D. Leavitt, C. Dahl, D. T. Johnston and I. A. C. Pereira, *Science (80-.).*, 2015, **350**, 1541–1545.
60 C. Rückert, *Curr. Opin. Microbiol.*, 2016, **33**, 140–146.
61 D. M. de S. Simone Manfredi, Karen Allacker, Kirana Chomkhamsri, Nathan Pelletier, *Product Environmental Footprint (PEF) Guide*, 2012.
62 J. Huang, B. Mendoza, J. S. Daniel, C. J. Nielsen, L. Rotstayn and O. Wild, *Clim. Chang. 2013 Phys. Sci. Basis Work. Gr. I Contrib. to Fifth Assess. Rep. Intergov. Panel Clim. Chang.*, 2013, **9781107057**, 659–740.
63 J. G. Chen, R. M. Crooks, L. C. Seefeldt, K. L. Bren, R. M. Bullock, M. Y. Darensbourg, P. L. Holland, B. Hoffman, M. J. Janik, A. K. Jones, M. G. Kanatzidis, P. King, K. M. Lancaster, S. V Lymar, P. Pfromm, W. F. Schneider and R. R. Schrock, *Science (80-.).*, 2018, **360**, eaar6611.
64 V. Singh, I. Dincer and M. A. Rosen, eds. I. Dincer, C. O. Colpan and O. B. T.-E. Kizilkan Energetic and Environmental Dimensions, Academic Press, 2018, pp. 935–959.
65 United State Environmental Protection Agency (EPA), *Off. Air Radiat.*, 2010, 1–43.
66 C. T. Corporation, *Final Report on SURVEY OF ELECTROCHEMICAL PRODUCTION OF INORGANIC COMPOUNDS*, Argonne, IL, 1980.
67 A. Al-Dallal, *Al-Khwarizmi Eng. J.*
68 I. Garcia-Herrero, M. Margallo, R. Onandía, R. Aldaco and A. Irabien, *Sci. Total*

Environ., 2017, **580**, 147–157.
69 S. Deutz and A. Bardow, *Nat. Energy*, 2021, **6**, 203–213.
70 R. Stropnik, A. Lotrič, A. Bernad Montenegro, M. Sekavčnik and M. Mori, *Energy Sci. Eng.*, 2019, **7**, 2519–2539.
71 J. Xu, G. Liu, J. Li and X. Wang, *Electrochim. Acta*, 2012, **59**, 105–112.
72 L. C. Weng, A. T. Bell and A. Z. Weber, *Phys. Chem. Chem. Phys.*, 2018, **20**, 16973–16984.
73 N. J. Claassens, G. Bordanaba-Florit, C. A. R. Cotton, A. De Maria, M. Finger-Bou, L. Friedeheim, N. Giner-Laguarda, M. Munar-Palmer, W. Newell, G. Scarinci, J. Verbunt, S. T. de Vries, S. Yilmaz and A. Bar-Even, *Metab. Eng.*, 2020, **62**, 30–41.
74 Y. M. Bar-On and R. Milo, *Proc. Natl. Acad. Sci. U. S. A.*, 2019, **116**, 4738–4743.
75 R. Milo, *BioEssays*, 2013, **35**, 1050–1055.
76 K. B. Andersen and K. Von Meyenburg, *J. Bacteriol.*, 1980, **144**, 114–123.
77 F. Salimijazi, J. Kim, A. M. Schmitz, R. Grenville, A. Bocarsly and B. Barstow, *Joule*, 2020, **4**, 2101–2130.
78 M. Lin, L. Han, M. R. Singh and C. Xiang, *ACS Appl. Energy Mater.*, 2019, **2**, 5843–5850.
79 M. R. Singh, E. L. Clark and A. T. Bell, *Phys. Chem. Chem. Phys.*, 2015, **17**, 18924–18936.
80 M. Calvin and A. A. Benson, *Science (80-.).*, 1948, **107**, 476–480.
81 M. C. Evans, B. B. Buchanan and D. I. Arnon, *Proc. Natl. Acad. Sci. U. S. A.*, 1966, **55**, 928–934.
82 L. Ljungdahl, *Annu. Rev. Microbiol.*, 1986, **40**, 415–450.
83 D. Higgins, C. Hahn, C. Xiang, T. F. Jaramillo and A. Z. Weber, *ACS Energy Lett.*, 2019, **4**, 317–324.
84 Y. Chen, A. Vise, W. E. Klein, F. C. Cetinbas, D. J. Myers, W. A. Smith, T. G. Deutsch and K. C. Neyerlin, *ACS Energy Lett.*, 2020, **5**, 1825–1833.
85 S. Bajracharya, K. Vanbroekhoven, C. J. N. Buisman, D. Pant and D. P. B. T. B. Strik, *Environ. Sci. Pollut. Res.*, 2016, **23**, 22292–22308.
86 L. C. Weng, A. T. Bell and A. Z. Weber, *Energy Environ. Sci.*, 2019, **12**, 1950–1968.
87 L. C. Weng, A. T. Bell and A. Z. Weber, *Energy Environ. Sci.*, 2020, **13**, 3592–3606.
88 A. Bar-Even, E. Noor, A. Flamholz and R. Milo, *Biochim. Biophys. Acta - Bioenerg.*, 2013, **1827**, 1039–1047.
89 S. Pirbadian, M. S. Chavez and M. Y. El-Naggar, *Proc. Natl. Acad. Sci. U. S. A.*, 2020, **117**, 20171–20179.
90 K. D. Fong, H. K. Bergstrom, B. D. McCloskey and K. K. Mandadapu, *AIChE J.*, , DOI:10.1002/aic.17091.
91 X. Wu, R. Altman, M. A. Eiteman and E. Altman, *Appl. Environ. Microbiol.*, 2014, **80**, 2880–2888.
92 I. Hamdallah, N. Torok, K. M. Bischof, N. Majdalani, S. Chadalavada, N. Mdluli, K. E. Creamer, M. Clark, C. Holdener, P. J. Basting, S. Gottesman and J. L. Slonczewski, *Appl. Environ. Microbiol.*, , DOI:10.1128/AEM.00520-18.
93 H. M. Jensen, A. E. Albers, K. R. Malley, Y. Y. Londer, B. E. Cohen, B. A. Helms, P. Weigele, J. T. Groves and C. M. Ajo-Franklin, *Proc. Natl. Acad. Sci.*, 2010, **107**, 19213–19218.
94 M. Kishi and T. Toda, *J. Appl. Phycol.*, 2018, **30**, 401–410.

95 D. Y. Sorokin, T. P. Tourova and J. G. Kuenen, *Extremophiles*, 2000, **4**, 237–245.
96 D. Y. Sorokin and J. G. Kuenen, *FEMS Microbiol. Ecol.*, 2005, **52**, 287–295.
97 K. J. Bowers, N. M. Mesbah and J. Wiegel, *Saline Systems*, , DOI:10.1186/1746-1448-5-9.
98 K. J. Bowers and J. Wiegel, *Extremophiles*, 2011, **15**, 119–128.
99 J. Feng, P. Zhou, Y. G. Zhou, S. J. Liu and K. Warren-Rhodes, *Int. J. Syst. Evol. Microbiol.*, 2005, **55**, 149–152.
100 S. Kim, S. N. Lindner, S. Aslan, O. Yishai, S. Wenk, K. Schann and A. Bar-Even, *Nat. Chem. Biol.*, 2020, **16**, 538–545.
101 S. Gleizer, R. Ben-Nissan, Y. M. Bar-On, N. Antonovsky, E. Noor, Y. Zohar, G. Jona, E. Krieger, M. Shamshoum, A. Bar-Even and R. Milo, *Cell*, 2019, **179**, 1255-1263.e12.
102 J. Luo, J. H. Im, M. T. Mayer, M. Schreier, M. K. Nazeeruddin, N. G. Park, S. D. Tilley, H. J. Fan and M. Grätzel, *Science (80-.).*, 2014, **345**, 1593–1596.
103 E. Edri, S. Aloni and H. Frei, *ACS Nano*, 2018, **12**, 533–541.
104 J. A. Cornejo, H. Sheng, E. Edri, C. M. Ajo-Franklin and H. Frei, *Nat. Commun.*, , DOI:10.1038/s41467-018-04707-6.
105 A. Elbourne, S. Cheeseman, P. Wainer, J. Kim, A. E. Medvedev, K. J. Boyce, C. F. McConville, J. Van Embden, R. J. Crawford, J. Chapman, V. K. Truong and E. Della Gaspera, *ACS Appl. Bio Mater.*, 2020, **3**, 2997–3004.
106 M. Lv, S. Su, Y. He, Q. Huang, W. Hu, D. Li, C. Fan and S. T. Lee, *Adv. Mater.*, 2010, **22**, 5463–5467.
107 A. Buttler and H. Spliethoff, *Renew. Sustain. Energy Rev.*, 2018, 82, 2440–2454.
108 P. Dürre and B. J. Eikmanns, *Curr. Opin. Biotechnol.*, 2015, **35**, 63–72.
109 D. P. Webster, M. A. TerAvest, D. F. R. Doud, A. Chakravorty, E. C. Holmes, C. M. Radens, S. Sureka, J. A. Gralnick and L. T. Angenent, *Biosens. Bioelectron.*, 2014, **62**, 320–324.
110 S. Zou and Z. He, *Water Res.*, 2018, **131**, 62–73.
111 R. Liu, X. Zheng, M. Li, L. Han, X. Liu, F. Zhang and X. Hou, *Water Res.*, 2019, **158**, 401–410.
112 M. Liboiron, *Pollution Is Colonialism*, Duke University Press, 2021.

Chapter 6: How to power electromicrobial production on Mars[†]

6.1 Abstract

In the preceding chapters, I analyzed several electromicrobial production (EMP) technologies that could be used to support sustainable commodity chemical production from CO_2. These chapters focused on Earth-based applications, and therefore used a life cycle assessment (LCA) framework to analyze and compare technology options. These efforts were supported by the Center for the Utilization of Biological Engineering in Space (CUBES), which is primarily interested in proposing, evaluating, designing, and implementing (bio)technologies that would enable human exploration on Mars. A central question surrounding such exploration on Mars is whether crewed missions can be supported using *in situ* resources – that is, the physical "stuff" of Martian geology and atmosphere. As on Earth, this *in situ* manufacturing scheme must be powered. Here, I show that photovoltaics-based power systems would be adequate and practical to sustain a crewed outpost for an extended period over a large fraction of Mars' surface. Climate data were integrated into a radiative transfer model to predict spectrally-resolved solar flux across the Martian surface. This informed detailed balance calculations for solar cell devices that identified optimal bandgap combinations for maximizing production capacity over a Martian year. I then quantified power systems, manufacturing, and agricultural demands for a six-person mission, which revealed that photovoltaics-based power generation would require <10 t of carry-along mass, outperforming alternatives over ~50% of Mars' surface.

6.2 Introduction

Long-duration space missions or continuously-occupied extraterrestrial outposts require Earth-independent power and chemical supply. Mars has an abundance of *in situ* resources, including (sub)surface water ice[1] and carbon and nitrogen in atmospheric CO_2 and N_2.[2] Efficient conversion of these resources to reduced forms of hydrogen, nitrogen, and carbon would represent an enabling step towards sustaining a permanent human presence in space. In analogy to the proposed terrestrial "Hydrogen Economy", molecular hydrogen (H_2) can be used as a platform molecule for energy storage, on-demand power supply, and as a reactant driving CO_2 and N_2 (bio)chemical reduction on Mars.[3–5]

[†]This chapter was originally published in *Frontiers in Astronomy and Space Sciences* and has been adapted with permission from the coauthors.

Water electrolysis with selective catalysts can drive water reduction to H_2 on cathode surfaces. This technology is attractive for space manufacturing applications since reactions can proceed at high rates at room temperature, enabling the use of low-weight, 3D-printable plastic reactors.[4] Commercial electrolyzers can evolve H_2 from water with up to ~80% energy efficiency.[6] Directly solar-powered (*i.e.*, photoelectrochemical) devices have also received significant attention, with solar-to-chemical efficiencies reaching >19% for H_2 production.[7] Once generated, H_2 can drive N_2 reduction to ammonia *via* the Haber-Bosch process for crop fertilizer,[5] CO_2 reduction to CH_4 *via* the Sabatier process or methanogenesis for ascent propellant generation,[8] and CO_2 reduction to bioplastics following a variety of metabolic processes for habitat and spare parts manufacturing.[4,9]

The primary alternatives for powering life support systems and chemical production facilities on Mars are miniaturized nuclear fission reactors[10] and photovoltaic (PV) arrays. While fission reactors are expected to behave similarly regardless of their location, the productivity limits of PV and photoelectrochemical (PEC) devices are not well-characterized for the Martian surface mainly due to differences in the surface temperature and solar intensity and spectrum from typical conditions on Earth or in space. In an effort to determine the potential of PV and PEC devices to support a crewed mission to Mars, a collaborator, Aaron Berliner, integrated relevant climate data from the Mars Climate Database[11] into a radiative transfer model, libRadtran,[12] to predict spectrally-resolved solar flux across the Martian surface over the course of a year. Next, I determined the maximum practical production capacity of solar cell-based devices and compared these production rates to expected daily demands for commodity chemicals on a six-person mission. The analysis demonstrates that solar cell arrays can support a crewed habitat on Mars and that photovoltaics-based power generation outcompetes other technologies over a large fraction on the planet's surface.

6.3 Computational Methods

Photovoltaic and photoelectrochemical efficiency calculations

I use the detailed balance model to calculate the energy efficiency of one-, two-, and three-bandgap photovoltaic solar cells and one- and two-bandgap photoelectrochemical devices. This model has been used to calculate the limiting efficiency of ideal photovoltaic and photoelectrochemical devices for single and multiple bandgap architectures previously.[13–15]

The current density (J)-voltage (V) dependence for a single bandgap is given by

$$J(V, E_g) = J_G(E_g) + J_R(V, E_g) \tag{213}$$

where J_G is the photogeneration current, J_R is the recombination current due to radiative recombination, and E_g is the bandgap of the absorber material. The generation current is calculated according to

$$J_G(E_g) = q \int_{E_g}^{E_{max}} \Gamma(E) dE \tag{214}$$

where q is the electronic charge, $\Gamma(E)$ is the photon flux at a given photon energy (E), and $E_{\max}$ is maximum photon energy in the solar spectrum. A minimum wavelength of 300 nm is used in the calculations, corresponding to a maximum photon energy of ~4.14 eV because photons above 4 eV contribute negligibly to the photon flux.[13] The recombination current density is calculated according to

$$J_{\mathrm{R}}(V, E_{\mathrm{g}}) = \frac{2\pi q}{c^2 h^3} \int_{E_{\mathrm{g}}}^{\infty} \frac{E^2}{\exp\left(\frac{E - qV}{kT}\right) - 1} dE \tag{215}$$

where c is the speed of light in vacuum, h is Planck's constant, k is Boltzmann's constant, and T is the temperature of the device (I assume the local surface temperature in these calculations).

The photovoltaic energy efficiency at a given operating voltage is written as

$$\eta_{\mathrm{PV}}(V, E_{\mathrm{g}}) = \frac{J(V, E_{\mathrm{g}})V}{\Gamma} \tag{216}$$

where Γ is the calculated total power flux at the Martian surface. The operating voltage can then be selected to maximize the efficiency for a given bandgap. In technoeconomic calculations (see below), I assume the device efficiency is 80% of the calculated detailed balance limit to account for absorber material and device inefficiencies (*i.e.*, nonradiative recombination losses not captured by the detailed balance limit).

The photoelectrochemical device energy efficiency is given by

$$\eta_{\mathrm{PEC}}(V, E_{\mathrm{g}}) = \frac{J(V, E_{\mathrm{g}})E^0}{\Gamma} \tag{217}$$

where E^0 is the minimum thermodynamic potential required to drive the electrochemical reaction (1.23 V for H_2 generation from water splitting). In practical devices, the operating voltage of the photoelectrochemical device will be larger than E^0 to account for anode and cathode overpotentials and resistive potential drop in the electrolyte and electrodes. Hence, for these devices the operating voltage is

$$V = E^0 + V_{\mathrm{o}} \tag{218}$$

where V_{o} is the overpotential associated with the above-mentioned losses. In all carry-along mass calculations (see below) I assume the overvoltage is 700 mV, corresponding to a practical minimum that also accounts for absorber material inefficiencies (*i.e.*, nonradiative recombination losses not captured by the detailed balance limit).[14]

For two- and three-bandgap tandem devices, I assume the absorber layers are connected optically and electronically in series. Generation and recombination currents are calculated as described above, with the modification that $E_{\max}$ is substituted with $E_{\mathrm{g},n-1}$ for absorber n (counted sequentially starting with the top absorber) to reflect the assumption that each absorber layer is

optically thick (*i.e*, absorbs all the above-bandgap light incident on its surface). In tandem devices, the total current density must be equal in each absorber layer, while the total operating voltage is given by the sum of the voltages developed across each cell. For example, for a three-absorber photovoltaic device,

$$J(V) = J_1(V_1, E_{g,1}) = J_2(V_2, E_{g,2}) = J_3(V_3, E_{g,3}) \tag{219}$$

and

$$V = V_1 + V_2 + V_3 \tag{220}$$

For tandem devices, the efficiency is calculated analogously to the single-junction devices but as a function of each absorber bandgap.

For all calculations the solar flux (Γ) at a given point on the Martian surface was calculated as described in Abel and Berliner *et al.*[16] over a full year of orbit. Then, the photovoltaic power generation rate or photoelectrochemical H_2 generation rate is calculated by

$$P_{PV} = \Gamma \eta_{PV} \tag{221}$$

and

$$\dot{m}_{H_2} = \frac{Z\Gamma}{E^0 nF} \eta_{PEC} \tag{222}$$

where Z is the molar mass of H_2, n is the number of moles of electrons required to produce one mole of H_2, and F is Faraday's constant. The optimal average production rate of power or H_2 generation is determined by maximizing P_{PV} and $\dot{m}_{H_2}$ by changing absorber bandgaps or bandgap combinations (for tandem cells). These values are then used to calculate carry-along mass requirements for solar cell arrays, as described next.

Carry-along mass requirements and minimization

I consider four different power production and energy storage scenarios for comparison (Fig. S1 in Appendix E): (1) nuclear power generation with the Kilopower system; (2) photovoltaic power generation with battery energy storage; (3) photovoltaic power generation with compressed H_2 energy storage; and (4) photoelectrochemical H_2 generation with compressed H_2 energy storage.

In all cases, power and/or energy demand is driven by continuous power required for habitat operations, including lighting, heating/cooling, pressurization, power draw for *in situ* resource utilization (ISRU) processes and for rover travel, and by materials demand for ISRU-based manufacturing. I assume that ammonia, methane, and plastics are produced using H_2 as the starting material (along with N_2 and CO_2 sourced from the atmosphere), which I use to calculate power demands based on water electrolysis to produce H_2. I note that methane could be diverted for bioproduction (dashed lines in Fig. S1 in Appendix E), although I don't explicitly consider this

scenario here because it wouldn't change the relative mass requirements of the four systems under consideration.

To compare the carry-along mass for each system, I include the mass of elements unique to or uniquely sized for a given energy supply scenario. For example, I consider the mass of photovoltaic cells because the area of cells necessary to power the habitat and ISRU manufacturing will be different depending on the strategy for energy storage. However, I don't include the mass of the Sabatier reactor for methane production, since this mass will be equivalent regardless of the upstream processes producing H_2 and collecting CO_2 from the atmosphere. In this way, I determine the mass contributions only of the uniquely necessary components for each energy supply scenario.

Nuclear power

Power derived from the Kilopower nuclear reactor system is fed directly to habitat power systems and to an electrolyzer producing H_2 for ISRU manufacturing. Hence, the power draw is given by:

$$P_{\mathrm{K}} = P_{\mathrm{Hab}} + \alpha_{\mathrm{E}}\left(\dot{N}\alpha_{\mathrm{HB}} + \dot{M}\alpha_{\mathrm{S}} + \dot{B}\alpha_{\mathrm{BP}}\right) \tag{223}$$

where P_{K} is the total power draw for Kilopower nuclear reactor system, P_{Hab} is the power draw for the habitat, α_{E} is the energy demand per unit of H_2 produced for the electrolyzer, $\dot{N}$ is the ammonia demand rate, $\dot{M}$ is the methane demand rate, $\dot{B}$ is the bioplastic demand rate, and α_i is the conversion factor between, *e.g.*, the ammonia demand rate and the H_2 demand rate for the Haber-Bosch process.

The carry-along mass requirements for this scenario is given by

$$M_{\mathrm{K}} = \frac{P_{\mathrm{K}}}{p_{\mathrm{K}}} + \frac{\left(\dot{N}\alpha_{\mathrm{HB}} + \dot{M}\alpha_{\mathrm{S}} + \dot{B}\alpha_{\mathrm{BP}}\right)}{p_{\mathrm{E}}} \tag{224}$$

where p_{K} is the specific power of the Kilopower reactor (6.25 W/kg) and p_{E} is the specific productivity of the electrolyzer (kg H_2/h/kg).

Photovoltaic power with battery energy storage (PV+B)

Power generated by photovoltaic cells can be transferred either directly to power-drawing systems (habitat systems, water electrolysis) or diverted to battery stacks for storage to enable continuous operation either at night or during low-sunlight days (due to high dust conditions). I define the fraction of power supplied directly to power systems as χ, which, for photovoltaic systems, can be thought of as the fraction of the day that solar cells produce equal or more power than what is consumed by power-drawing systems. Unless otherwise stated, I assume $\chi = 1/3$. Hence, the total power draw for the PV+B system is given by:

$$\begin{aligned} P_{\mathrm{PV+B}} = \chi P_{\mathrm{Hab}} + \frac{1-\chi}{\eta_{\mathrm{B}}} P_{\mathrm{Hab}} + \chi\alpha_{\mathrm{E}}\left(\dot{N}\alpha_{\mathrm{HB}} + \dot{M}\alpha_{\mathrm{S}} + \dot{B}\alpha_{\mathrm{BP}}\right) \\ + \frac{1-\chi}{\eta_{\mathrm{B}}}\alpha_{\mathrm{E}}\left(\dot{N}\alpha_{\mathrm{HB}} + \dot{M}\alpha_{\mathrm{S}} + \dot{B}\alpha_{\mathrm{BP}}\right) \end{aligned} \tag{225}$$

where $P_{\mathrm{PV+B}}$ is the total power draw for the PV+B system and η_{B} is the energy efficiency of the battery storage system. More compactly,

$$P_{\mathrm{PV+B}} = \left(\chi + \frac{1-\chi}{\eta_{\mathrm{B}}}\right)\left[P_{\mathrm{Hab}} + \alpha_{\mathrm{E}}\left(\dot{N}\alpha_{\mathrm{HB}} + \dot{M}\alpha_{\mathrm{S}} + \dot{B}\alpha_{\mathrm{BP}}\right)\right] \tag{226}$$

The carry-along mass required for the PV+B scenario is given by

$$M_{\mathrm{PV+B}} = \frac{P_{\mathrm{PV+B}}}{p_{\mathrm{PV}}} + \frac{\left[P_{\mathrm{Hab}} + \alpha_{\mathrm{E}}\left(\dot{N}\alpha_{\mathrm{HB}} + \dot{M}\alpha_{\mathrm{S}} + \dot{B}\alpha_{\mathrm{BP}}\right)\right] \times t_{\mathrm{store}}}{e_{\mathrm{B}}} + \frac{\left(\dot{N}\alpha_{\mathrm{HB}} + \dot{M}\alpha_{\mathrm{S}} + \dot{B}\alpha_{\mathrm{BP}}\right)}{p_{\mathrm{E}}} \tag{227}$$

where p_{PV} is the specific power of photovoltaic cells (kW/kg), t_{store} is the desired back-up power availability time, and e_{B} is the specific energy of the battery stack (units kWh/kg).

Photovoltaic power with H_2 energy storage (PV+E)

In this scenario, power generated by photovoltaic cells can either be directly fed to habitat systems or to an electrolyzer, which produces H_2 for consumption in ISRU manufacturing and for consumption by fuel cells the supply power to the habitat and other demands when direct power cannot (*e.g.*, at night). Here, the total power demand for the system is given by

$$P_{\mathrm{PV+E}} = \chi P_{\mathrm{Hab}} + \alpha_{\mathrm{E}}\dot{m}_{\mathrm{H_2}} \tag{228}$$

where $P_{\mathrm{PV+E}}$ is the total power draw for the PV+E system and $\dot{m}_{\mathrm{H_2}}$ is the flow rate of H_2 necessary to support the remaining system requirements. This flow rate is written as

$$\dot{m}_{\mathrm{H_2}} = \frac{(1-\chi)P_{\mathrm{Hab}}\alpha_{\mathrm{FC}} + \left(\dot{N}\alpha_{\mathrm{HB}} + \dot{M}\alpha_{\mathrm{S}} + \dot{B}\alpha_{\mathrm{BP}}\right)}{1 - \alpha_{\mathrm{HS}}\alpha_{\mathrm{FC}}} \tag{229}$$

where α_{FC} is the H_2 consumed per unit of energy produced by the fuel cell and α_{HS} is the energy consumed per unit of H_2 stored by the H_2 storage tanks (driven by compression of H_2).

The carry-along mass required for the PV+E scenario is given by

$$M_{\mathrm{PV+E}} = \frac{P_{\mathrm{PV+E}}}{p_{\mathrm{PV}}} + \frac{\dot{m}_{\mathrm{H_2}}}{p_{\mathrm{E}}} + \frac{P_{\mathrm{Hab}} + \alpha_{\mathrm{HS}}\dot{m}_{\mathrm{H_2}}}{p_{\mathrm{FC}}} + \frac{\left[P_{\mathrm{Hab}}\alpha_{\mathrm{FC}} + \left(\dot{N}\alpha_{\mathrm{HB}} + \dot{M}\alpha_{\mathrm{S}} + \dot{B}\alpha_{\mathrm{BP}}\right)\right] \times t_{\mathrm{store}}}{e_{\mathrm{HS}}} \tag{230}$$

where p_{FC} is the specific power of the fuel cell and e_{HS} is the specific mass of the H_2 storage tanks (in units $\mathrm{kgH_2/kg_{tank}}$).

Photoelectrochemical (PEC) H_2 generation with H_2 energy storage

This scenario uses a H_2 demand as opposed to a power demand to size the PEC array. The total H_2 demand rate is given by

$$\dot{m}_{\mathrm{H_2}} = \frac{P_{\mathrm{Hab}}\alpha_{\mathrm{FC}} + \left(\dot{N}\alpha_{\mathrm{HB}} + \dot{M}\alpha_{\mathrm{S}} + \dot{B}\alpha_{\mathrm{BP}}\right)}{1 - \alpha_{\mathrm{HS}}\alpha_{\mathrm{FC}}} \tag{231}$$

The carry-along mass required for the PEC scenario is given by

$$M_{\mathrm{PEC}} = \frac{\dot{m}_{\mathrm{H_2}}}{m_{\mathrm{PEC}}} + \frac{P_{\mathrm{Hab}} + \alpha_{\mathrm{HS}}\dot{m}_{\mathrm{H_2}}}{p_{\mathrm{FC}}} + \frac{\left[P_{\mathrm{Hab}}\alpha_{\mathrm{FC}} + \left(\dot{N}\alpha_{\mathrm{HB}} + \dot{M}\alpha_{\mathrm{S}} + \dot{B}\alpha_{\mathrm{BP}}\right)\right] \times t_{\mathrm{store}}}{e_{\mathrm{HS}}} \tag{232}$$

where m_{PEC} is the specific productivity (kg H_2/h/kg) of PEC cells. All parameters for these calculations are compiled in Table S1 in Appendix E.

6.4 Results and Discussion

The modeling overview and sample calculations for Jezero Crater are provided in Fig. 6.1. Sunlight incident on the surface originating from the top of the atmosphere (TOA) is mediated by orbital geometry and local atmospheric composition of gases, ice, and dust for a given location (Fig. 6.1A). The partial pressures of constituent gases (Fig. 6.1B) and the concentrations and effective radii of ice (Fig. 6.1C) and dust (Fig. 6.1D) particles were determined as a function of altitude above the surface and provided these data as inputs to a downstream radiative transfer model (diagrammed in Fig. 6.1E). The spectrally-resolved solar flux (Fig. 6.1F) was then calculated. At short wavelengths (<400 nm), light transmission through the atmosphere is limited by molecular scattering (primarily by CO_2) and scattering from dust particles.[17] Scattering and absorption by gas molecules is significant at wavelengths below 300 nm, but this region is not considered here because it represents a very small fraction of the available solar flux (<0.5%). Above 400 nm, most transmission loss is due to scattering from dust particles. This is markedly different from the case on Earth, where significant molecular absorption by water molecules limits the transmission of near-infrared light.

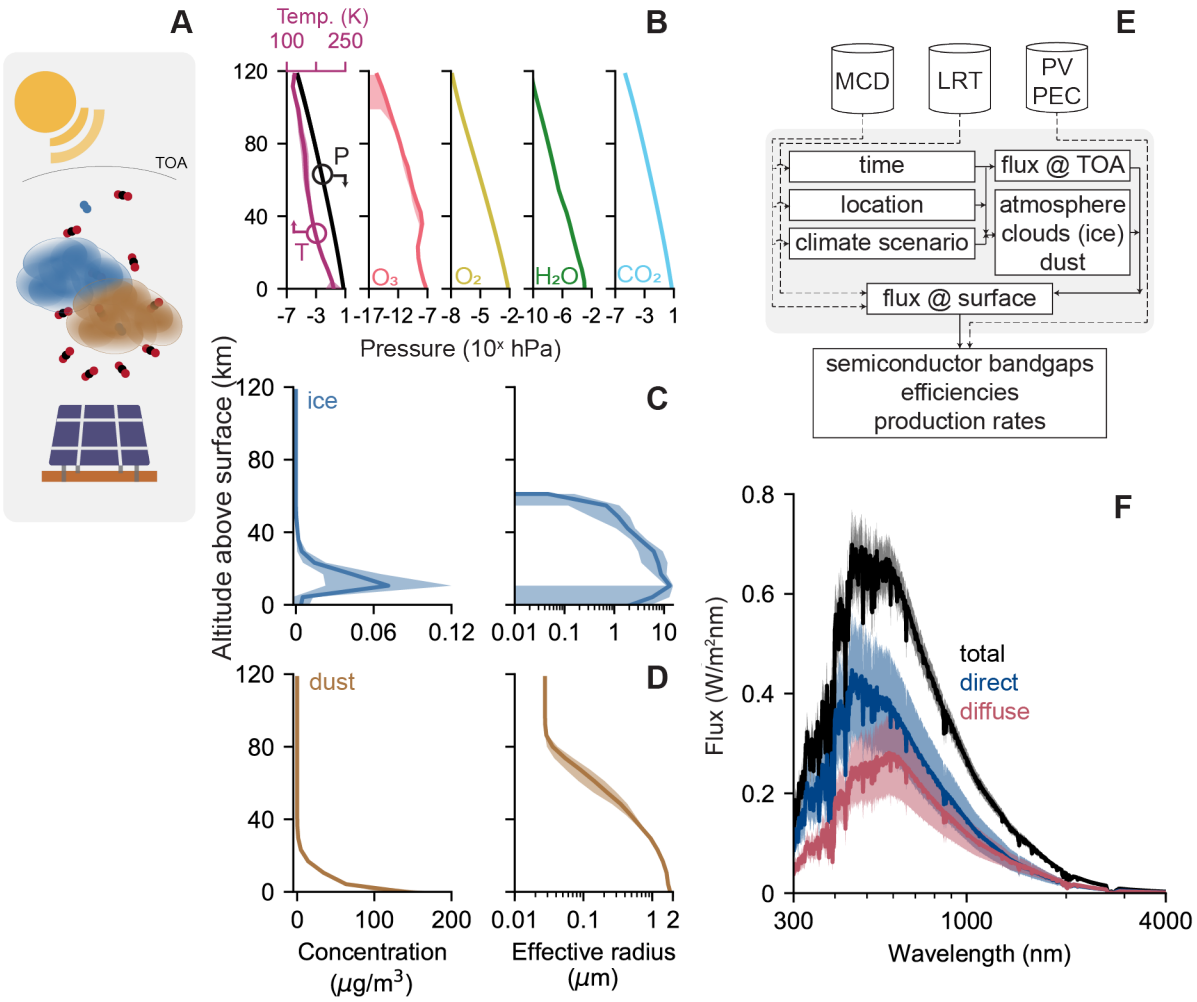

Figure 1. Overview and calculation of spectral flux using atmospheric data. (A) Sunlight incident on the solar cells is mediated by orbital geometry and local atmospheric composition of gases, ice, and dust. (**B**, **C**, and **D**) Temperature, partial pressure of atmospheric gases and concentration and effective radii of ice and dust particles as a function of altitude above the surface. (**E**) Information flow in the calculation scheme. Dotted lines represent functions used for calculations; solid lines represent data used as parameters. MCD, Mars Climate Database; LRT, LibRadtran. (**F**) Total (black), direct (blue), and diffuse (red) solar flux at Jezero Crater at solar noon averaged over the course of a typical Martian year. In (**B**), (**C**), (**D**), and (**F**), solid lines represent yearly averages and shaded regions represent the standard deviation as a result of seasonal variation.

The modeling results were used to inform efficiency calculations for PV and PEC devices producing electricity and H_2. Detailed balance calculations (see Computational Methods)[13,14] revealed ideal current-voltage characteristics for optically-thick devices consisting of 1-, 2-, and 3- junction PV and 1- and 2-junction PEC absorbers dependent on the bandgaps associated with each absorber (Fig. 6.2). Absorber numbers were selected to represent historical choices for PV devices on Martian rovers[18,19] and state-of-the-art PEC devices.[7,20,21] For PEC devices, I assumed an electrical load consisting of the thermodynamic redox potential and a variable overvoltage term

that incorporates loss mechanisms inevitable to a practical PEC device beyond radiative recombination already considered in the detailed balance.[13,14]

The maximum efficiency for PV devices increases from 31.4% (1-junction; E_g=1.23 eV) to 51.3% (3-junction; $E_{g,1}$ = 1.77 eV, $E_{g,2}$ = 1.16 eV, $E_{g,3}$ = 0.72 eV) with judicious choice of bandgaps (Fig. 6.2A-C). For PEC devices, optimal bandgap choice and efficiency are strongly dependent on system losses (Fig. 6.2D-F), reflecting the importance of careful device construction and catalyst selection.[15] For a realistic overvoltage loss of 700 mV,[13–15] a maximum solar-to-chemical efficiency of 27.8% is feasible for H_2 production.

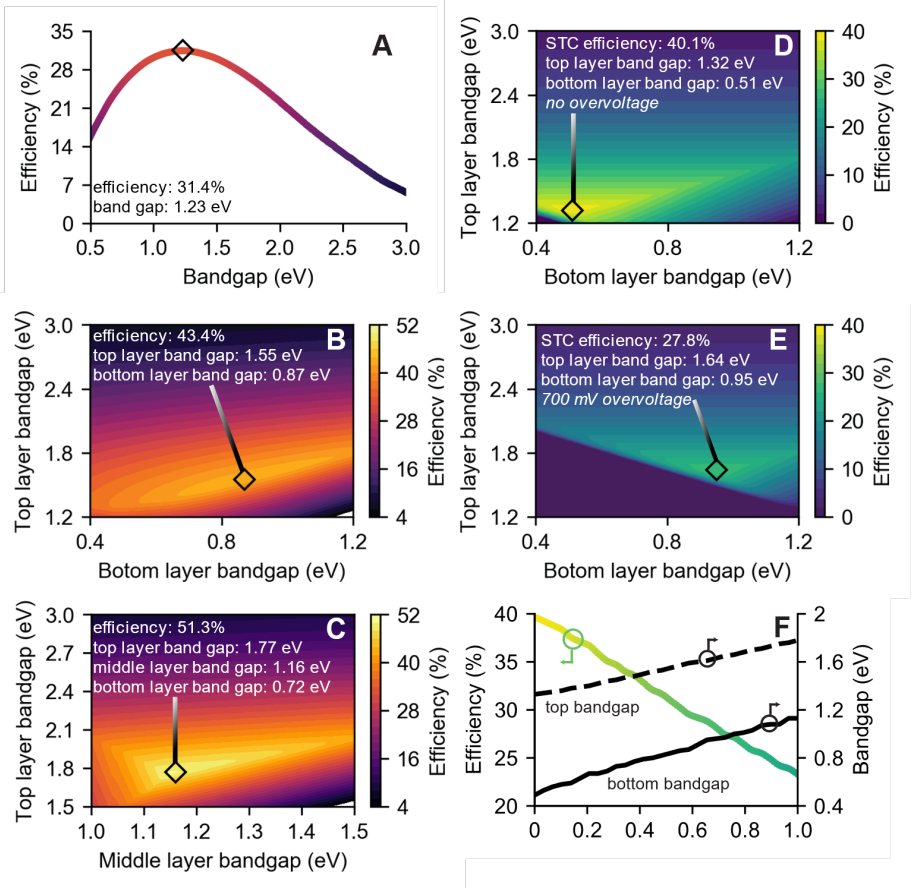

Figure 2. Theoretical efficiencies of PV and PEC devices. Detailed-balance efficiency limits as a function of bandgap energies for (**A**) single-junction, (**B**) two-junction, (**C**) three-junction photovoltaic devices. (**D**, and **E**) Solar-to-chemical (STC) efficiency for two-junction water splitting PEC devices producing molecular hydrogen with 0 mV (**D**) and 700 mV (**E**) overvoltage. (**F**) STC efficiency and optimal bandgaps for two-junction H_2-generating PEC devices as a function of overvoltage. Coloring in (**A**) and (**F**) correspond to contour coloring in (**B, C**) and (**D, E**) respectively. Average flux at solar noon at Jezero Crater is used as the reference solar spectrum.

To evaluate the potential for solar cells to supply power and commodity chemicals, I determined the maximum practical production capacity for 3-junction PV (operating at 80% of the detailed balance limit) and 2-junction PEC devices (with a 700-mV overvoltage) over the course of a Martian year (Fig. 6.3). Daily and seasonal variation in solar flux and temperature (Fig. 6.3A, B) cause substantial (~27% deviation from the yearly average) changes in production rates (Fig. 6.3C, D). I defined solar day (sol) 0 at a solar longitude (Ls) of 0° (vernal equinox) and assumed the solar cell operating temperature was equal to the surface temperature at all points. Dust storm season begins at sol ~372 (Ls~180°) and is primarily responsible for the drop in production capacity from a peak of ~1.7 kWh/m^2/day at Jezero Crater to a minimum of ~1.0 kWh/m^2/day at the height of dust storm intensity around the winter solstice (Ls ~270°, sol ~514).

Bandgap combinations that maximize production over the course of a year are 5-15% different from those that optimize efficiency at solar noon (Table S2 in Appendix E). For both PV and PEC devices, the top junction bandgap shifted up (for H_2-generating PEC devices, from 1.64 eV to 1.77 eV), while the bottom junction bandgap shifted down (from 0.95 eV to 0.83 eV). Hence, the photon absorption window for the bottom junction is broadened (by ~35% for the PEC device). This likely works to maximize productivity during the less dusty season (higher solar flux, Fig. 6.3B) by accounting for the relative blue-shift of surface-incident light (Fig. 6.1F) due to reduced scattering.

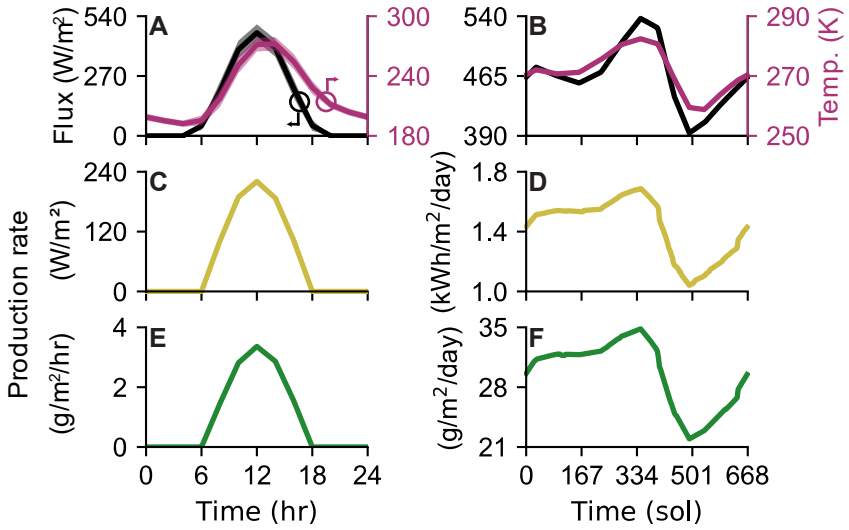

Figure 3. PV and PEC production rates. (**A**) Average and (**B**) daily maximum solar flux (black, left axis) and surface temperature (purple, right axis) as function of (**A**) time of day and (**B**) time of year. (**C**, **E**) average and (**D**, **F**) daily maximum production capacity of power (**C**, **D**) and H_2 (**E, F**) using 3-junction PV and 2-junction PEC cells as described in the main text. Solid lines in (**A**, **C**, **E**) correspond to averages; shaded areas represent the standard deviation as a result of seasonal variation. Jezero Crater is used as the location for plots.

Production capacity of power and commodity chemicals must compare favorably to the demand necessary to sustain a Martian habitat and depends on the outpost location on the planet surface (Fig. 6.4A). Moreover, energy storage capacity is crucial for solar-powered production systems because the sun sets daily. I therefore developed a detailed process model to account for power systems demands, including habitat maintenance (for example, habitat temperature control and pressurization), fertilizer production for agriculture, methane production for ascent propellant, and bioplastics production for spare parts manufacturing (Fig S1). I considered four different power generation scenarios: (1) nuclear power generation with the miniaturized nuclear fission Kilopower system; (2) PV power generation with battery energy storage (PV+B); (3) PV power generation with compressed H_2 energy storage produced via electrolysis (PV+E); and (4) PEC H_2 generation with compressed H_2 energy storage (PEC). In these calculations, I assumed a capacity factor of 75% to account for the solar flux deviation throughout the Martian year (Fig. 6.3) and sized energy storage systems (batteries or compressed H_2) to enable 1 full day of operations from reserve power. I then calculated the carry-along mass requirements for each of the power generation systems considered.

Of the three solar-driven power generation options, only the PV+E system outcompetes the nuclear system based on carry-along mass (Fig. 6.4B, C; supplementary Fig. S2 in Appendix E). For the PV+E system, the total carry-along mass increases from ~8.3 t near the equator to ~22.4 t near the South Pole (Fig. 6.4B), corresponding to the reduced average daily power generation of the PV array as the latitude is adjusted away from 0° (Fig. 6.4A). The nuclear power system is predicted to require ~9.5 t; hence, the PV+E system out-performs this option across ~50% of the planet's surface (Fig. 6.4B).

In addition to predicting production capacity and carry-along mass, the model provides design rules for optimal solar cell design. Optimal absorber bandgaps for the PV array are strongly dependent on the location on the surface of Mars (Fig. 6.4C-E). Several factors cause this variation: the total depth of the air column above a given location (*i.e.*, the difference between the height of the atmosphere and the altitude), gradients in dust and ice concentrations and particle radii, and orbital geometry effects that cause different effective air column thicknesses for locations near the poles. Lower elevations, higher dust and/or ice concentrations, and increasing distance away from the equator (near-polar latitudes) all cause an increase in the optical depth of the air column, which enhances the fraction of light that is scattered. Because the spectrum of scattered light is slightly red-shifted with respect to direct light (Fig. 6.1F), optimal bandgaps decrease to capture more lower-energy photons (Fig. 6.4C-E) in regions where the optical depth is higher. For example, at equivalent latitudes, the optimal bandgaps are wider for regions with higher elevations than for those with lower elevations because the fraction of light that gets scattered is lower. Regional differences in atmospheric conditions can drive countervailing effects; because the Northern Hemisphere experiences generally lower dust concentrations than the Southern Hemisphere, the lower elevation in the Northern Hemisphere does not result in (on average) narrower optimal bandgaps. Instead, the reduced dust concentration (relative to that of the Southern Hemisphere) results in a reduced optical depth, resulting in wider optimal bandgap combinations (Fig. 6.4C-E).

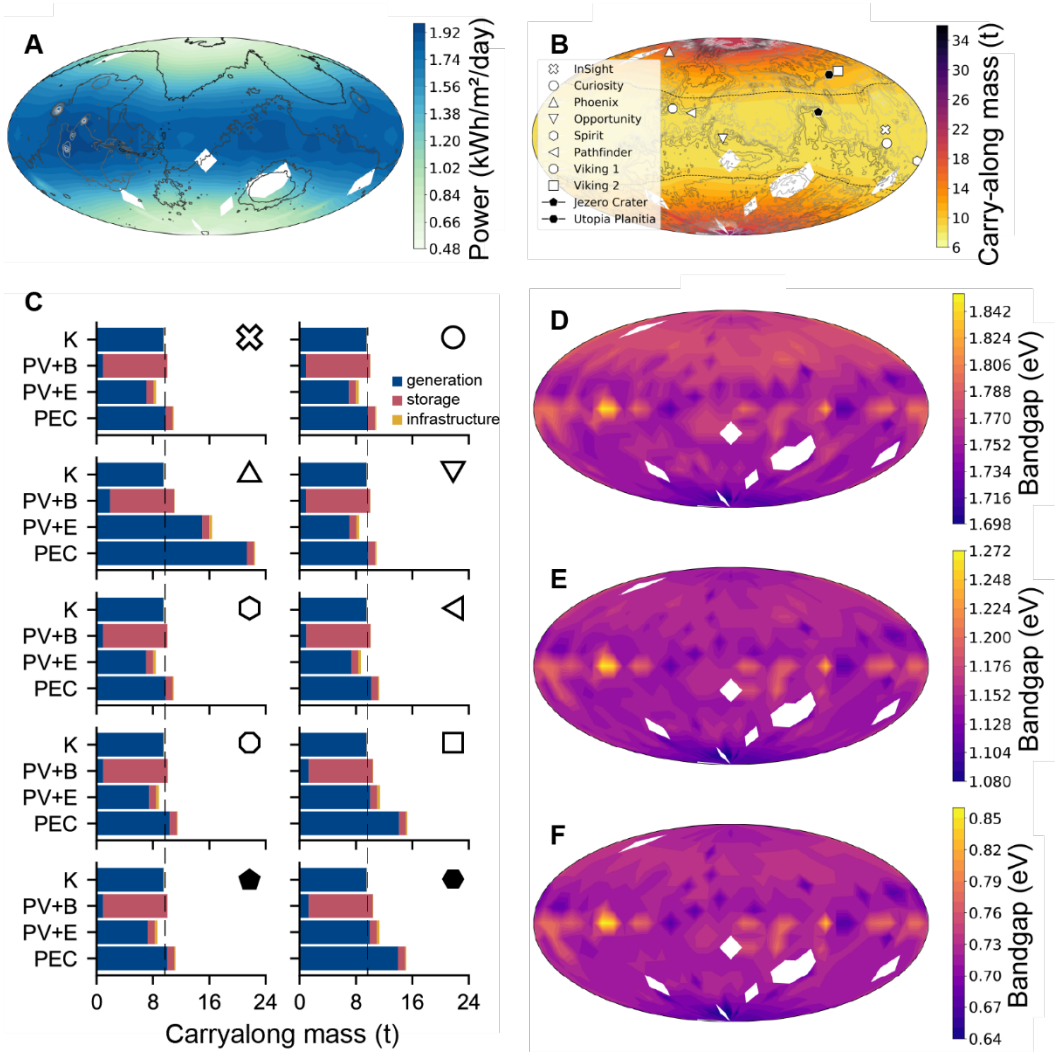

Figure 4. Solar productivity across the Martian surface. (**A**) Average daily solar power production capacity across the Martian surface. (**B**) Total carry-along mass required for power production using the PV+E generation system. Black dashed line corresponds to breakeven location with nuclear power generation. (**C**) Carry-along mass breakdown for locations in (**B**) for each power generation option. Optimal (**D**) top, (**E**) middle, (**F**) bottom bandgaps for the 3-junction PV array.

6.5 Conclusion

In summary, solar cell arrays designed with careful attention to semiconductor choice and device construction represent a promising technology for sustaining an Earth-independent crewed habitat on Mars. This analysis provides design rules for solar cells on the Martian surface and

shows that solar cells can offer substantial reduction in carry-along mass requirements compared to alternative technology over a large fraction of the planet's surface.

6.6 References

1 J. T. Wilson, V. R. Eke, R. J. Massey, R. C. Elphic, W. C. Feldman, S. Maurice and L. F. A. Teodoro, *Icarus*, 2018, **299**, 148–160.

2 C. R. Webster, P. R. Mahaffy, G. J. Flesch, P. B. Niles, J. H. Jones, L. A. Leshin, S. K. Atreya, J. C. Stern, L. E. Christensen, T. Owen, H. Franz, R. O. Pepin and A. Steele, *Science (80-.).*, 2013, **341**, 260–263.

3 G. Marbán and T. Valdés-Solís, *Int. J. Hydrogen Energy*, 2007, **32**, 1625–1637.

4 A. J. Berliner, J. M. Hilzinger, A. J. Abel, M. J. McNulty, G. Makrygiorgos, N. J. H. Averesch, S. Sen Gupta, A. Benvenuti, D. F. Caddell, S. Cestellos-Blanco, A. Doloman, S. Friedline, D. Ho, W. Gu, A. Hill, P. Kusuma, I. Lipsky, M. Mirkovic, J. Luis Meraz, V. Pane, K. B. Sander, F. Shi, J. M. Skerker, A. Styer, K. Valgardson, K. Wetmore, S.-G. Woo, Y. Xiong, K. Yates, C. Zhang, S. Zhen, B. Bugbee, D. S. Clark, D. Coleman-Derr, A. Mesbah, S. Nandi, R. M. Waymouth, P. Yang, C. S. Criddle, K. A. McDonald, L. C. Seefeldt, A. A. Menezes and A. P. Arkin, *Front. Astron. Sp. Sci.*, 2021, **8**, 1–14.

5 J. G. Chen, R. M. Crooks, L. C. Seefeldt, K. L. Bren, R. M. Bullock, M. Y. Darensbourg, P. L. Holland, B. Hoffman, M. J. Janik, A. K. Jones, M. G. Kanatzidis, P. King, K. M. Lancaster, S. V Lymar, P. Pfromm, W. F. Schneider and R. R. Schrock, *Science (80-.).*, 2018, **360**, eaar6611.

6 A. Ursúa, L. M. Gandía and P. Sanchis, *Proc. IEEE*, 2012, **100**, 410–426.

7 W. H. Cheng, M. H. Richter, M. M. May, J. Ohlmann, D. Lackner, F. Dimroth, T. Hannappel, H. A. Atwater and H. J. Lewerenz, *ACS Energy Lett.*, 2018, **3**, 1795–1800.

8 A. A. Menezes, J. Cumbers, J. A. Hogan and A. P. Arkin, *J. R. Soc. Interface*, , DOI:10.1098/rsif.2014.0715.

9 S. N. Nangle, M. Y. Wolfson, L. Hartsough, N. J. Ma, C. E. Mason, M. Merighi, V. Nathan, P. A. Silver, M. Simon, J. Swett, D. B. Thompson and M. Ziesack, *Nat. Biotechnol.*, 2020, **38**, 401–407.

10 B. G. Drake, S. J. Hoffman and D. W. Beaty, *IEEE Aerosp. Conf. Proc.*, 2010, 1–24.

11 P. L. Read, M. Collins, F. Forget, R. Fournier, F. Hourdin, S. R. Lewis, O. Talagrand, F. W. Taylor and N. P. J. Thomas, *Adv. Sp. Res.*, 1997, **19**, 1213–1222.

12 B. Mayer and A. Kylling, *Atmos. Chem. Phys. Discuss.*, 2005, **5**, 1319–1381.

13 M. C. Hanna and A. J. Nozik, *J. Appl. Phys.*, , DOI:10.1063/1.2356795.

14 H. Döscher, J. F. Geisz, T. G. Deutsch and J. A. Turner, *Energy Environ. Sci.*, 2014, **7**, 2951–2956.

15 S. Hu, C. Xiang, S. Haussener, A. D. Berger and N. S. Lewis, *Energy Environ. Sci.*, 2013, **6**, 2984–2993.

16 A. J. Abel, A. J. Berliner, M. Mirkovic, W. D. Collins, A. P. Arkin and D. S. Clark, *arXiv*.

17 Á. Vicente-Retortillo, F. Valero, L. Vázquez and G. M. Martínez, *J. Sp. Weather Sp. Clim.*, 2015, **5**, A33.

18 G. A. Landis, in *Conference Record of the Thirty-first IEEE Photovoltaic Specialists Conference, 2005.*, IEEE, pp. 858–861.

19 P. M. Stella, R. C. Ewell and J. J. Hoskin, in *Conference Record of the Thirty-first IEEE Photovoltaic Specialists Conference, 2005.*, IEEE, pp. 626–630.

20 J. L. Young, M. A. Steiner, H. Döscher, R. M. France, J. A. Turner and T. G. Deutsch, *Nat. Energy*, 2017, **2**, 17028.
21 J. Jia, L. C. Seitz, J. D. Benck, Y. Huo, Y. Chen, J. W. D. Ng, T. Bilir, J. S. Harris and T. F. Jaramillo, *Nat. Commun.*, 2016, **7**, 1–6.

Appendices

Appendix A: Supplementary information for Chapter 2

Supplementary tables

Table S1. Base case model parameters

Parameter	Value	Units	References
Operating conditions			
P_{CO_2}	0.2	atm	--
D_{gas}	100	hr^{-1}	--
T	30 (*C. necator*)	°C	DSMZ
	35 (*S. ovata*)		DSMZ
	37 (*E. coli*)		DSMZ
Microbial growth			
C. necator (formatotrophy)			
$\mu_{max,opt}$	0.18	hr^{-1}	1
$Y'_{X/F,maz}$	0.169	mol mol^{-1}	1
$Y'_{L/F,maz}$	0.11	mol mol^{-1}	calculated
θ_F	75.11	mM	1
$K_{S,F}$	10	µM	2
K_{S,O_2}	2.5	µM	3
pH_{opt}	7	--	1
pH_{min}	4	--	4
pH_{max}	9	--	4
$c_{Na,min}$	0.2	M	5
$c_{Na,max}$	1.05	M	5
C. necator (hydrogenotrophy)			
$\mu_{max,opt}$	0.18	hr^{-1}	6
Y'_{X/H_2}	0.19	mol mol^{-1}	6
Y'_{L/H_2}	0.11	mol mol^{-1}	calculated
K_{S,H_2}	20.4	µM	7
K_{S,O_2}	2.5	µM	3
K_{S,CO_2}	9.38	µM	7
pH_{opt}	7	--	1
pH_{min}	4	--	4
pH_{max}	9	--	4
$c_{Na,min}$	0.2	M	5
$c_{Na,max}$	1.05	M	5
S. ovata (acetogenesis)			
$\mu_{max,opt}$	0.044	hr^{-1}	8
K_{S,H_2}	20	µM	9
K_{S,CO_2}	20	µM	9
n	0.47	--	10
pH_{opt}	7	--	8
pH_{min}	4	--	assumed
pH_{max}	9	--	assumed

$c_{\mathrm{Na,min}}$	0.2	M	[5]
$c_{\mathrm{Na,max}}$	1.05	M	[5]
E. coli (acetotrophy)			
$\mu_{\mathrm{max,opt}}$	0.3	hr^{-1}	[11]
$Y'_{\mathrm{X/Ac}}$	0.936	mol mol^{-1}	[11]
$Y'_{\mathrm{L/Ac}}$	0.5	mol mol^{-1}	calculated
$K_{\mathrm{S,O_2}}$	2.5	µM	[3]
$K_{\mathrm{S,Ac}}$	10	µM	assumed
$K_{\mathrm{I,Ac}}$	0.83	M	[12]
$\mathrm{pH_{opt}}$	7	--	[11]
$\mathrm{pH_{min}}$	4	--	[13–15]
$\mathrm{pH_{max}}$	9.5	--	[13–15]
$c_{\mathrm{Na,min}}$	0.2	M	[5]
$c_{\mathrm{Na,max}}$	1.05	M	[5]
Acid/base reactions			
S_5	-71.0	J mol^{-1} K^{-1}	[16]
S_6	-92.4	J mol^{-1} K^{-1}	[16]
S_{w}	-80.66	J mol^{-1} K^{-1}	[16]
H_5	-0.12	kJ mol^{-1}	[16]
H_6	-0.4	kJ mol^{-1}	[16]
H_{w}	55.84	kJ mol^{-1}	[16]
K_7	1.38×10^{-4}	mol L^{-1}	[16]
k_{+1}	$\exp\left(1246.98 - \frac{6\times10^4}{T} - 183\ln(T)\right)$	s^{-1}	[17]
k_{+2}	59.44	s^{-1}	[17]
k_{+3}	2.23×10^3	L mol^{-1} s^{-1}	[17]
k_{+4}	6.0×10^9	L mol^{-1} s^{-1}	[17]
k_{+5}	10	s^{-1}	assumed
k_{+6}	10	s^{-1}	assumed
k_{+7}	10	s^{-1}	assumed
$k_{+\mathrm{w}}$	2.4×10^{-5}	L mol^{-1} s^{-1}	[18]
Gas/liquid mass transfer			
$k_{\mathrm{L}}a_{\mathrm{O_2}}$	200	hr^{-1}	assumed
A_{S}	0.56	m^{-1}	assumed
Diffusion coefficients			
$D_{\mathrm{CO_2}}$	$14.68 \times 10^{-9}\left(\frac{T}{217.206} - 1\right)^{1.997}$	m^2 s^{-1}	[19]
$D_{\mathrm{H_2}}$	$\frac{2.290\times10^{-11}}{\mu^{0.819}}T$	m^2 s^{-1}	[2]
$D_{\mathrm{O_2}}$	$10\text{^}\left[-8.410 + \frac{773.8}{T} - \left(\frac{506.4}{T}\right)^2\right]$	m^2 s^{-1}	[20]
Bunsen coefficients			
$A_{1,\mathrm{CO_2}}$	-60.2409	--	[21]
$A_{2,\mathrm{CO_2}}$	93.4517	--	[21]
$A_{3,\mathrm{CO_2}}$	23.3585	--	[21]
$B_{1,\mathrm{CO_2}}$	2.3517×10^{-2}	--	[21]
$B_{2,\mathrm{CO_2}}$	-2.3656×10^{-2}	--	[21]
$B_{3,\mathrm{CO_2}}$	4.7036×10^{-3}	--	[21]

A_{1,O_2}	-58.3877	--	[22]
A_{2,O_2}	85.8079	--	[22]
A_{3,O_2}	23.8439	--	[22]
B_{1,O_2}	3.4892×10^{-2}	--	[22]
B_{2,O_2}	1.5568×10^{-2}	--	[22]
B_{3,O_2}	-1.9387×10^{-3}	--	[22]
A_{1,H_2}	-39.9611	--	[23]
A_{2,H_2}	53.9381	--	[23]
A_{3,H_2}	16.3135	--	[23]
B_{1,H_2}	2.3517×10^{-2}	--	[23]
B_{2,H_2}	1.7566×10^{-2}	--	[23]
B_{3,H_2}	-2.3010×10^{-3}	--	[23]
pH controller			
K_C	0.1	hr^{-1}	--
τ	60	s	--
Combustion energy			
$\Delta_r G_X^0$	-479	kJ mol^{-1}	Note 4
$\Delta_r G_E^0$	-479	kJ mol^{-1}	Note 4
$\Delta_r G_{H_2}^0$	-260	kJ mol^{-1}	Note 4
$\Delta_r G_{FFA}^0$	-240	kJ mol^{-1}	Note 4
$\Delta_r G_{LLA}^0$	-1370	kJ mol^{-1}	Note 4
$\Delta_r G_{AAA}^0$	-870	kJ mol^{-1}	Note 4
CO_2 electrolyzer			
j	140	mA cm^{-2}	[24]
η_F	94	%	[24]
V_e	3.5	V	[24]
$c_{FFA,eff}$	2.08	M	[24]
H_2 electrolyzer			
j	1000	mA cm^{-2}	[25]
η_F	99	%	[25]
V_e	2.0	V	[25]
Electrodialysis – lactic acid			
a_{ED}	0.5154	kWh kg^{-1}	Note 5
b_{ED}	3.7×10^{-2}	Wh L^{-1}	Note 5
Γ_{max}	7.56	kg m^2 h^{-1}	Note 5
κ_M	51.5	g L^{-1}	Note 5
Electrodialysis – formic acid			
$\eta_{ED,F}$	3	%	Note 5
Γ_{max}	6.42	kg m^2 h^{-1}	Note 5
κ_M	26.3	g L^{-1}	Note 5

Table S2. Power breakdown for subprocesses.

Process power (kWh/kg CDW)	**Value**			
	Formatotrophic	*Knallgas*	*Acetogenic*	*Theoretical*

Substrate generation	47.26	22.61	19.55	5.32
Gas-liquid mass transfer and fluid mixing	0.48	0.43	1.38	0
Liquid heating	0.26	0.13	0.91	0
Direct air capture of CO_2	4.22	3.56	4.2	0.22
Haber-Bosch ammonia production	1.68	1.68	1.89	0.88
Chlor-alkali process (pH control)	0.38	0	4.01	0

Supplementary notes

Note 1: Optimizing full-system productivity in the acetate-mediated system

For both biomass and enzyme production, the acetotrophic portion of the acetate-mediated system is limited ultimately by O_2 gas-liquid mass transfer, as described in the main text. The feed concentration of acetate/ic acid, therefore, plays no role in determining the productivity of this reactor because the dilution rate can be adjusted in the opposite direction of a change in the feed acetate/ic acid concentration to maintain a constant productivity. Hence, the full-system productivity is maximized by maximizing the productivity of the upstream acetogenesis reactor. Acetate/ic acid productivity in the acetogenesis reactor is maximized by an intermediate normalized dilution rate of ~0.55 (Fig. S1a).

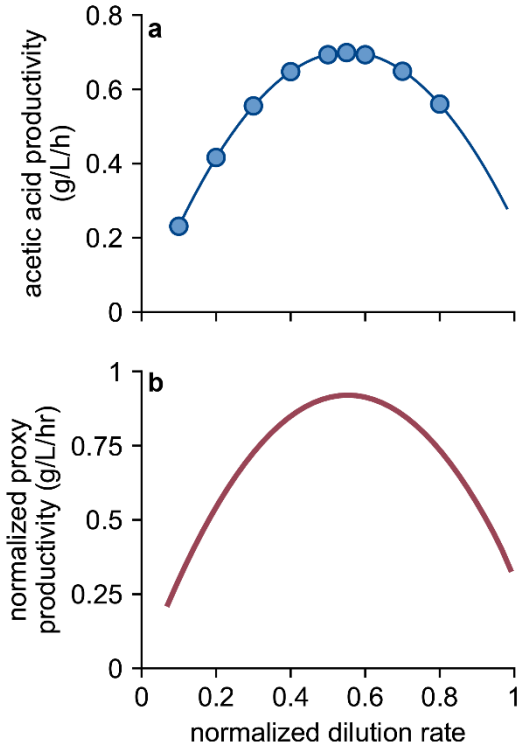

Figure S1. Optimal productivity in the acetate-mediated system. Maximum (**a**) acetate/ic acid productivity in the acetogenic reactor and (**b**) proxy full-system lactic acid productivity as a function of the normalized dilution rate in the acetogenic reactor. In both cases, the productivity is maximized at a normalized dilution rate of 0.55.

This trend is analogous to that of lactic acid production in the H_2-mediated case as described in the main text, where the product (lactic acid or acetic acid) concentration is negatively proportional to the dilution rate (in this case, $c_{\mathrm{AAA}} \propto -D_{\mathrm{liq,A}}$) such that the reactor productivity is negatively proportional to the square of the dilution rate (here, $\dot{m}_{\mathrm{AAA,A}} = D_{\mathrm{liq,A}} c_{\mathrm{AAA}}$, so $\dot{m}_{\mathrm{AAA,A}} \propto -\left(D_{\mathrm{liq,A}}\right)^2$.

The picture is more complicated for lactic acid production in this system because the acetate/ic acid feed concentration does contribute to the maximum lactic acid productivity in the acetotrophic reactor; specifically, $\dot{m}_{\mathrm{LLA,Ac}} \propto Y'_{\mathrm{L/Ac}} D_{\mathrm{liq,Ac}} c_{\mathrm{AAA,f}}$, where $c_{\mathrm{AAA,f}}$ represents the total acetate/ic acid concentration fed to the acetotrophic reactor. The maximum dilution rate is negatively proportional to the fed acetic acid concentration, that is, $D_{\mathrm{liq,Ac}} \propto -c_{\mathrm{AAA,f}}$ (see analogous description below in Note 2 for an explanation of this point), such that the productivity in the acetotrophic reactor is negatively proportional to the square of the acetate/ic acid feed concentration: $\dot{m}_{\mathrm{LLA,Ac}} \propto -\left(c_{\mathrm{AAA,f}}\right)^2$. From eq. 73 in the main text, the overall productivity of lactic acid is proportional to the productivity in the acetotrophic reactor and the ratio of the dilution rates in each reactor, equivalently $\dot{m}_{\mathrm{LLA,AA}} \propto \dot{m}_{\mathrm{LLA,Ac}} \left(\frac{D_{\mathrm{liq,A}}}{D_{\mathrm{liq,Ac}}}\right)$. The feed acetate/ic acid concentration to the acetotrophic reactor ($c_{\mathrm{AAA,f}}$) is equivalent to the exit acetate/ic acid concentration in the acetogenic reactor (c_{AAA}, above). The dilution rate in the acetotrophic reactor is negatively proportional to the feed concentration, which is in turn negatively proportional to the dilution rate in the acetogenic reactor. Hence, this dependence cancels out and $\dot{m}_{\mathrm{LLA,AA}} \propto \dot{m}_{\mathrm{LLA,Ac}}$, which indicates that $\dot{m}_{\mathrm{LLA,AA}} \propto -\left(c_{\mathrm{AAA,f}}\right)^2$, or equivalently, $\dot{m}_{\mathrm{LLA,A}} \propto -\left(D_{\mathrm{liq,A}}\right)^2$. We use the acetate feed rate ($D_{\mathrm{liq,Ac}} c_{\mathrm{AAA}}$) as a proxy for the overall productivity (since they are proportional to each other) and plot the relationship between this proxy and the dilution rate in the acetogenic reactor (Fig. S1b). Interestingly, the productivity proxy is maximized at the same normalized dilution rate (~0.55) that maximizes acetate/ic acid productivity. Hence, in all base-cases in our model, $\delta_{\mathrm{A}} = 0.55$ and $c_{\mathrm{AAA}} \approx 0.48$ M.

Note 2: Optimizing lactic acid productivity in the formate-mediated system

The productivity of lactic acid (and any generic product) is given by $D_{\mathrm{liq}} c_{\mathrm{LLA}}$. The titer, c_{LLA}, is proportional to the product of the lactic acid yield on formate ($Y'_{\mathrm{L/F}}$) and the feed concentration of formate ($c_{\mathrm{FFA,f}}$), that is, $c_{\mathrm{LLA}} \propto Y'_{\mathrm{L/F}} c_{\mathrm{FFA,f}}$. The dilution rate, D_{liq}, is typically thought of as independently controllable. However, the dilution rate is bounded by the maximum specific growth rate, μ_{max}. The maximum specific growth rate is a function of the sodium concentration, specifically, $\mu_{\mathrm{max}} \propto -c_{\mathrm{Na}}$ (eq. 47 in the main text). The sodium concentration, in turn, is a function of the lactic acid titer (specifically, $c_{\mathrm{Na}} \propto c_{\mathrm{LLA}}$) because sodium hydroxide is added to neutralize the proton liberated by lactic acid production. Hence, because c_{LLA} is proportional to $c_{\mathrm{FFA,f}}$, the maximum specific growth rate is negatively proportional to the feed concentration of formate/ic acid (that is, $\mu_{\mathrm{max}} \propto -c_{\mathrm{FFA,f}}$). This also means that the maximum dilution rate is negatively proportional to the feed concentration because the dilution rate is bounded by the specific growth rate ($D_{\mathrm{liq}} \propto -c_{\mathrm{FFA,f}}$). Together, this means the productivity of lactic acid in the formate mediated system ($\dot{m}_{\mathrm{LLA,F}}$) is negatively proportional to the squared feed

concentration of formate/ic acid, that is, $\dot{m}_{\mathrm{LLA,F}} \propto -\left(c_{\mathrm{FFA,f}}\right)^2$. Hence, we should expect to see a feed formate/ic acid concentration that maximizes the lactic acid productivity. Fig. S2 shows the maximum lactic acid productivity as a function of the feed concentration of formic acid and demonstrates a maximum productivity at ~5.1 M formate/ic acid. We therefore selected a 5.1 M feed stream for formatotrophic production of lactic acid and considered the life cycle impact of an electrodialysis process to concentrate the effluent from the CO_2 electrolysis reactor.

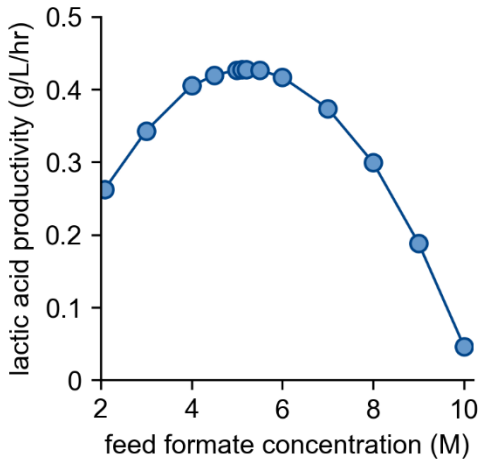

Figure S2. Optimal formate feed concentration for lactic acid productivity. Maximum lactic acid productivity as a function of the formate feed concentration. Maximum value of ~0.42 g/L/h is achieved at a feed concentration of ~5.1 M.

Note 3: Intrinsically safer operation of the H_2-mediated system

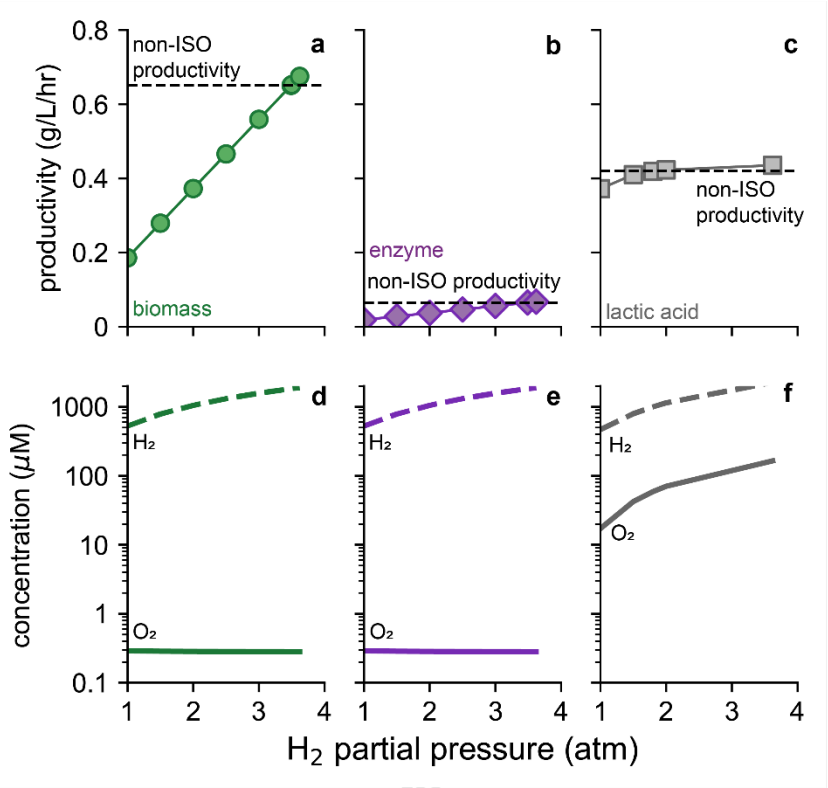

Figure S3. Intrinsically-safer operation of the H_2-mediated system. Productivity (**a**, **b**, **c**) and liquid-phase concentration of H_2 and O_2 (**d**, **e**, **f**) for the H_2-mediated EMP system under intrinsically-safer operation (ISO, p_{H2}:p_{O2} = 10:1) producing biomass (**a**, **d**), enzyme (**b**, **e**), and lactic acid (**c**, **f**). Horizontal black dashed lines in (**a**, **b**, **c**) correspond to the non-ISO (p_{H2}:p_{O2} = 1:0.21) base-case productivity for each of the three products. Low (<10 μM) O_2 concentration (solid lines in **d**, **e**, **f**) indicate O_2 gas-liquid mass transfer limitation on the productivity.

Note 4: calculating combustion energies

To calculate combustion energies, we adopted the strategy of Claassens *et al.*[26] Briefly, we used eQuilibrator[27] to calculate the $\Delta_r G'^0$ of the combustion reaction at a pH of 7.0 and ionic strength of 0.1 M. The biomass combustion energy was adopted from previous calculations.[28,29]

Note 5: calculating parameters for electrodialysis-based separations

Data from Hábová *et al.*[30] were used to determine parameters for membrane electrodialysis. Energy consumption as a function of lactic acid feed concentration was determined according to a linear model, eq. 87 in the main text. The linear model fit well to reported data ($R^2 = 0.73$), as shown in Fig. S4a. Lactic acid flux parameters were determined similarly and fit well to the proposed model ($R^2 = 0.85$), as shown in Fig. S4b.

Because relatively little data exist on formic acid concentration in membrane electrodialysis, we used the same dataset to estimate an average energy efficiency ($\eta_{ED,F}$) of 3%. We also used the same fitting parameters but modified the values to account for the different molar masses and diffusivities of lactic acid and formic acid.

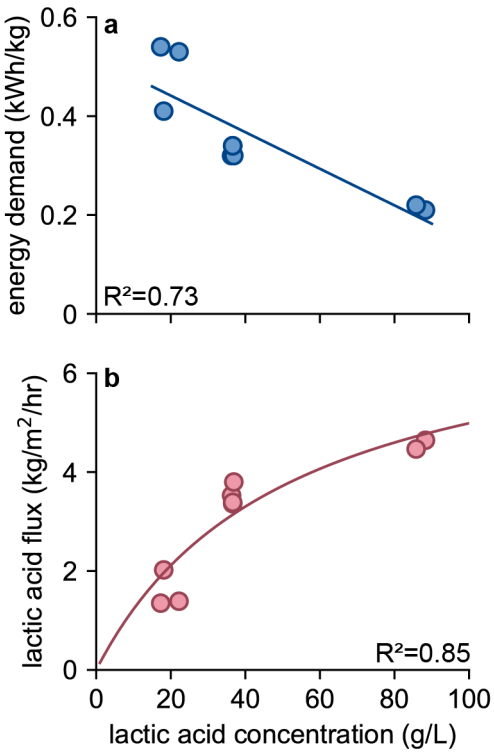

Figure S5. Fitting parameters for membrane electrodialysis. (**a**) energy demand and (**b**) through-membrane lactic acid flux for membrane electrodialysis as a function of the fed lactic acid concentration. Circles represent data from Hábová *et al.* and solid lines are fitted equations.

Note 7: reactor model parameter sensitivity calculations

When some parameters (*e.g.*, the maximum specific growth rate, $\mu_{\max,\mathrm{opt}}$) are adjusted, operating conditions such as the liquid dilution rate (D_{liq}) have different optima. In these cases, we identified the new optimal operating conditions and report system outputs based on these.

References

1 S. Grunwald, A. Mottet, E. Grousseau, J. K. Plassmeier, M. K. Popović, J. L. Uribelarrea, N. Gorret, S. E. Guillouet and A. Sinskey, *Microb. Biotechnol.*, 2015, **8**, 155–163.

2 A. J. Abel and D. S. Clark, *ChemSusChem*, 2021, **14**, 344–355.

3 D. A. Stolpera, N. P. Revsbech and D. E. Canfield, *Proc. Natl. Acad. Sci. U. S. A.*, 2010, **107**, 18755–18760.

4 A. Y. Dursun and O. Tepe, *J. Hazard. Mater.*, 2005, **126**, 105–111.

5 X. Wu, R. Altman, M. A. Eiteman and E. Altman, *Appl. Environ. Microbiol.*, 2014, **80**, 2880–2888.

6 A. Ishizaki and K. Tanaka, *J. Ferment. Bioeng.*, 1990, **69**, 170–174.

7 T. Takeshita and A. Ishizaki, *J. Ferment. Bioeng.*, 1996, **81**, 83–86.

8 X. C. Shi, P. L. Tremblay, L. Wan and T. Zhang, *Sci. Total Environ.*, 2021, **754**, 142440.

9 J. Chen, J. A. Gomez, K. Höffner, P. I. Barton and M. A. Henson, *Biotechnol. Biofuels*, 2015, **8**, 1–12.

10 A. G. Fast and E. T. Papoutsakis, *Curr. Opin. Chem. Eng.*, 2012, **1**, 380–395.

11 K. B. Andersen and K. Von Meyenburg, *J. Bacteriol.*, 1980, **144**, 114–123.

12 Y. Xiao, X. Feng, A. M. Varman, L. He, H. Yu and Y. J. Tang, *Ind. Eng. Chem. Res.*, 2012, **51**, 15855–15863.

13 E. F. Gale and H. M. R. Epps, *Biochem. J.*, 1942, **36**, 600–618.

14 D. Blankenhorn, J. Phillips and J. L. Slonczewski, *J. Bacteriol.*, 1999, **181**, 2209–2216.

15 K. A. Presser, T. Ross and D. A. Ratkowsky, *Appl. Environ. Microbiol.*, 1998, **64**, 1773–1779.

16 D. R. Lide, Ed., *CRC Handbook of Chemistry and Physics, 84th edition*, CRC Press, 84th edn., 2004.

17 K. G. Schulz, U. Riebesell, B. Rost, S. Thoms and R. E. Zeebe, *Mar. Chem.*, 2006, **100**, 53–65.

18 P. W. Atkins, *Physical Chemistry*, Oxford University Press, 4th edn., 1990.

19 R. E. Zeebe, *Geochim. Cosmochim. Acta*, 2011, **75**, 2483–2498.

20 P. Han and D. M. Bartels, *J. Phys. Chem.*, 1996, **100**, 5597–5602.

21 Ulf Riebesell, Victoria J. Fabry, Lina Hansson and Jean-Pierre Gattuso, *Guide to best practices for ocean acidification research and data reporting*, 2011.

22 R. F. Weiss, *Deep. Res. Oceanogr. Abstr.*, 1970, **17**, 721–735.

23 T. E. Crozier and S. Yamamoto1, *Solubility of Hydrogen in Water, Seawater, and NaCI Solutions*, 1974, vol. 19.

24 H. Yang, J. J. Kaczur, S. D. Sajjad and R. I. Masel, *J. CO2 Util.*, 2017, **20**, 208–217.
25 A. Buttler and H. Spliethoff, *Renew. Sustain. Energy Rev.*, 2018, 82, 2440–2454.
26 N. J. Claassens, C. A. R. Cotton, D. Kopljar and A. Bar-Even, *Nat. Catal.*, 2019, **2**, 437–447.
27 A. Flamholz, E. Noor, A. Bar-Even and R. Milo, *Nucleic Acids Res.*, , DOI:10.1093/nar/gkr874.
28 R. O. N. Grosz and G. Stephanopoulos, *Biotechnol. Bioeng.*, 1983, **25**, 2149–2163.
29 C. Liu, B. C. Colón, M. Ziesack, P. A. Silver and D. G. Nocera, *Science (80-.).*, 2016, **352**, 1210–1213.
30 V. Hábová, K. Melzoch, M. Rychtera and B. Sekavová, *Desalination*, 2004, **162**, 361–372.

Appendix B: Supplementary information for Chapter 3

Supplementary Table 1. Model parameters.

Parameter	Value	Units	References
Base case conditions			
T	303.15 (*C. necator*) or 310.15 (*E. coli*)	K	--
P_{tot}	1.2	atm	--
$y_{\mathrm{F,CO_2}}$	0.6	--	--
D	0.05	hr^{-1}	--
pH_0	7.1	--	--
$C_{\mathrm{NaNO_3,0}}$	20	mM	--
Reactor geometry			
S_{A}	100	m^{-1}	--
l_{BL}	100	μm	Supp. note 3
$l_{\mathrm{electrode}}$	100	μm	--
Diffusion coefficients[a]			
$D_{\mathrm{Na^+}}$	$\frac{3.984\times10^{-15}}{\mu}T$	$m^2\,s^{-1}$	Supp. note 4
$D_{\mathrm{NO_3^-}}$	$\frac{5.077\times10^{-15}}{\mu}T$	$m^2\,s^{-1}$	Supp. note 4
$D_{\mathrm{H^+}}$	$1.56\times10^{-10}(T-273.15)+5.49\times10^{-9}$	$m^2\,s^{-1}$	Supp. note 4
$D_{\mathrm{OH^-}}$	$4.52\times10^{-4}\exp\left[-1618\left(\frac{1}{T}+\frac{1}{273.15}\right)\right]$	$m^2\,s^{-1}$	Supp. note 4
$D_{\mathrm{CO_2}}$	$14.68\times10^{-9}\left(\frac{T}{217.206}-1\right)^{1.997}$	$m^2\,s^{-1}$	1
$D_{\mathrm{HCO_3^-}}$	$7.016\times10^{-9}\left(\frac{T}{204.028}-1\right)^{2.3942}$	$m^2\,s^{-1}$	1
$D_{\mathrm{CO_3^{2-}}}$	$5.447\times10^{-9}\left(\frac{T}{210.265}-1\right)^{2.193}$	$m^2\,s^{-1}$	1
D_{HCOOH}	$\frac{7.71\times10^{-12}}{\mu}T$	$m^2\,s^{-1}$	2
$D_{\mathrm{HCOO^-}}$	$\frac{4.34\times10^{-12}}{\mu}T$	$m^2\,s^{-1}$	Supp. note 4
$D_{\mathrm{H_2}}$	$\frac{2.290\times10^{-11}}{\mu^{0.819}}T$	$m^2\,s^{-1}$	Supp. note 4
$D_{\mathrm{O_2}}$	$10\text{^}\left[-8.410+\frac{773.8}{T}-\left(\frac{506.4}{T}\right)^2\right]$	$m^2\,s^{-1}$	3
Homogeneous reactions			
S_1	-96.31	$J\,mol^{-1}\,K^{-1}$	4
S_2	-148.1	$J\,mol^{-1}\,K^{-1}$	4
S_5	-71.0	$J\,mol^{-1}\,K^{-1}$	4
S_{w}	-80.66	$J\,mol^{-1}\,K^{-1}$	4
H_1	7.64	$kJ\,mol^{-1}$	4
H_2	14.85	$kJ\,mol^{-1}$	4
H_5	-0.12	$kJ\,mol^{-1}$	4
H_{w}	55.84	$kJ\,mol^{-1}$	4
k_1	$\exp\left(1246.98-\frac{6\times10^4}{T}-183\,ln(T)\right)$	s^{-1}	5
k_2	59.44	s^{-1}	5
k_3	2.23×10^3	$L\,mol^{-1}\,s^{-1}$	5
k_4	6.0×10^9	$L\,mol^{-1}\,s^{-1}$	5
k_5	10	s^{-1}	Supp. note 5
k_{w}	2.4×10^{-5}	$L\,mol^{-1}\,s^{-1}$	6

Bunsen coefficients[b]			
A_{1,CO_2}	-60.2409	--	[7]
A_{2,CO_2}	93.4517	--	[7]
A_{3,CO_2}	23.3585	--	[7]
B_{1,CO_2}	2.3517×10^{-2}	--	[7]
B_{2,CO_2}	-2.3656×10^{-2}	--	[7]
B_{3,CO_2}	4.7036×10^{-3}	--	[7]
A_{1,O_2}	-58.3877	--	[8]
A_{2,O_2}	85.8079	--	[8]
A_{3,O_2}	23.8439	--	[8]
B_{1,O_2}	3.4892×10^{-2}	--	[8]
B_{2,O_2}	1.5568×10^{-2}	--	[8]
B_{3,O_2}	-1.9387×10^{-3}	--	[8]
A_{1,H_2}	-39.9611	--	[9]
A_{2,H_2}	53.9381	--	[9]
A_{3,H_2}	16.3135	--	[9]
B_{1,H_2}	2.3517×10^{-2}	--	[9]
B_{2,H_2}	1.7566×10^{-2}	--	[9]
B_{3,H_2}	-2.3010×10^{-3}	--	[9]
Gas/liquid mass transfer			
$k_L a_{CO_2}$	300	hr^{-1}	assumed
$k_L a_{O_2}$	300	hr^{-1}	assumed
Electrochemistry			
A_{CO_2RR}	1.0613×10^{4}	mA cm^{-2}	[10]
A_{HER}	8.684×10^{-3}	mA cm^{-2}	[10]
A_{OER}	9.4×10^{-7}	mA cm^{-2}	[11]
E_{a,CO_2RR}	34.4	kJ mol^{-1}	[10,12]
$E_{a,HER}$	4.19	kJ mol^{-1}	[10,12]
$E_{a,OER}$	11 + pH	kJ mol^{-1}	[11]
$\alpha_{a/c,CO_2RR}$	0.5	--	[10]
$\alpha_{a/c,HER}$	0.5	--	[10]
$\alpha_{a,OER}$	1.5	--	[11]
$\alpha_{c,OER}$	0.1	--	[13]
Microbial growth			
$Y'_{X/F,max,Calvin}$	0.169	mol mol^{-1}	[14]
$Y'_{X/F,max,rGlyP,Cn}$	0.215	mol mol^{-1}	Supp. note 1
$Y'_{X/F,max,rGlyP,Ec}$	0.215	mol mol^{-1}	calculated
$Y'_{X/H,Calvin,Cn}$	0.191	mol mol^{-1}	[15]
$Y'_{X/H,rGlyP,Cn}$	0.348	mol mol^{-1}	Supp. note 1
$\theta_{F,Cn}$	75.11	mM	[14]
$\theta_{F,Ec}$	153	mM	[16]
$K_{S,F}$	10	mM	Supp. note 1
K_{S,O_2}	2.5	µM	[17]
K_{S,H_2}	20.4	µM	[18]
K_{S,CO_2}	9.38	µM	[18]
$\mu_{opt,Cn}$	0.18	hr^{-1}	[14]

$\mu_{\mathrm{opt,Ec}}$	0.18	hr^{-1}	assumed
$pH_{\mathrm{min,Cn}}$	4	--	Supp. note 6
$pH_{\mathrm{max,Cn}}$	9	--	Supp. note 6
$pH_{\mathrm{opt,Cn}}$	7	--	[14]
$pH_{\mathrm{min,Ec}}$	4	--	Supp. note 6
$pH_{\mathrm{max,Ec}}$	9.5	--	Supp. note 6
$pH_{\mathrm{opt,Ec}}$	7	--	Supp. note 6
$T_{\mathrm{min,Cn}}$	286.65	K	Supp. note 6
$T_{\mathrm{max,Cn}}$	308.15	K	Supp. note 6
$T_{\mathrm{opt,Cn}}$	303.15	K	[14]
$T_{\mathrm{min,Ec}}$	286.65	K	[19]
$T_{\mathrm{max,Ec}}$	321.15	K	[19]
$T_{\mathrm{opt,Ec}}$	310.15	K	[16]

[a] For diffusion coefficients, μ corresponds to the viscosity of water defined in the supplementary information and described by Kestin *et al*.[29]
[b] Note that the coefficients given here result in β in units M atm^{-1} for CO_2 and mL(gas at STP) L^{-1} (water) for O_2 and H_2.

Supplementary note 1: Stoichiometric cell yield calculations using complete or partial formate oxidation or H_2 oxidation coupled to CO_2 and/or formate reduction

Formate oxidation coupled to CO_2 fixation

Microbes support energy carrier (NAD(P)H and ATP) regeneration by using NAD^+-dependent formate dehydrogenases to catalyze the reaction

$$\mathrm{HCOO^-} + \mathrm{NAD^+} \rightarrow \mathrm{CO_2} + \mathrm{NADH} \tag{S96}$$

NADH is then used to regenerate ATP following aerobic respiration (oxidative phosphorylation):

$$\mathrm{NADH} + \mathrm{H^+} + \frac{1}{2}\mathrm{O_2} + (\mathrm{P/O})(\mathrm{ADP} + \mathrm{P_i}) \rightarrow \mathrm{NAD^+} + \mathrm{H_2O} + (\mathrm{P/O})\mathrm{ATP} \tag{S97}$$

where $\mathrm{P/O}$ is the oxidative phosphorylation ratio. I also assume NADH can be used to regenerate NAD(P)H according to:

$$1.33\mathrm{NADH} + \mathrm{NADP^+} + 0.33\mathrm{H^+} \rightarrow 1.33\mathrm{NAD^+} + \mathrm{NADPH} \tag{S98}$$

If the Calvin cycle is used to fix CO_2, seven ATP and five NADH are consumed to fix three CO_2 molecules into one pyruvate molecule:

$$\begin{aligned} 3\mathrm{CO_2} + 5\mathrm{NADH} + 7\mathrm{ATP} + 4\mathrm{H^+} \\ \rightarrow \mathrm{C_3H_3O_3^-} + 5\mathrm{NAD^+} + 7(\mathrm{ADP} + \mathrm{P_i}) + 3\mathrm{H_2O} \end{aligned} \tag{S99}$$

The reductive glycine pathway makes more efficient use of energy carriers:

$$\begin{aligned} 2\mathrm{HCOO^-} + \mathrm{CO_2} + 2\mathrm{NADPH} + 1\mathrm{NADH} + 2\mathrm{ATP} + 4\mathrm{H^+} \\ \rightarrow \mathrm{C_3H_3O_3^-} + 2\mathrm{NAD(P)^+} + 1\mathrm{NAD^+} + 2(\mathrm{ADP} + \mathrm{P_i}) \\ + 3\mathrm{H_2O} \end{aligned} \tag{S100}$$

in part because formate is a more energetic carbon source than CO_2. The resulting overall reaction for the production of pyruvate can then be written as

$$\left(5+\frac{7}{\mathrm{P/O}}\right)\mathrm{HCOO^-}+\left(4+\frac{7}{\mathrm{P/O}}\right)\mathrm{H^+}+\frac{7}{2(\mathrm{P/O})}\mathrm{O_2} \rightarrow \left(2+\frac{7}{\mathrm{P/O}}\right)\mathrm{CO_2}+\left(3+\frac{7}{\mathrm{P/O}}\right)\mathrm{H_2O}+\mathrm{C_3H_3O_3^-} \quad \text{(S101)}$$

for the Calvin cycle, and as

$$\left(5.66+\frac{2}{\mathrm{P/O}}\right)\mathrm{HCOO^-}+\left(4.66+\frac{2}{\mathrm{P/O}}\right)\mathrm{H^+}+\frac{1}{\mathrm{P/O}}\mathrm{O_2} \rightarrow \left(2+\frac{2}{\mathrm{P/O}}\right)\mathrm{CO_2}+\left(3.66+\frac{2}{\mathrm{P/O}}\right)\mathrm{H_2O}+\mathrm{C_3H_3O_3^-} \quad \text{(S102)}$$

for the reductive glycine pathway.

From these equations, I calculate theoretical pyruvate yields on formate of 0.118 – 0.136 mol/mol using the Calvin cycle and 0.150 – 0.158 mol mol^{-1} using the reductive glycine pathway for P/O ratios of 2 – 3. Therefore, to model the reductive glycine pathway, I increased the maximum experimental biomass yield on formate (0.169 mol mol^{-1}) by a factor of ~27% corresponding to the predicted increased pyruvate yield associated with a P/O ratio of 2.

Hydrogen oxidation supporting CO_2 fixation

NAD-reducing hydrogenases support energy carrier regeneration according to:

$$\mathrm{H_2}+\mathrm{NAD^+}\rightarrow \mathrm{H^+}+\mathrm{NADH} \quad \text{(S103)}$$

Oxidative phosphorylation is used to regenerate ATP according to eq. (S2). Both the Calvin cycle and the reductive glycine pathway can be used to fix carbon. For the Calvin cycle, the overall equation for the production of pyruvate is given by

$$\left(5+\frac{7}{\mathrm{P/O}}\right)\mathrm{H_2}+3\mathrm{CO_2}+\frac{7}{2(\mathrm{P/O})}\mathrm{O_2} \rightarrow \mathrm{C_3H_3O_3^-}+\mathrm{H^+}+\left(3+\frac{7}{\mathrm{P/O}}\right)\mathrm{H_2O} \quad \text{(S104)}$$

For the reductive glycine pathway, the overall equation is written as

$$\left(3.66+\frac{2}{\mathrm{P/O}}\right)\mathrm{H_2}+\mathrm{CO_2}+2\mathrm{HCOO^-}+\frac{1.33}{\mathrm{P/O}}\mathrm{O_2}+\mathrm{H^+} \rightarrow \mathrm{C_3H_3O_3^-}+\left(3.66+\frac{2}{\mathrm{P/O}}\right)\mathrm{H_2O} \quad \text{(S105)}$$

From these equations, I calculate theoretical pyruvate yields on H_2 of 0.118 – 0.136 mol mol^{-1} using the Calvin cycle and 0.215 – 0.231 mol mol^{-1} using the reductive glycine pathway for P/O ratios of 2 – 3. To model the reductive glycine pathway in *C. necator*, I increased the experimental biomass yield on H_2 (~0.191 mol mol^{-1}) by a factor of ~82%, corresponding to the predicted increased pyruvate yield associated with a P/O ratio of 2. I also updated the biomass-generating reaction to account for the additional consumption of formate and reduced consumption of CO_2.

Half-saturation Monod constant for formate

The half-saturation constant expresses the growth rate-dependence on substrate concentration. I am unaware of available literature reporting this value for *C. necator*. However, Pilát and Prokop report a $K_{S,F}$ of ~30–33 mM for the yeast strain *Candida boidini* 11 Bh.[20] Additionally, the soluble formate dehydrogenase in *C. necator* (then *Alcaligenes eutrophus*) was reported to have an apparent Michaelis-Menten half-saturation constant of 3.3 mM.[21] I used the geometric mean of these two values in the main text (10 mM) since I expect the half-saturation constant in *C. necator* to ultimately be controlled by its formate dehydrogenase. In Fig. S2, I plot the biomass productivity at 2.3 V as a function of $K_{S,F}$ for an S_A of 333 m^{-1} and with $y_{F,CO_2} = 0.6$. The biomass productivity decreases from ~1.56 g/L/hr at a $K_{S,F}$ of 0.1 mM to ~1.25 g/L/hr at a $K_{S,F}$ of 30 mM. Therefore, the biomass productivity changes by ~22% over a 300-fold change in $K_{S,F}$, indicating that the actual value of $K_{S,F}$ does not significantly impact the conclusions of the model.

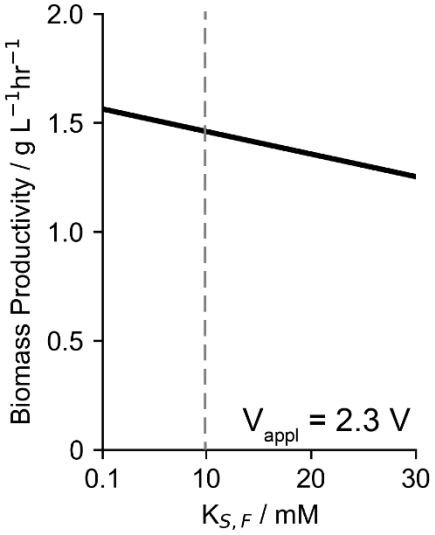

Figure S1. Effect of formate half-saturation coefficient on biomass productivity. Biomass productivity at an applied voltage of 2.3 V as a function of formate half saturation coefficient for $y_{F,CO_2} = 0.6$ and an S_A of 333 m^{-1}. Dashed line at 10 mM corresponds to the $K_{S,F}$ value used in the main text.

Supplementary note 2: derivation of the maximum productivity as a function of dilution rate for a simplified mediated MES reactor model

For a simplified mediated MES reactor model, a generic substrate (S) is generated at an electrode surface and consumed by cells (X). The mass balances for substrate and cells are given as

$$\frac{dS}{dt} = -DS - \frac{1}{Y_{\mathrm{X/S}}}\mu X + \frac{iS_{\mathrm{A}}}{nF} \tag{S106}$$

and

$$\frac{dX}{dt} = \mu X - DX \tag{S107}$$

where D is the dilution rate, $Y_{X/S}$ is the cell yield, μ is the specific growth rate, i is the current density, S_A is the electrode surface area to reactor volume ratio, n is the number of electrons required to produce one S molecule, and F is Faraday's constant. Using standard Monod growth kinetics,

$$\mu = \mu_{\max}\left(\frac{S}{K_{\mathrm{S}} + S}\right) \tag{S108}$$

the steady-state substrate concentration and cell density are given by

$$S_{\mathrm{SS}} = \frac{DK_{\mathrm{S}}}{\mu_{\max} - D} \tag{S109}$$

and

$$X_{\mathrm{SS}} = -Y_{\mathrm{X/S}}S_{\mathrm{SS}} + \frac{Y_{\mathrm{X/S}}iS_{\mathrm{A}}}{DnF} \tag{S110}$$

The biomass productivity, DX_{SS}, is maximized with respect to the dilution rate by setting the derivative equal to 0:

$$\frac{d(DX_{\mathrm{SS}})}{dD} = -Y_{\mathrm{X/S}}\frac{DK_{\mathrm{S}}\mu_{\max}}{(\mu_{\max} - D)^2} = 0 \tag{S111}$$

which is satisfied only when $D = 0$. To confirm that this is a maximum, I confirm the second derivative is also <0:

$$\frac{d^2(DX_{\mathrm{SS}})}{dD^2} = \frac{-Y_{\mathrm{X/S}}K_{\mathrm{S}}\mu_{\max}(\mu_{\max} + D)}{(\mu_{\max} - D)^3} < 0 \tag{S112}$$

Supplementary note 3: boundary layer thickness

The electrochemical reduction of CO_2 depends strongly on the concentration polarization that develops due to CO_2 consumption at the electrode surface.[22] Clark *et al.* measured the hydrodynamic boundary layer thickness (l_{BL}) in an aqueous cell as a function of the CO_2 gas flowrate (*i.e.* fluid mixing was generated *via* gas bubbling) and showed that increasing the flowrate decreased the boundary layer thickness but that the effect diminishes as the flowrate increased, approaching a minimum of ~40 μm at CO_2 flowrates >~20 sccm.[22] The model assumes a boundary layer of 100 μm (associated with a CO_2 flowrate of ~5 sccm in their system) in the main text and

show how reduced boundary layer thicknesses impact biomass productivity in Fig. S2. The biomass productivity increases from ~1.5 g/L/hr to ~1.95 g/L/hr by decreasing the boundary layer thickness from 100 μm to 40 μm at an applied potential of 2.3 V (Fig. S2). Significant further enhancement is possible (to >2.5 g/L/hr) by further reducing the boundary layer but this will likely require substantial agitation or other strategies to reduce the boundary layer thickness. Boundary layer thickness therefore plays a significant role in limiting the productivity of integrated MES systems and should be measured in experimental systems.

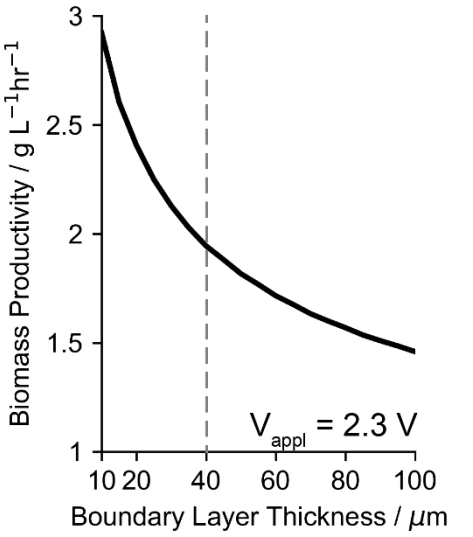

Figure S2. Effect of boundary layer thickness on biomass productivity. Biomass productivity at an applied voltage of 2.3 V as a function of the hydrodynamic boundary layer thicknesses (l_{BL}) for $y_{\mathrm{F,CO_2}} = 0.6$ and an S_{A} of 333 m^{-1}. Dashed line at 40 μm corresponds to the minimum boundary layer thickness Clark *et al.* (supplementary ref. 1) was able to achieve via fluid mixing due solely to gas bubbling.

Supplementary note 4: diffusion coefficients of Na^+, NO_3^-, $HCOO^-$, H^+, OH^-, and H_2

To estimate the temperature-dependence of the Na^+ diffusion coefficient, I used the well tabulated value of 1.334×10^{-15} m^2/s at 25 °C[4] and used this value to fit a Stokes radius (R) according to the Stokes-Einstein relationship:

$$R = \frac{k_{\mathrm{B}}T}{6\pi D\mu} \tag{S113}$$

where k_{B} is the Boltzmann constant and μ is the viscosity of water (in Pa·s). Once R is calculated, I used this value to determine the diffusion coefficient as a function of temperature by rearranging this same equation. I used the same procedure to determine the temperature-dependent diffusivity of NO_3^- ions, this time using the value of 1.7×10^{-9} m^2/s at 25 °C.[23]

To describe the diffusivity of formate as a function of temperature, I used the Wilke-Chang correlation modified for carboxylic acids[2]:

$$D = \frac{6.6\times10^{-6}(XM)^{1/2}T}{\mu V^{0.6}} \tag{S114}$$

where $X = 2.6$ is the solvent constant for water, M is the molecular weight of the solvent, and V is the molar volume of the solute at normal boiling point.

To estimate the diffusion coefficients of H^+ and OH^- in water, I used specific conductance data from Light *et al.*[24] and converted these values to diffusion coefficients following the Nernst-Planck equation, resulting in

$$D_i = \frac{RT\lambda_i}{z^2F^2} \tag{S115}$$

where λ_i is the specific conductance. I then fit these data to equations of the form:

$$D_i = Aexp\left[-B\left(\frac{1}{T}+\frac{1}{273.15}\right)\right] \tag{S116}$$

following Weng *et al.*[25] This equation fit OH^- data well (Fig. S3A) but did not sufficiently capture H^+ data (Fig. S3B). For H^+, I attempted two additional fits, one following the functional form of CO_2, HCO_3^-, and CO_3^{2-} diffusion coefficients (eq. S15) and a simple linear relationship (eq. S16):

$$D_i = A\left(\frac{T}{B}-1\right)^C \tag{S117}$$

$$D_i = m(T-273.15)+b \tag{S118}$$

The linear relationship fit best (Fig. S3B), so I used this relationship to describe the diffusivity of H^+ ions.

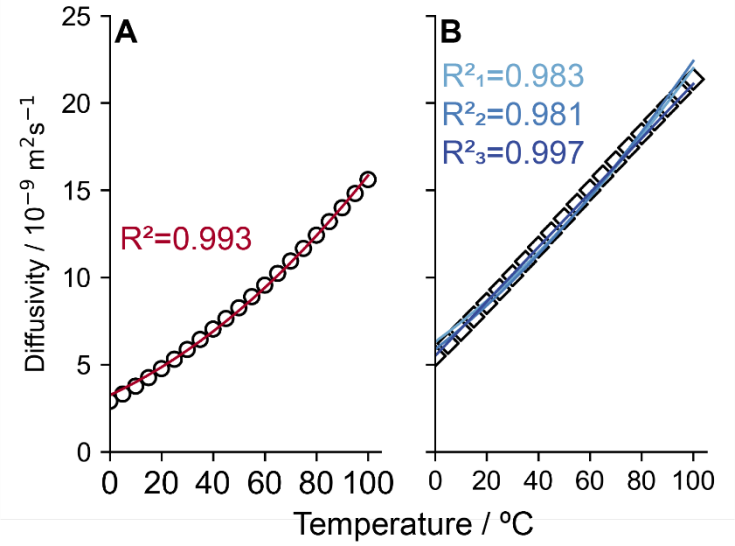

Figure S3. Fitted diffusion coefficients of OH^- and H^+ ions. Experimental diffusion coefficients (black symbols) and fitted equations (colored, solid lines) for (**A**) OH^- and (**B**) H^+ ions. Subscripts "1", "2", and "3" in (**B**) correspond to eqs. S14, S15, and S16 in the supplementary text.

For molecular hydrogen (H_2), the diffusivity was given as a function of temperature by Ferrell and Himmelblau[26] as:

$$D\ (\mathrm{cm^2s^{-1}}) = \frac{4.8\times10^{-7}T}{\mu^{\alpha}}\left(\frac{1+\Lambda^{*2}}{V_{\mathrm{m}}}\right)^{0.6} \tag{S119}$$

where μ is the viscosity of water (in centipoise), V_m is the molar volume of H_2 at its normal boiling point, Λ^* is the quantum parameter, and α is given by

$$\alpha = \frac{\sigma}{\left(\frac{V_\mathrm{m}}{N}\right)^{1/3}} \tag{S120}$$

where σ is the Lennard-Jones 6-12 potential. I used $V_\mathrm{m} = 22.3897\ \mathrm{cm^3 mol^{-1}}$ from Scott and Brickwedde[27], $\sigma = 2.96 \times 10^{-10}\ m$ and $\Lambda^* = 1.729$ from Nakanishi *et al.*,[28] and calculated μ (note that this equation returns μ in Pa·s, so the appropriate unit conversion to centipoise must be made) according to[29]

$$\log_{10} \mu = \frac{247.8}{T - 140} - 4.6173 \tag{S121}$$

Unfortunately, the resulting equation for D did not sufficiently capture the data originally tabulated by Ferrell and Himmelblau, possibly because I used the viscosity of pure water. To account for this discrepancy, I adjusted the numerical fitting parameter, resulting in:

$$D = \frac{5.61 \times 10^{-7} T}{\mu^{\alpha}} \left(\frac{1 + \Lambda^{*2}}{V_\mathrm{m}}\right)^{0.6} \tag{S122}$$

I simplified this equation to have only numerical parameters (except for the viscosity) in Table S1. The original and improved fits are shown overlaid on the experimental data in Fig. S4.

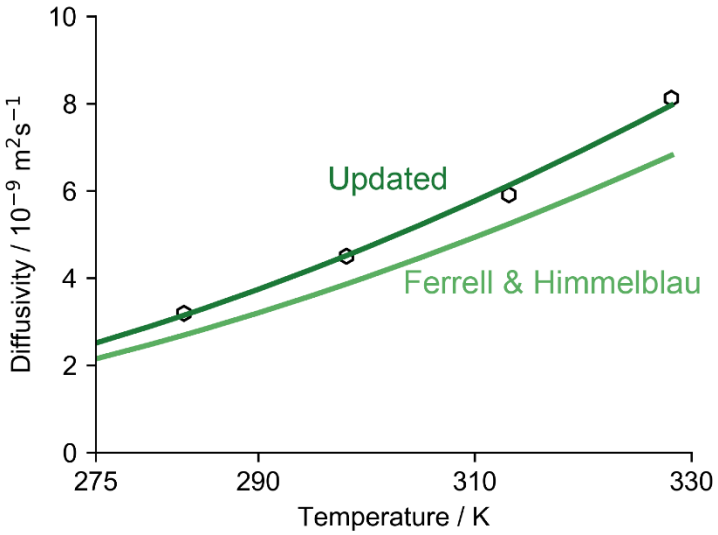

Figure S4. Fitted diffusion coefficient of H_2. Experimental diffusion coefficients (black symbols) and fitted equations (colored, solid lines) for H_2. The lighter solid line corresponds to the unmodified equation reported by Ferrell and Himmelblau (supplementary ref. 26); the darker solid line corresponds to the modification reported here.

Supplementary note 5: Rate constant of the formic acid dissociation reaction

I am unaware of literature reporting the rate of formic acid dissociation to formate and protons in water. In Fig. S5 I plot the biomass productivity (Fig. S5A) and pH at each electrode surface and in the reactor bulk (Fig. S5B) as a function of the forward rate constant k_5. Changes of <1% occur as k_5 varies from 0.1 s^{-1} to 100 s^{-1}, indicating that this parameter has a minimal influence on the conclusions of the model.

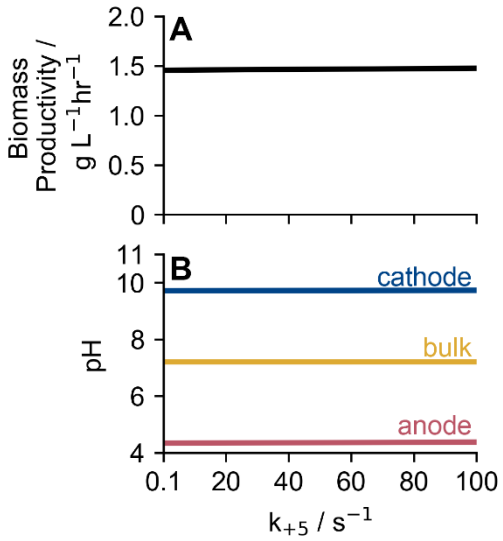

Figure S5. Effect of formic acid dissociation rate constant. (A) Biomass productivity and (B) pH at different locations in the reactor at an applied voltage of 2.3 V as a function of the formic acid dissociation rate constant for $y_{F,CO_2} = 0.6$ and an S_A of 333 m^{-1}.

Supplementary note 6: pH and temperature growth ranges for *C. necator* and *E. coli*

Growth of *E. coli* has been reported at pHs as low as 4.0 and in excess of 9.0.[30–32] I used this range for both *E. coli* and *C. necator* and tightened the window to 4.0–9.0 for *C. necator* since this is the widest range I am familiar with in the literature.[33] Under the conditions modeled in this study, the pH in the bulk phase never exceeded a pH of ~7.5.

For the temperature effects on the growth rate of *C. necator*, I used the lower bound set by *E. coli*,[19] and the upper bound reported by Dursun and Tepe.[33] Note, however, that I only considered *C. necator* and *E.* coli growth at their optimal temperatures (30 °C and 37 °C, respectively), since temperature effects due to other factors appeared to cancel out (see section the in the main text). Future modeling studies that include heat generation effects by microbial growth can use the temperature-dependent framework reported here.

Supplementary references

1 R. E. Zeebe, *Geochim. Cosmochim. Acta*, 2011, **75**, 2483–2498.
2 D. E. Bidstrup and C. J. Geankoplis, *J. Chem. Eng. Data*, 1963, **8**, 170–173.
3 P. Han and D. M. Bartels, *J. Phys. Chem.*, 1996, **100**, 5597–5602.
4 D. R. Lide, Ed., *CRC Handbook of Chemistry and Physics, 84th edition*, CRC Press, 84th edn., 2004.
5 K. G. Schulz, U. Riebesell, B. Rost, S. Thoms and R. E. Zeebe, *Mar. Chem.*, 2006, **100**, 53–65.
6 P. W. Atkins, *Physical Chemistry*, Oxford University Press, 4th edn., 1990.
7 Ulf Riebesell, Victoria J. Fabry, Lina Hansson and Jean-Pierre Gattuso, *Guide to best*

practices for ocean acidification research and data reporting, 2011.
8 R. F. Weiss, *Deep. Res. Oceanogr. Abstr.*, 1970, **17**, 721–735.
9 T. E. Crozier and S. Yamamoto1, *Solubility of Hydrogen in Water, Seawater, and NaCI Solutions*, 1974, vol. 19.
10 H. Li and C. Oloman, *J. Appl. Electrochem.*, 2007, **37**, 1107–1117.
11 L. C. Weng, A. T. Bell and A. Z. Weber, *Energy Environ. Sci.*, 2019, **12**, 1950–1968.
12 H. Wang, D. Y. C. Leung and J. Xuan, *Appl. Energy*, 2013, **102**, 1057–1062.
13 S. Haussener, C. Xiang, J. M. Spurgeon, S. Ardo, N. S. Lewis and A. Z. Weber, *Energy Environ. Sci.*, 2012, **5**, 9922–9935.
14 S. Grunwald, A. Mottet, E. Grousseau, J. K. Plassmeier, M. K. Popović, J. L. Uribelarrea, N. Gorret, S. E. Guillouet and A. Sinskey, *Microb. Biotechnol.*, 2015, **8**, 155–163.
15 A. Ishizaki and K. Tanaka, *J. Ferment. Bioeng.*, 1990, **69**, 170–174.
16 S. Kim, S. N. Lindner, S. Aslan, O. Yishai, S. Wenk, K. Schann and A. Bar-Even, *Nat. Chem. Biol.*, 2020, **16**, 538–545.
17 D. A. Stolpera, N. P. Revsbech and D. E. Canfield, *Proc. Natl. Acad. Sci. U. S. A.*, 2010, **107**, 18755–18760.
18 T. Takeshita and A. Ishizaki, *J. Ferment. Bioeng.*, 1996, **81**, 83–86.
19 S. L. Herendeen, R. A. VanBogelen and F. C. Neidhardt, *J. Bacteriol.*, 1979, **139**, 185–194.
20 P. Pilát and A. Prokop, *Folia Microbiol. (Praha).*, 1976, **21**, 306–314.
21 J. Friedebold and B. Bowien, *J. Bacteriol.*, 1993, **175**, 4719–4728.
22 E. L. Clark, J. Resasco, A. Landers, J. Lin, L. T. Chung, A. Walton, C. Hahn, T. F. Jaramillo and A. T. Bell, *ACS Catal.*, 2018, **8**, 6560–6570.
23 C. Picioreanu, M. C. M. Van Loosdrecht and J. J. Heijnen, *Water Sci. Technol.*, 1997, **36**, 147–156.
24 T. S. Light, S. Licht, A. C. Bevilacqua and K. R. Morash, *Electrochem. Solid-State Lett.*, , DOI:10.1149/1.1836121.
25 L. C. Weng, A. T. Bell and A. Z. Weber, *Phys. Chem. Chem. Phys.*, 2018, **20**, 16973–16984.
26 R. T. Ferrell and D. M. Himmelblau, *AIChE J.*, 1967, **13**, 702–708.
27 R. B. Scott and F. G. Brickwedde, *J. Res. Natl. Bur. Stand. (1934).*, 1937, **19**, 237.
28 K. Nakanishi, E. M. Voigt and J. H. Hildebrand, *J. Chem. Phys.*, 1965, **42**, 1860–1863.
29 J. Kestin, M. Sokolov and W. A. Wakeham, *J. Phys. Chem. Ref. Data*, 1978, **7**, 101.
30 E. F. Gale and H. M. R. Epps, *Biochem. J.*, 1942, **36**, 600–618.
31 D. Blankenhorn, J. Phillips and J. L. Slonczewski, *J. Bacteriol.*, 1999, **181**, 2209–2216.
32 K. A. Presser, T. Ross and D. A. Ratkowsky, *Appl. Environ. Microbiol.*, 1998, **64**, 1773–1779.
33 A. Y. Dursun and O. Tepe, *J. Hazard. Mater.*, 2005, **126**, 105–111.

Appendix C: Supplementary information for Chapter 4

Supplementary Tables

Supplementary Table 1. Stoichiometric analysis for energy carrier regeneration with O_2 and NO_3^- respiration.

Terminal electron acceptor	Proton motive force (H^+ to periplasm)	QH_2	NADH	ATP	Fd_{red}
O_2	$3/e^-$	$1/2e^-$	$1/3.33e^-$	$1/e^-$	$1/4e^-$
NO_3^-	$0.8/e^-$	$1/2e^-$	$1/7e^-$	$1/3.75e^-$	$1/9.5e^-$

Supplementary Table 2. Energetic requirements of carbon fixation for pyruvate production.

Pathway	Energetic requirements to fix one mole of pyruvate				
	Mol NAD(P)H	Mol ATP	Mol Fd_{red}	Mol e^-	Reference
Calvin (O_2)	5	7	0	23.67	[1]
Calvin (NO_3^-)	5	7	0	61.25	[1]
Reductive TCA	3	2	2	47.5	[2]
Fuchs-Holo (O_2)	6	7	0	25	[3,4]
Fuchs-Holo (NO_3^-)	6	7	0	66.25	[3,4]
Wood-Ljungdahl	2	1	3	46.25	[5]

Supplementary Table 3. Model parameters.

Parameter	Value	Unit	Reference/Notes
Operating conditions			
T	298	K	
P	1	atm	
D	1	hr^{-1}	
pH_0	7.4	--	
$C_{\mathrm{NaNO_3},0}$	0.250	M	
Reactor geometry			
l_{bl} (boundary layer thickness)	100	μm	Supplementary note 6
l_{m} (membrane thickness)	100	μm	Assumed
ϵ_{p} (biocathode porosity)	0.48	--	Assumed
r_{cell} (cell radius)	0.5	μm	Assumed
Diffusion coefficients			

D_{Na^+}	1.34×10^{-5}	$cm^2\ s^{-1}$	6
$D_{NO_3^-}$	1.7×10^{-5}	$cm^2\ s^{-1}$	7
D_{H^+}	9.311×10^{-5}	$cm^2\ s^{-1}$	8
D_{OH^-}	5.293×10^{-5}	$cm^2\ s^{-1}$	8
$D_{HCO_3^-}$	1.185×10^{-5}	$cm^2\ s^{-1}$	8
$D_{CO_3^{2-}}$	5.293×10^{-5}	$cm^2\ s^{-1}$	8
D_{CO_2}	1.91×10^{-5}	$cm^2\ s^{-1}$	9
Homogeneous reactions			
K_1	$10^{-6.37}$	M	10
k_{+1}	3.71×10^{-2}	s^{-1}	10
K_2	$10^{-10.32}$	M	10
k_{+2}	59.44	s^{-1}	10
k_{+3}	2.23×10^3	$L\ mol^{-1}\ s^{-1}$	10
k_{+4}	6.0×10^9	$L\ mol^{-1}\ s^{-1}$	10
K_w	10^{-14}	M^2	11
k_{+w}	2.4×10^{-5}	$mol\ L^{-1}\ s^{-1}$	11
Charge transfer reactions			
E^0_{OER}	1.23	V	11
$i_{0,OER}$	1×10^{-8}	$A\ cm^{-2}$	12
$\alpha_{a,OER}$	1.7	--	12
$\alpha_{c,OER}$	0.1	--	12
$E^0_{CO_2RR}$	0.314	V	Supplementary note 7
i_{0,CO_2RR}	1.38×10^{-8}	$A\ cm^{-2}$	13
α_{a,CO_2RR}	0.5	--	13
α_{c,CO_2RR}	0.5	--	13
Enzyme kinetics			
$k_{cat,CBB}$	10	s^{-1}	Supplementary note 2
$k_{cat,rTCA}$	17.5	s^{-1}	Supplementary note 2
$k_{cat,FH}$	2.1	s^{-1}	Supplementary note 2
$k_{cat,WL}$	0.47	s^{-1}	Supplementary note 2
$n_{E,CBB}$	7.08×10^4	$cell^{-1}$	Supplementary note 2
$n_{E,rTCA}$	7.08×10^4	$cell^{-1}$	Supplementary note 2
$n_{E,FH}$	7.08×10^4	$cell^{-1}$	Supplementary note 2
$n_{E,WL}$	2.124×10^5	$cell^{-1}$	Supplementary note 2
Electrode conductivity			
$\kappa_{s,anode}$	1×10^4	$S\ m^{-1}$	Assumed
$\kappa_{s,biocathode}$	1×10^{-1}	$S\ m^{-1}$	Supplementary note 8
Gas-liquid mass transfer			
k_La	5×10^{-1}	s^{-1}	Supplementary note 5
γ	1.25×10^4	$mol\ m^{-3}\ s^{-1}$	14

Supplementary Table 4. Technology readiness levels (TRLs) for dEMP

TRL	Description
1	electroautotrophy capable (predicted)

2	dEMP capable (experimentally verified)
3	dEMP capable AND genetic tools (single gene knockout or gene disruption, single gene expression from a plasmid)
4	dEMP capable AND advanced genetic tools (multiple gene insertion/deletion, substantial rewiring of metabolic flux)
5	dEMP capable AND advanced genetic tools AND industrial scaling (deployed in a commercial bioprocess)

Supplementary notes

Supplementary note 1. Comparing intracellular diffusion and reaction rates for substrates in carbon fixation pathways. The rate of intracellular diffusion of substrates can be compared to the reaction rate of substrates using the Thiele modulus, defined for Michaelis-Menten kinetics by:[15]

$$\phi = \frac{r_{\text{cell}}}{3}\left(\frac{v_{\max}}{K_{\text{M}} D_{\text{eff}}}\right)^{1/2} \tag{123}$$

where r_{cell} is the microbial cell radius, $v_{\max}$ is the maximum reaction rate per unit volume of catalyst, K_{M} is the Michaelis-Menten constant for the enzyme, and D_{eff} is the effective diffusion coefficient of the substrate inside the microbial cell. Using values tabulated in the main text (Table 3), with $K_{\text{M}} = 0.34$ mM[16], $\phi = 9.8 \times 10^{-3}$ for carbon fixation with CO_2 as the substrate and RuBisCo as the rate-limiting enzyme.

This low value ($\phi = 9.8 \times 10^{-3}$) indicates that the carbon fixing reaction is limited intracellularly by enzymatic catalysis and not by intracellular diffusion; in other words, energy carriers and CO_2 have complete and effectively immediate access to intracellular enzymes once generated at or delivered to the cell surface. Therefore, the carbon fixing reaction can be treated as occurring at the cell surface without any loss in model validity. This calculation supports the application of eq. 41 in the model, which enables treatment of intracellular biochemical reactions as occurring on the cell surface.

Note that this assumption becomes less valid as the turnover number, intracellular enzyme concentration, or cell radius increases and therefore caution that this assumption should be re-evaluated for larger microbes, higher turnover numbers, or increased expression of rate-limiting enzymes. In cases where this assumption is no longer valid, a model that includes an effectiveness factor for enzyme utilization can be included following, for example, the method of Vos *et al.*[17] for biofilm catalysts.

Supplementary note 2. Number density and turnover number of CO_2-fixing enzymes in autotrophic organisms. Key enzymes in carbon fixation pathways are well characterized.[18,19] I used BRENDA (http://brenda-enzymes.org) to identify turnover number ranges for RuBisCo (Calvin cycle), ATP citrate lyase (rTCA cycle), 4-hydroxybutyryl-CoA dehydratase (Fuchs-Holo cycle), and carbon monoxide dehydrogenase (Wood-Ljungdahl pathway). I selected representative turnover numbers from Mueller-Cajar *et al.*[20] and Tcherkez *et al.*[16] for RuBisCo, Wahlund *et al.*[21]

and Kim *et al.*[22] for ATP citrate lyase, Hawkins *et al.* for 4-hydroxybutyryl-CoA dehydratase,[23] and Roberts *et al.*[24] for carbon monoxide dehydrogenase.

To estimate the enzyme count in cells, I used the approximate total enzyme amount in *E. coli*[25] and estimated the fraction of total cell protein comprised by key enzymes in carbon fixation pathways. I used a value of 3% for RuBisCo, ATP citrate lyase, and 4-hydroxybutyryl-CoA dehydratase based on estimates for RuBisCo by Bar-On *et al.*[26] and 9% for carbon monoxide dehydrogenase based on an estimate by Roberts *et al.*[24]

Supplementary note 3. Supplementary note 7: O_2 limited production. To determine the O_2-limited production rate, I simplify the model by assuming that O_2 is fully saturated in the bulk electrolyte and assume that aerobic respiration functions at O_2 concentrations >3 nM.[27] Pyruvate production in this scenario is limited primarily by the low solubility in electrolyte solutions (~176 μM at atmospheric O_2 partial pressure in the system).

Supplementary note 4: An applied voltage minimum as a function of biofilm thickness. The fundamental tradeoff between reduced activation overpotential and increased transport losses when the biofilm thickness increases implies the existence of a minimum in the applied voltage necessary to achieve a specific pyruvate production rate. For microbes fixing carbon using the rTCA cycle in the model, this minimum occurs at 85, 60, and 54 μm for 5, 10, and 15 μmol/cm^2/hr production rates, respectively. However, these minima are likely to be highly sensitive to the properties of specific reactors and operating conditions: at 10 μmol/cm^2/hr, biofilms between 35 and 94 μm thick operate at voltages within 1% of the calculated applied voltage minimum, suggesting that minute adjustments of biofilm thickness (*e.g.* via dilution rate or agitation[28,29]) are unlikely to improve efficiency at a given production rate.

Supplementary note 5: CO_2 gas-liquid mass transfer. Typical ranges for $k_{\mathrm{L}}a$ are 10^{-2}–10^{0} s^{-1} .[30] I picked $k_{\mathrm{L}}a = 5 \times 10^{-1}$ s^{-1} to limit the conditions under which the reactor is limited by the mass transfer of CO_2 from the gas phase to the liquid phase. I show the impact of the mass transfer coefficient on the operating voltage in Fig. S1. The mass transfer coefficient has only a slight impact on the operating voltage for a given production rate. However, below certain values, the CO_2 feed rate is insufficient to match the consumption rate in the biocathode layer. Thus, the mass transfer coefficient should be maintained at values >~0.1 to ensure sufficient CO_2 to drive high production rates.

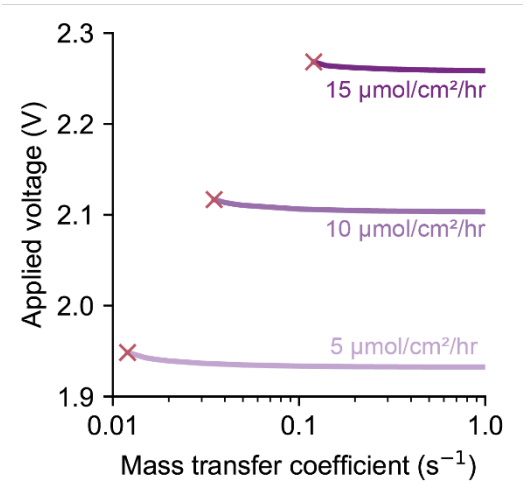

Figure S1. Effect of CO_2 gas-liquid mass transfer on operating voltage. Voltage necessary to operate the MES reactor for a 50 µm biofilm fixing carbon using the rTCA cycle as a function of the CO_2 gas-liquid mass transfer coefficient ($k_L a$) for different pyruvate production rates. Red crosses indicate the point at which CO_2 feed to the reactor is insufficient to match the consumption rate in the biocathode.

Supplementary note 6: boundary layer thickness. The (bio)electrochemical reduction of CO_2 depends strongly on the concentration polarization that develops because bicarbonate solutions are relatively weak buffers. The pH and CO_2 concentration at the biocathode surface and throughout the biocathode layer will vary significantly from that in the bulk electrolyte; the magnitude of this variance will depend primarily on the hydrodynamics of the electrochemical cell. Clark *et al.* measured hydrodynamic boundary layer thicknesses in an aqueous cell as function of the CO_2 gas flowrate and showed that increasing the flowrate decreased the boundary layer thickness but that the effect diminishes as the flowrate was increased, approaching a minimum of ~40 µm at CO_2 flowrates greater than ~20 sccm.[31] The model assumes a boundary layer of 100 µm (associated with a CO_2 flowrate of ~5 sccm in their system) in the main text and I show how reduced boundary layer thicknesses impact operating voltages for the reactor geometry in Fig. S2. At a production rate of 15 µmol/cm^2/hr, the total voltage increases from ~2.17 V to ~2.26 V, indicating an increased overpotential of ~100 mV. Reduced boundary layer thickness, therefore, plays an important role in MES reactor efficiency at high production rates (current densities) and is worth considering in the context of expected reactor productivity.

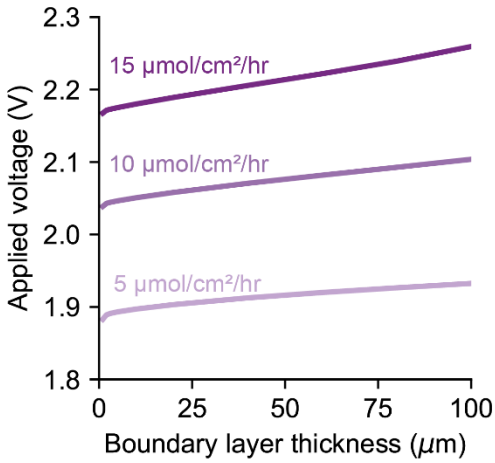

Figure S2. Effect of boundary layer thickness on supplied voltage. Voltage necessary to operate the MES reactor at for a 50 µm biofilm fixing carbon using the rTCA cycle as a function of the boundary layer thickness for different pyruvate production rates.

Supplementary note 7: equilibrium potential for mtrCAB reduction. Multiheme cytochromes typically exhibit a potential window rather than a single equilibrium potential at which electrons are reversibly exchanged with an electron (*e.g.* –400 mV to +100 mV *vs.* SHE for MtrF, an MtrC analog) corresponding to the different redox environments for each heme group within the protein.[32,33] I use –0.1 V *vs.* SHE at pH 7 (0.314 V *vs.* RHE) as a representative midpoint of the potential window for MtrCAB that remains electropositive enough to reduce the quinone pool (~–80 mV *vs.* SHE at pH 7).

Supplementary note 8: biofilm conductivity. The importance of biofilm conductivity in determining the productivity of biofilms in either microbial fuel cells or MES systems is the subject of ongoing debate. Some experimental studies have suggested conductivity is a critical parameter, while some modeling studies suggest the opposite.[34,35] I use a biofilm conductivity of 1 mS/cm to match that of the *Geobacter sulfurreducens* BEST strain and plot the dependency of cell voltage on biofilm conductivity in Fig. S3. Increasing conductivity above ~1 mS/cm confers only a very small reduction in total applied voltage for low production rates. However, at higher production rates (>10 µmol/cm^{2}hr), the necessary applied voltage increases rapidly for biofilm conductivities <1 mS/cm. Conductivities above 1 mS/cm have been readily achieved for *Geobacter* spp. biofilms, so synthetic strategies to increase biofilm conductivity (*e.g.* using metal or semiconducting nanowire scaffolds) are unlikely to result in significant performance enhancements in the short term, especially relative to the additional cost and complexity of fabrication.

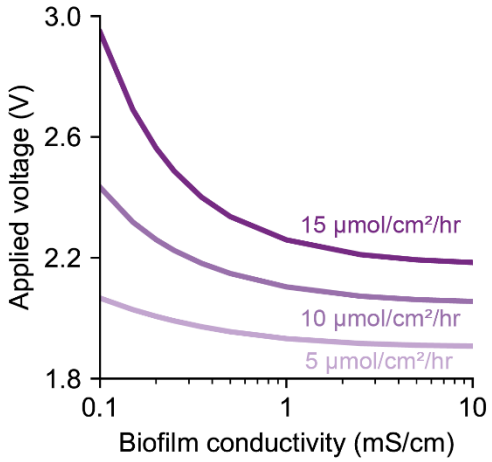

Figure S3. Effect of biofilm conductivity on operating voltage. Voltage necessary to operate the MES reactor 50 µm biofilm fixing carbon using the rTCA cycle as a function of the biofilm conductivity for different pyruvate production rates.

Supplementary note 9: which processes can limit the CO_2 fixation rate in the biocathode layer? Several processes could limit the overall CO_2 fixation rate in the biocathode layer. Any process in the electron transfer pathway, including electron uptake, passage through the electron conduit proteins, electron transfer into the quinone pool, and regeneration of reducing equivalents (including electron transfer from the quinone pool and ATP synthesis), could limit the CO_2 fixation rate. Enzyme kinetics within the carbon fixation pathway could also limit the CO_2 fixation rate. Finally, the availability of a necessary substrate (CO_2 or the terminal electron acceptor) could limit the CO_2 fixation rate.

Electron transfer from the electrode to the exterior heme groups in MtrC would limit the overall reaction rate when the overpotential driving the charge transfer reaction is low (following Butler-Volmer kinetics). In principle, this rate could be made to be arbitrarily fast, so at high overpotentials this transfer process would not limit the overall reaction rate.

Electron hopping through the MtrCAB/CctA/CymA conduit could also limit the overall reaction rate. Previous analyses demonstrated that the rate of electron hopping through heme groups in MtrC and MtrF is on the order of 10^5 s^{-1}, [36] and that there are ~72,000 MtrC proteins per *Shewanella* cell.[37] In contrast, rate-limiting carbon fixing enzymes have a turnover number of ~2-20 s^{-1} with a comparable intracellular enzyme concentration of~70,000/cell (Supplementary Note 2). Hence, even accounting for the ~50 e^- required per CO_2 fixed (Supplementary Table 2), electron hopping through the electron conduit proteins is likely to be at least 2 orders of magnitude faster than electron consumption via CO_2 fixation. Hence, there is no likely scenario in which this electron hopping mechanism would limit the overall reaction rate.

Either aerobic or anaerobic respiration and energy carrier regeneration, could also limit the overall rate of carbon fixation. However, aerobic and anaerobic nitrate respiration support heterotrophic growth rates significantly faster than autotrophic growth regardless of the terminal electron acceptor.[38–40] The upper bound kinetics of respiration and energy carrier regeneration are therefore unlikely to limit the overall reaction rate.

The availability of CO_2 or the terminal electron acceptor in the biocathode layer could also limit the reaction rate. In the case of O_2, the overall reaction rate (except at extremely low overpotentials, as noted above) is severely limited by O_2 availability. Nitrate availability, in contrast, never limits the overall reaction rate in the system because its solubility is substantially greater than that of CO_2. Hence, in the case of nitrate respiration, neither respiration nor energy carrier regeneration limit the overall reaction rate.

Hence, there are three processes that may limit the overall CO_2 fixation rate: the enzyme kinetics of carbon fixation, the charge transfer kinetics of electron uptake, and the availability of CO_2. I account for these processes in the model as described in the main text.

Supplementary References

1 M. Calvin and A. A. Benson, *Science (80-.).*, 1948, **107**, 476–480.
2 M. C. Evans, B. B. Buchanan and D. I. Arnon, *Proc. Natl. Acad. Sci. U. S. A.*, 1966, **55**, 928–934.
3 S. Herter, G. Fuchs, A. Bacher and W. Eisenreich, *J. Biol. Chem.*, 2002, **277**, 20277–20283.
4 H. Holo, *Arch. Microbiol.*, 1989, **151**, 252–256.
5 L. Ljungdahl, *Annu. Rev. Microbiol.*, 1986, **40**, 415–450.
6 B. V Vitagliano and P. A. Lyons, *J. Am. Chem. Soc.*, 1956, **78**, 1549–1552.
7 C. Picioreanu, M. C. M. Van Loosdrecht and J. J. Heijnen, *Water Sci. Technol.*, 1997, **36**, 147–156.
8 J. Newman and K. E. Thomas-Alyea, *Electrochemical Systems*, Wiley, Hoboken, N. J., 3rd edn., 2004.
9 E. L. Cussler, *Diffusion: Mass Transfer in Fluid Systens*, Cambridge University Press, Cambridgeshire, New York, 3rd edn., 2009.
10 K. G. Schulz, U. Riebesell, B. Rost, S. Thoms and R. E. Zeebe, *Mar. Chem.*, 2006, **100**, 53–65.
11 P. W. Atkins, *Physical Chemistry*, Oxford University Press, 4th edn., 1990.
12 S. Haussener, C. Xiang, J. M. Spurgeon, S. Ardo, N. S. Lewis and A. Z. Weber, *Energy Environ. Sci.*, 2012, **5**, 9922–9935.
13 L. A. Meitl, C. M. Eggleston, P. J. S. Colberg, N. Khare, C. L. Reardon and L. Shi, *Geochim. Cosmochim. Acta*, 2009, **73**, 5292–5307.
14 M. Lin, L. Han, M. R. Singh and C. Xiang, *ACS Appl. Energy Mater.*, 2019, **2**, 5843–5850.
15 H. W. Blanch and D. S. Clark, *Biochemical Engineering*, CRC Press, 2nd edn., 1997.
16 G. G. B. Tcherkez, G. D. Farquhar and T. J. Andrews, *Proc. Natl. Acad. Sci. U. S. A.*, 2006, **103**, 7246–7251.
17 H. J. Vos, P. J. Heederik, J. J. M. Potters and K. C. A. M. Luyben, *Bioprocess Eng.*, 1990, **5**, 63–72.
18 B. H. Kim and G. M. Gadd, *Bacterial Physiology and Metabolism*, Cambridge University Press, New York, USA, 2008.
19 I. A. Berg, *Appl. Environ. Microbiol.*, 2011, **77**, 1925–1936.
20 O. Mueller-Cajar, M. Morell and S. M. Whitney, *Biochemistry*, 2007, **46**, 14067–14074.
21 T. M. Wahlund and F. R. Tabita, *J. Bacteriol.*, 1997, **179**, 4859–4867.

22 W. Kim and F. Robert Tabita, *J. Bacteriol.*, 2006, **188**, 6544–6552.
23 A. B. Hawkins, M. W. W. Adams and R. M. Kelly, *Appl. Environ. Microbiol.*, 2014, **80**, 2536–2545.
24 J. R. Roberts, W.-P. P. Lu and S. W. Ragsdale, *J. Bacteriol.*, 1992, **174**, 4667–4676.
25 R. Milo, *BioEssays*, 2013, **35**, 1050–1055.
26 Y. M. Bar-On and R. Milo, *Proc. Natl. Acad. Sci. U. S. A.*, 2019, **116**, 4738–4743.
27 D. A. Stolpera, N. P. Revsbech and D. E. Canfield, *Proc. Natl. Acad. Sci. U. S. A.*, 2010, **107**, 18755–18760.
28 J. C. Cotton, A. L. Pometto and J. Gvozdenovic-Jeremic, *Appl. Microbiol. Biotechnol.*, 2001, **57**, 626–630.
29 V. Janakiraman, D. Englert, A. Jayaraman and H. Baskaran, *Ann. Biomed. Eng.*, 2009, **37**, 1206–1216.
30 L. Labík, R. Vostal, T. Moucha, F. Rejl and M. Kordač, *Chem. Eng. J.*, 2014, **240**, 55–61.
31 E. L. Clark, J. Resasco, A. Landers, J. Lin, L. T. Chung, A. Walton, C. Hahn, T. F. Jaramillo and A. T. Bell, *ACS Catal.*, 2018, **8**, 6560–6570.
32 F. Kracke, I. Vassilev and J. O. Krömer, *Front. Microbiol.*, 2015, **6**, 1–18.
33 T. A. Clarke, M. J. Edwards, A. J. Gates, A. Hall, G. F. White, J. Bradley, C. L. Reardon, L. Shi, A. S. Beliaev, M. J. Marshall, Z. Wang, N. J. Watmough, J. K. Fredrickson, J. M. Zachara, J. N. Butt and D. J. Richardson, *Proc. Natl. Acad. Sci.*, 2011, **108**, 9384–9389.
34 A. C. L. De Lichtervelde, A. Ter Heijne, H. V. M. Hamelers, P. M. Biesheuvel and J. E. Dykstra, *Phys. Rev. Appl.*, 2019, **12**, 14018.
35 N. S. Malvankar, M. T. Tuominen and D. R. Lovley, *Energy Environ. Sci.*, 2012, **5**, 5790–5797.
36 X. Jiang, B. Burger, F. Gajdos, C. Bortolotti, Z. Futera, M. Breuer and J. Blumberger, *Proc. Natl. Acad. Sci.*, 2019, **116**, 3425–3430.
37 D. E. Ross, S. L. Brantley and M. Tien, *Appl. Environ. Microbiol.*, 2009, **75**, 5218–5226.
38 K. B. Andersen and K. Von Meyenburg, *J. Bacteriol.*, 1980, **144**, 114–123.
39 V. Stewart, Y. Lu and A. J. Darwin, *J. Bacteriol.*, 2002, **184**, 1314–1323.
40 A. Ishizaki and K. Tanaka, *J. Ferment. Bioeng.*, 1990, **69**, 170–174.

Appendix D: Supplementary information for Chapter 5

Supplementary Figures

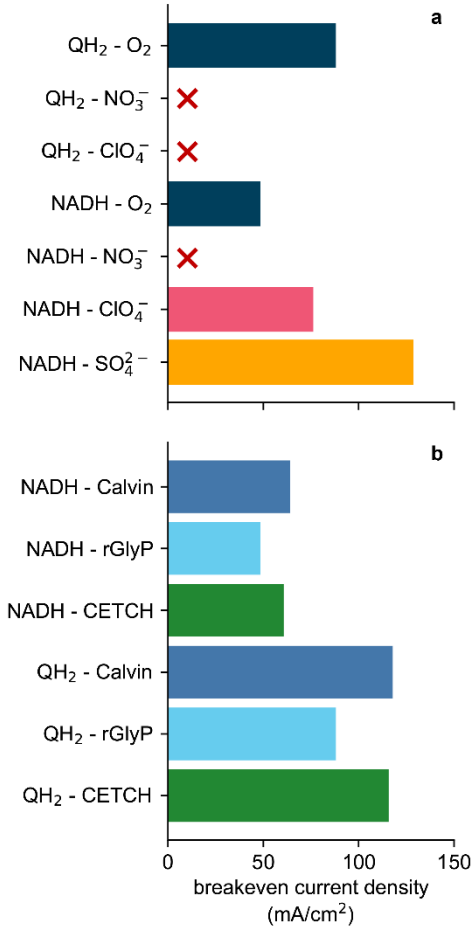

Figure S1. Breakeven current densities. Current density at which the GWP of DET-based EMP is equal to the GWP of H_2-mediated EMP operating at 90% carbon efficiency. Red "x"s indicate that a given DET metabolic strategy is unable to achieve parity with H_2-mediated system. All bars in (**a**) assume the reductive glycine pathway is used to fix carbon. All bars in (**b**) assume O_2 is the terminal electron acceptor. Note that these values do not consider the additional energy demand necessary to overcome efficiency losses in the DET reactor.

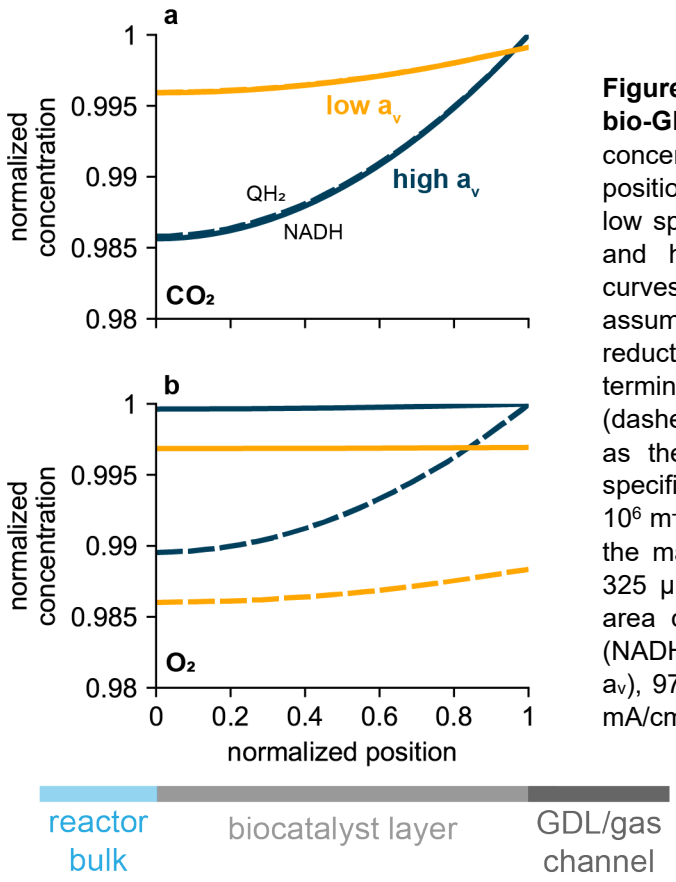

Figure S2. CO_2 and O_2 transport in the bio-GDE. Liquid phase (**a**) CO_2 and (**b**) O_2 concentration as a function of normalized position within the biocatalyst layer for the low specific surface area (yellow curves) and high specific surface area (blue curves) GDE cases. Microbes are assumed to be fixing carbon using the reductive glycine pathway, with O_2 as the terminal electron acceptor and QH_2 (dashed curves) or NADH (solid curves) as the electron sink. "High" and "low" specific surface areas correspond to 1 × 10^6 m^{-1} and 5.6 × 10^4 m^{-1}, as described in the main text. These calculations use a 325 μm biocatalyst layer; the projected-area current densities are 173 mA/cm^2 (NADH, high a_v), 283 mA/cm^2 (QH_2, high a_v), 97 mA/cm^2 (NADH, low a_v), and 158 mA/cm^2 (QH_2, low a_v).

Table S1. Model parameters for the bio-GDE.

Parameter	Value	Units	References
Operating conditions			
T	310.15	K	fixed
P_0	2	atm	fixed
$y_{\mathrm{f,CO_2}}$	0.5	--	fixed
$y_{\mathrm{f,O_2}}$	0.5	--	fixed
l_{bCL}	325	μm	fixed
Geometry			
θ^{CM}	0.2	--	[1]
$a_{\mathrm{v}}^{\mathrm{CM}}$	1×10^6 (high surface area) 5.6×10^5 (thick biofilm)	m^{-1}	assumed
t^{X}	1 (high surface area) 10 (thick biofilm)	μm	assumed
S	0.64	--	[2]
r_{P}	1.47	μm	[2]
Liquid-phase diffusion coefficients			
$D^{\mathrm{L}}_{\mathrm{CO_2}}$	$14.6836\times10^{-9}\left(\frac{T}{217.2056}-1\right)^{1.997}$	$m^2\ s^{-1}$	[3]
$D^{\mathrm{L}}_{\mathrm{O_2}}$	$10\text{^}\left(8.410+\frac{773.8}{T}-\left(\frac{506.5}{T}\right)^2\right)$	$m^2\ s^{-1}$	[4]

Gas-phase diffusion coefficients			
$D_{O_2-CO_2}$	0.156	$cm^2\ s^{-1}$	5
$D_{N_2-CO_2}$	0.165	$cm^2\ s^{-1}$	5
$D_{O_2-N_2}$	0.225	$cm^2\ s^{-1}$	5
Gas-phase transport parameters			
μ^G	1.9×10^{-5}	Pa s	6
κ^G	1.72×10^{-7}	cm^2	2
Enzyme kinetics			
k_{cat,CO_2}	100	s^{-1}	7
E_{CO_2}	0.224	mM	Note 1
K_{M,CO_2}	3.3	mM	8
$k_{cat,O_2} \times E_{O_2}$	2083	$mmol\ L^{-1}\ s^{-1}$	9
K_{M,O_2}	3	nM	10

Table S2. Full electrochemical model parameters.

Parameter	Value	Unit	References
Operating conditions			
T	310.15	K	fixed
P	2	atm	fixed
y_{f,CO_2}	0.5	--	fixed
$c'_{sucrose}$	100	$g\ L^{-1}$	fixed
Geometry			
S_A	100	m^{-1}	assumed
$l_{membrane}$	100	µm	assumed
l_{BL}	100	µm	assumed
l_{bCL}	325	µm	assumed
Diffusion coefficients			
D_{H^+}	$1.56\times10^{-10}(T-273.15)+5.49\times10^{-9}$	$m^2\ s^{-1}$	8
D_{OH^-}	$4.52\times10^{-4}\exp\left(-1618\left(\frac{1}{T}+\frac{1}{273.15}\right)\right)$	$m^2\ s^{-1}$	8
D_{Na^+}	$8.85\times10^{-12}T$	$m^2\ s^{-1}$	8
$D_{HCO_3^-}$	$7.016\times10^{-9}\left(\frac{T}{204.028}-1\right)^{2.3942}$	$m^2\ s^{-1}$	3
$D_{CO_3^{2-}}$	$5.447\times10^{-9}\left(\frac{T}{210.265}-1\right)^{2.192}$	$m^2\ s^{-1}$	3
$D_{NO_3^-}$	$5.08\times10^{-12}T$	$m^2\ s^{-1}$	8
D_{CO_2}	$14.6836\times10^{-9}\left(\frac{T}{217.2056}-1\right)^{1.997}$	$m^2\ s^{-1}$	3
D_{O_2}	$14.6836\times10^{-9}\left(\frac{T}{217.2056}-1\right)^{1.997}$	$m^2\ s^{-1}$	3
Acid-base reactions			
S_1	-96.31	$J\ mol^{-1}\ K^{-1}$	6
S_2	-148.1	$J\ mol^{-1}\ K^{-1}$	6
S_W	-80.66	$J\ mol^{-1}\ K^{-1}$	6
H_1	7.64	$kJ\ mol^{-1}$	6

H_2	14.85	kJ mol^{-1}	6
H_W	55.84	kJ mol^{-1}	6
k_1	$\exp\left(1246.98 - \left(6 \times \frac{10^4}{T} - 183\ln(T)\right)\right.$	s^{-1}	11
k_2	59.44	s^{-1}	11
k_3	2.23×10^3	L mol^{-1} s^{-1}	11
k_4	6.0×10^9	L mol^{-1} s^{-1}	11
k_W	2.4×10^{-5}	L mol^{-1} s^{-1}	12
Gas solubility			
A_1	-60.2409	--	13
A_2	93.4517	--	13
A_3	23.3585	--	13
B_1	2.3517×10^{-2}	--	13
B_2	-2.3656×10^{-2}	--	13
B_3	4.7036×10^{-3}	--	13
Electrode reactions – anode			
$i_{0,OER}$	1×10^{-8}	A cm^{-2}	14
E^0_{OER}	1.23	V	12
$\alpha_{a,OER}$	1.7	--	14
$\alpha_{c,OER}$	0.1	--	14
Electrode reactions – biocatalyst layer			
$i_{0,X}$	1.368×10^{-8}	A cm^{-2}	15
E^0_X	0.314 (QH_2) 0.064 (NADH)	V	Eq. 7, 8
$\alpha_{a,X}$	0.5	--	15
$\alpha_{c,X}$	0.5	--	15
Electron transport			
σ_{GDE}	220	S m^{-1}	2

Supplementary Note 1: Intracellular CO_2-fixation enzyme concentration

To estimate the intracellular concentration of formate dehydrogenase (which is assume to be the rate-limiting step in the reductive glycine pathway, following Bar Even *et al.*[7]), I use the estimate that the total intracellular protein count is ~2.36×10^6,[16] and assume that formate dehydrogenase comprises ~3% of the total protein count. This number is based on the estimate that RuBisCo comprises ~3% of all proteins in autotrophic microbes that use the Calvin cycle to fix carbon.[17] I also assume a cell diameter of 1 μm, in accordance with the geometric assumptions regarding the bCL.

References

1 Fuel Cell Store, *Sigracet GDL 34 & 35 Series Gas Diffusion Layer*, 2020.

2 L. C. Weng, A. T. Bell and A. Z. Weber, *Phys. Chem. Chem. Phys.*, 2018, **20**, 16973–16984.

3 R. E. Zeebe, *Geochim. Cosmochim. Acta*, 2011, **75**, 2483–2498.

4 P. Han and D. M. Bartels, *J. Phys. Chem.*, 1996, **100**, 5597–5602.

5 E. L. Cussler, *Diffusion: Mass Transfer in Fluid Systens*, Cambridge University Press, Cambridgeshire, New York, 3rd edn., 2009.

6 D. R. Lide, Ed., *CRC Handbook of Chemistry and Physics, 84th edition*, CRC Press, 84th edn., 2004.
7 A. Bar-Even, E. Noor, A. Flamholz and R. Milo, *Biochim. Biophys. Acta - Bioenerg.*, 2013, **1827**, 1039–1047.
8 A. J. Abel and D. S. Clark, *ChemSusChem*, 2021, **14**, 344–355.
9 K. B. Andersen and K. Von Meyenburg, *J. Bacteriol.*, 1980, **144**, 114–123.
10 D. A. Stolpera, N. P. Revsbech and D. E. Canfield, *Proc. Natl. Acad. Sci. U. S. A.*, 2010, **107**, 18755–18760.
11 K. G. Schulz, U. Riebesell, B. Rost, S. Thoms and R. E. Zeebe, *Mar. Chem.*, 2006, **100**, 53–65.
12 P. W. Atkins, *Physical Chemistry*, Oxford University Press, 4th edn., 1990.
13 Ulf Riebesell, Victoria J. Fabry, Lina Hansson and Jean-Pierre Gattuso, *Guide to best practices for ocean acidification research and data reporting*, 2011.
14 S. Haussener, C. Xiang, J. M. Spurgeon, S. Ardo, N. S. Lewis and A. Z. Weber, *Energy Environ. Sci.*, 2012, **5**, 9922–9935.
15 A. J. Abel, J. M. Hilzinger, A. P. Arkin and D. S. Clark, *Bioelectrochemistry*, 2022, 108054.
16 R. Milo, *BioEssays*, 2013, **35**, 1050–1055.
17 Y. M. Bar-On and R. Milo, *Proc. Natl. Acad. Sci. U. S. A.*, 2019, **116**, 4738–4743.

Appendix E: Supplementary information for Chapter 6

Supplementary figures

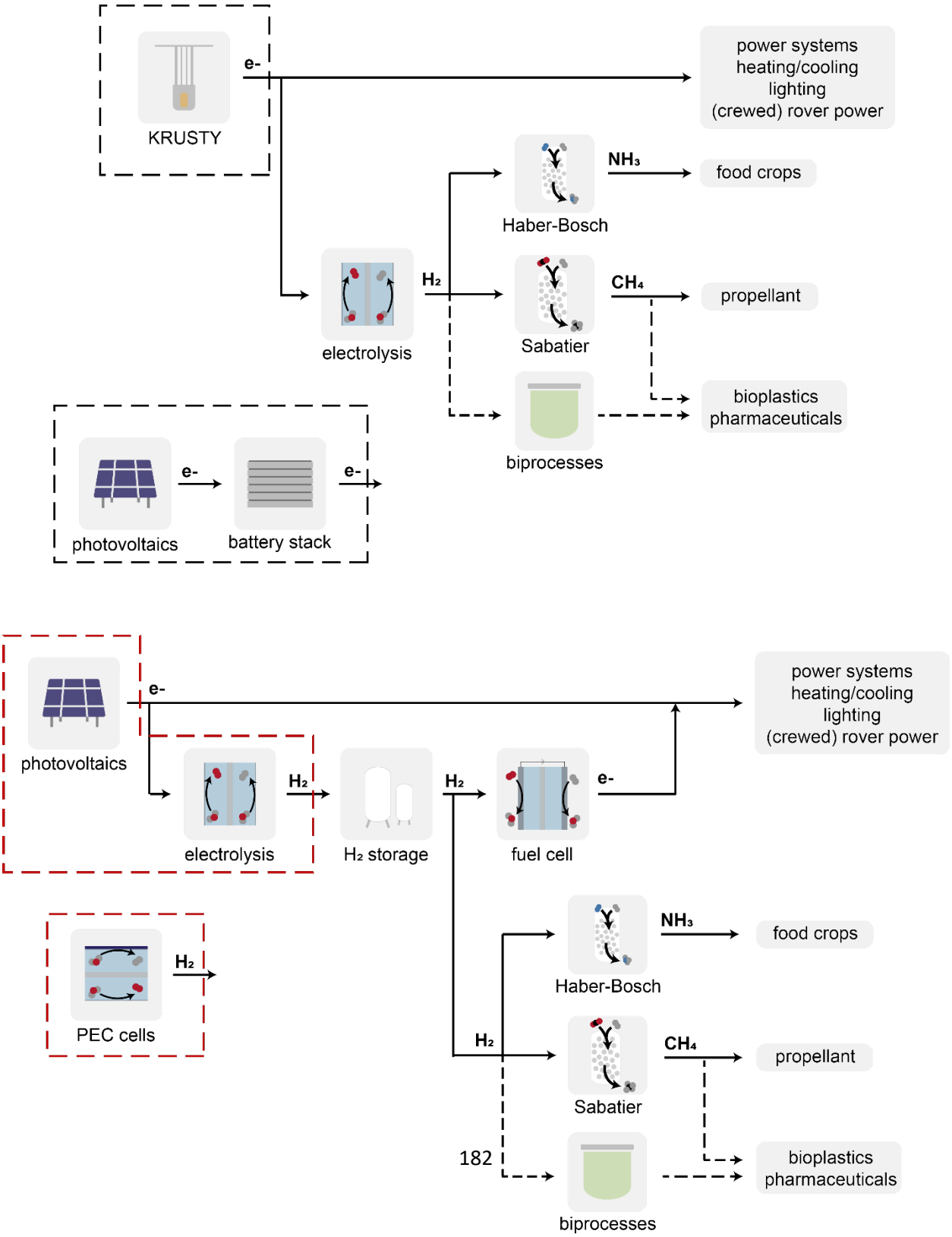

Figure S1. Power generation systems options. Habitat power systems and ammonia, propellant, and bioplastics production can be powered by nuclear power generation (KRUSTY), photovoltaics with battery storage (PV+B), photovoltaics with H_2 energy storage from hydrolysis (PV+E), or photoelectrochemical H_2 generation and storage (PEC).

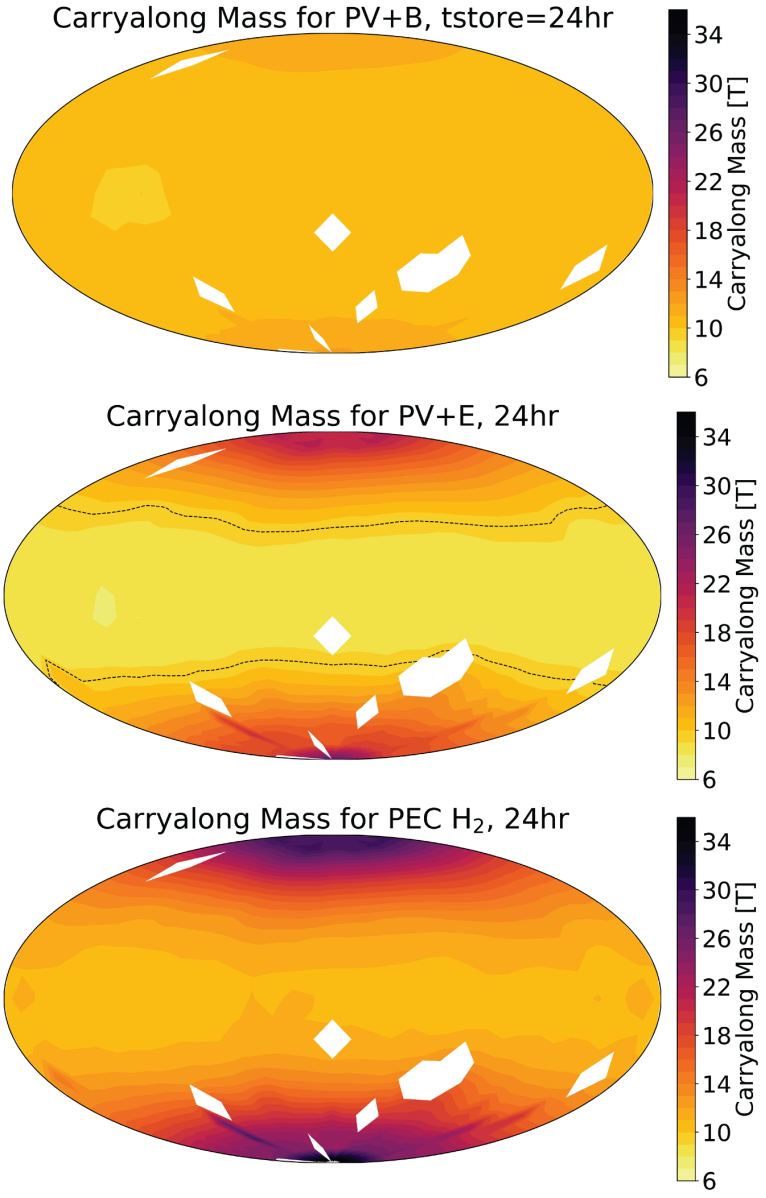

Figure S2. Carry-along mass for different power generation scenarios. Carry-along mass across the Martian surface for PV+B, PV+E, and PEC power generation systems. PV+B and PEC systems cannot reach parity with nuclear power generation in terms of carry-along mass (no locations at which the projected mass of the PV+B or PEC systems are less than the project mass of the nuclear system).

Supplementary tables

Table S1. Parameters for power and energy demand calculations.

Parameter	Value	Unit	Reference
Power and Material Demands			
P_{Hab}	40	kW	Note 1.1
$\dot{N}$	8.33×10^{-3}	kg h^{-1}	Note 1.2
$\dot{M}$	0.61	kg h^{-1}	Note 1.3
$\dot{B}$	0.10	kg h^{-1}	Note 1.4
Conversion factors			
α_{HB}	0.196	kgH_2 $kgNH_3^{-1}$	Note 1.2
α_{S}	0.554	kgH_2 $kgCH_4^{-1}$	Note 1.3
α_{BP}	0.155	kgH_2 $kgAcH^{-1}$	Note 1.4
α_{E}	54.13	kWh kgH_2^{-1}	Note 1.5
α_{FC}	0.064	kgH_2 kWh^{-1}	Note 1.5
α_{HS}	3.39	kWh kgH_2^{-1}	Note 1.5
Power and energy density			
p_{K}	6.25×10^{-3}	kW kg^{-1}	[1]
η_{B}	80	%	[2]
p_{E}	1.14×10^{-2}	kgH_2 h^{-1} kg^{-1}	Note 1.5
e_{B}	0.16	kWh kg^{-1}	[3]
p_{FC}	0.365	kW kg^{-1}	Note 1.5
e_{HS}	7.18×10^{-2}	kgH_2 kg^{-1}	Note 1.5
Solar cell array mass			
M_{PV}	2.0	kg m^{-2}	Note 1.6
M_{PEC}	2.4	kg m^{-2}	Note 1.6
Other parameters			
χ	0.33	--	Assumed
t_{store}	24.6	h	Assumed

Table S2. Comparison of optimal bandgaps for different optimization strategies.

Commodity	Best efficiency at averaged solar noon	Best production over a year
Power (3-junction PV)	Top: 1.77 eV Middle: 1.16 eV Bottom: 0.72 eV	Top: 1.83 eV Middle: 1.16 eV Bottom: 0.67 eV
H_2 (PEC, 2-junction)	Top: 1.64 eV Bottom: 0.95 eV	Top: 1.77 eV Bottom: 0.83 eV

Supplementary notes

Note 1.1 – Habitat power demand
Continuous power demand estimates for a Martian habitat range between 4 and ~100 kW. We use 40 kW as a baseline value following the NASA Baseline Values and Assumptions Document (BVAD).[4] This value includes ISRU power demands, including for crop growth, so we only calculated additional power demands for H_2 production for the ISRU processes considered.

Note 1.2 – ammonia demand
To calculate an upper-bound ammonia demand, we followed the optimization strategy by Do *et al.* assuming no recycling of nitrogen via urea recovery.[5] Briefly, we assumed that the metabolic demands for six crewmembers would be met entirely by food crops grown in hydroponic chambers. We used values from the BVAD and Wheeler (2003) to calculate nitrogen demand per nutrient availability for a given crop.[4,6] The optimization function was defined to balance minimization of area necessary for crop growth with maximization of crop variability for human morale:

$$\begin{aligned} \mathrm{f} &= \mathrm{w}_1 \sum_i A_i + w_2 \sigma(\boldsymbol{A}) \\ &\text{S.T.} \\ \sum_i A_i r_i x_{i,j} &\geq X_j \end{aligned} \tag{233}$$

where f is the optimization function, A_i is the growth area for crop i, σ is the standard deviation of the vector of crop areas ($\boldsymbol{A}$), r_i is the static growth rate, $x_{i,j}$ is the nutritional content of crop i for nutrient j, and X_j is the crewmember demand for nutrient j. The relative weights w_1 and w_2 are related by $w_2 = 1 - w_1$, and w_1 was varied between 0 and 1. Using $w_1 = 0.25$, all 5 crops we considered (soybean, wheat, lettuce, potato, peanut) were included, resulting in a total crop growth area of ~421 m^2 and an ammonia demand of ~205 g/sol, which we converted to 8.33 g/h for consistent units in Table S1. The nitrogen demand ranged between ~285 g/sol and ~194 g/sol for $0 < w_1 < 1$.

We assume ammonia is produced *via* the Haber-Bosch process with the characteristic reaction

$$\mathrm{N_2} + 3\mathrm{H_2} \rightarrow 2\mathrm{NH_3} \tag{234}$$

Hence, the H_2:NH_3 conversion factor is 0.196 kg H_2/kg NH_3 assuming 90% conversion of H_2.

Note 1.2 – methane demand
Resupply and crewmember return to Earth from Mars will require that interplanetary transit vehicles can be refueled on Mars. We use the estimate by Kleinhenz and Paz[7] that such refueling requires 6978 kgCH_4 produced every 480 sols, corresponding to a CH_4 production rate of 0.61 kg/h. We assume this methane is produced via the Sabatier reaction:

$$CO_2 + 4H_2 \rightarrow CH_4 + 2H_2O \quad (235)$$

resulting in an H_2:CH_4 conversion factor of 0.554 kg H_2/kg CH_4 assuming 90% conversion efficiency.

Note 1.4 – bioplastics and biopharmaceutical demand
Bioplastics and pharmaceutical demands for a Martian habitat are not well-defined in the literature. For a system where 50% of spare parts necessary for a habitat are generated via additive manufacturing based on ISRU, Owens *et al.* estimated that 9800 kg of spare parts mass would be necessary over 260 months (an extremely long duration with multiple resupplies and crewmember exchanges).[8] Assuming these spares are generated from bioplastics, which are in turn produced from acetic acid at 50% yield by C_2 feedstock-utilizing microorganisms,[9] this corresponds to ~0.1 kg/h acetic acid demand. We assume acetic acid is produced by acetogens with a molar ratio of 4.2:1 (corresponding to 95% of H_2 reducing power diversion to acetic acid production, a common value for acetogens), this corresponds to an H_2:CH_3COOH ratio of 0.155 kg H_2/kg CH_3COOH assuming 90% conversion.

Pharmaceutical demand is not expected to exceed 1 g/sol, so we neglect this amount for the purposes of our calculations here.

Note 1.5 – water electrolyzer, H_2 fuel cell, and H_2 storage systems
Water electrolysis and H_2 fuel cell power demands are based on commercially available, low-weight fuel cell systems designed for transportation vehicles (G-HFCS-6kW Hydrogen Fuel Cell Power Generator (Fuel Cell Store, Product Code: 1035012)). The electrolyzer requires 54.13 kWh/kg H_2, while the fuel cell requires 0.064 kg H_2/kWh. We assume H_2 storage is accomplished with Type IV compression chambers at 350 bar, which stores H_2 at 20.77 kgH_2/m^3 with a tank mass of 289.23 kg/m^3, corresponding to a H_2 storage density of 0.0718 kgH_2/kg.[10,11] For these systems, 3.39 kWh/kgH_2 is required to compress H_2 to 350 bar, which we account for in the total power demand.[10]

Note 1.6 – solar cell array mass
Commercial low-weight, flexible solar cell arrays have an installed mass of 2.0 kg/m^2 (MiaSolé Flex-03W Series Module with adhesive). We are not aware of similarly commercial PEC arrays, so we assume that the installed mass is driven primarily by the absorber material as opposed to the catalyst layers or ion exchange membrane. We therefore estimate an installed mass of 2.4 kg/m^2 by assuming the absorber and housing components comprise 80% of the installed mass.

References

1 L. Palac, Donald Gibson, Marc Mason and R. C. Mcclure, Patrick Ray Robinson, *Nucl. Emerg. Technol. Sp. 2018*.
2 A. Eftekhari, *Sustain. Energy Fuels*, 2017, **1**, 2053–2060.
3 M. A. Hannan, M. M. Hoque, A. Hussain, Y. Yusof and P. J. Ker, *IEEE Access*, 2018, **6**, 19362–19378.
4 M. S. Anderson, M. K. Ewert, J. F. Keener and M. S. Anderson, .
5 S. Do, A. Owens, K. Ho, S. Schreiner and O. De Weck, *Acta Astronaut.*, 2016, **120**, 192–

228.
6 R. M. Wheeler, *NASA Sci. Tech. Inf.*, 2003.
7 J. E. Kleinhenz and A. Paz, *10th Symp. Sp. Resour. Util. 2017*, 2017, 1–11.
8 A. Owens, S. Do, A. Kurtz and O. de Weck, *45th Int. Conf. Environ. Syst.*, 2015, 1–17.
9 A. J. Berliner, J. M. Hilzinger, A. J. Abel, M. J. McNulty, G. Makrygiorgos, N. J. H. Averesch, S. Sen Gupta, A. Benvenuti, D. F. Caddell, S. Cestellos-Blanco, A. Doloman, S. Friedline, D. Ho, W. Gu, A. Hill, P. Kusuma, I. Lipsky, M. Mirkovic, J. Luis Meraz, V. Pane, K. B. Sander, F. Shi, J. M. Skerker, A. Styer, K. Valgardson, K. Wetmore, S.-G. Woo, Y. Xiong, K. Yates, C. Zhang, S. Zhen, B. Bugbee, D. S. Clark, D. Coleman-Derr, A. Mesbah, S. Nandi, R. M. Waymouth, P. Yang, C. S. Criddle, K. A. McDonald, L. C. Seefeldt, A. A. Menezes and A. P. Arkin, *Front. Astron. Sp. Sci.*, 2021, **8**, 1–14.
10 P. Di Profio, S. Arca, F. Rossi and M. Filipponi, *Int. J. Hydrogen Energy*, 2009, **34**, 9173–9180.
11 H. Barthelemy, M. Weber and F. Barbier, *Int. J. Hydrogen Energy*, 2017, **42**, 7254–7262.